NORTHWESTERN UNIVERSITY

Probing the Molecular Details of Particulate Methane Monooxygenase in Micelles to Cells

A DISSERTATION

SUBMITTED TO THE GRADUATE SCHOOL

IN PARTIAL FULFILLMENT OF THE REQUIREMENTS

for the degree

DOCTOR OF PHILOSOPHY

Field of Interdisciplinary Biological Sciences

By

Soo Yeon Ro

EVANSTON, ILLINOIS

September 2019

ABSTRACT

Harnessing the metabolic potential of methanotrophic bacteria is a compelling strategy for the bioremediation of environmentally harmful methane gas. Methanotrophs can activate a 105 kcal/mol C-H bond in methane at ambient conditions using metalloenzymes called methane monooxygenases (MMOs). Particulate methane monooxygenase (pMMO) is a copper-dependent, membrane-bound enzyme that is the predominant biological methane sink in nature. Despite its significant impact on the global carbon cycle, a molecular and mechanistic understanding of the pMMO active site is limited. The challenges stem from the structural complexity of pMMO and difficulties in manipulating the host organisms.

At the beginning of this dissertation work in 2014, multiple crystal structures had already been obtained, which showed three subunits, PmoB, PmoA, and PmoC, assembled into a larger $\alpha_3\beta_3\gamma_3$ complex. These structures, along with spectroscopic studies, identified three metal centers that may house the catalytic copper ions, the Cu_B, bis-His, and Cu_C sites. However, low resolution structures, a mixture of copper species, and low enzymatic activity hampered characterization of the active site. Furthermore, the lack of a heterologous expression system or facile mutagenesis of methanotrophs limited pMMO studies to traditional biochemical and spectroscopic methods.

Hence in this thesis dissertation, pMMO was investigated in native-like environments to more closely mimic its in vivo structure and function. pMMO reconstituted into membrane-mimetics exhibited methane oxidation activity, which confirmed the importance of studying pMMO in a membrane-dependent context. The active enzyme-membrane complex was further characterized via native top-down mass spectrometry (nTDMS) metal localization studies, which provided evidence that a monocopper Cu_C site was essential for activity. Recently developed

genetic toolkits were applied to pMMO mutagenesis in an attempt to elucidate the essential residues involved in activity. Furthermore, the scope of this thesis was extended beyond pMMO to include isolation of a lanthanide-dependent methanol dehydrogenase and study of its interaction with pMMO. Additionally, mutagenesis of the extended *pmo* and *mbn* operons helped to identify key enzymes involved in copper uptake and transport. This dissertation highlights the benefits of interdisciplinary approaches that will shape future pMMO investigations.

ACKNOWLEDGEMENTS

I can proudly declare that my time as a graduate student at Northwestern University has been the richest experience in my life. After college, I decided to pursue a graduate degree in biology because science, despite all its unknowns, was the only thing that made sense to me. At that point in my life, science represented happiness, acceptance, security, and most importantly hope. Six years later, these associations have solidified. I felt my intellectual potential was challenged in a safe environment while surrounded by brilliant and open-minded individuals. On a daily basis, I felt grateful for the privilege to grow on a professional and individual level, and I can now walk away from this journey with absolutely zero regrets. These positive thoughts and experiences are only possible due to my amazing mentors, coworkers, and friends, whom I would like to thank.

I am very lucky to have joined Dr. Amy Rosenzweig's laboratory. Amy's mentorship style is my type; she allows her students independence but is always around to provide guidance at crucial moments. I admire her extreme productivity and pragmatism that couples well with her patient and understanding nature. Her high expectations and professionalism provide a great model that I will work on emulating throughout my career. Under her mentorship, I have become a better scientist, communicator, and overall person, and I feel confident that this evolved version of myself is fit for the next journey. I will definitely miss having her as my scientific mentor and know that I have been spoiled so early in my career by having an awesome boss. I will also miss seeing her face and her slightly mischievous smile every day, her five million shoes, her hair, her lox and bagels, and my routine of yelling "Hi!" into her office to surprise her. Not many graduate students have the chance of working with an amazing mentor like Amy, so if I went back in time, I would choose her lab all over again without a doubt.

I felt very accepted and comfortable when I joined the lab, all thanks to Dr. Sarah Sirajuddin, my graduate mentor and now close friend. By the time I got to know her, I could see Sarah picked up some of Amy's good traits. She had developed strong communication skills and a professional attitude. She taught me everything about pMMO in a short timeframe in an effective and positive manner. Sarah's defining characteristic was her positivity that I easily connected with. Every day in lab, we laughed together about something or another. Her friendly attitude encouraged me to continue to find moments of happiness on a daily basis, which I believe was instrumental in my overall positive experiences in graduate school.

I would also like to thank past lab members for my great time here. I really appreciate Dr. Aaron Smith for his leadership and mentorship skills. Dr. Laura Dassama was also a source of great wisdom in science and life – thank you for the excellent buffalo sauce dip recipe. Dr. Thomas Lawton made me feel comfortable coming up to him to ask for scientific advice, drinks, and apparently his pony tail! I am still amazed with all his antics that was tolerated by Amy. Dr. Grace Kenney was also an important mentor and collaborator, and I had fun working with her at night and complaining about methanotrophs. Dr. Rahul Purohit was a great collaborator and friend; he has such a nice soul and I look forward to continuing my friendship with him.

I also highly appreciate my relationships with current lab members. Matt Ross has been a great collaborator and fellow pMMO member. I have had many fun times with Dr. Oriana Fisher, from scientific collaborations, opera nights, cat sitting, to chill drinking. I appreciate the new lab members for bringing new energy and knowledge into our lab – fiery Ricky Jodts, calm Madison Sendzik, comically paranoid Gerri Roberts, and cool Dr. Tasha Manesis. I would like to mention Dr. Yun Ji Park and Chris Koo, who were my main support group in lab. I thank Yun Ji for the million meals she has cooked for me, her quirky personality, and most importantly her friendship.

Chris and I started as comrades in our battle with pMMO and developed a close friendship with many shared experiences. He is a great coworker, collaborator, and friend, and I feel lucky our lives intersected at this moment. Yun Ji, Chris, and I are now inseparable and forever tied together, and I feel excited for our future journey.

I am also so lucky to have such a great collaborator as Luifer Schachner, a fellow graduate student in the Kelleher group. He and I have great chemistry and work well together. We went through many scientific tribulations together to create a wonderful story. Through this relationship, I have learned the importance of collaborations and how fun it can be. I hope to one day work with him again!

I have also made unexpected friendships with my undergraduate mentees. Yue Wen Deng was my first undergraduate student and now she is a sister I've never had. Yue Wen was a brilliant undergraduate student that impressed the lab members with her dedication to science. I appreciate her mom's unlimited dim sum and care when I visited her hometown. I expect Yue Wen to be my future unofficial doctor and unofficial sister-in-law. She is forever trapped. I am also very fortunate to meet my second mentee Amanda Tam. Her positivity always brings a refreshing presence in our lab and I appreciate her efforts to finish all my grunt work. I am surprised that I have made life-long friendships with these two people and I am lucky for it.

My thesis committee was the best committee I could have ever asked for. Dr. Rick Silverman, Dr. Heather Pinkett, and Dr. Keith Tyo were all very reasonable and efficient during every meeting. They treated me respectfully and professionally, and I appreciate all of their advice and questions. I recommend other students to book these professors for their thesis committee. Also, I can't thank the staff members of IBiS enough, in particular Cathy Prullage and Deborah

Dehring for all their efforts to keep IBiS running smoothly. In particular, Cathy provided me important advice for many situations, and I can't imagine my experiences in IBiS without her.

I would also like to shout out to my friends who were an important support system. Nicolle Bonar is my roommate and friend, and I am lucky we connected and shared our last two years in our apartment together. I am sorry for pepper spraying you by microwaving chili powder, but it is just so funny every time I think about it. I thank Bola Adeniran, Joe Muldoon, Alexandra de Paz, Miranda Jacobs, Deanna Badong, Dina Kats, and all my other girls for the memories and company. I also need to mention the love of my life, Hermione the cat. She was the first cat that I have ever babysitted and the best cat I have met so far. True to her Siamese nature, she is super friendly, vocal, needy, soft, and cuddly, basically the best cat one could have. Because of her, I have found a new love for cats, and I hope to eventually steal her from her owner or clone her for myself. Lastly, I would like to thank the other love of my life, my family. I am lucky to share such a love with my parents and my brother, and that is all that matters.

I end this chapter of my life with 100% gratitude and 0% regret. What more can I ask for?

TABLES OF CONTENTS

LIST OF FIGURES

LIST OF TABLES

CHAPTER 1: INTRODUCTION TO PARTICULATE METHANE MONOOXYGENASE

INTRODUCTION

Aerobic methanotrophic bacteria are unique in their ability to utilize methane, a potent greenhouse gas, as their sole carbon source[1]. Methanotrophs are classified as γ- or α-proteobacteria based on the inclusion of either the ribulose monophosphate or serine cycles, respectively, in their metabolism as well as their phospholipid compositions, cell morphologies, and membrane arrangements[1,2]. In the first step of their metabolic pathway, methane is oxidized to methanol via activation of a 105 kcal/mol C-H bond in methane by methane monooxygenases (MMOs). There are two types of MMOs, a soluble iron-containing enzyme (sMMO) and a "particulate" intracytoplasmic membrane-bound copper-containing enzyme (pMMO)[3]. With the exception of the *Methylocella* and *Methyloferula* genera, pMMO is expressed and functional under copper-replete conditions (> 4 μM)[2,4]. Under copper-depleted conditions (< 0.8 μM), some methanotrophs can switch to sMMO expression, and certain *Methylosinus* and *Methylocystis* species can also produce the copper chelator methanobactin[5]. pMMO is the predominant methane oxidation catalyst in nature, but its mechanism for methane oxidation is much less understood than that of sMMO. Hence this thesis focuses on the characterization of the metal centers, substrate binding sites, and protein interaction partners of pMMO.

OVERALL ARCHITECTURE OF pMMO

pMMO is found in the intracytoplasmic membranes and requires copper ions for activity[3]. Crystal structures of pMMOs from γ- and α-proteobacterial methanotrophs reveal a 300-kDa

$\alpha_3\beta_3\gamma_3$ trimer composed of subunits PmoB (47 kDa), PmoA (24 kDa), and PmoC (22 kDa)[6-10]. PmoC and PmoA are integral membrane subunits, whereas PmoB consists of a periplasmic domain with two cupredoxin-like β-barrels linked by two transmembrane helices (Fig. 1.1). In published structures of pMMOs from α-proteobacteria, electron density is observed between PmoC helices 22-44 and 60-83 and modeled as a single transmembrane helix.

pMMO structures from six methanotroph species have been solved to date, and the highest resolution structure at 2.2 Å resolution is reported in Chapter 6 of this thesis[6-10]. Up to three metal binding sites have been observed in these pMMO crystal structures. PmoB contains two copper binding sites in the periplasmic domain. The conserved PmoB copper center (Cu_B) is coordinated by residues His 33, His 137, and His 139 and has been modeled as a dicopper site with a Cu-Cu distance of 2.6 Å in pMMO from *Methylococcus* (*Mcc.*) *capsulatus* (Bath) (Bath-pMMO) (Fig. 1.2)[11]. However, in some pMMOs, only one copper ion can be modeled at this site[7,10]. At the interface of the two cupredoxin domains, a nonconserved monocopper (bis-His) site is coordinated by His 48 and His 72 (Bath-pMMO numbering) (Fig. 1.2) and is electron paramagnetic resonance (EPR) silent and thus identified as Cu(I)[12]. The bis-His site is present only in γ- proteobacterial methanotrophs and copper binding at this site has only been observed for Bath-pMMO[6]. PmoC contains a variable metal binding site (Cu_c), in which the metal ion is coordinated by residues Asp 127, His 131, and His 144 (Bath-pMMO numbering), in addition to Glu 201 in pMMO from *Methylocystis* sp. str. Rockwell (Rockwell-pMMO) (Fig. 1.2). The Cu_C site has been observed to be occupied by copper, zinc, and detergent, or disordered[6-10].
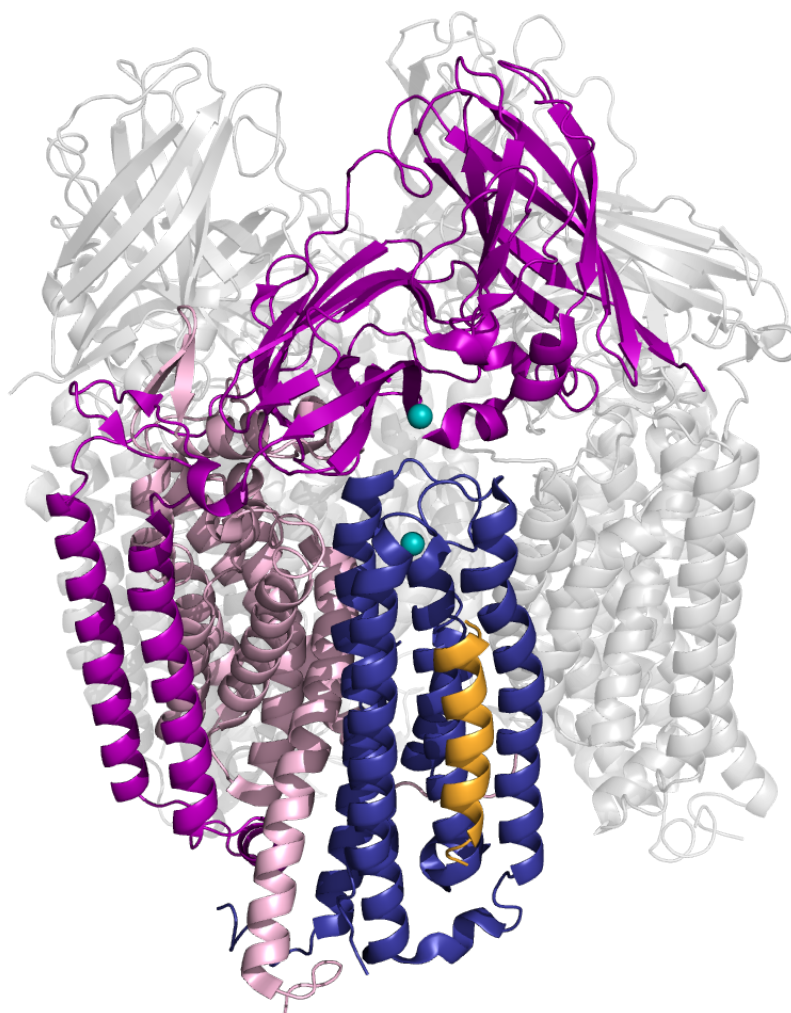
Figure 1.1. Structure of particulate methane monooxygenase.
A pMMO protomer from *Methylocystis* sp. str. Rockwell (4PHZ) with subunits PmoB, PmoA, PmoC shown in *purple*, *pink*, and *blue*, respectively. An unassigned helix and the copper ion are shown in yellow and teal, respectively. The other two protomers are shown in transparent *gray*.
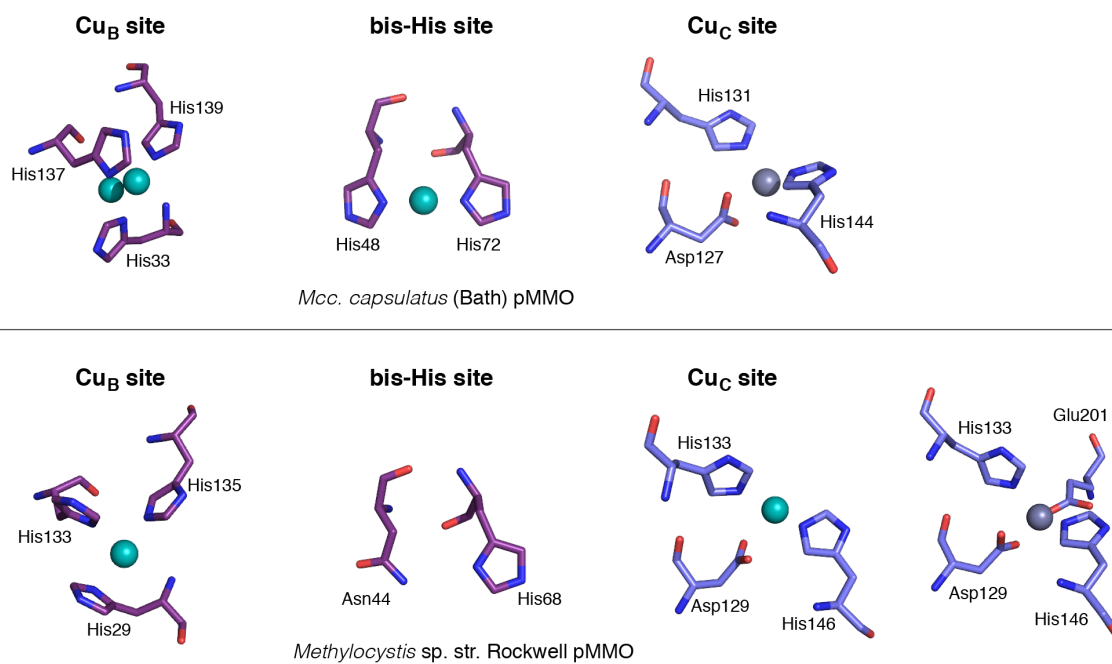
Figure 1.2. The metal centers of pMMO.
Metal centers of *Mcc. capsulatus* Bath pMMO (above) and *Methylocystis* sp. str. Rockwell pMMO (below). Metal binding ligands of the Cu_B and bis-His sites are represented as *purple* sticks, and those of the Cu_C sites are colored *blue*. Copper and zinc ions are shown as *teal* and *gray* spheres, respectively.

THE ACTIVE SITE OF pMMO

Dicopper active site model

On the basis of the first pMMO crystal structure, the active site was proposed to be a dinuclear copper center located in the PmoB Cu_B site with one copper ion coordinated by ligands His 137 and His 139 and the second copper coordinated by His 33 and the N-terminal amino group (Bath-pMMO numbering)[6]. This assignment was supported by EXAFS analysis reporting a short-Cu-Cu scattering distance of 2.57 Å as well copper stoichiometry measurements[13]. Thereafter, a heterologously-expressed truncated variant of the PmoB periplasmic domain (spmoB) exhibited methane oxidation activity[14], and systematic point mutations of the PmoB metal binding residues isolated the activity to the Cu_B site.

EPR spectra of pMMO and spmoB exhibited a type 2 Cu(II) signal, albeit with line broadening and poorly resolved copper hyperfine features in comparison to other type 2 copper sites[12]. The EPR signal was interpreted to originate from a mixed valent Cu(I)Cu(II) site in pMMO. Mutation of a ligand to the bis-His site in spmoB (H48N) did not affect the EPR spectrum, whereas mutation of the ligands to the Cu_B site (H137A/H139A) resulted in the loss of the type 2 Cu(II) signal, thereby assigning the signal to the Cu_B site.

Density functional theory (DFT) calculations were also performed to investigate the possible mechanism of methane hydroxylation at the dicopper Cu_B site[15]. In the proposed mechanism, O_2 binds to a reduced Cu(I)Cu(I) site to form a μ-$\eta2$:$\eta2$-peroxo-Cu(II)Cu(II) species. PmoB Tyr 374 is then proposed to participate in O-O cleavage via H atom transfer or proton-coupled electron transfer to generate a reactive (μ-oxo)(μ-hydroxo)$Cu^{II}Cu^{III}$ species that hydroxylates methane. The calculations suggest that this species is more energetically favorable than a bis(μ-oxo)Cu(II)Cu(III) species. However, Tyr 374 is not conserved in pMMOs from α-

proteobacterial methanotrophs, casting some doubt on its importance. Its role is investigated experimentally in Chapter 6 of this thesis.

Monocopper active site model

Recent biophysical and biochemical studies have shifted the narrative of the nuclearity of the active site. A crystal structure and EXAFS analysis of active purified pMMO from *Mm. alcaliphilum* 20Z (20Z-pMMO), presented in Chapter 2, provide evidence of a mononuclear Cu_B site[7]. In addition, recent quantum refinement of the Bath-pMMO crystal structure (3RGB) favors a monocopper rather than a dicopper model for the Cu_B site[16].

A recent EPR study of ^{15}N labelled pMMO in whole cells and in purified form determined that pMMO only contains two monocopper sites, one in the Cu_B site and the other in the Cu_C site[17]. Whole-cell EPR was conducted on *Mcc. capsulatus* (Bath) cells grown on ^{15}N and ^{63}Cu. Consistent with a previous whole-cell EPR study[18], a type 2 Cu(II) signal consistent with the presence of four N ligands was observed. ^{15}N ENDOR experiments indicated the presence of three histidine imidazole ligands, which can only be supplied by the PmoB Cu_B site. Furthermore, EPR spectra of Bath-pMMO that was oxidized during purification exhibited a second Cu(II) signal. To determine the location of this second Cu(II) site, Cu(II)-Cu(II) distances in purified Bath-pMMO were measured using double electron-electron resonance (DEER) spectroscopy. A predominant distance distribution peak was visible at 4.5 nm. Of all the possible Cu-Cu distances observed in the Bath-pMMO structure, the intermolecular distance between two adjacent PmoC metal sites at 4.4 nm best fit the DEER calculated distance, indicating that the second Cu(II) ion is located in the Cu_C site.

The two monocopper centers were also localized via native top-down mass spectrometry (nTDMS), as reported in Chapter 3 of this thesis[19]. 20Z-pMMO solubilized in Triton X-100 micelles and 20Z-pMMO reconstituted in nanodiscs were subjected to nTDMS analysis. The observed mass species of the three pMMO subunits in MS^2 were confirmed via MS^3 fragmentation and bottom-up MS. PmoB was predominately bound to one copper ion, and a small population of PmoC was also bound to one copper ion. Further fragmentation of the PmoB mass species yielded copper-bound peptide fragment ions containing His 137 and His 139. Interestingly, exogenous copper addition during nanodisc reconstitution yielded higher copper stoichiometry and rescued methane oxidation activity for Rockwell-pMMO nanodisc complexes. nTDMS analysis of this sample showed a higher population of copper-bound PmoC, suggesting that the monocopper Cu_c site is essential for activity.

Other lines of evidence also raise the possibility of a monocopper Cu_c active site. Further spmoB characterization using additional protein constructs indicated that the methane oxidation activity is not attributable to the protein[17]. Furthermore, in a mutagenesis study of hydrocarbon monooxygenase (HMO), a homolog of pMMO,[20] single residue mutations of the Cu_c site abolished HMO activity, whereas a H139V variant of the subunit homologous to PmoB still exhibited ~ 15% of wildtype activity. However, it is possible that a copper ion can be coordinated by His 33 and His 137 at the Cu_B site. Additionally, the His residues of the Cu_B site are not conserved in pMMOs from the *Verruomicrobia* phylum, whereas the Cu_C site is strictly conserved in all pMMOs. Further characterization of the Cu_C site is necessary to understand the roles of each metal center. pMMO from *Methylacidiphilum kamchatkense* Kam1, which does not contain the Cu_B site, is an ideal candidate for such future studies, as reported in Chapter 7 of this thesis.

Finally, DFT calculations of mononuclear active site models in Bath-pMMO may be relevant to a monocopper Cu_c active site. In the bis-His site, Cao *et al.* proposed O_2 incorporation into the Cu(I) intermediate forms a Cu(II)-superoxo species, followed by H atom transfer from a Tyr to form Cu(II)-hydroperoxo species that is transformed in the reactive Cu(III)-oxo by H-atom abstraction from another Tyr[16]. In DFT calculations based on a mononuclear Cu_B site[16], the Cu(III)-oxo species can bind methane and extract a H atom with an activation barrier of 22 kJ mol^{-1}, which is lower than other barrier calculations[21].

Tricopper active site model

A trinuclear Cu(II) active site model has also been proposed for pMMO. Chan *et al.* conducted a low temperature EPR analysis of Bath-pMMO which exhibited a type 2 Cu(II) signal and an almost featureless isotropic signal at g ≈ 2.1 that was assigned as a (μ_3-oxo)-Cu(II)Cu(II)Cu(II) tricopper cluster[22]. This tricopper cluster was proposed to reside at a PmoA-PmoC interface with the following ligand pairs coordinating each copper ion: PmoC Glu 154 and PmoA His 38, PmoA Met 42 and Asp 47, and PmoA Asp 49 and Glu 100 (Fig. 1.2)[23]. A DFT study suggested that the most probable model for the active species is the bis(μ_3-oxo)-trinuclear copper Cu(II)Cu(II)(μ-O)$_2$Cu(III) complex[24].

Thereafter, the same group expressed inactive full length PmoB and maltose binding protein (MBP) fused variants PmoB$_{33-414}$ and PmoB$_{55-414}$ with N-terminal truncations preceding residues 33 and 55, respectively, in *E. coli* K12 TB1 cells[25]. They observed 10-11 copper ions in full length PmoB, 3 of which were attributed to the bis-His and Cu_B sites and 7 of which were assigned as Cu(I) ions. The 7 Cu(I) ions could not be oxidized by O_2 and exhibited high redox

potentials. The MBP variants exposed to O_2 were subjected to EXAFS analysis, which exhibited a Cu-Cu scattering of distance 2.7 Å and suggested a Cu-Cu pair capable of forming either a μ-$(\eta^2{:}\eta^2)$- peroxodicopper(II,II) or bis(μ-oxo)dicopper(III,III) intermediate. The authors speculate that the Cu(I) sites provide reducing equivalents via the Cu_B site to regenerate the Cu(I)Cu(I)Cu(I) tricopper active site. However, tricopper clusters have not been observed in any crystal structures nor have been implicated in other biochemical investigations. Additionally, copper binding in the bis-His and Cu_B sites of PmoB$_{55\text{-}414}$ seems unlikely since His 33 and His 48 are not present in this variant. The authors suggest that Tyr 374 plays a role in stabilizing copper binding, but the study presents no evidence for such a role.

THE SUBSTRATE BINDING SITE

pMMO has been reported to oxidize C1-C5 n-alkanes and terminal alkenes[26]. Due to a lack of structures of pMMO bound to substrate and/or product analogs, the substrate binding site and interacting residues have not been identified. Lieberman and Rosenzweig identified a hydrophobic cavity suitable for CH_4 binding near the PmoB copper center comprised of residues Leu 78, Ile 163, Val 164 from PmoC and Pro 94 from PmoB[6], and Chan et al. proposed a hydrophobic channel near the tricopper site lined by residues Trp 48, Phe 50, Trp 51, and Trp 54 from PmoA[23], but the structures do not unambiguously reveal the substrate binding side. For pMMO from *Ms. trichosporium* OB3b (OB3b-pMMO), the calculated cavity volume required for pentane and butane oxidation is too large to explain pMMO specificity for methane, leading to the suggestion that there are two different substrate binding sites, one for methane and one for longer alkanes, also been proposed for ammonia monooxygenases (AMOs)[26,27]. In *Methylocystis* SB2, two pMMO isozymes with different affinities for methane were identified[28]. *Methylocystis* SB2 contains two

distinct *pmo* operons, *pmoCAB1* and *pmoCAB2*. Knock out studies of each operon showed that *pmoCAB2* can sustain cell growth with low methane concentrations whereas *pmoCAB1* could not. pMMO1 and pMMO2 share ~60% overall protein sequence identity, but no obvious differences could be linked to methane affinity upon inspection of the sequence alignment for each subunit.

The most convincing investigation of substrate binding is the mutagenesis study of HMO[20]. HmoC residue 139 (Bath-pMMO numbering), which is an Asp in pMMO and an Ala in HMO, was mutated to Asp (A151D), resulting in a 50% reduction in oxidation of propane and butane, while ethane oxidation was not affected. The presence of a bulkier residue thus shifts the substrate preference of HMO away from longer alkanes and may more closely resemble the cavity in pMMO. Hence, this cavity in pMMO may also be involved in substrate specificity.

Inhibition studies of pMMO suggest a possible substrate or product channel[29]. Acetylene has been shown to inhibit pMMO activity, in which acetylene is converted to ketene at the active site and migrates through a product/substrate channel to irreversibly modify the enzyme. PmoC residue Lys 196, located near the lipid-cytoplasmic interface and 37 Å away from the Cu_C site, was determined to be acetylated via MALDI-TOF/MS and LC-MS/MS, suggesting the PmoC transmembrane domains are involved in substrate access. However, a similar study on AMO identified acetylation at AmoA residue His 191, located near the lipid-periplasm interface and 20 Å and 28 Å away from the Cu_B and Cu_C sites, respectively [30]. The mechanism of acetylene inhibition requires further investigation.

PHYSIOLOGICAL REDUCANT AND OTHER INTERACTING PROTEINS

The physiological source of electrons for the reduction of the copper active site is unknown. A type 2 NADH:quinone oxidoreductase (NDH-2) has been isolated from *Mcc. capsulatus* (Bath)

membranes. Due to its ability to reduce duroquinone, menaquinone, and coenzyme Q_0, NDH-2 was suggested to be the electron donor for pMMO[31]. However, recent genome-scale metabolic modeling studies of *Mm. buryatense* 5GB1C and *Mcc. capsulatus* (Bath) propose that NADH as source electrons for pMMO cannot support growth[32,33]. Instead, these studies suggest that methanol oxidation by methanol dehydrogenases (MDHs) provides the electrons for methane oxidation. The proposed modes of electron transfer are (a) the redox-arm mode in which electrons pass from MDH to cytochrome c_{555} to ubiquinone to pMMO, (b) the direct coupling mode in which MDH transfers electron to cytochrome c_{555} to pMMO directly, and (c) the uphill electron transfer in which electrons pass from cytochrome c_{553} to ubiquinol cytochrome c reductase to the ubiquinol pool, as shown in Fig. 1.3 by Lievan et al. The *Mm. buryatense* 5GB1C metabolic model best fits with direct coupling mode while the *Mcc. capsulatus* Bath metabolic model fits with both direct coupling and uphill transfer modes.

MDH has also been shown to directly interact with pMMO. A low-resolution EM structure was modeled as a pMMO trimer bound to a calcium-dependent MDH (MxaF)[34]. Electron density of a three-pronged star-shaped cap is observed above the PmoB periplasmic domain and has been modeled as three MxaF monomers, with each monomer interacting with a PmoB subunit. However, a stable pMMO-MDH complex has yet to be isolated for further structural characterization. The crystal structure and protein interaction studies of MxaF from *Mcc. capsulatus* (Bath) indicated that MxaF exists as a dimer and interacts with full length pMMO and spmoB, most likely at the periplasmic domain[35]. A monomeric form of the lanthanide-dependent MDH (XoxF) was also shown to interact with pMMO, as reported in Chapter 4[36]. Without a higher resolution structure of a stable pMMO-MDH complex, the nature of this interaction is still under debate.
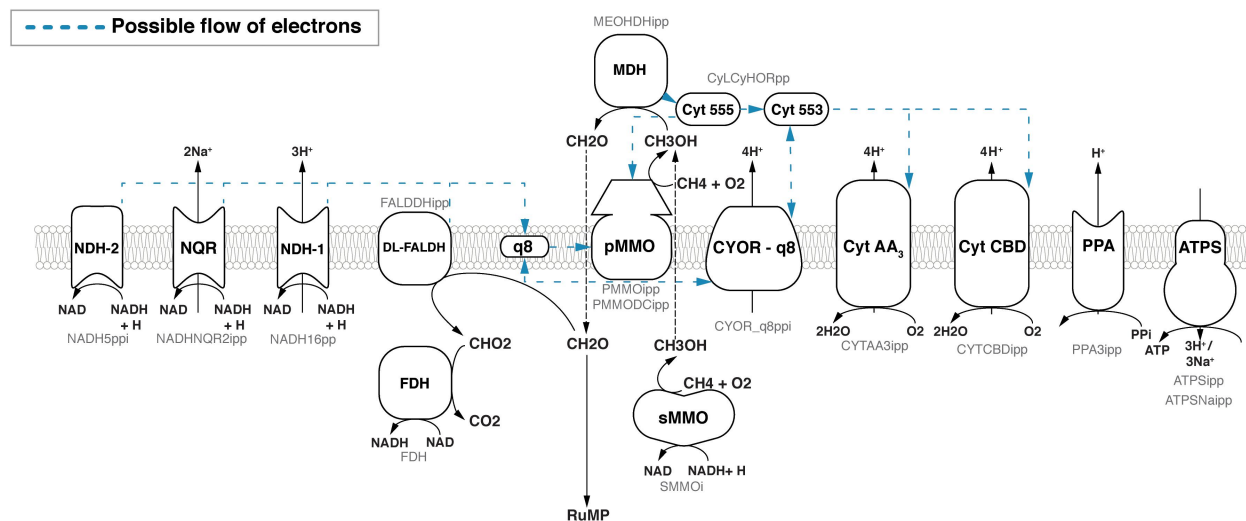
Figure 1.3. A model of the respiratory chain in *Mcc. capsulatus* (Bath).
Proteins involved in the electron transport chain are depicted in this figure. Blue dotted lines represent possible flow of electrons. This figure was created by Lieven et al., 2018.

In crystal structures of pMMOs from α-proteobacterial methanotrophs, unassigned electron density is observed between two PmoC helices spanning residues 22-44 and 60-83 (Rockwell-pMMO numbering)[8-10]. This density could not be modeled with the N-terminus of PmoC and was instead modeled with twenty alanine residues forming a transmembrane helix. Identification of the unknown protein has been difficult due to impurity of the pMMO samples. Potential candidates include supernumerary single transmembrane helices that have been observed in other membrane protein complexes and are suspected to aid in complex stabilization[37]. Another candidate is PmoD, a Cu_A protein sometimes encoded within the *pmo* operon[38]. PmoD is comprised of a single transmembrane helix and a periplasmic domain containing the Cu_A site. Knock out of the *pmoD* gene in *Ms. trichosporium* OB3b abolished cell growth in copper-replete conditions, suggesting PmoD is somehow involved in copper-dependent activity of pMMO.

METHANOTROPH MUTAGENESIS

Historically, methanotrophs have been genetically intractable. Recent advancements in the development of genetic tools have benefited many studies related to methanotrophy. Conjugation has been commonly used to introduce foreign genetic material into methanotrophs[39]. First, shuttle vectors are introduced into donor strain *E. coli* S17-1. Mating between the donor and methanotroph strains is followed by isolation of transconjugant methanotroph strains via antibiotic selection. Some methanotrophs are innately resistant to nalidixic acid (*Ms. trichosporium* OB3b) or rifamycin (*Methylomicrobium*), which removes the donor strain after successful gene transfer. Finally, the plasmid can integrate into the genome or replicate in the cell, depending on plasmid type.

The most common shuttle vectors, such as pCM184, contain *loxP* sequences that utilize Cre recombinase to remove the selection marker for reuse[40]. Alternatively, markerless mutants can be created with counterselection using the *sacB*-based system[41]. *sacB* encodes for sucrose sensitivity, and the mutants tend to remove this selection marker from the genome when grown in high sucrose concentrations, producing a markerless mutant. These plasmids are used for gene knockouts and markerless site-directed mutagenesis and have aided in studies of methanobactin biosynthesis and transport[5], the lanthanide transcriptional switch, sMMO regioselectivity, and copper transport[38,42-44]. Optimized shuttle vectors, such as pCM433kanT and pk18mobsacB_p15a, have reduced plasmid size and lower copy number for facile cloning[45,46].

Broad host range replicating vectors are used for homo- and heterologous protein expression in methanotrophs. Some methanotrophs contain native plasmids, so the variety of replicons, IncP, pBBR, and IncQ, in these expression vectors allows for testing of heterologous and native plasmid co-replication[47]. An IncP replicon pAWP89 has been shown to replicate in both γ- and α-proteobacterial methanotrophs and its derivative plasmid was used for heterologous expression of lactate dehydrogenase in *M. buryatense* 5G for lactate production[46,48,49].

In particular, γ-proteobacterial methanotrophs, including *Methylomicrobium* genera and *Mcc. capsulatus* (Bath), have been the focus for genome editing platform development. Electroporation of foreign plasmids and linear dsDNA has been successfully demonstrated for all these species, upon knockout of genes encoding restriction enzymes and optimization of the electroporation buffer[49,50]. A CRISPR-Cas9 genome editing platform has been developed for *Mcc. capsulatus* (Bath), which can be used to produce markerless mutations[51]. These developments can significantly expedite the timeline for methanotroph mutagenesis compared to using conjugation.

Additionally, various promoters and ribosome binding sites (RBS) have been tested for varying levels of protein expression[48,49,52]. Genetic tools have also been developed in α-proteobacterial methanotrophs, reported in Chapter 5 of this thesis[28,43,46,53].

INDUSTRIAL APPLICATION OF METHANOTROPHS

These genetic tools are essential for creating industrially useful methanotroph strains. Due to difficulties of storing and transporting methane, off-shoot methane from shale gas fracking sites is not fully utilized[54]. Furthermore, synthetic catalysts require high pressure and temperature conditions to break the C-H bond in methane, which is not economically feasible. Since methanotrophs can carry out the same reaction at ambient conditions, methanotrophs can be used to design low complexity and low cost gas-to-liquid (GTL) processes[55]. There have been numerous metabolic engineering efforts in γ-proteobacterial methanotrophs, including production of succinate, biopolyester polyhydroxyalkanoates (PHAs), and short chain carboxylic acids[55-57]. Ectoine biosynthesis is a promising industrial target with a market price at $1000 kg^{-1} as is 2,3-butanediol, a useful bulk feedstock[49,55].

SCOPE OF THESIS

The prospect of engineering biological methane oxidation for production of fuels and chemicals is promising, but knowledge of methanotrophs and pMMO in particular is still lacking. This dissertation reports pMMO characterization in a native-like environment and focuses on the importance of the PmoC subunit.

In chapter 2, purified pMMO was reconstituted into a membrane mimetic bicelles for membrane-dependent characterization[7]. Upon reconstitution, methane oxidation activity was rescued and comparable to that of as-isolated pMMO membranes. EPR analysis and copper stoichiometry studies of purified and bicelle-bound pMMOs showed no substantial alternations to the copper content or copper geometry. A 2.7 Å resolution crystal structure of 20Z-pMMO was obtained and showed the transmembrane PmoC subunit as highly disordered, further suggesting the importance of the membrane. Additionally, the structural and EXAFS analysis proposed a monocopper Cu_B site in 20Z-pMMO. However, the Cu_C site could not be visualized due to the highly disordered PmoC subunit, and crystallization of bicelle-bound pMMO did not result in any diffracting crystals.

Hence, in chapter 3, 20Z-pMMO was embedded into membrane mimetic nanodiscs for metal localization studies using nTDMS[19]. nTDMS analysis showed a predominant copper-bound PmoB and a small population of copper-bound PmoC, confirming the previous determination of a monocopper Cu_B site and a monocopper Cu_C site[17]. Rockwell-pMMO reconstituted into nanodiscs with copper supplementation exhibited higher methane oxidation activity. nTDMS analysis localized the additional copper binding event to PmoC, providing evidence that a monocopper Cu_C site is essential for copper-dependent biological methane oxidation. Furthermore, this is the first study to utilize multi-step MS fragmentation for metal localization in complex membrane proteins.

In chapter 4, a lanthanide-dependent methanol dehydrogenase from *Mm. buryatense* 5GB1C (5G-XoxF) was isolated, and its interaction with pMMO was investigated{Deng:2018hg}. Size exclusion chromatography suggested 5G-XoxF is a monomer, in contrast to the predominant dimeric form of other MDHs. A 1.85 Å resolution crystal structure was obtained and investigation of the structure suggested key residues that might result in the monomeric form. XoxF exhibited

interaction with pMMO from *Mm. buryatense* 5GB1C (5G-pMMO) via a biolayer interferometery assay. This study proposes an alternative model of MDH-pMMO association, in which a XoxF monomer may bind to pMMO.

Chapters 5-7 cover the utilization of methanotroph mutagenesis. Mutagenesis of *Ms. trichosporium* OB3b was developed to improve gene knockout, site-directed mutagenesis, and native homologous protein expression to characterize proteins encoded in the extended *pmo* and *mbn* operons. In 5G-pMMO, PmoB residue Tyr 374 was mutated to Phe or Ala to determine its possible role in the catalytic mechanism. The mutation suggests Tyr 374 is not essential for activity, and mutation to Ala increases methane oxidation activity. This study aims to characterize Tyr 374 and its effect on activity.

Lastly, chapter 7 reports the initial characterization of pMMO from *Ma. kamchatkense* Kam1 (Kam1-pMMO) that only contains the Cu_C site. This pMMO is an ideal candidate to investigate the role of Cu_C metal center alone. Initial growth trials and purification show that pMMO can be isolated for characterization, although further growth trials are required to improve yield. Future directions include copper loading to obtain active Kam1-pMMO for spectroscopic and structural investigations. These chapters seek to address the fundamental mysteries of pMMO and provide advancements in methanotroph and pMMO mutagenesis.

CHAPTER 2: FROM MICELLES TO BICELLES: EFFECT OF THE MEMBRANE ON PARTICULATE METHANE MONOOXYGENASE ACTIVITY

ABSTRACT

Particulate methane monooxygenase (pMMO) is a copper-dependent integral membrane metalloenzyme that converts methane to methanol in methanotrophic bacteria. Studies of isolated pMMO have been hindered by loss of enzymatic activity upon its removal from the native membrane. To characterize pMMO in a membrane-like environment, we reconstituted pMMOs from *Methylococcus* (*Mcc.*) *capsulatus* (Bath) and *Methylomicrobium* (*Mm.*) *alcaliphilum* 20Z into bicelles. Reconstitution into bicelles recovers methane oxidation activity lost upon detergent solubilization and purification without substantial alterations to copper content or copper electronic structure, as observed by electron paramagnetic resonance (EPR) spectroscopy. These findings suggest that loss of pMMO activity upon isolation is due to removal from the membranes rather than caused by loss of the catalytic copper ions. A 2.7 Å resolution crystal structure of pMMO from *Mm. alcaliphilum* 20Z reveals a mononuclear copper center in the PmoB subunit and indicates that the transmembrane PmoC subunit may be conformationally flexible. Finally, results from extended X-ray absorption fine structure (EXAFS) analysis of pMMO from *Mm. alcaliphilum* 20Z were consistent with the observed monocopper center in the PmoB subunit. These results underscore the importance of studying membrane proteins in a membrane-like environment and provide valuable insight into pMMO function.

INTRODUCTION

Methanotrophic bacteria convert methane, the second most abundant greenhouse gas, to methanol in the first step of their metabolic pathway[1,58]. As the main methane sink in nature, these microorganisms are promising biological tools for methane remediation and biofuel production[47,54,59,60]. Methanotrophs activate a 105 kcal/mol C-H bond in methane using metalloenzymes called methane monooxygenases (MMOs)[59], which are classified as soluble or membrane-bound (particulate, pMMO)[61]. pMMO is the predominant methane oxidation catalyst in nature but is less well-characterized[3]. A detailed understanding of methane oxidation by pMMO has the potential to guide synthetic catalyst design and facilitate methanotroph engineering.

pMMO is a complex integral membrane enzyme that requires copper for activity[10,14,31]. Crystal structures of pMMO from four different methanotrophs reveal a 300-kDa $\alpha_3\beta_3\gamma_3$ trimer composed of the subunits PmoA, PmoB, and PmoC[8-11]. PmoA and PmoC are integral membrane subunits, whereas PmoB consists of two periplasmic domains linked by two transmembrane helices. Present in all of these structures is a copper site at the N terminus of PmoB, with the N-terminal histidine of PmoB and two histidines from an HXH motif as ligands. This copper center, assigned as the active site[14], has been modeled with either one or two copper ions in the different structures. An additional PmoB monocopper site is found only in the structure of pMMO from *Methylococcus* (*Mcc.*) *capsulatus* (Bath)[11]. The PmoC subunit houses a variable metal binding site that can be occupied by copper or zinc, depending on the crystallization conditions.

The presence of multiple subunits with variable metal content has complicated efforts to determine the nuclearity of the copper active site and the roles of the other observed metal centers. Moreover, all studies of pMMO have been hindered by significant decreases in enzymatic activity upon isolation from the membranes and solubilization with detergents[10]. In some cases, activity

appears to be completely abolished upon removal from the membranes. As a result, the physiological relevance of structural and spectroscopic studies of purified pMMO has been questioned, and alternative hypotheses for the active site have been proposed, largely based on the assumption that solubilization and purification of pMMO removes catalytically essential copper ions[62,63].

An alternative possibility is that removal of pMMO from the membranes, rather than loss of copper, has deleterious effects on activity. Detergent micelles are frequently used for membrane protein characterization because of ease of use and compatibility with many experimental methods[64,65]. However, detergent micelles lack the structure and pressure provided by lipid bilayers and can cause instability and loss of function[66,67]. Membrane mimetics provide a way to study membrane proteins in more native-like environments. In many cases, addition of lipids or use of these mimetics has restored functional activity to purified membrane proteins[68-71]. In particular, bicelles, discoidal lipid bilayers surrounded by detergent, have been used to characterize and crystallize a range of membrane proteins[72-75].

To address the hypothesis that pMMO inactivation upon solubilization is due to removal from the native membranes, we have reconstituted purified pMMO from *Methylomicrobium* (*Mm.*) *alcaliphilum* 20Z (20Z-pMMO) and *Mcc. capsulatus* (Bath) (Bath-pMMO) into bicelles. Bicelle reconstitution recovers the methane oxidation activity of both pMMOs without addition of exogenous copper ions or substantial alteration in the copper sites, as observed by electron paramagnetic spectroscopy (EPR). A crystal structure of 20Z-pMMO provides some insight into how solubilization might affect protein stability. Finally, extended X-ray absorption fine structure (EXAFS) analysis of 20Z-pMMO does not indicate the presence of

the short copper–copper interaction observed in previous samples, prompting further investigation of the active site nuclearity.

RESULTS

Recovery of ^{13}C methane oxidation activity by bicelle reconstitution

To systematically investigate loss of pMMO activity, methane oxidation activity was measured for as-isolated, solubilized, purified, and bicelle-reconstituted pMMO samples. pMMO activity assays are typically performed using either NADH or duroquinol as a reductant. Duroquinol can directly reduce pMMO, whereas a type 2 NADH dehydrogenase (NDH-2) likely oxidizes NADH and reduces quinones for subsequent electron transfer to pMMO[31]. Solubilization with the detergent dodecyl maltoside (DDM) separates pMMO from the membranes (solubilized pMMO), which abrogates NADH-driven activity (Fig. 2.1). Solubilized pMMO was then reconstituted in bicelles to mimic the lipid bilayer and to investigate membrane-dependent activity loss. Methane oxidation activity was measured for as-isolated membranes, solubilized and purified pMMO in detergent (DDM), and bicelle (3% (w/v) DMPC-CHAPSO) reconstituted pMMO using both reductants (Fig. 2.1). Because of ^{12}C methanol contamination in many buffers and reagents, a new activity assay was developed in which conversion of ^{13}C methane to ^{13}C methanol is detected via GC-MS.
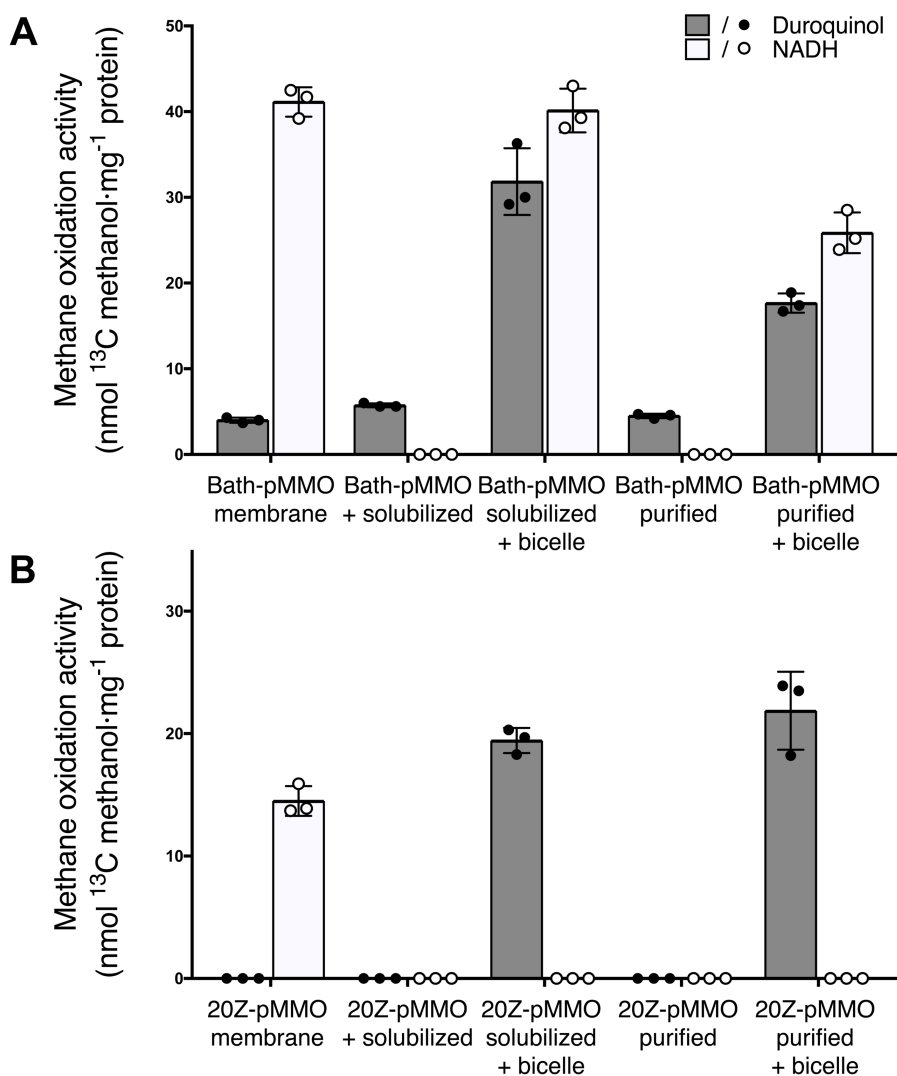
Figure 2.1. Methane oxidation activity of pMMOs in membranes, detergent, and bicelles. Activity values are shown for Bath-pMMO (**A**) and 20Z-pMMO (**B**) in as-isolated membranes, solubilized in detergent, solubilized in bicelles, purified in detergent, and purified in bicelles using both duroquinol (*gray*) and NADH (*white*) as reductants. Error bars represent standard deviations of three measurements, and the *black* and *white* dots represent the individual measurements.

Methane oxidation activities for Bath-pMMO and 20Z-pMMO were measured at 30 °C after 5 min because of solidification of bicelles at higher temperatures and longer incubation times. NADH-driven activity (41.1 ± 1.7 and 14.5 ± 1.2 nmol ^{13}C methanol mg^{-1} protein for Bath-pMMO and 20Z-pMMO, respectively) is abolished upon solubilization and purification (Fig. 2.1 and Table S2.1). For membrane-bound and solubilized samples, the activity measured using duroquinol was significantly lower than the NADH-driven activity for Bath-pMMO and not detected for 20Z-pMMO (Fig. 2.1). For both pMMOs, reconstitution into bicelles recovers the methane oxidation activity of solubilized and purified samples using duroquinol as a reductant (Fig. 2.1 and Table S2.1). However, NADH-driven activity is only restored for Bath-pMMO. It may be that an NDH-2 or other components of the electron transport chain responsible for NADH-dependent methane oxidation are not properly reassembled after solubilization and reconstitution of 20Z-pMMO.

Notably, for both pMMOs, duroquinol-driven activity is significantly higher for bicelle-reconstituted samples than for as-isolated membranes and is comparable with NADH-driven activity in membranes (Fig. 2.1 and Table S2.1). The different properties of phosphatidylcholine (PC), the main lipid in DMPC bicelles, and phosphatidylethanolamine (PE), the predominant phospholipid found in these methanotrophs[76-78], provide a possible explanation for this observation. The amine head group of PC is less polar than that of PE and may increase the solubility and access of duroquinol as well as O_2 and methane. Additionally, DMPC is composed of saturated 14:0 PC, whereas methanotroph PEs are primarily composed of a saturated and unsaturated mixture of 16:0 and 16:1 PE. The various head groups and acyl chain compositions can affect lipid packing, membrane fluidity, and even the structure of membrane proteins[79]. Finally, in as-isolated membranes, it is possible that the native quinones occupy the binding site
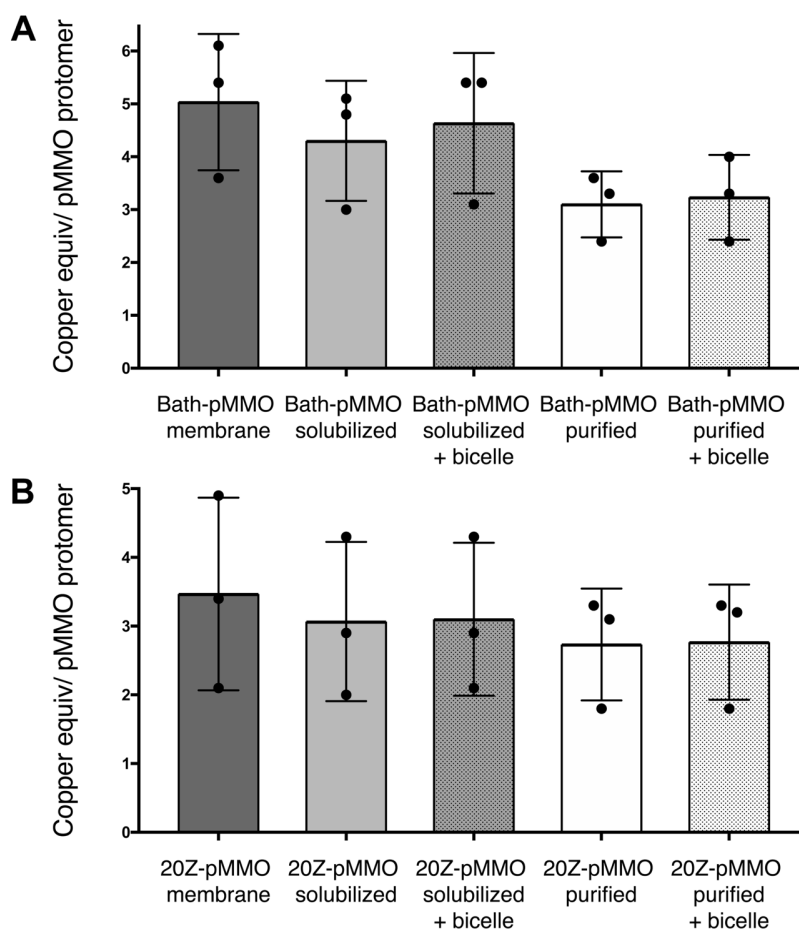
Figure 2.2. Copper content of pMMOs in native membranes, detergent, and bicelles.
Copper stoichiometry of Bath-pMMO (**A**) and 20Z-pMMO (**B**) in as-isolated membranes, solubilized in detergent, solubilized in bicelles, purified in detergent, and purified in bicelles. Error bars represent standard deviations of three measurements, and the *black* dots represent individual measurements.

duroquinol needs to access to reduce pMMO. Taken together, these results indicate that solubilized pMMOs are not irreversibly inactivated. Interestingly, solubilized or purified pMMO samples were reconstituted in bicelles without the addition of copper, suggesting that bicelles alone are responsible for the recovered activity.

Effect of bicelle reconstitution on pMMO copper centers

To further investigate the relationship between bicelle reconstitution and the pMMO copper sites, the copper concentrations of pMMO samples in as-isolated membranes, detergent, and bicelles were measured using inductively coupled plasma optical emission spectroscopy. The presence of approximately three copper ions per protomer in purified Bath-pMMO (Fig. 2.2 and Table S2.2) is consistent with previous studies[6]. Purified 20Z-pMMO contains ~2.7 eq of copper per protomer (Table S2.1). The copper contents of the native membranes and solubilized pMMOs are batch-dependent, accounting for the variability in copper stoichiometry values for these samples. Loss of some adventitiously bound copper is also typically observed during solubilization and purification[10].

The copper stoichiometry does not change between pMMO samples in detergent and in bicelles (Fig. 2.1 and Table S2.1). This observation, in conjunction with the recovered activity, indicates that the catalytically essential copper ions are still present in detergent-solubilized pMMO samples. The differences in activity between as-isolated membranes, detergent-solubilized pMMO, and bicelle-reconstituted pMMO therefore cannot be attributed to changes in copper content. Consequently, the membrane, and not copper depletion, is a crucial factor contributing to activity loss upon solubilization.

To directly assess the Cu^{2+} electronic and geometric structure through the bicelle reconstitution process, we collected EPR spectra of Bath-pMMO and 20Z-pMMO before and after bicelle reconstitution (Fig. 2.3). A previous EPR analysis of purified Bath-pMMO revealed two distinct type 2 Cu^{2+} signatures[12]. The bicelle-reconstituted Bath-pMMO exhibits the same Cu^{2+} EPR spectrum as the purified Bath-pMMO and is simulated with the same parameters as reported previously. However, the bicelle-reconstituted enzyme contains slightly more Cu^{2+} per protomer than the purified sample. Consequently, some of the Cu^{2+} observed in the bicelle-reconstituted sample is Cu^{1+} in the purified sample and oxidizes to Cu^{2+} during the reconstitution procedure.

The purified 20Z-pMMO EPR spectrum exhibits the Cu^{2+} spectrum seen in both forms of Bath-pMMO as well as a small contribution from additional Cu^{2+} resonance (Fig. 2.3B and Table S2.2), suggesting adventitious Cu^{2+} binding to 20Z-pMMO in a site either unoccupied or containing Cu^{1+} in Bath-pMMO. Similar to Bath-pMMO, incorporation of 20Z-pMMO into bicelles oxidizes some Cu^{1+} to Cu^{2+}, as evidenced by the slightly altered $g_\perp$ region and increased amount of Cu^{2+} per protomer (Table S2.2), but the signal is otherwise the same as observed for the purified sample.

Importantly, the EPR spectra of both pMMOs show that the Cu^{2+} ligation is not substantially altered by the bicelle incorporation procedure. Therefore, the appreciable recovery of pMMO activity upon insertion of Bath-pMMO into the bicelle is not due to differences in the active site copper structure, consistent with the notion that the membrane environment plays a critical role in modulating activity.
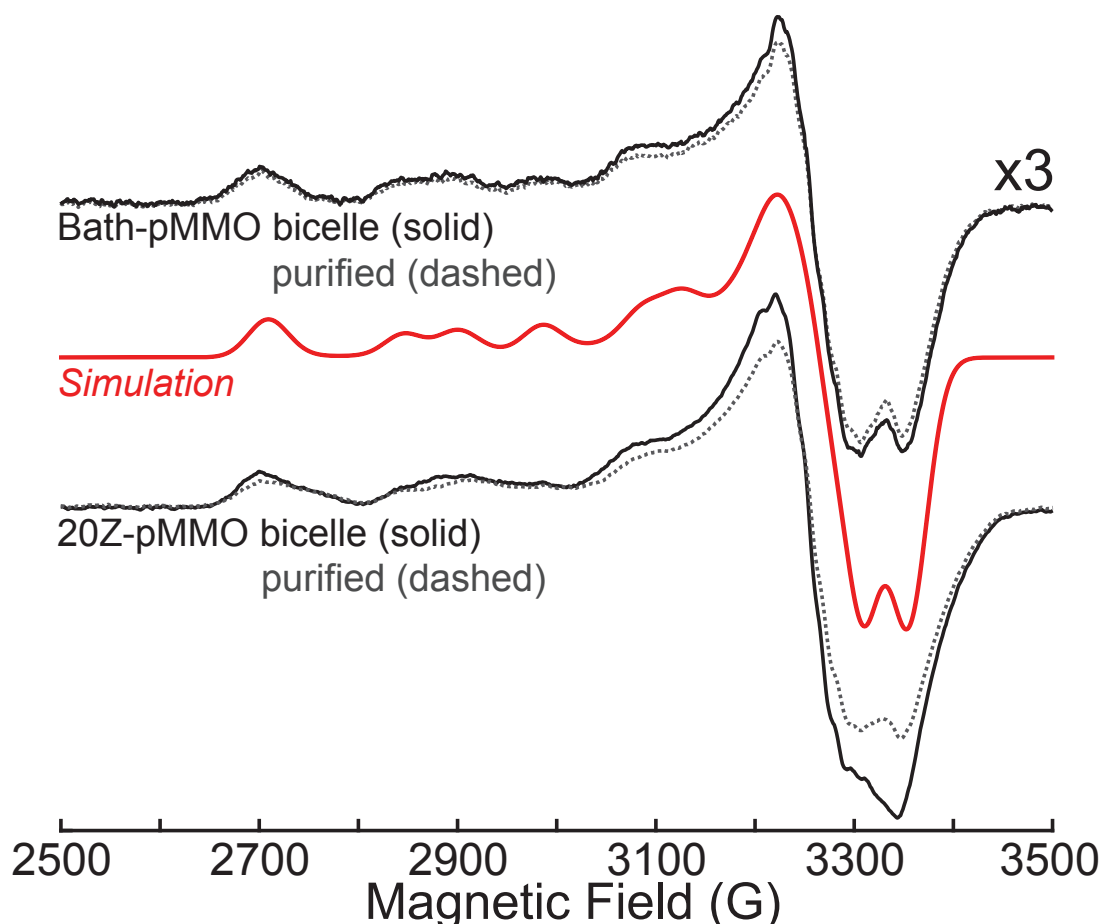
Figure 2.3. X-band EPR spectra of Bath-pMMO and 20Z-pMMO.
Spectra of pMMO purified in detergent (*gray*, *dotted lines*) and after bicelle reconstitution (*black*, *solid lines*) are normalized to protein concentration. For purified and bicelle-reconstituted Bath-pMMO, EPR intensity was increased 3-fold for ease of comparison. *Red solid lines* depict simulations using the (very slightly adjusted) previously defined Cu^{2+} spin Hamiltonian parameters (33): equal contributions of $(His)_2$-Cu^{2+} ($g_\parallel = 2.235$, $g_\perp = 2.047$, $A_\parallel = 585$ MHz, $A_\perp = 65$ MHz) and (His, Amine)-Cu^{2+} ($g_\parallel = 2.295$, $g_\perp = 2.047$, $A_\parallel = 450$ MHz, $A_\perp = 40$ MHz). Collection conditions were as follows: 9.36–9.37 GHz microwave frequency, 20 K temperature, 160 ms time constant, 16 G modulation amplitude, 60-s scans, average of at least 10 scans.

Crystal structure of 20Z-pMMO

To further characterize 20Z-pMMO, a crystal structure was determined to 2.7 Å resolution (Table 2.1). The protein was purified in the presence of DDM, exchanged into the detergent Cymal-5, and then crystallized with ammonium sulfate as the precipitant. Varying the concentration of this precipitant was crucial for obtaining well-diffracting crystals. The 20Z-pMMO structure exhibits a similar overall architecture to Bath-pMMO, with an $\alpha_3\beta_3\gamma_3$ trimeric structure. Unlike previous pMMO structures[6,8-10], there is a single protomer in the asymmetric unit (Fig. 2.4A)

Despite the overall structural similarity, the PmoC subunit of 20Z-pMMO is significantly disordered compared with the previous structures[6,8-10] (Fig. 2.4B). Electron density is not observed for 60% of the PmoC subunit, including residues 1–89, 123–156, and 193–218. These disordered regions include the variable metal binding site (Asp-128, His-132, and His-145) and surrounding residues. This significant disorder may result from destabilization of PmoC in detergent and could be related to the complete loss of activity upon detergent solubilization and purification (Fig. 2.1B). PmoC, at least in 20Z-pMMO, is thus more flexible than suggested by previous structures.

The metal binding sites of 20Z-pMMO also differ from those observed in previous pMMO structures[6,8-10]. In the Bath-pMMO PmoB subunit, there is a monocopper site coordinated by His-48 and His-72 [6]. Although both residues are conserved in 20Z-pMMO, electron density attributable to copper or any other metal ion is not present (Fig. 2.4C). It is unclear why this site is only occupied in Bath-pMMO, but the metal binding residues are not conserved in all pMMOs, with His-48 substituted by Asn and Gln in type II methanotrophs, indicating that this metal center is not essential for methane oxidation. The PmoB subunit also contains a bound copper that is

Table 2.1. Data collection and refinement statistics for 20Z-pMMO.
Values in parentheses refer to the highest resolution shell.

	20Z-pMMO	20Z-pMMO (copper anomalous)
Data collection		
Space group	$P6_3$	$P6_3$
Cell dimensions		
a, b, c	143.84, 143.84, 146.15,	
Resolution	2.70 Å	3.00 Å
Wavelength	1.03329 Å	1.37760 Å
R_{pim}	0.025 (0.220)	0.022 (1.32)
R_{meas}	0.07 (0.588)	0.06 (0.337)
$CC_{1/2}$	0.999 (0.953)	0.998 (0.984)
$I/\sigma I$	40.6 (2.5)	113.5 (11.2)
Completeness	99.1% (92%)	99.7% (97.7%)
Redundancy	9.0 (6.4)	6.9 (5.7)
Anisotropy correction		
Truncation limit	3.1, 3.1, 2.7 Å	
Completeness	74.9%	
Refinement		
No. of reflections	35,187	
R_{work}/R_{free}	0.2133/0.267	
Average B-factor ($Å^2$)	39.69	
Root mean square deviations		
Bond lengths (Å)	0.010 Å	
Bond angles (°)	1.313°	
Ramachandran favored	87.39%	
Ramachandran allowed	10.64%	
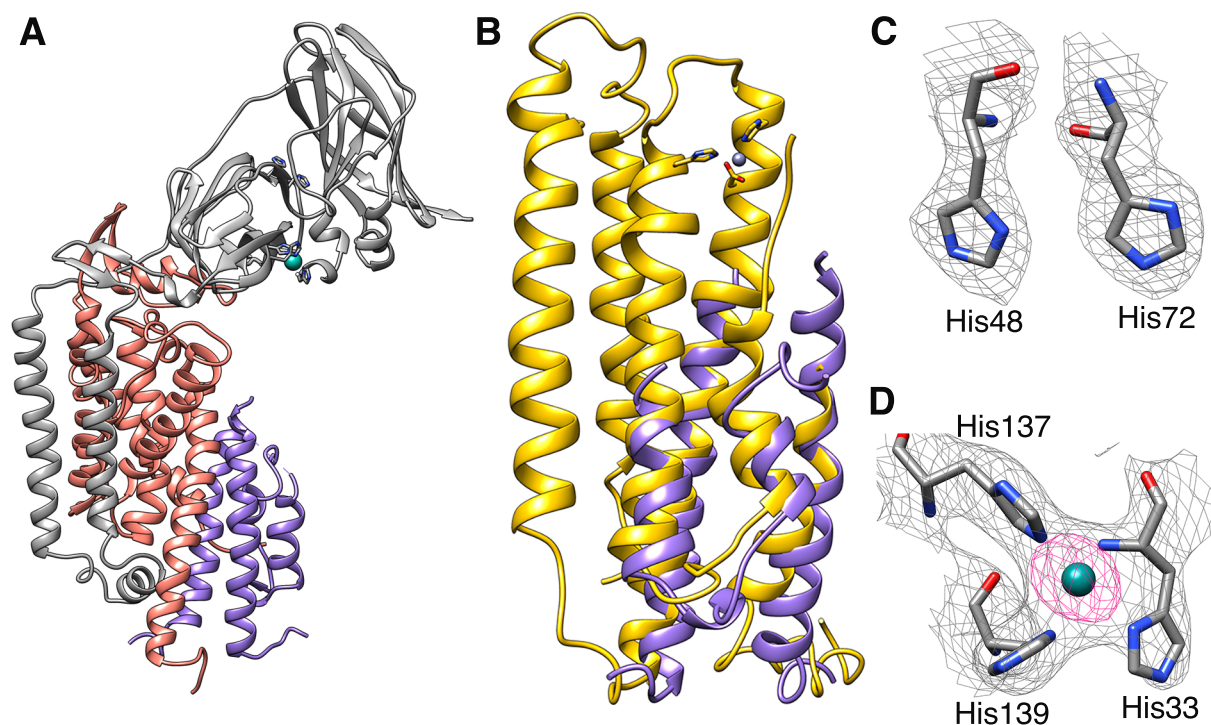
Figure 2.4. Crystal structure of 20Z-pMMO.

A, the 20Z-pMMO protomer with PmoB, PmoA, and PmoC shown in *gray*, *salmon*, and *purple*, respectively. The copper ion is depicted as a *teal sphere.* **B**, superposition of the 20Z-pMMO PmoC subunit (*purple*) with the Bath-pMMO PmoC subunit (PDB code 3RGB, *yellow*). The zinc ion in the Bath-pMMO variable metal-binding site is shown as a *sphere* (*gray*) and is coordinated by two histidines and an aspartic acid. This region is disordered in 20Z-pMMO. **C**, the site of the monocopper center in Bath-pMMO is unoccupied in 20Z-pMMO. **D**, the 20Z-pMMO copper site. The copper anomalous difference density map (*magenta*, 20 σ) is superimposed on the $2F_o$-F_c map (*gray*, 1.0 σ).

coordinated by residues His-33, His-137, and His-139 and has been assigned as the active site. In some pMMO structures, this site has been modeled with two copper ions, including Bath-pMMO[6,8,9]. The dicopper site model is based on EXAFS data that consistently indicate the presence of a short copper–copper distance as well as the measured copper stoichiometry upon purification [8-10,13,14]. However, in other structures, the site has been modeled with a single copper ion[9,10].

In the 20Z-pMMO structure, this PmoB site is also best modeled with one copper ion (Fig. 2.4D). The site is square planar with copper–nitrogen distances of 2.1 Å for the His-137 δN, 2.1 Å for the His-139 εN, 2.5 Å for the His-33 δN, and 1.9 Å for the N-terminal nitrogen of His-33. The electron density for His-33 is not as well-defined as that for other two histidine residues. Interestingly, very strong additional electron density is observed for PmoB residue Lys-155 in PmoB appended to the side-chain ζN atom. We could not conclusively model this density, but it could potentially arise from posttranslational modification of this residue.

XANES and EXAFS analysis of 20Z-pMMO

The copper X-ray absorption near edge structure (XANES) spectra measured for 20Z-pMMO indicate a mixed Cu(I) and Cu(II) metal environment. A subtle transition, observed at 8978.8 eV (Fig. 2.5A) is consistent with the forbidden 1s → 3d transition for Cu(II)[11]. Additional edge transitions, observed at 8983 and 8986.3 eV and illustrated in the first derivative of the edge at 8982.3 and 8985.5 eV in (Fig. 2.5A), *inset*, are characteristic of the 1s → 4p transitions often observed for systems containing a mixture of Cu(I) and Cu(II)[11].
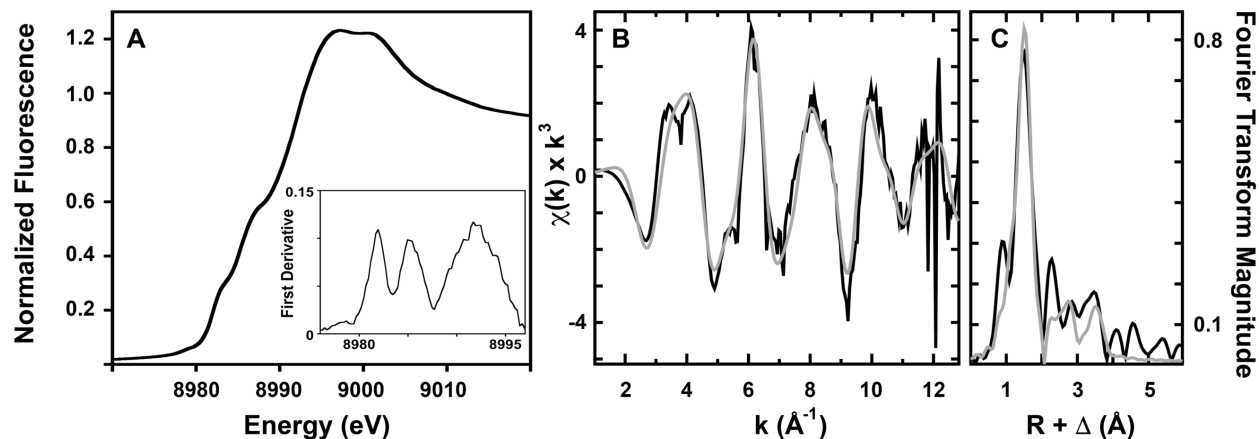
Figure 2.5. XANES and EXAFS analysis of 20Z-pMMO.
A, copper XANES spectra for 20Z-pMMO. *Inset*, the first derivative of near edge and edge features is displayed to more clearly highlight the features. **B**, raw copper EXAFS for 20Z-pMMO. Simulations were fit using a standard conservative approach that follows rules governing both spectral resolution relative to acceptable intraligand scattering interaction bond lengths and acceptable bond lengths (55). **C**, fourier transform of the EXAFS. Raw unfiltered data are shown in *black*, and the best fit simulations are shown in *gray*. EXAFS were fit over a *k* range of 1.0–12.85 Å^{-1}.

Table 2.2. Summary of the best fit Cu EXAFS simulations for 20Z-pMMO sample.
EXAFS were fit over the k-range of 1.0-12.85 Å^{-1}, for a spectral resolution of 0.13 Å

Nearest Neighbor Ligand Environment				Long-Range Ligand Environment				
Atom [b]	R(Å) [c]	CN [d]	σ^{2} [e]	Atom [b]	R(Å) [c]	CN [d]	σ^{2} [e]	F' [f]
O/N	1.96	2.5	5.23	C	2.97	1.5	3.73	0.4
				C	3.36	0.75	4.25	
				C	3.96	3.0	4.22	

[a] Independent metal-ligand scattering environment
[b] Scattering atoms: O (oxygen), N (nitrogen), Cu (copper)
[c] Average metal-ligand bond length from two independent samples
[d] Average metal-ligand coordination number from two independent samples
[e] Average Debye-Waller factor in Å^{2} x 10^{3} from two independent samples
[f] Number of degrees of freedom weighted mean square deviation between data and fit.

Analysis of the copper EXAFS spectra for 20Z-pMMO suggest a mononuclear copper ligand environment constructed by only oxygen and nitrogen within the first ligand sphere (Fig. 2.5B). Simulations of copper–oxygen/nitrogen nearest neighbor ligand scattering suggest a disordered ligand environment composed of approximately 2.5 to 3.5 oxygen/nitrogen ligands at an average bond length of 1.96 Å (Table 2.2). Inclusion of a direct copper–copper scattering vector was not justified in our simulations. Long-range scattering could be simulated using low Z (carbon/nitrogen) scattering at bond lengths of 2.97, 3.36, and 3.97 Å, reminiscent of patterns observed because of imidazole scattering interactions from coordinated histidines[80]. In support of imidazole scattering, the pronounced camelback feature at 4 $Å^{-1}$, characteristic of metal–histidine ligation[81], is also observed.

DISCUSSION

The recovery of methane oxidation activity upon pMMO reconstitution into bicelles underscores the importance of studying membrane proteins in native-like environments. Although studying membrane proteins in a membrane context seems obvious, detergent micelles are still typically used instead. Besides their amphipathic nature, detergent micelles lack important lipid bilayer characteristics that provide structural support[66]. Reconstitution of pMMO into bicelles restores the methane oxidation activity of inactive detergent-solubilized pMMOs close to levels measured for membrane-bound pMMO (Fig. 2.1) The copper stoichiometries and EPR spectroscopic features are nearly identical for inactive detergent-solubilized and active bicelle-reconstituted pMMO samples and are consistent with previous observations[6,12].

These data indicate that the copper centers detected in detergent-solubilized pMMO are functionally relevant. In previous pMMO crystal structures, one to three copper ions were modeled

per protomer, found only in the PmoB and PmoC metal centers, and only the PmoB site coordinated by His-33, His-137, and His-139 consistently houses copper ions[6,8-10]. Chan and Yu[62] and Chan and co-workers[63] have proposed that Bath-pMMO instead contains ~15 copper ions, including a tricopper active site in PmoA and six to seven Cu^{1+} ions bound to the C terminus of PmoB, and have suggested that copper loss from these sites upon membrane solubilization is responsible for the reduced activity of purified Bath-pMMO. However, the recovered activity of bicelle-reconstituted pMMO samples indicates that large numbers of essential copper ions are not lost during isolation from the membranes.

The crystal structure of 20Z-pMMO provides some insight into how removal from the membrane could affect activity. PmoC is largely disordered, suggesting destabilization upon solubilization and resultant activity loss. PmoB only contains two transmembrane helices, and PmoA is sandwiched between PmoB and PmoC, features that may contribute to their structural stability in detergent micelles. In contrast, only the PmoC helices near PmoA are ordered (Fig. 2.4A), whereas the disordered regions are exposed to the lipid membrane and perhaps more susceptible to perturbations upon reconstitution into detergent micelles. Without lateral pressure or specific lipid binding, PmoC may be structurally less stable in micelles. PmoC is positioned directly adjacent to the proposed PmoB active site and could be involved in stabilization of the active site or copper binding that may be essential for activity. In addition, for a hydrocarbon monooxygenase homolog of pMMO, mutation of the PmoC metal binding residues reduces activity, suggesting an important functional role[20]. Previous efforts have mainly focused on characterizing perturbations in PmoB to explain activity loss. Some of this attention should be

shifted to understanding how the transmembrane subunits, particularly PmoC, play an essential role in methane oxidation.

Finally, a mononuclear copper active site remains a viable possibility[3,60]. The 20Z-pMMO PmoB site is best modeled as monocopper (Fig. 2.4). Additionally, the short copper–copper distance detected in the EXAFS analysis of other pMMOs[9-11] is not present in 20Z-pMMO (Fig. 2.5). Its absence in 20Z-pMMO could be due to lower protein concentrations, a heterogeneous distribution of copper–copper vectors in the samples that cancel out the overall signal, or even the reduced presence of other copper contaminant proteins that could contribute to the observed feature. This result is consistent with a recent quantum refinement of the Bath-pMMO PmoB copper site[16]. Most relevant to a pMMO monocopper active site are the lytic polysaccharide monooxygenases (LPMOs), which utilize a monocopper active site for oxidative cleavage of glyosidic bonds. Both the PmoB copper site and the LPMO active site contain a histidine brace metal-binding motif. However, LPMOs lack a third histidine ligand and additional metal binding sites. In addition, some contain a methylated histidine ligand. Moreover, the substrates of pMMO and LPMO are drastically different[82-84]. Overall, studying pMMO in a membrane-bound context has validated past characterizations and provides new insights into the importance of the PmoC subunit and the nature of the active site. It will be important to continue this approach in future studies of pMMO activity and mechanism.

METHODS

Methanotroph cell growth

Mm. alcaliphilum 20Z was cultured as described previously[39,45]. Briefly, cells were grown in 1× modified nitrate mineral salts medium, 0.5 M NaCl, 2.3 mM phosphate buffer, and 50

mM carbonate buffer (pH 9.5) supplemented with 40 μM $CuSO_4 \cdot H_2O$ and trace elements solution under a 1:3 methane-to-air ratio in 12 liters bioreactors. *Mcc. capsulatus* (Bath) cells were grown in $1\times$ nitrate mineral salts medium and 3.9 mMphosphate buffer (pH 6.8) supplemented with 50 μM $CuSO_4 \cdot H_2O$, 40 μM iron NaFe(III)EDTA, and trace element solution under a 1:4 methane-to-air ration in 12 liters of bioreactors[10]. All bioreactor cell growths were harvested at an OD_{600} of 8–10 and centrifuged at $8{,}000 \times g$ for 30 min. Cell pellets were flash-frozen in liquid nitrogen and stored at $-80\ °C$ for future use.

Membrane isolation

Mm. alcaliphilum 20Z cell pellets (10 g) were resuspended in 100 ml of 25 mM PIPES and 500 mM NaCl (pH 7) supplemented with EDTA-free protease inhibitor tablets (Roche). The cells were manually stirred for resuspension on ice. The cell resuspension was sonicated at 4 °C for 1.5 min with an on/off interval of 1 s/3 s at 25% amplitude and centrifuged at $8{,}000 \times g$ for 1 h to remove cell debris. The supernatant was centrifuged at $100{,}000 \times g$ for 1 h to isolate the pelleted membranes containing pMMO. The membrane pellet was washed twice with a Dounce homogenizer in 25 mMPIPES and 250 mM NaCl (pH 7). 1-ml aliquots of pMMO-containing membranes at total protein concentrations of 10 mg/ml (measured by Bio-Rad DC assay using BSA as a standard) were flash-frozen in liquid nitrogen and stored at $-80\ °C$. *Mcc. capsulatus*(Bath) membranes were isolated as described previously[85].

pMMO purification and bicelle reconstitution

Membranes were solubilized using 1.2 mg of DDM (Anatrace) per 1 mg of crude protein at 4 °C for 1 h. The solubilized protein was centrifuged at $100{,}000 \times g$ for 1 h, and the supernatant

was collected for purification. Solubilized 20Z-pMMO was buffer-exchanged into 25 mM PIPES, 50 mM NaCl (pH 7), and 0.02% (w/v) DDM using a 100-kDa molecular mass cutoff Amicon (Millipore). 20Z-pMMO was purified using a 15Q anion exchange column (GE Healthcare) and eluted using a 50–800 mM NaCl gradient (Figs. S2.1-2). Solubilized Bath-pMMO was concentrated to 1 ml using a 100-kDa molecular mass cutoff Amicon and loaded onto a 120-ml Superdex 200 size exclusion column (Fig. S2.3). All eluted pMMOs were concentrated using a 100-kDa molecular mass cutoff Amicon to 10 mg/ml in 25 mM PIPES, 250 mM NaCl (pH 7), and 0.02% (w/v) DDM. Freshly solubilized or purified pMMO at 10 mg/ml was reconstituted with a 30% (w/v) DMPC:CHAPSO 2.8:1 bicelle solution (Molecular Dimensions) using a 4:1 volumetric ratio and incubated on ice for at least 30 min to prepare pMMO samples at 8 mg/ml reconstituted in 6% (w/v) bicelles. The copper concentration was measured by inductively coupled plasma optical emission spectroscopy at the Quantitative Bio-element Imaging Center at Northwestern University.

[13]C Methane oxidation activity assay

To measure the methane oxidation activity of membrane-bound, solubilized, purified, and 6% (w/v) bicelle-reconstituted pMMOs, samples were diluted to 4 mg/ml (or 3% (w/v) bicelles) in 100-μl reactions consisting of reductant (280 μM NADH (Sigma-Aldrich) or excess duroquinol) in 2-ml screw-top vials with septa tops (Agilent). A 1-ml volume of headspace gas was withdrawn and replaced with 1.5 ml of ^{13}C methane (Sigma-Aldrich). All reactions were performed at 30 °C (bicelle samples solidify at 45 °C, the temperature typically used for Bath-pMMO activity assays). pMMO reconstituted in 3% or 1.5% (w/v) bicelles gave the highest activity, which decreased with lower bicelle concentrations (Fig. S2.4). Reactions were incubated at 30 °C and 200 rpm for 5 min,

put on ice for 5 min, and then quenched with 500 μl of chloroform spiked with 1 mMdichloromethane. The reaction was vortexed at 2,000 rpm for 10 min and centrifuged at 2,000 × g for 30 min to separate precipitate from the chloroform mixture. 2.5 μl of sample was injected onto a PoraBOND Q column (25 m × 250 μm × 3 μm) on an Agilent 7890B/5977A MSD GC/MS instrument with a split ratio of 10:1. The GC was maintained under a constant flow of 1.2 ml/min of helium gas. The initial oven temperature was maintained at 80 °C for 3.5 min, followed by an increase of 50 °C/min to 150 °C and held for 1.5 min. A second ramp rate of 15 °C/min was used to reach the final temperature of 300 °C, held for 1 min. The mass spectrometer was maintained under an ion source temperature of 230 °C, quad temperature of 150 °C, 70 eV, and a detector voltage of 2,999 V. Masses 31, 33, and 49 were monitored for detection of ^{12}C methanol, ^{13}C methanol and dichloromethane (dwell times of 10 ms, 100 ms, and 10 ms, respectively). The ^{13}C methanol peak area was integrated, quantified from a standard calibration curve, and normalized to the concentration of the internal standard dichloromethane. The lower limit of detection was determined to be 10 μM ^{13}C methanol, and a stringent cutoff for minimum concentration was set at 30 μM. Methane oxidation activity values using ^{13}C methanol detection by GC-MS compared with ^{12}C methanol detection using the GC-flame ionization detector (FID) are shown in (Table S.2.3).

EPR spectroscopy

EPR samples were prepared by aliquoting 100 μM (DDM samples) or 80 μM pMMO (bicelle samples) in 25 mM PIPES, 250 mM NaCl (pH 7), and 0.02% (w/v) DDM or 6% (w/v) bicelles into Wilmad quartz EPR tubes (Sigma-Aldrich). Measurements were collected on a continuous wave X-band Bruker ESP-300 spectrometer using a liquid helium flow Oxford

Instruments ESR-900 cryostat. Spectra were corrected for background resonance by subtraction of a spectrum of 50 mM Tris (pH 8.0), 150 mMNaCl collected under the same conditions. Cu^{2+} spin quantitation was performed by double integral area comparison of pMMO spectra to Cu^{2+}–EDTA standards containing 25–500 μM Cu^{2+}. All EPR simulations were performed using EasySpin[86].

Crystallization and structural determination of 20Z-pMMO

Purified pMMO in 0.02% (w/v) DDM was buffer-exchanged into 0.12% (w/v) Cymal-5 using a 100-kDa molecular mass cutoff Amicon. pMMO crystals were obtained from sitting drops containing 1 μl of 10 mg/ml protein in 25 mM PIPES, 250 mM NaCl (pH 7), 0.12% (w/v) Cymal-5, 1 μl of 2.8 M $AmSO_4$, and 0.2 M MES (pH 6). Crystals were harvested in saturated $LiSO_4$ cryoprotectant solution and flash-frozen in liquid nitrogen.

Crystals were screened for diffraction at the LS-CAT and GM/CA-CAT beamlines at the Advanced Photon Source at Argonne National Laboratory. Datasets were processed using HKL2000[87] (Table 2.1). Anisotropic processing using the UCLA anisotropy server[88] was found to improve the electron density maps. Phenix[89] was used for molecular replacement with the Bath-pMMO coordinates as a starting model (PDB code 3RGB) to solve the structure of 20Z-pMMO. 20Z-pMMO has 72%:78%:77% identity to the Bath-pMMO PmoB, PmoA, and PmoC subunits, respectively. Structure modeling and refinement were performed using Coot[90] and Phenix, and model quality was assessed using MolProbity[91]. The final model for the 20Z-pMMO structure includes PmoB residues 33–414; PmoC residues 90–122, 157–192, and 219–250; PmoA residues 4–244; one copper ion; and two Cymal-5 molecules.

X-ray absorption spectroscopy

Purified 20Z-pMMO samples were concentrated to 385 µM using a 100-kDa molecular mass cutoff Amicon centrifugal concentrator and resuspended in 30% (v/v) glycerol. The copper concentration of the 20Z pMMO samples was 732 µM. These samples were loaded into Lucite XAS cells wrapped with Kapton tape, flash-frozen in liquid nitrogen, and stored at −80 °C. XAS data were collected at the Stanford Synchrotron Radiation Lightsource on beamline 9-3, equipped with a Si[220] double-crystal monochromator that contains an upstream mirror used for focusing and harmonic rejection. Fluorescence spectra were collected using a 100-element Ge solid-state Canberra detector. During data collection, the Oxford Instruments continuous-flow liquid helium cryostat was stabilized at 10 K. Copper excitation data were collected using a 6-µm nickel Lytle filter and solar slits placed between cryostat and detector to reduce scattering fluorescence. XAS spectra were measured using 5 eV steps in the pre-edge region (8,750–8,960 eV), 0.25 eV steps in the edge region (8,986–9,050 eV), and 0.05 Å^{-1} increments in the EXAFS region (to $k = 13.3$ Å^{-1}), integrating from 1 to 25 s in a k^3 weighted manner for a total scan length of ~40 min. A copper foil spectrum was collected simultaneously with each protein spectrum for real-time spectral energy calibration, with an assigned first inflection point for the copper foil spectrum at 8,980.3 eV. Spectra were closely monitored for any photodamage, and slight photoreduction was observed. To diminish the extent and impact of photoreduction, six individual spectra were collected at unique positions on the sample surface, following a matrix positioning grid to ensure a new radiation exposure surface, and only the initial exposure spectrum at each position was used during overall data analysis. Spectra were collected on duplicate independent samples, and data presented in this report represent the average of six scans.

XAS spectra were processed and analyzed using the EXAFSPAK program suite written for Macintosh OS-X[92] integrated with the Feff v8 software[93] for theoretical model generation. EXAFS fitting analysis was performed on raw/unfiltered data. Single scattering models were calculated for oxygen, nitrogen, sulfur, copper, and carbon coordination to simulate possible copper ligand environments, with values for the scale factors (Sc) and E_0 calibrated by previous fittings of characterized Cu(I)/Cu(II) crystallographic copper model compounds[11]. Standard criteria for judging the best-fit EXAFS simulations included a reasonable Debye–Waller factor for the fit ($\sigma^2 < 0.006$ Å^2) [94]; the spectral resolution of the data, calculated based on the energy range extent of usable data[95]; and the lowest mean square deviation between data and fit width, corrected for the number of degrees of freedom (F')[95]. During the standard criteria simulations, only the bond length and Debye–Waller factor were allowed to vary for each ligand environment. A dimensionless Sc = 1 and E_0 values of −12, −14, and −16 eV were used for Cu(I,II)-C/N/O, -S, and -Cu theoretical model calibrations, respectively, during simulations[11].

CHAPTER 3: NATIVE TOP-DOWN MASS SPECTROMETRY PROVIDES INSIGHTS INTO THE COPPER CENTERS OF MEMBRANE-BOUND METHANE MONOOXYGENASE

ABSTRACT

Aerobic methane oxidation is catalyzed by particulate methane monooxygenase (pMMO), a copper-dependent, membrane metalloenzyme composed of subunits PmoA, PmoB, and PmoC. Characterization of the copper active site has been limited by challenges in spectroscopic analysis stemming from the presence of multiple copper binding sites, effects of detergent solubilization on activity and crystal structures, and the lack of a heterologous expression system. Here we utilize nanodiscs coupled with native top-down mass spectrometry (nTDMS) to determine the copper stoichiometry in each pMMO subunit and to detect post-translational modifications (PTMs). These results indicate the presence of a mononuclear copper center in both PmoB and PmoC. pMMO-nanodisc complexes with a higher stoichiometry of copper-bound PmoC exhibit increased activity, suggesting that the PmoC copper site is essential for methane oxidation. These results provide key insights into the pMMO copper centers and demonstrate the ability of nTDMS to characterize membrane-bound metalloenzymes with complete molecular specificity.

INTRODUCTION

Particulate methane monooxygenase (pMMO) is an integral membrane metalloenzyme that oxidizes methane to methanol[61] in methanotrophic bacteria[1]. pMMO comprises three subunits, PmoB, PmoA, and PmoC, assembled into a larger $\alpha_3\beta_3\gamma_3$ complex[6-10]. The enzymatic activity of pMMO depends on the presence of copper, with approximately two copper ions per $\alpha\beta\gamma$ protomer required for optimal activity[10,14]. Extensive efforts have been devoted to elucidating the nature of the pMMO copper active site[61,63], with the ultimate goal of identifying the reactive copper-oxygen intermediate responsible for activating the 105 kcal/mol C-H bond in methane[611]. A molecular and mechanistic understanding of the pMMO active site is essential for the design of methane remediation tools, including synthetic catalysts and engineered methanotrophs[47,60], and may also provide new insight into copper-mediated oxidation chemistry.

Candidate locations for the copper active site were first identified in the crystal structure of *Methylococcus capsulatus* (Bath) pMMO (Bath-pMMO), which revealed three metal centers[6]. Two copper centers were modeled in PmoB: a nonconserved monocopper site ligated by His 48 and His 72 (bis-His site) that is not observed in other pMMO structures, and a conserved site at the amino terminus ligated by His 33, His 137, and His 139 (Cu_B site). The latter site was initially modeled as dicopper on the basis of extended X-ray absorption fine structure (EXAFS) data[9-11], but later analysis and crystal structures indicated that this site may instead be monocopper (Fig. 3.1)[7,10,16]. In addition, a third site occupied by zinc from the crystallization buffer was present in the PmoC subunit with ligands Asp 127, His 131, and His 144. This site, sometimes called the variable metal binding site, can also be occupied by copper[10] and is located in a chronically disordered region of the PmoC subunit[7].
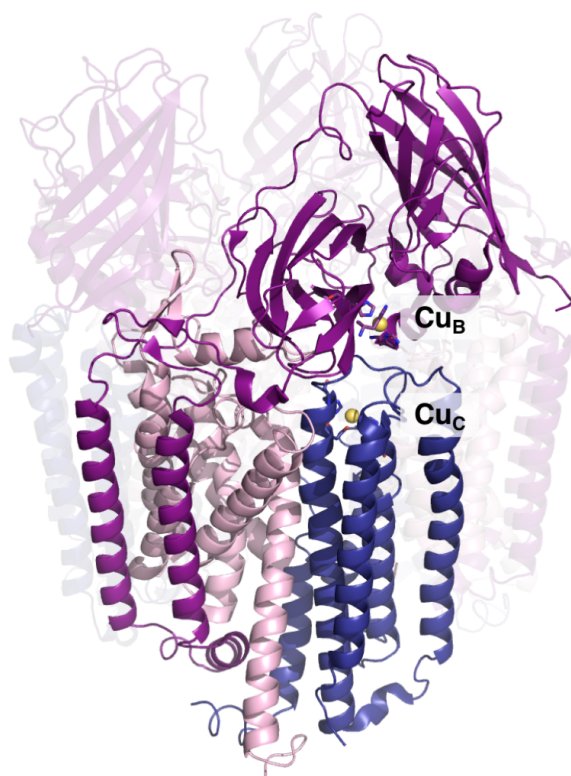
Figure 3.1. The pMMO structure and location of the metal centers.
In the crystal structure of Rockwell-pMMO (4PHZ), there is a monocopper center in PmoB coordinated by residues His 29, His 133, and His 135 (Cu$_B$), and a monocopper center in PmoC coordinated by Asp 129, His 133, and His 146 (Cu$_C$). PmoA, PmoB, and PmoC are shown in *pink*, *purple*, and *blue*, respectively, with one of the three protomers highlighted. Copper ions are shown as *yellow* spheres.

The nuclearity of the Cu_B site has been defined unambiguously by recent in vivo advanced electron paramagnetic resonance (EPR) spectroscopic characterization of *Methylococcus capsulatus* (Bath). In addition, the presence of a second monocopper center at the PmoC variable metal binding site, denoted the Cu_C site, was demonstrated using double electron-electron resonance (DEER) spectroscopy[17]. These data established an important correlation between the sites observed in the crystal structure and the sites present in the cell. While the Cu_B site was previously assigned as the active site[14], our more recent studies indicate that it is not sufficient for methane oxidation, consistent with the requirement for two copper ions[10,14]. The possibility that methane oxidation occurs at the PmoC Cu_C site has been raised[17], but lacks direct experimental support.

The study of pMMO has been hindered by the limitations of traditional biochemical, structural, and spectroscopic approaches. Metal analyses indicating the presence of 2-3 copper ions provide no insight into the specific locations of these metal ions, necessitating inferences based on combined crystallography and spectroscopy. The crystal structures are subject to artifacts from the crystallization buffer such as the presence of zinc in the PmoC site[6,9] as well as unknown effects of detergent solubilization and the crystallization process. In addition, some flexible regions are never observed in the electron density maps[7]. Spectroscopic data collected on pMMO reflect a mixture of copper species, rendering it nontrivial and in the case of EXAFS, impossible, to separate signals arising from different sites. This issue is compounded by the fact that pMMO has not been expressed heterologously, precluding facile site-directed mutagenesis. These challenges are not specific to pMMO; determination of metal stoichiometry and localization can be a major challenge for large, multisubunit metalloprotein complexes.

An emerging alternative approach for metal center characterization is native mass spectrometry (nMS), which typically employs electrospray ionization at neutral pH from volatile, non-reducing buffers[96], and instrument settings that faithfully preserve the primary and quaternary composition of complexes in the sample[97,98]. Coupling tandem MS (MS^n) activation of a non-covalent protein assembly to the nMS analysis[99] can help to characterize liberated components from the complex, such as subunits[18]. Moreover, measurement of intact mass values by nMS followed by gas-phase protein fragmentation, termed native top-down mass spectrometry (nTDMS)[100,101], enables the identification and characterization of specific proteoforms emanating from encoding genes including those containing underlying sequence changes due to polymorphisms, unexpected truncations, or post-translational modification (PTM)[100-105]. In particular, nTDMS can be used to determine metal stoichiometry of each subunit and even the identities of the metal binding ligands[106-108]. In 2013[100], a nTDMS platform achieved a three-tiered tandem mass spectrometry (MS) process, comprising measurement of an intact protein complex (MS^1), analysis of ejected monomer(s) (MS^2), and backbone fragmentation of each monomer (MS^3, or pseudo-MS^3) measured at isotopic resolution (Fig. 3.2)[100,101].

Here we have applied nTDMS to pMMO. While some membrane proteins have been characterized by nMS[109-112], this is the first nTDMS characterization of a multisubunit, membrane metalloenzyme via MS^3 fragmentation of individual subunits for metal ion identification, localization, and stoichiometric determination. Our nTDMS analysis of pMMO in micelles and nanodiscs[113] has identified proteoforms of pMMO subunits and PTMs that may have functional implications. Most importantly, the data support the presence of one copper ion each in the PmoB
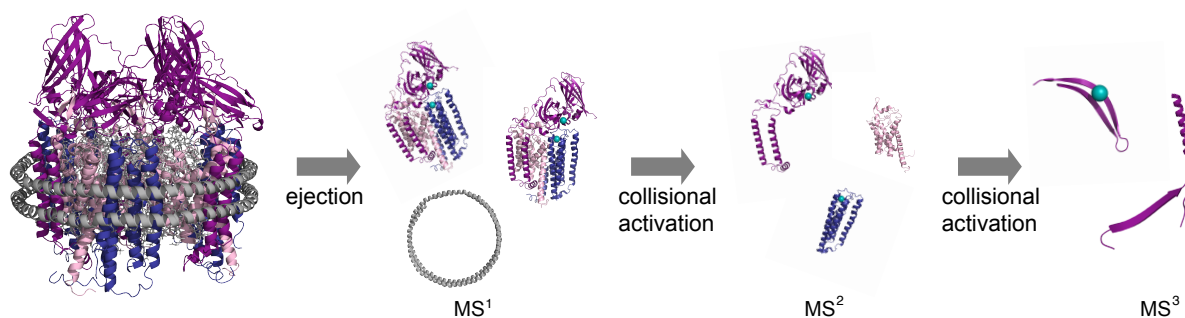
Figure 3.2. The nTDMS platform for pMMO characterization.
The pMMO-nanodisc complex is subjected to ejection from the nanodisc using collision-induced dissociation (CID) at the source resulting in the stabilization of pMMO protomer species (MS^1). Increasing collisional activation breaks up the protomer into individual pMMO subunits (MS^2). Further collisional activation enables backbone fragmentation of each subunit using higher energy collisional dissociation (HCD) in the HCD cell of the instrument (MS^3).

and PmoC subunits, and in combination with activity profiles of pMMO in nanodiscs, show that the copper ion bound to PmoC is essential for oxidation of methane to methanol.

RESULTS

Defining the proteoform composition of pMMO by nTDMS.

Our initial nTDMS studies focused on pMMO from *Methylomicrobium alcaliphilum* 20Z (20Z-pMMO). Methanotrophs from the genus *Methylomicrobium (Mm.)* have attracted interest as tractable model systems in engineering applications for methane-to-biofuel conversion, and *Mm. alcaliphilum* 20Z has been the subject of several studies[49,114,115], including the recent characterization of its pMMO[7]. In the crystal structure of 20Z-pMMO, one copper ion was modeled into the Cu_B site, supported by EXAFS analysis. However, metal quantitation and EPR analysis indicated the presence of two copper ions per pMMO protomer. In the crystal structure, the PmoB bis-His site is unoccupied and the PmoC subunit is mostly disordered, rendering it impossible to determine if it houses any metal ions. Thus, additional data are needed to assess the metal centers in 20Z-pMMO, motivating its investigation by nTDMS.

20Z-pMMO was solubilized from as-isolated membranes and purified by anion exchange chromatography[7]. After reconstituting 20Z-pMMO in Triton X-100 micelles, the complex was subjected to nMS analysis for characterization. The MS[1] analysis (Fig. S3.1a) produced a species exhibiting a 15-18+ charge state distribution. Deconvolution of the charge states of the major species present at 93% (Fig. S3.1a, labeled in purple) yielded a mass of 98,696.0 ±1.1 Da (Fig. 3.3a). The theoretical mass of an unmodified pMMO protomer, 99,255.7 Da, is based on the amino acid sequences of the subunits, assuming the cleavage of a known signal peptide at the PmoB N-

Deconvoluted MS^1 and MS^2:
20Z-pMMO protomer ejected from micelle

a

98,698.5 ± 1.1

NL: 1.88E5

Signal Intensity

98,300   98,500   98,700   98,900   99,100

Mass (Da)

20Z-pMMO protomer
Obs. 98,698.5 ± 1.1 Da
Th. 99,255.7 Da
Δm: -557.2 Da

PmoA
Obs. 28,166.8 ± 0.4 Da
Th. 28,257.1 Da
Δm: -90.3 Da

PmoB
Obs. 42,221.6 ± 0.3 Da
Th. 42,147.17 Da
Δm: 74.4 Da

PmoC
Obs. 28,245.2 ± 0.5 Da
Th. 28,851.44
Δm: -606.24 Da

b

NL: 5.04E3

Truncated PmoC
28,245.2 ± 0.5

NL: 6.11E3

PmoB + Cu(II)
42,221.6 ± 0.3

PmoA
28,168.8 ± 0.4

PmoB
42,162.0 ± 0.5

+ Cu(II)

Signal Intensity

28,140   28,180   28,220   28,260   42,150   42,190   42,230

Mass (Da)

Figure 3.3. nTDMS analysis of 20Z-pMMO in Triton X-100 micelles.
a, deconvoluted MS^1 of 20Z-pMMO protomer upon ejection from a Triton X-100 micelle. Charge state deconvolution of the major species yields a mass of 98,696.5 ±1.1 Da. The theoretical mass is derived from the unmodified subunits of pMMO and accounts for the cleavage of a known signal peptide in PmoB. **b**, deconvoluted MS^2 of 20Z-pMMO subunits ejected from the 16+ charge state of the protomer after activation by collisions with neutral gas. The spectrum shows detection of three species, labeled *pink*, *purple*, and *blue* and assigned to PmoA, PmoB, and PmoC, respectively. Adding the measured masses of the ejected subunits yields 98,633.6 Da, which is 62.4 Da smaller than the major protomer mass measured in the MS^1. NL values reflect maximum signal intensity in the spectrum.

terminus[116] (theoretical mass of a protomer with an uncleaved PmoB is 102,638.7 Da). While the observed mass of the predominant species is lower than the theoretical mass that assumes cleavage of the PmoB signal peptide (mass shift, Δm = -559.7 Da), the close match suggests that the species ejected from the Triton X-100 micelle is a modified pMMO protomer.

To investigate the possible presence of PTMs and metal cofactors in proteoforms comprising the pMMO protomer, the 16+ charge state of the pMMO-micelle complex was subjected to nTDMS. First, intact pMMO protomer was activated by collisions with neutral gas in the ESI source region to produce a pseudo-MS^2 of the ejected subunits (Fig. 3.1b). Three major protein species that correspond closely in mass to each one of the pMMO subunits were detected (Fig. 3.3b). The PmoA subunit, with a theoretical mass of 28,257.1 Da, was tentatively assigned to the 28,166.8 ± 0.4 Da proteoform, with a Δm of -89.1 Da consistent within a dalton for the removal of the initiator methionine (Met$_{OFF}$) and the addition of N-terminal acetylation (NtAc) to the new N-terminus. The 42,221.6 ± 0.3 Da proteoform, which is closest in mass to PmoB (theoretical mass 42,147.17 Da, Δm = +74.4 Da), could result from the replacement of two protons by one copper(II) ion[4] (+61.5 Da) and a potential PTM. The third species had a mass of 28,245.2 ± 0.5 Da, which may be attributable to a truncated proteoform of PmoC (theoretical mass 28,851.4 Da, Δm = -606.2 Da). The addition of the three detected masses yields an αβγ protomer of 98,633.6 Da, which is 62.4 Da smaller than the observed protomer via MS^1. This mass loss suggests that a copper ion (theoretical average mass of 61.5 Da) may be lost upon subunit ejection from the pMMO-micelle complex.

To confirm subunit assignments and characterize their mass shifts, intact proteoforms need to be fragmented by tandem MS. Attempts at tandem MS on subunits ejected from the Triton X-

100 micelle were unsuccessful due to the limited ability to activate ions in the ESI source; for example, disrupting the micelle to produce intact pMMO ions required relatively high settings of 150-195 V. This precluded further activation of the complex in the ESI source (200 V max), which is essential for individual subunits to be isolated and further dissociated in the high-energy collision dissociation cell (HCD) within the instrument.

nTDMS analysis of pMMO proteoforms ejected from nanodiscs.

To achieve further collisional activation and to potentially stabilize the copper ion lost upon subunit ejection, Triton X-100 micelles were substituted with nanodiscs, discoidal lipid bilayers absent of detergent and commonly used to stabilize membrane proteins[117]. Nanodiscs have been reported to minimize coulomb-induced unfolding in the gas phase, suggesting that they can be protective of labile non-covalent interactions upon ejection from the assembly[110-112]. 20Z-pMMO was embedded in nanodiscs using POPC lipids and the membrane scaffold proteins MSP2N2 or MSP1E3D1 (Fig. S3.2-3.3)[113]. Nanodiscs formed using MSP2N2 and MSP1E3D1 have diameter distances of up to 17 nm and 12 nm, respectively, and can accommodate the 9 nm pMMO complex. MSP1E3D1 provided higher reconstitution yields and stability than MSP2N2, potentially because the smaller diameter of MSP1E3D1 allows for a tighter fit with pMMO. Two-dimensional class averages of cryo-electron microscopy images and SDS-PAGE were used to assess reconstitution and confirm the presence of all three pMMO subunits in MSP2N2 nanodiscs (Fig. 3.4, Fig. S3.4); MSP1E3D1 nanodiscs were analyzed by negative stain electron microscopy images and SDS-PAGE.
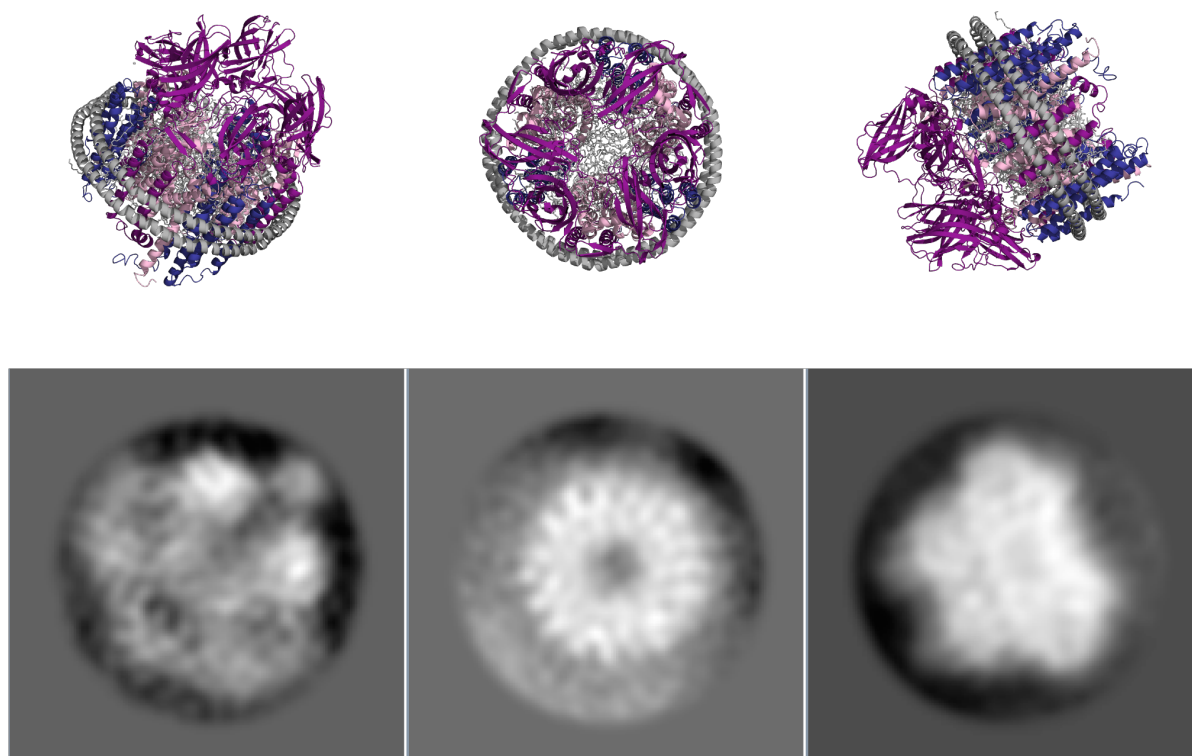
Figure 3.4. Cryo-EM 2D class averages of 20Z-pMMO in MSP2N2 nanodiscs.
Tilted, top, and side views of 20Z-pMMO reconstituted in nanodiscs.

The 20Z-pMMO nanodisc complex was subjected to the nTDMS platform, which presented some initial challenges. First, we were unable to obtain an intact mass of the complex given the heterogeneity of the signals detected. Second, excess of lipids in the nanodiscs led to the detection of lipid clusters, which dominated the signal in MS^1 spectra. We overcame these difficulties by titrating the lipid content in the nanodiscs to an optimal concentration that reduced signals from lipid clusters, as measured by nMS, while still preserving enzymatic activity. Additionally, we tuned the ion optics of the mass spectrometer, including the C-trap entrance lens voltage, to filter out high intensity lipid cluster ions. The pMMO complex was subjected to subunit ejection from the nanodisc complex using collision-induced dissociation (CID) at the source. The successful ejection of the individual subunits (Fig. S3.5) with 195 eV of source fragmentation enabled their subsequent isolation by the quadrupole mass filter and fragmentation in the HCD cell. A deconvoluted MS^2 spectrum shows detection of protein species that were targeted for fragmentation (Fig. 3.5a). HCD generated *b* and *y* ions from fragmentation at backbone amide positions that were mapped onto the sequence of the pMMO subunits (Fig. 3.5b), thereby localizing mass shifts[118].

Notably, as shown in the graphical fragment maps in Fig. 3.5b, PmoB includes residues His 33 to Ile 414, consistent with the presence of a leader sequence that is cleaved post-translationally[116]. PmoB residue Lys 36 was found to be methylated, a modification localized by the nTDMS to residues 33-51 and pinpointed by tandem MS of pepsin-digested peptides of 20Z-pMMO (Fig. S3.6a). This lysine is located 8.3 Å from the Cu_B site and does not appear methylated in the electron density map[7], yet was present at ~100% stoichiometry from the nTDMS data. It is not known whether this methylation is functionally important. PmoA was characterized to be

a **Deconvoluted MS²: 20Z-pMMO subunits ejected from nanodisc-pMMO complex**

NL: 3.90E3

NL: 7.94E2

Signal Intensity

Truncated PmoC c
28,244.8 ± 0.8

28,166.9 ± 1.2 PmoA

Truncated PmoC + Cu(II) 28,308.2 ± 1.2

PmoC 28,761.4 ± 1.0

PmoB + Cu(II) 42,222.0 ± 0.6

28100 28200 28300 28400 28500 28600 28700 28800   42180 42220 42260

Mass (Da)

20Z-pMMO Theoretical MW accounting for PTMs:

PmoA	**28,167.1 Da** Δ*m*: 0.2 Da
PmoB + Cu(II)	**42,222.7 Da** Δ*m*: 0.7 Da
PmoC	**28,762.3 Da** Δ*m*: 1.1 Da
Truncated PmoC	**28,246.8 Da** Δ*m*: 2.0 Da
Truncated PmoC + Cu(II)	**28,308.3 Da** Δ*m*: 0.1 Da

b **MS³: Fragmentation of ejected 20Z-pMMO subunits**

PmoA p-score: 3.2x10⁻³⁹

```
N  S A S Q S A V R S R A E A V K V S R T F D Y M I L  25
26 F T V F F V V L G G Y H I H Y M L T G G D W D F W  50
51 T D W K D R R L W V T V A P I V S I T F P A A V Q  75
76 A V L W W R Y R I A W G A T L C V L G L L L G E W  100
101 I N R Y F N F W G W T Y F P V N F V F P S N L M P  125
126 G A I V L D V I L M L S N S M T L T A V V G G L A  150
151 W G L L F Y P G N W P I I A P L H V P V E Y N G M  175
176 M M T L A D L Q G Y H Y V R T G T P E Y I R M V E  200
201 K G T L R T F G K D V A P V S A F F S G F V S I L  225
226 I Y F L W H F F G S W F G S E K F V Q A A  C
```

PmoC p-score: 3.7x10⁻¹⁴

```
N  A A T T E S V K A D A A E A P L L N K K N I I A G  25
26 A S L Y L V F Y A W V R W Y E G V Y G W S A G L D  50
51 S F A P E F E T Y W M N F L Y I E M V L E V L T A  75
76 S V L W G Y I W K S R D R K V M S I T P R E E L R  100
101 R H F T H W T W L M M Y G I A I Y F G A S Y F T E  125
126 Q D G T W H Q T I V R D T D F T P S H I I E F Y L  150
151 S Y P I Y I I T G G A S F L Y A K T R L P T Y Q Q  175
176 G L S L Q Y L V V V V G P F M I L L P N V G L N E W  200
201 G H T F W F M E E L F V A P L H Y G F V F F G W S  225
226 A L G V L G V I N I E L G A L S K L L K K D L A  C
```

PmoB p-score: 6x10⁻¹⁵

```
N 33 H G E K S Q A A F M R M R T I H W F D L N W S K D  57
58    Q V S V N E T M S I S G K F H V F A G W P E T V D  82
83    K P E V A F L N I G I P G P V F I R A G S W I G G  107
108   Q L V P R S V S L E L G E T Y E F K V L L K A R R  132
133   P G D W H V H T M M N V Q G G G P I I G P G K W V  157
158   T I T G S M G D F K N P I T T L T G E T I D L E T  182
183   Y A L D G V Y G W H L F W Y L L G V A W M V Y W C  207
208   R K P V F I P R R I A V D A G K A D S L I T P T D  232
233   K K V G M A F A A G T L A I V A V S M G Q A N E K  257
258   Y P V T T P L Q A G L M R G I K S L E L P Q P T V  282
283   S V K V V D A S Y R V P G R A M Q M T L E I T N N  307
308   G D S A V R L A E F N T A S V R F L D A D V Y E D  332
333   D T N Y P D D L L A E E G L S V S D N S P L A P G  357
358   E T R T V D V T A S D A A W E V Y R L A D L I Y D  382
383   P D S R F A G L L F F I D E D G N R Q M T M V D A  407
408   P L I P T F I  C
```

⌐ **N-terminal fragment**
∟ **C-terminal fragment**
∟⌐ **Bidirectional (N & C) fragment**

[N] **N-terminal acetylation**
[K] **Lysine methylation**

Figure 3.5. nTDMS analysis of 20Z-pMMO in MSP2N2 nanodiscs.
a, deconvoluted MS² showing detection of 20Z-pMMO subunit masses upon ejection from the nanodisc-pMMO complex. The panel on the right contains the theoretical masses of the subunits, accounting for the modifications characterized by tandem MS. **b**, graphical fragment maps of pMMO subunits derived from the MS³ step in the nTDMS platform. Fragments are depicted as blue flags in the graphical fragment maps, indicating which regions of the protein sequence can be accounted for in mass by the fragments. The pMMO subunits were found to be modified by N-terminal acetylation (PmoA and PmoC), N-terminal truncation (PmoC), and lysine methylation (PmoB). The graphical fragment map of PmoB begins at residue His 33, showing cleavage of the known N-terminal signal peptide.

Met$_{OFF}$ and NtAc (Fig. 3.5b), as suggested by analysis of the micelle sample. The MS^2 from the nanodisc reflects two populations of PmoC. A minor species is observed with Met$_{OFF}$ and NtAc while the major PmoC species is a truncated form without the first six N-terminal residues (MAATTE) (Fig. 3.5a, Fig. S3.6b).

Localization of the copper binding sites in pMMO.

We next sought to determine the stoichiometry of metal binding to each pMMO subunit. The copper in 20Z-pMMO was determined by EPR analysis to be predominantly in the Cu(II) oxidation state[7]. Deconvolution of the MS^2 generated upon ejection of pMMO from the nanodisc (Fig. 3.5a) revealed that the predominant PmoB proteoform has a mass consistent with a methylation (14 Da) and one Cu(II) ion (61.5 Da). Given that one copper ion remains associated with PmoB even after subunit ejection, we hypothesized that some copper might remain bound to fragments generated in the pseudo-MS^3 analysis[100] of this proteoform, thereby helping to verify the location of the Cu$_B$ site[108]. Two b-type fragment ions, b_{165} and b_{186} (corresponding to the numbering indicated in the graphical fragment map in Fig. 3.5b), were identified with mass shifts consistent with the binding of one Cu(II) ion (Fig. S3.7) as demonstrated by the fitting of the theoretical isotopic distributions for copper-bound fragment ions. Notably, both copper-bound fragment ions occurred C-terminal to an aspartic acid residue, which is consistent with known fragmentation propensities under native ESI[103]. No copper binding was observed for fragment b_{135} or for any other downstream b ions. In congruence with the crystal structure, these copper-bound fragment ions suggest that the copper binding region (green underline in Fig. S3.7) may be confined to the region spanning Trp 136-Asp 186, which contains the coordinating residues His 137 and His 139, but not the ligands to the bis-His site, His 48 and His 72. Copper binding fragment

ions containing His 33 were not observed, perhaps due to the labile nature of this ligand suggested by the crystal structures[6,7,9,10]. Moreover, there is no copper binding observed in the C-terminal cupredoxin domain, previously suggested to bind ~10 copper ions[119].

PmoC ejected from the pMMO-nanodisc complex has a proteoform present at 16% relative abundance that is consistent with a copper ion bound to the truncated PmoC species (Fig. 3.5a). Reduced copper stoichiometry in pMMO is observed upon nanodisc reconstitution (Fig. S3.8), suggesting that bound copper may be lost from PmoC during the reconstitution. To determine whether the copper-binding stoichiometry of PmoC could be increased by exogenous addition of copper to the electrospray buffer, we added 1, 3, and 6 molar equivalents (eq.) of Cu(II) per protomer to 20Z-pMMO in nanodiscs and analyzed these samples by nTDMS (Fig. S3.9). We found that at 1 eq. of Cu(II) per protomer, 10.4% (±3%) of PmoC is bound to copper. At 3 eq. of Cu(II), copper binding increases to a maximum of 27% (±3%), with no further increase after addition of more copper. Notably, no additional copper binding is observed for PmoB, as shown in the inset of (Fig. S3.9b). The precursor intensity of copper-bound PmoC proteoform was too low for these samples and thus was not fragmented successfully for metal localization. Taken together, the spectra generated from the micelle and nanodisc systems indicate that 20Z-pMMO binds one copper ion near the PmoB N-terminus and one copper ion in the PmoC subunit.

To validate the copper localization in 20Z-pMMO, pMMOs from other methanotrophs were investigated via nTDMS. Interestingly, PmoC copper binding was observed for samples of pMMO from *Mm. buryatense* 5GB1C (5G-pMMO) in Triton X-100 micelles. The MS[1] analysis of 5G-pMMO shows a predominant mass species that correlates to a pMMO protomer bound to two copper ions (Fig. S3.10-3.11a), similar to 20Z-pMMO in micelles. MS[2] ejection (Fig. S3.11b-3.12) of the subunits confirms that the predominant species of PmoB also contains one copper ion

and has Lys 36 methylation. While MS^2 of 5G-pMMO in micelles indicated copper binding to the PmoC subunit, this was not the case for the 20Z-pMMO PmoC in micelles, possibly due to structural differences between the two PmoC subunits. Unfortunately, 5G-pMMO in nanodiscs exhibited poor ejection from the nanodisc complex and could not be characterized via nTDMS.

We then investigated pMMO from *Methylocystis* sp. strain Rockwell (Rockwell-pMMO). In the crystal structure of Rockwell-pMMO, the PmoC site is occupied by copper[10]. Unlike 5G-pMMO, Rockwell-pMMO in MSP1E3D1 nanodiscs (Fig. S3.13) ejected well from the nanodisc complex and was thus amenable to nTDMS analysis of the subunits. Subunit ejection (Fig. S3.14, Fig. 3.6a) and subsequent fragmentation of Rockwell-pMMO led to the identification of the PmoB and PmoC subunits (Fig. 3.6c). Similar to 20Z-pMMO, PmoB showed an intact mass shift of 61.5 Da that suggests 100% occupancy of a single Cu(II) ion. Unlike 20Z- and 5G-pMMO, PmoB methylation was not detected, indicating that this PTM may not be necessary for activity and may be specific to *Methylomicrobium* pMMOs. Truncated PmoC was observed in the apo form, but close examination of the spectrum (Fig. 3.6a) reveals a low abundance peak that is shifted by the mass of copper, consistent with inductively coupled plasma mass spectrometry (ICP-MS) data (vide infra) and with a labile metal interaction that is partially lost at high collision voltages or during nanodisc reconstitution, as observed for 20Z-pMMO.

a **Deconvoluted MS²:**
Rockwell-pMMO subunits ejected from nanodiscs

Signal Intensity

Truncated PmoC **28,701.0 ± 1.2** NL: 2.3E4
Truncated PmoC + Cu(II)
+Cu(II)
+17 Da +34 Da
28,763.0 ± 1.2
PmoB + Cu(II) **43,201.0 ± 1.2** NL: 2.4E4

28670 28690 28710 28730 28750 28770 28790   43100 43140 43180 43220 43260 43300
Mass (Da)

b

Signal Intensity

Full-length PmoC **29,118.6 ± 1.4** NL: 1.03E4
Full-length PmoC + Cu(II) **29,180.8 ± 0.9**
+Cu(II)
37(±2)% of total PmoC

29080 29100 29120 29140 29160 29180 29200 29220
Mass (Da)
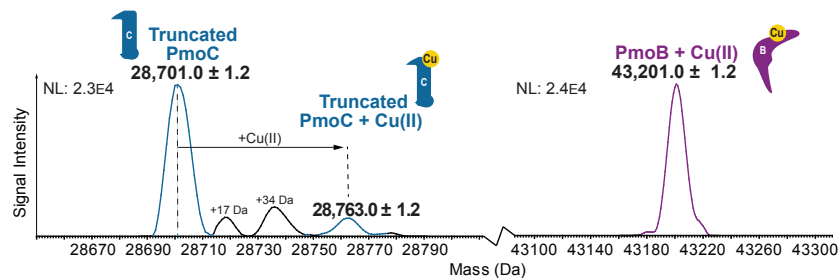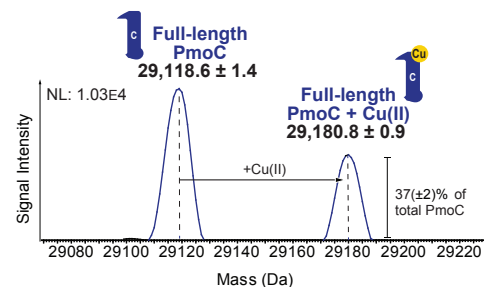
Rockwell-pMMO Theoretical MW accounting for PTMs:

PmoB + Cu(II)	**43,201.7 Da**	Δm: 0.7 Da
Truncated PmoC	**28,702.6 Da**	Δm: 1.6 Da
Truncated PmoC + Cu(II)	**28,764.1 Da**	Δm: 1.1 Da

c   **MS³: Fragmentation of ejected Rockwell-pMMO subunits**

Truncated PmoC p-score: 3.5×10^{-34}

```
N   S A A A G A A A E V E S V V D L R G M W I G L V L  30
31  L N V F Y L I V R I Y E Q V F G W R A G L D S F A  55
56  P E F Q T Y W M S I L W T E I P L E L V S G L G L  80
81  A G Y L W K T R D R N V D A V T P R E E M R R L V  105
106 V L V Q W L V V Y G I A I Y W G A S F F T E Q D G  130
131 T W H M T V I R D T D F T P S H I I E F Y M S Y P  155
156 I Y S V I A V G A F F Y A K T R I P Y F A H G Y S  180
181 L A F L I V A I G P F M I I P N V G L N E W G H T  205
206 F W F M E L L F V A P L H W G F V F F G W M A L G  230
231 V F G V V L Q I L M R I H A L V G K E G V K L L T  255
256 E  C
```

N-Terminal Fragment
C-Terminal Fragment

PmoB p-score: 3.5×10^{-8}

```
N 29 H G E K S Q Q A F L R M R T L N W Y D V Q W S K T  53
54   T V N V N E E M V L S G K V H V F S A W P Q A V A  78
79   N P R V S F L N A G E P G P V L V R T A Q F I G E  103
104  Q F A P R S V S L E I G K D Y A F S I N L R G R R  128
129  A G R W H V H A Q I N V E G G G P I I G P G Q W I  153
154  E I K G D M K D F T D P V T L L D G S T V D L E H  178
179  Y G I S R V Y A W H L P W M A V G A A W I F F W F  203
204  V R K G I I T S Y I R V A E G K A D D V I G D D D  228
229  R R I G A I V L A L T I L A T I V G Y A V T N S T  253
254  F P R T I P L Q A G L Q K P L T P I E T E G T V G  278
279  V G K E N V T T E L N G G V Y K V P G R E L T I N  303
304  V K V K N N T S Q P L R L G E Y T A A G L R F L N  328
329  P D V F T T K P D F P D Y L L A D R G L S V D A T  353
354  P I A P G E A K E I V V K I Q D A R W D I E R L S  378
379  D L A Y D T D S Q I G G L L F F F S P D G K R Y A  403
404  S E I G G P V I P K F V A G D M P  C                 420
```

Figure 3.6. nTDMS analysis of Rockwell-pMMO in MSP1E3D1 nanodiscs.
a, Deconvoluted MS² demonstrating detection of Rockwell-pMMO subunit masses upon ejection from the nanodisc without or **b**, with copper supplementation during nanodisc reconstitution. The panel on the right contains the theoretical masses of the subunits, accounting for the modifications characterized by tandem MS. The two species shifted in mass from PmoC by +17 and +34 Da likely correspond to the replacement of one and two protons by ammonium adducts (Th. 17.03 Da and 34.06 Da, respectively) on PmoC commonly observed in nESI[60]. **c**, The MS³ of truncated PmoC and PmoB yielded fragment ions, depicted as blue flags in the graphical fragment maps that indicate which regions of the protein sequence can be accounted for in mass by the fragments. Truncated PmoC lacks the first five residues of the N-terminus (MSSTT), and its graphical fragment map begins at residue Ser 6. The graphical fragment map of PmoB begins at residue His 29, consistent with the cleavage of the known N-terminal signal peptide.

Linking pMMO activity to copper binding by PmoC.

In the crystal structures, the PmoC metal binding site is occupied by zinc[6,9] or copper (Rockwell-pMMO)[8,10], or is completely disordered[7]. However, it has thus far been unclear whether metal binding at this site is functionally relevant[10]. Given that the nTDMS data indicate the presence of some copper in the PmoC subunits from three different organisms, and that pMMO activity requires more than one copper ion, we investigated the effect of exogenous copper addition on Rockwell-pMMO by both nTDMS and activity assays. Membrane-bound Rockwell-pMMO exhibits the highest methane oxidation activity at 30 °C out of all characterized pMMOs[7,10], but upon reconstitution into nanodiscs, the activity dramatically decreased compared to that of the as-isolated membranes (Fig. 3.7a).

Upon addition of one equivalent of $CuSO_4$ per pMMO protomer during the nanodisc reconstitution process, the methane oxidation activity of the pMMO-nanodisc complex increased six-fold (Fig. 3.7a). The activity was higher than that of membrane-bound pMMO using duroquinol as a reductant, similar to the increased activity observed for pMMOs reconstituted into bicelles[4]. ICP-MS analysis of the pMMO-nanodisc samples prepared with and without copper supplementation showed that in the absence of copper supplementation, approximately 0.7 ± 0.2 copper ion per pMMO protomer is present (Fig. 3.7b). Upon copper addition and incorporation into the pMMO-nanodisc complex, the copper content increased to approximately 1.8 ± 0.5 copper ions per pMMO protomer, consistent with the presence of up to two copper binding sites. These copper-supplemented Rockwell-pMMO nanodisc samples were then analyzed by nTDMS to determine the location of the second copper ion (Fig. 3.6b, Fig. S3.15). The nTDMS analysis of the active Rockwell-pMMO prepared with exogenous addition of copper showed a significantly
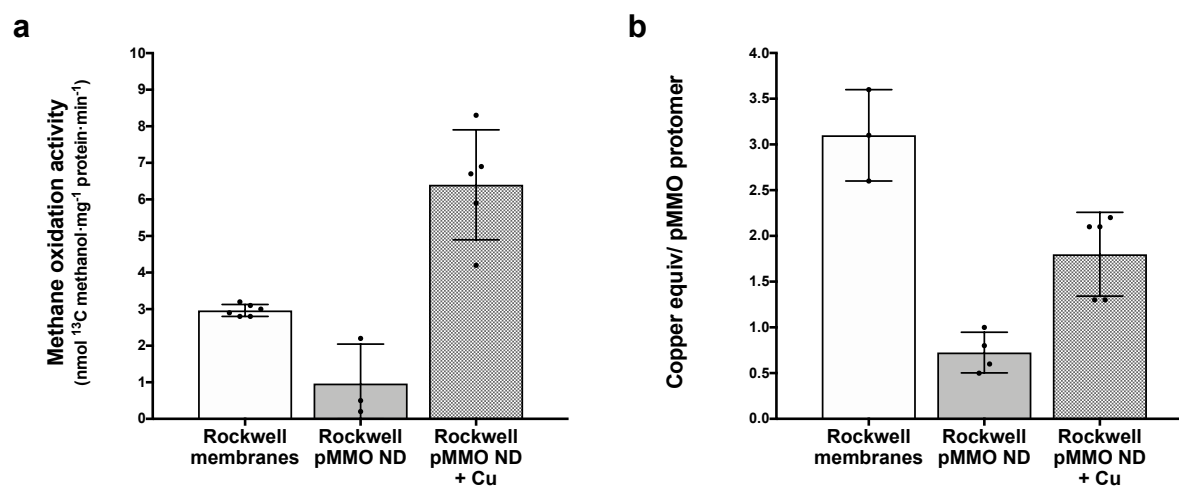
Figure 3.7. Activity and metal content of Rockwell-pMMO in nanodiscs.
a, ^{13}C methane oxidation activity of Rockwell-pMMO in membranes and in nanodiscs (ND) without or with copper supplementation. Values are shown in nmol ^{13}C methanol•mg^{-1} protein•min^{-1}, $3 \leq n \leq 6$. **b**, Copper equivalents per pMMO protomer for Rockwell-pMMO in membranes and in nanodiscs without or with copper supplementation, $3 \leq n \leq 5$. Error bars represent standard deviation, and the black dots represent individual measurements.

higher amount of copper bound PmoC ($37 \pm 2\%$, Fig. 3.6a) compared to the inactive sample (Fig. 3.6a). The correlation between this result and the activity data suggests that the copper ion in PmoC, likely corresponding to the spectroscopically assigned Cu_C site[17], is essential for methane oxidation activity.

DISCUSSION

The nTDMS analysis presented here advances our understanding of pMMO in several ways. First, we have obtained accurate intact masses for the pMMO protomer and individual subunits and have detected a previously unknown methylation of residue Lys 36 in the PmoB subunits of 20Z-pMMO and 5G-pMMO. The importance of this PTM, which is not found in Rockwell-pMMO, is unclear. This methylation might afford protection against reaction with radicals and oxidative damage, as proposed for methyl-coenzyme M reductase[120] and lytic polysaccharide monooxygenases[121], or provide additional hydrophobic interactions important for methane binding. Alternatively, this methylated lysine may be an off-target product formed by methyltransferases responsible for synthesizing osmolytes in haloalkaliphiles[122]. The observation of these modifications, including the truncated proteoforms of PmoC, highlights the importance of measuring the intact masses of proteoforms, as such modifications were not readily observed in previous biochemical studies[7] and may have functional implications.

Second, we have directly localized the copper sites in pMMO and for the first time, have established a correlation between the PmoC site and methane oxidation activity. The observation of one copper ion in PmoB and one copper ion in PmoC is consistent with in vivo EPR and DEER data[14], and confirms that the two copper ions detected in pMMO by metal analysis occupy these two sites. Previous studies have suggested that the PmoC site is important for activity. In particular,

mutagenesis of the PmoC metal binding ligands in hydrocarbon monooxygenase (HMO), a homolog of pMMO, abrogates enzyme activity[20]. Additionally, inhibition of pMMO by zinc has been attributed to zinc binding in the PmoC site[3]. However, the different occupancies of this site in the crystal structures, including the presence of zinc[6,9,10], copper[8,10], or no observable metal ion[7], have obscured its biological relevance. Here we show unambiguously that copper and activity loss upon nanodisc reconstitution can be restored by addition of exogenous copper, which increases copper occupancy of the PmoC site (Figs. 3.6-3.7). These results suggest that the PmoC Cu_C site plays an essential role in methane oxidation. Disruption of the native membrane may account for the increased lability of this site as compared to the consistently observed Cu_B site, which is in the periplasmic region of PmoB.

The Cu_C site and the respective roles of both monocopper sites in pMMO must be investigated further. The Cu_C site resides in a disordered yet highly conserved region of PmoC, and additional information on its coordination environment is desirable. It may be that the two monocopper centers function analogously to the non-coupled monocopper sites in peptidylglycine α-hydroxylating monooxygenase and dopamine β-monooxygenase[123], in which the Cu_M site is involved in O_2 activation and the Cu_H site, located 11 Å away across a solvent-filled cleft, provides the second electron to the Cu_M site for turnover. In the pMMO crystal structures, the PmoB and PmoC metal centers are 20 Å apart, but in the membrane, the PmoB periplasmic domain may shift towards the lipid bilayer, altering this distance. The combined activity and nTDMS data show that increased loading of the Cu_C site enhances activity, providing support for the idea that methane and oxygen bind at this site[17]. It remains unclear whether the Cu_B site is absolutely necessary for activity. While this site is consistently observed, its three histidine ligands are not present in the verrucomicrobial pMMO PmoB sequences[124], suggesting that methane oxidation may occur in its

absence. In comparison, the Cu_C ligands are conserved in all pMMOs[124,125], and its location in the intracytoplasmic membrane may facilitate methane access[126]. Additional experimental evidence is needed to determine the functions of the two monocopper sites.

Through an alternative approach coupling membrane mimetics with nTDMS analysis, we have gained valuable new insights into the active form of pMMO. The nTDMS platform relies on the isolation of distinct mass peaks using a quadrupole mass filter optimized for selection of high m/z ions produced by native electrospray[100]. Native-mode TDMS also circumvents protein contamination issues, is sensitive to the dynamic nature of large protein assemblies, and can resolve functionally different proteoforms of metal-bound subunits. The technological advances described here can overcome difficulties intrinsic to membrane proteins[127] and challenges associated with nanodisc samples[110,112]. Moreover, the ability to localize metal ions fills a gap in the traditional bioinorganic toolbox to characterize metalloproteins. Therefore, the experimental findings not only impact pMMO, but have broad implications for the improved characterization of myriad challenging membrane-bound complexes in metallobiology.

METHODS

Membrane scaffold protein expression and purification

The membrane scaffold proteins MSP1E3D1 and MSP2N2, each with TEV-cleavable N-terminal 7-histidine tags, were expressed and purified[113]. *E. coli* BL21(DE3) cells were transformed with plasmids pMSP1E3D1 or pMSP2N2 (Addgene), and 1 L cultures were inoculated at a starting OD_{600} of 0.1 in Terrific Broth media and grown for four hours at 37 °C with shaking at 200 rpm until an OD_{600} of 2.3 was reached. The cultures were induced with 1 mM isopropyl ß-D-1-thioglactopyranoside (IPTG) (RPI) and were grown for an additional 4 h at 37 °C

for protein expression, yielding 5 g wet cell pellets per L of culture. Cell pellets were harvested by centrifugation at 8,000 x g for 10 min, flash-frozen in liquid nitrogen, and stored at -80 °C.

Cells were resuspended in buffer A (40 mM Tris, pH 7.3, 250 mM NaCl, 20 mM imidazole) at 50 mL per 10 g cell pellet. EDTA-free protease inhibitor cocktail (1 tablet per 50 mL, Roche) and chicken egg lysozyme (10 mg per 50 mL, Sigma-Aldrich) were added. Once resuspended, Triton X-100 (Sigma-Aldrich) was added to a final concentration of 1% v/v and stirred. Cells were lysed on ice by sonication at 35% amplitude for 10 min (1 s on, 1 s off) and cell debris was removed by centrifugation at 10,000 x g for 30 min. The soluble fraction was loaded onto a column containing 10 mL Ni-NTA beads (Qiagen). The beads were washed with 50 mL of buffer B (40 mM, Tris pH 7.3, 250 mM NaCl, 20 mM imidazole, 50 mM sodium cholate) followed by 150 mL buffer A. The protein was then eluted with buffer C (40 mM Tris, pH 7.3, 250 mM NaCl, 250 mM imidazole).

The elution fractions were pooled and TEV protease was added at a mass ratio w/w of 1:40 TEV:protein. This mixture was dialyzed using a 10 MWCO SnakeSkin dialysis tubing (Thermo Fisher Scientific) in 1 L of buffer D (40 mM Tris, pH 7.3, 250 mM NaCl, 20 mM imidazole, 1mM EDTA) overnight with a buffer change after 1 h. TEV protease was removed by applying the sample to a Ni-NTA column and collecting the flowthrough, which was then dialyzed overnight against 1 L of buffer E (25 mM PIPES, pH 7.3, 250 mM NaCl) with a buffer change after 1 hr. The purified MSP proteins were concentrated using an Amicon centrifugal concentrator (10 kDa MWCO, Millipore) to a concentration of 4.5 mg/mL, measured by A_{280} using extinction coefficients of 26,930 and 36,900 $M^{-1} \cdot cm^{-1}$ for MSP1E3D1 and MSP2N2, respectively. The protein was flash frozen on liquid nitrogen and stored at -80 °C.

Methanotroph cell growth

Mm. alcaliphilum 20Z and *Mm. buryatense* 5GB1C were cultured following established methods[7,36]. Briefly, 12 L bioreactor cultures were grown in 1X modified nitrate mineral salts (NMSA) medium, 0.5 M NaCl (*Mm. alcaliphilum* 20Z) or 0.130 M NaCl (*Mm. buryatense* 5GB1C), 2.3 mM phosphate buffer, 50 mM carbonate buffer, pH 9.5, supplemented with 40 µM $CuSO_4 \cdot 5H_2O$ and trace elements solution (*Mm. alcaliphilum* 20Z 2000X stock solution: 0.5 g/L $Na_2 \cdot ETDA$, 0.2 g/L $FeSO_4 \cdot 7H_2O$, 0.01 g/L $ZnSO_4 \cdot 7H_2O$, 0.003 g/L $MnCl_2 \cdot 4H_2O$, 0.03 g/L H_3BO_3, 0.02 g/L $CoCl_2 \cdot 6H_2O$, 0.002 g/L $NiCl_2 \cdot 6H_2Ol$, 0.003 g/L $Na_2MoO_4 \cdot 2H_2O$; *Mm. buryatense* 5GB1C 500x stock solution: 1.0 g/L $Na_2 \cdot EDTA$, 2.0 g/L $FeSO_4 \cdot 7H_2O$, 0.8 g/L $ZnSO_4 \cdot 7H_2O$, 0.03 g/L $MnCl_2 \cdot 4H_2O$, 0.03 g/L H_3BO_3, 0.2 g/L $CoCl_2 \cdot 6H_2O$, 0.02 g/L $NiCl_2 \cdot 6H_2O$, 0.05 g/L $Na_2MoO_4 \cdot 2H_2O$). *Mc.* sp. str. Rockwell cells were cultured in 1X NMS medium, 3.9 mM phosphate buffer, pH 6.8, supplemented with 50 µM $CuSO_4 \cdot 5H_2O$, 40 µM $FeSO_4 \cdot 7H_2O$, and trace elements solution (500X stock solution: 0.288 g/L $ZnSO_4 \cdot 7H_2O$, 0.166 g/L $MnCl_2 \cdot 4H_2O$, 0.062 g/L H_3BO_3, 0.048 g/L $Na_2MoO_4 \cdot 2H_2O$, 0.048 g/L $CoCl_2 \cdot 6H_2O$, 0.083 g/L KI)[3]. These cultures were grown under a continuous gas flow using a 1:3 methane-to-air ratio at 1.2 L/min at 30 °C with 300 rpm agitation. All bioreactor cultures were harvested at an OD_{600} of 8-10, centrifuged at 8,000 x *g* for 1 h, flash frozen in liquid nitrogen, and stored at - 80 °C.

Membrane isolation

Membranes from the three methanotrophs were isolated following established methods[7,10,36]. 10 g of cells were resuspended in 100 mL of 25 mM PIPES, pH 7.3, 500 mM NaCl (*Mm. alcaliphilum* 20Z) or 250 mM NaCl (*Mm. buryatense* 5GB1C), supplemented with EDTA-free protease inhibitor tablets (Roche). Resuspended cells were sonicated for 1.5 min with an 1 s

on, 3 s off interval at 25% sonication amplitude. *Mc.* sp. str. Rockwell cells (16 g) were resuspended in 70 mL of 25 mM PIPES, pH 7.3, 250 mM NaCl, supplemented with 500 µM CuSO$_4$•5H$_2$O, and sonicated for 7 min with an 1 s on, 3 s off interval at 25% sonication amplitude. All lysed cells were centrifuged at 8,000 x *g* for 1 h at 4 °C. The supernatant was then centrifuged at 100,000 x *g* for 1 h at 4 °C. The resulting membrane pellet was washed twice in a Dounce homogenizer with 25 mM PIPES, pH 7.3., 250 mM NaCl. 1 mL aliquots of membranes (5-10 mg/mL) were flash frozen in liquid nitrogen and stored at -80 °C. Protein concentrations were measured using the DC Lowry Assay (Bio-Rad) with BSA as a standard.

pMMO solubilization

pMMO was solubilized from the membranes using 1.2 mg of n-Dodecyl β-D-maltoside (DDM) (Anatrace) per 1 mg of protein at 4 °C for 1 h[7,10,36]. Membranes were pelleted at 100,000 x *g* for 30 min at 4 °C, and the solubilized protein fraction was collected and buffer exchanged into 25 mM PIPES, pH 7.3, 250 mM NaCl, 0.02% DDM using a 100 kDa MWCO Amicon centrifugal concentrator (Millipore). Protein concentrations were measured using the DC Lowry Assay (Bio-Rad) with BSA as a standard.

pMMO reconstitution into nanodiscs using dialysis

20Z- and Rockwell-pMMO were reconstituted into nanodiscs via dialysis using the membrane scaffold proteins MSP1E3D1 or MSP2N2 and 1-palmitoyl-2-oleoyl-sn-glycero-3-phosphocholine (POPC) lipids. A stock of 50 mM POPC was prepared from POPC powder (Avanti) in 100 mM sodium cholate, 25 mM PIPES, pH 7.3 and 250 mM NaCl. POPC was dissolved into the buffer by cycling the glass tube through 20 s round of vortexing, a 20 s sonication

step in an ultrasonic bath, and a 20 s incubation at 50 °C in a heat bath; this cycle was repeated until the lipids dissolved. For 20Z-pMMO, a pMMO trimer:MSP2N2:POPC molar ratio of 1:13:2340 was used for 5-10 mL reconstitutions in 20 mM PIPES, pH 7.3, 250 mM NaCl, 0.02% DDM buffer. The final concentration of the components in the reconstitution mixture was 3.33 μM pMMO trimer, 43.3 μM MSP2N2, 7.8 mM POPC, and 20 mM sodium cholate. For 20Z-pMMO using MSP1E3D1, the reconstitution molar ratio of pMMO:MSP1E3D1:POPC was 1:13:390 with final concentrations of 3.33 μM pMMO trimer, 43.3 μM MSP1E3D1, 1.3 mM POPC, and 20 mM sodium cholate. For Rockwell-pMMO using MSP1E3D1, the molar ratio of pMMO:MSP1E3D1:POPC was also 1:13:390. The reconstitution mixtures were rotated on a tube revolver at 4 °C for 1 h, followed by an overnight dialysis at 4 °C using a 10 kDa MWCO Slide-A-Lyzer dialysis cassette (ThermoFisher). For 20Z-pMMO, the reconstituted mixture was buffer exchanged into 20 mM PIPES, pH 7.3, 50 mM NaCl, and loaded onto a 5 mL or 10 mL HiTrap Q FF anion exchange chromatography column (GE Healthcare). A 50-800 mM NaCl gradient was used to separate empty nanodiscs and pMMO-embedded nanodiscs. Empty nanodiscs eluted at 300 mM NaCl, and 20Z-pMMO nanodiscs eluted at 600 mM NaCl. pMMO-nanodisc fractions were collected and concentrated using a 100 kDa MWCO Amicon centrifugal concentrator (Millipore). The 20Z-pMMO (post anion exchange) samples were loaded onto a Superose 6 Increase 10/300 GL column (GE Healthcare). Fractions corresponding to the pMMO-nanodisc complex were collected and concentrated using a using a 100 kDa MWCO Amicon centrifugal concentrator (Millipore). Protein concentrations of 20Z-pMMO nanodisc samples were measured using the DC Lowry assay with BSA as a standard. Copper content of 20Z-pMMO samples was determined using inductively coupled plasma optical emission spectrometry (ICP-OES), and

copper content of Rockwell-pMMO samples was determined by ICP-MS, both at Northwestern University's Quantitative Bio-element Imaging Center (QBIC). Copper concentrations were quantified using 0-500 ppb copper standards (Inorganic Ventures).

pMMO reconstitution into nanodiscs using Bio-Beads

For copper supplementation experiments, Rockwell-pMMO was reconstituted into MSP1E3D1 nanodiscs using Bio-Beads (Bio-Rad). pMMO, MSP1E3D1, and POPC were mixed together for 2 h at 4 °C at a molar ratio of 1:4:240 pMMO:MSP1E3D1:POPC. For copper supplementation experiments, one molar equivalent of $CuSO_4 \cdot 5H_2O$ per solubilized Rockwell-pMMO protomer was added into the mixture. Self-assembly of the nanodisc was initiated by adding 0.5 g/mL wet Bio-Beads to the mixture followed by rotating on a tube rotator for 2 h at 4 °C. Wet Bio-Beads were prepared by mixing dry Bio-Beads with 25 mM PIPES, pH 7.3, 250 mM NaCl. Wet Bio-Beads were weighed by decanting onto a weigh boat followed by removal of the excess liquid with a Pasteur pipet. After reconstitution, Bio-Beads were removed from the nanodisc mixture by passing the mixture through a 0.22 μm syringe filter. The nanodiscs were then concentrated and purified by size-exclusion chromatography using a Superose 6 Increase 10/300 GL column (GE Healthcare). Fractions were collected and concentrated using a 100 kDa MWCO Amicon centrifugal concentrator (Millipore).

Empty nanodiscs could not be separated from the Rockwell-pMMO nanodisc samples, so the DC-Lowry Assay could not be used for accurate protein concentration measurements. Instead, Rockwell-pMMO nanodisc complexes were quantified using SDS-PAGE and ImageJ software[128]. Solubilized Rockwell-pMMO of known concentration (measured using the DC Lowry assay, Bio-Rad) was loaded onto a 15% SDS-PAGE gel at concentrations of 4 mg/mL, 2 mg/mL, and 1

mg/mL. ImageJ was then used to generate a standard curve, correlating the intensity of the PmoB subunit band with the known concentrations. The PmoB subunit was used for the standard curve since it was well separated from the PmoA, PmoC, and MSP bands on the gel. The concentration of the Rockwell-pMMO nanodisc sample was measured by comparing the intensity of its PmoB band against the standard curve generated above. Copper content was determined using inductively coupled plasma mass spectrometry (ICP-MS) at Northwestern University's Quantitative Bio-element Imaging Center (QBIC). Copper concentrations were quantified using 0-500 ppb copper standards (Inorganic Ventures).

Cryo-EM sample preparation and data acquisition

Freshly purified 20Z-pMMO sample in MSP2N2 nanodisc (3 μL at ~0.5 mg/mL) was deposited onto glow-discharged 400 mesh 1.2/1.3 C-Flat grids (Protochips). The Vitrobot Mark IV (FEI) sample chamber was kept at 100% relative humidity and the grid was blotted for 5-8 s before plunge freezing in a liquid ethane bath cooled by liquid nitrogen. The grids were imaged using a JEOL 3200FS microscope operating at 300 kV. Data were acquired on a K2 summit camera (Gatan) using Leginon[129] with a defocus range between 1.5-3.5 μm using counting mode with a pixel size of 1.1 Å. Movies were recorded for 6 s exposure with a dose rate of approximately 8e-/pix/s (equivalent to 6.6e-/Å^2/s on the plane of the sample).

Recorded movies were subjected to gain correction and then beam-induced motion correction with MotionCor2[130]. Following contrast transfer function (CTF) estimation with CTFFIND4[131], micrographs with the best quality were then selected for further processing. Particles were then picked, extracted, and classified for 2D classification by applying C3 symmetry

using the Scipion[132] software environment using XMIPP programs[133,134]. Three best 2D classes representing different orientations of 20Z-pMMO in nanodiscs are shown in Fig. 3.4.

[13]C methane oxidation activity assay

Methane oxidation activity levels of pMMO-nanodisc complexes were performed[7]. Rockwell-pMMO in nanodiscs (~2-4 mg/mL) was resuspended in 25 mM PIPES, pH 7.2, 250 mM NaCl in 100 μL reactions containing reductant (excess duroquinol) in 2 mL screw top vials sealed with septa (Agilent). A 1 mL volume of headspace gas was withdrawn from the reaction vial and replaced with 1.5 mL of ^{13}C methane gas (Sigma-Aldrich). All reactions were performed at 30 °C and 200 rpm for 5 min. The reactions were placed on ice for 5 min followed by quenching with 500 μL of chloroform containing 1 mM dichloromethane. The reaction was vortexed at 2,000 rpm for 10 min and centrifuged at 2,000 x *g* for 30 min. 2.5 μL of the chloroform mixture was injected into a PoraBOND Q column (25 m x 250 μm x 3 μm) on an Agilent 7890B/5977A MSD GC/MS instrument with a split ratio of 10:1. The column was under a constant flow of 1.2 mL/min of helium gas. The GC protocol was as follows: oven temperature was maintained at 80 °C for 3.5 min, ramped 50 °C/min to 150 °C and held for 1.5 min, and then ramped 15 °C/min to 300 °C and held for 1 min. The MS instrument protocol was as follows: 230 °C ion source temperature, 150 °C quad temperature, 70 eV, and a detector voltage of 2,999 V. Ion masses 31, 33, and 49 were monitored for detection of ^{12}C methanol, ^{13}C methanol, and dichloromethane with dwell times of 10 ms, 100 ms, and 10 ms, respectively. [13]C methanol concentrations were quantified using a standard calibration curve and the dichloromethane internal standard.

Native mass spectrometry analysis

pMMO-nanodiscs samples for nTDMS analysis were dialyzed overnight using 10 kDa MWCO Slide-A-Lyzer MINI dialysis devices (Thermo Scientific) into 200 mM ammonium acetate, pH 7.2 (adjusted using ammonium hydroxide), and concentrated to approximately 30 μM pMMO-nanodisc complex. For detergent-solubilized pMMO samples, pMMO solubilized in DDM detergent were buffer exchanged into 200 mM ammonium acetate, pH 7.2, 0.155% (w/v) Triton X-100. Samples were analyzed using a Q Exactive HF mass spectrometer with Extended Mass Range and data were collected using XCalibur QualBrowser 4.0.27.10 (Thermo Fisher Scientific, Waltham, MA). The nTDMS platform employs direct infusion of sample into a native electrospray ionization (nESI) source held at +2 kV, C-trap entrance lens voltage setting between 1.8 - 4 V, HCD gas pressure setting between 2-4 V, and collision-induced dissociation (CID) voltage set at 50-100 V for desalting and 150-195 V for protein ejection from detergent micelles or nanodisc complexes. The nTDMS platform is coupled to a three-tiered tandem MS process. The first step in the process[19] is the analysis of the intact protein complex (MS[1]), which provides the total mass (reported as a deconvoluted neutral average mass value). In stage two, the complex is collisionally activated with nitrogen gas to eject monomers (MS[2]), thereby liberating the subunits that comprise each intact complex. In stage three, further vibrational activation of the ejected subunits via collisions with nitrogen gas yields backbone fragmentation products from each monomer (MS[3]) that are recorded at isotopic resolution (120,000 resolving power at *m/z* 400). These fragments are used to characterize the primary sequence of the monomers and localize posttranslational modifications. Intact mass values for pMMO complexes and ejected subunits were determined by deconvolution to convert data from the *m/z* to the mass domain using MagTran 1.03[135]. Intact mass measurements are reported as neutral average masses; errors represent 1σ

deviation from the mean of the masses calculated for of all sampled charge states. Fragmentation data were processed using mMass 5.5.0 (www.mmass.org), ProSight Lite 1.4[118], and TDValidator 1.0[136] to assign recorded fragment ions to the primary sequence of the subunits. The PmoA, PmoB, and PmoC subunits of 20Z-pMMO were identified by mapping backbone fragment ions to the amino acid sequence of pMMO subunits using ProSight Lite, with the p-scores[38] of 3.2×10^{-39} (PmoA), 6×10^{-15} (PmoB), and 3.7×10^{-14} (PmoC). The PmoB and PmoC subunits of Rockwell-pMMO were identified using ProSight Lite with p-scores of 3.5×10^{-8} and 1.6×10^{-34}, respectively[137]. Unexplained mass shifts (Δm) observed at the MS^1, MS^2, and MS^3 levels for the intact complex and subunits, respectively, were manually interrogated using the UNIMOD database as a reference for candidate modifications.

Bottom-up proteomics methods

pMMO subunits from solubilized 20Z- and 5G-pMMO samples were separated using a reverse-phase HPLC 214TP54 analytical C4 column (Grace Vydac) on an Agilent 1100 HPLC[38]. Briefly, 100 μL of 30 μM pMMO trimer was injected onto the column and eluted using a gradient from 100% solvent A (63.75% formic acid, 10% acetonitrile, 5% *i*-PrOH) to 100% solvent B (70% formic acid, 30% *i*-PrOH). Eluted fractions were diluted 1:8 with water and digested with 2 μg pepsin (Promega) overnight at 37 °C. Pepsin was inactivated by heating samples at 95 °C for 10 min. The peptides were desalted on a C18 spin column (Pierce), and eluted with 80% acetonitrile in 0.1% formic acid. Samples were then lyophilized, resuspended with 5% acetonitrile in 0.1% formic acid, and injected onto a trap column (150 μm i.d. × 3 cm) coupled with a nanobore analytical column (75 μm i.d. × 15 cm, both ReproSil C18aq, 3 μm). Samples were separated using a linear gradient of solvent A (95% water, 5% acetonitrile, 0.1% formic acid) and solvent B (5%

water, 95% acetonitrile, 0.1% formic acid). MS data were collected using a Velos Orbitrap Elite (Thermo) mass spectrometer operating in data-dependent top 10 mode. MS^1 data were collected at a resolution of 60,000 at *m/z* 400 and an AGC target of 1,000,000. MS^2 data were collected from the top 10 peaks in each precursor scan isolated with a 1.5 *m/z* isolation width fragmenting with collision-induced dissociation (CID) with a normalized collision energy of 35 at an activation q of 0.25 and a duration of 10 ms at an AGC target of 10,000. The collected data were searched using Mascot 2.5 (Matrix Science) against custom proteomic databases for *Mm. buryatense* 5G and *Mm. alcaliphilum* 20Z constructed from their published genomes. Peptide MS^1 tolerance was 15 ppm, while MS^2 tolerance was 0.6 Da, no cleavage enzyme was selected, so all subsequences for each protein in the database were queried. Variable modifications of deamidation of asparagine/glutamine and oxidation of methionine were allowed. Peptide fragmentation data were reported at 1% false discovery rate in Scaffold 4.5 (Proteome Software). Peptides containing post-translational modifications were validated by manual inspection of the tandem MS data.

CHAPTER 4: STRUCTURE AND FUNCTION OF THE LANTHANIDE-DEPENDENT METHANOL DEHYDROGENASE XOXF FROM THE METHANOTROPH *METHYLOMICROBIUM BURYATENSE* 5GB1C

ABSTRACT

In methylotrophic bacteria, which use one-carbon (C1) compounds as a carbon source, methanol is oxidized by pyrroloquinoline quinone (PQQ)-dependent methanol dehydrogenase (MDH) enzymes. Methylotrophic genomes generally encode two distinct MDHs, MxaF and XoxF. MxaF is a well-studied, calcium-dependent heterotetrameric enzyme whereas XoxF is a lanthanide-dependent homodimer. Recent studies suggest that XoxFs are likely the functional MDHs in many environments. In methanotrophs, methylotrophs that utilize methane, interactions between particulate methane monooxygenase (pMMO) and MxaF have been detected. To investigate the possibility of interactions between pMMO and XoxF, XoxF was isolated from the methanotroph *Methylomicrobium buryatense* 5GB1C (5G-XoxF). Purified 5G-XoxF exhibits a specific activity of 0.16 µmol DCPIP reduced min^{-1} mg^{-1}. The 1.85 Å resolution crystal structure reveals a La(III) ion in the active site, in contrast to the calcium ion in MxaF. The overall fold is similar to other MDH structures, but 5G-XoxF is a monomer in solution. An interaction between 5G-XoxF and its cognate pMMO was detected by biolayer interferometry, with a K_D value of 50 ± 17 µM. These results suggest an alternative model of MDH-pMMO association, in which a XoxF monomer may bind to pMMO, and underscore the potential importance of lanthanide-dependent MDHs in biological methane oxidation.

INTRODUCTION

Methylotrophs, bacteria that utilize one carbon (C1) compounds (devoid of carbon–carbon bonds) such as methane, methanol, and methylated amines as a carbon source, play a key role in the carbon cycle[114,138]. Besides serving as the primary biological sink for methane and other methylated greenhouse gases, methylotrophs have been targeted as vehicles for bioremediation and production of fuels and chemicals[139,140]. In these organisms, methanol is oxidized by methanol dehydrogenase (MDH) enzymes that use pyrroloquinoline quinone (PQQ) as a cofactor. The canonical MxaF-type MDHs have been studied extensively. MxaF-type MDHs comprise a large MxaF subunit (64 kDa) and a small MxaI subunit (8.5 kDa)[141]. The catalytic center, housed in MxaF, contains the PQQ cofactor and a calcium ion[142]. In the past two decades, a homolog of MxaF, XoxF, has also been implicated in methanol oxidation. MxaF and XoxF exhibit less than 50% amino acid sequence identity[141,143], and *xoxF* genes are actually much more abundant than mxaF genes in methylotrophs, with some methylotroph genomes encoding only XoxF[143,144].

Of particular relevance to bioinorganic chemistry is the recent discovery that XoxFs are dependent on the presence of lanthanide rather than calcium ions[145-148]. Lanthanides are a group of metals with atomic numbers 57–71 that are collectively referred to as rare earth elements (REEs) despite the fact that they are actually relatively abundant in the earth's crust[143]. In initial studies, addition of La(III) and Ce(III) to methylotroph growth media was demonstrated to induce XoxF expression and promote growth on methanol[145-147]. In the case of methanotrophs, difficulties in culturing the Verrucomicrobial microbes isolated from Italian mudpots were solved by the addition of various REEs including La(III), Ce(III), Pr(III), and Nd(III)[148]. These lanthanides transcriptionally regulate the expression of MxaF and XoxF in a number of methylotrophs and methanotrophs[42,149-151]. For *Methylomicrobium (Mm.) buryatense* 5GB1C grown with 95 μM

calcium in the medium, 1 μM of supplemental lanthanum was sufficient to abolish mxa transcription[42]. Since environmental lanthanum concentrations have been reported to be significantly higher than the amount shown to inhibit mxa transcription[152], XoxF is likely to be the functional MDH in many environments[143]. Consistent with the dependence on lanthanides, the only available XoxF structures, those of the *Methylacidiphilum (Ma.) fumariolicum* SolV enzyme (SolV-XoxF), reveal Ce(III), La(III), or Eu(III) ions in the active site[148,153].

In methanotrophs, methylotrophs that utilize methane gas as their sole carbon source[1], the methanol substrate for MxaF and XoxF is produced by methane monooxygenase (MMO) enzymes. Both soluble and membrane-bound forms of MMO exist; the membrane-bound form, particulate MMO (pMMO), is predominant in nature[61]. Given the sequential action of pMMO and MDH in methanotroph metabolism, direct interactions between the two enzymes have been suggested and are supported by intracellular localization of MDH[154-156]. In addition, a putative pMMO-MDH supercomplex has been reported. Although purified samples of such a complex have not been obtained[34,35,45,157], specific protein–protein interactions between *Methylococcus* (*Mcc.*) *capsulatus* (Bath) MxaF and pMMO have been detected[35]. Beyond providing a direct route for methanol from pMMO to MDH, a pMMO-MDH complex could also facilitate transfer of electrons from methanol oxidation back to pMMO via the electron acceptor of MDH, cytochrome c_L[35]. The physiological reductant for pMMO remains unknown, but recent metabolic modeling for *Mm. buryatense* 5GB1C predicts that MDH may indeed mediate electron transfer to pMMO for methane oxidation[33], rather than the more widely accepted model involving NADH and a type 2 NADH:quinone oxidoreductase[31]. To gain further insight into potential pMMO-MDH interactions, particularly as pertains to the apparent prevalence of XoxF-type MDHs in the environment, we have isolated the lanthanum-containing XoxF from *Mm. buryatense* 5GB1C (5G-XoxF),

determined its crystal structure, and investigated its interaction with *Mm. buryatense* 5GB1C pMMO (5G-pMMO).

RESULTS AND DISCUSSION

Isolation and purification of XoxF from *Mm. buryatense* 5GB1C

In *Mm. buryatense* 5G, only one *xoxF* (METBUDRAFT_3845) is encoded in the *xox* operon, which also contains *xoxF* and *xoxJ*. Purification of 5G-XoxF has not been reported previously. In this study, 5G-XoxF was isolated from the soluble fraction, and supplementing the growth media with 0.5% methanol increased the growth rate by 40% and the yield of purified protein by tenfold. Similar effects of methanol supplementation were observed in previous XoxF studies[145,147]. During purification, 5G-XoxF can be monitored by the absorbance at 345 nm that corresponds to its PQQ cofactor (Fig. S4.1). After two column chromatography steps (anion exchange and size exclusion), the yield of purified 5G-XoxF is typically ~ 50 mg/L of cell culture. The protein identity was confirmed by in-gel protein sequencing, and ICP-OES measurements indicated the presence of 0.7 ± 0.1 La(III) ions per monomer (n = 3). Purified 5G-XoxF exhibits methanol oxidation activity of 0.16 ± 0.05 µmol DCPIP reduced min^{-1} mg^{-1} (n = 3). This value is comparable to activity of MxaF-type MDH from *Mcc. capsulatus* (Bath), but one order of magnitude less than values found for other characterized XoxFs (Table 4.1).

Solution oligomerization state of 5G-XoxF

The oligomeric state of purified 5G-XoxF was investigated via SEC-MALS at concentrations of 1, 5, and 10 mg/mL. The molecular weight of 5G-XoxF is 67.2 kDa, and for all samples, 5G-XoxF eluted as a single peak corresponding to 66 kDa (Fig. 4.1). Therefore, unlike

other MDHs, 5G-XoxF exists predominantly a monomer. All other MDHs are homodimers and that from Mc. capsulatus (Bath) forms higher order oligomers[35,145,147,148,158]. One exception is XoxF from *Candidatus Methylomirabilis oxyfera*, which was purified as a XoxF/MxaI heterotetramer[158]. In addition, the XoxF from *Methylobacterium extorquens* AM1 was initially reported to be a monomer based on size exclusion chromatography[159], but was later purified from the same organism and reported to be a homodimer[147].

It is possible that the oligomerization state of XoxF is not as strictly conserved as that of MxaF, which is an important consideration for studying the structural aspects of its interaction with pMMO. In particular, a 16 Å resolution cryoelectron microscopy structure of a complex containing *Mcc. capsulatus* (Bath) pMMO and MxaFI was interpreted to comprise an α3β3γ3 pMMO trimer interacting with an α3β3 trimer of MxaFI[34]. However, our later crystal structure of *Mcc. capsulatus* (Bath) MxaFI revealed a dimer, and a stable complex between purified pMMO and MxaFI could not be isolated[35]. Instead, we hypothesized that multiple MDH dimers might transiently assemble into a "bilayer" with the small positively charged MxaI subunit facilitating interaction with the stacked intracytoplasmic membrane structures that house pMMO. However, this model is not applicable to XoxF since it lacks the second subunit, and the observed monomeric state of 5G-XoxF may suggest that in the cell, the monomeric form interacts with pMMO as originally suggested for the *Mcc. capsulatus* (Bath) proteins[34].

Table 4.1. Enzyme activity of MDH from various methylotrophs.

Organism	Specific Activity*	V_{max}*	Reference
MxaF-type MDH			
Methylophilus methylotrophus	0.07[†]	1.15	[160]
Methylobacterium extorquens AM1	0.8	0.98	[161]
Methylococcus capsulatus (Bath)	0.18 ± 0.03	–	[35]
XoxF-type MDH			
Bradyrhizobium sp. MAFF211645	15.5	–	[146]
Methylobacterium extorquens AM1	10	–	[147]
Methylacidiphilum fumariolicum SolV	4	8	[148]
Candidatus Methylomirabilis oxyfera	9.66 ± 1.52[‡]	10	[159]
Methylomicrobium buryatense 5G	0.16 ± 0.05	0.18 ± 0.08	This study

*μmol DCPIP reduced min^{-1} mg^{-1} MDH

[†]μmol O_2 consumed min^{-1} mg^{-1} MDH

[‡]XoxF/MxaI heterotetramer
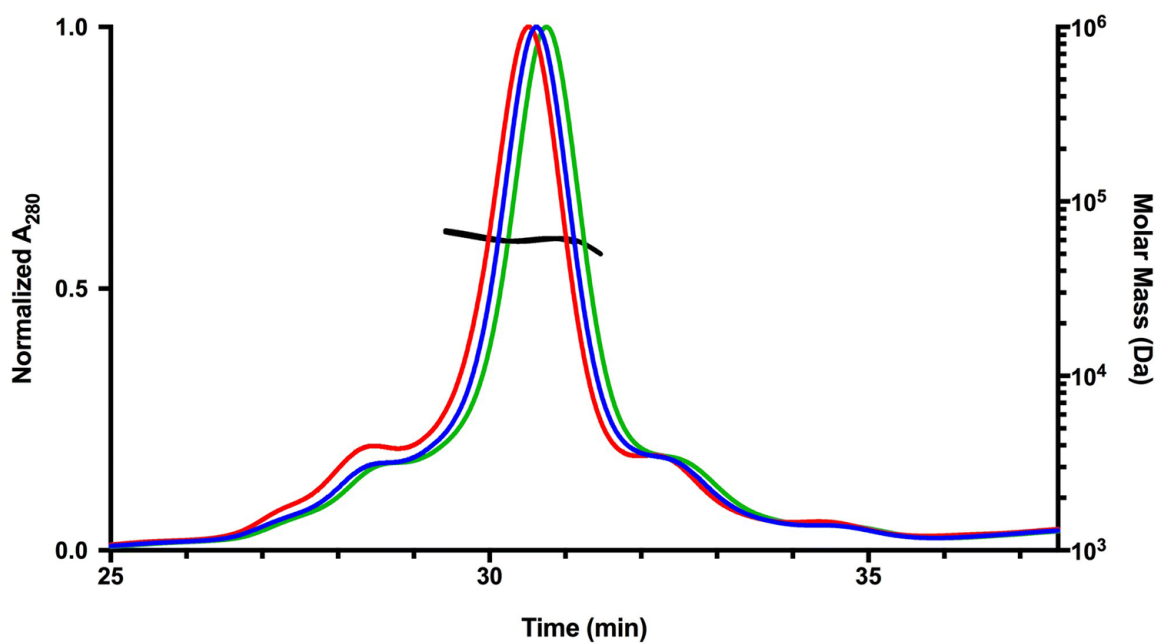
Figure 4.1. Solution oligomerization state of 5G-XoxF.
Signals from the MALS refractive index detector are shown as a function of elution time (*green* for 1 mg/mL, *blue* for 5 mg/mL, and *red* for 10 mg/mL). The *black* horizontal lines indicate the calculated molecular masses of the eluting peaks.

Interaction between XoxF and pMMO from *Mm. buryatense* 5GB1C

The possibility of protein–protein interactions between the 5G-XoxF monomer and purified 5G-pMMO was investigated using biolayer interferometry. A concentration-dependent interaction was observed between the two proteins (Fig. 4.2), yielding a KD value of 50 ± 17 μM. By contrast, a KD value of 9.0 ± 7.7 μM was measured for the interaction between pMMO and MxaF from *Mcc. capsulatus* (Bath)[35]. Not surprisingly, we were not able to detect a stable complex between the *Mm. buryatense* 5GB1C proteins by size exclusion chromatography, similar to the *Mcc. capsulatus* (Bath) proteins[35,157,162], and consistent with the inability to enhance pMMO propylene epoxidation activity by combining purified proteins[157,162]. As suggested previously, the association may be transient and/or facilitated by other components[35]. In addition, the weaker interaction could be characteristic of XoxF compared to MxaF or may be specific to the *Mm. buryatense* 5GB1C proteins. Analyses of multiple pMMO-MDH pairs is needed to further investigate the interaction between XoxF and pMMO. Regardless, these results indicate that the interaction with pMMO is not confined to MxaF-type MDHs, and does not require the presence of the small MxaI subunit.
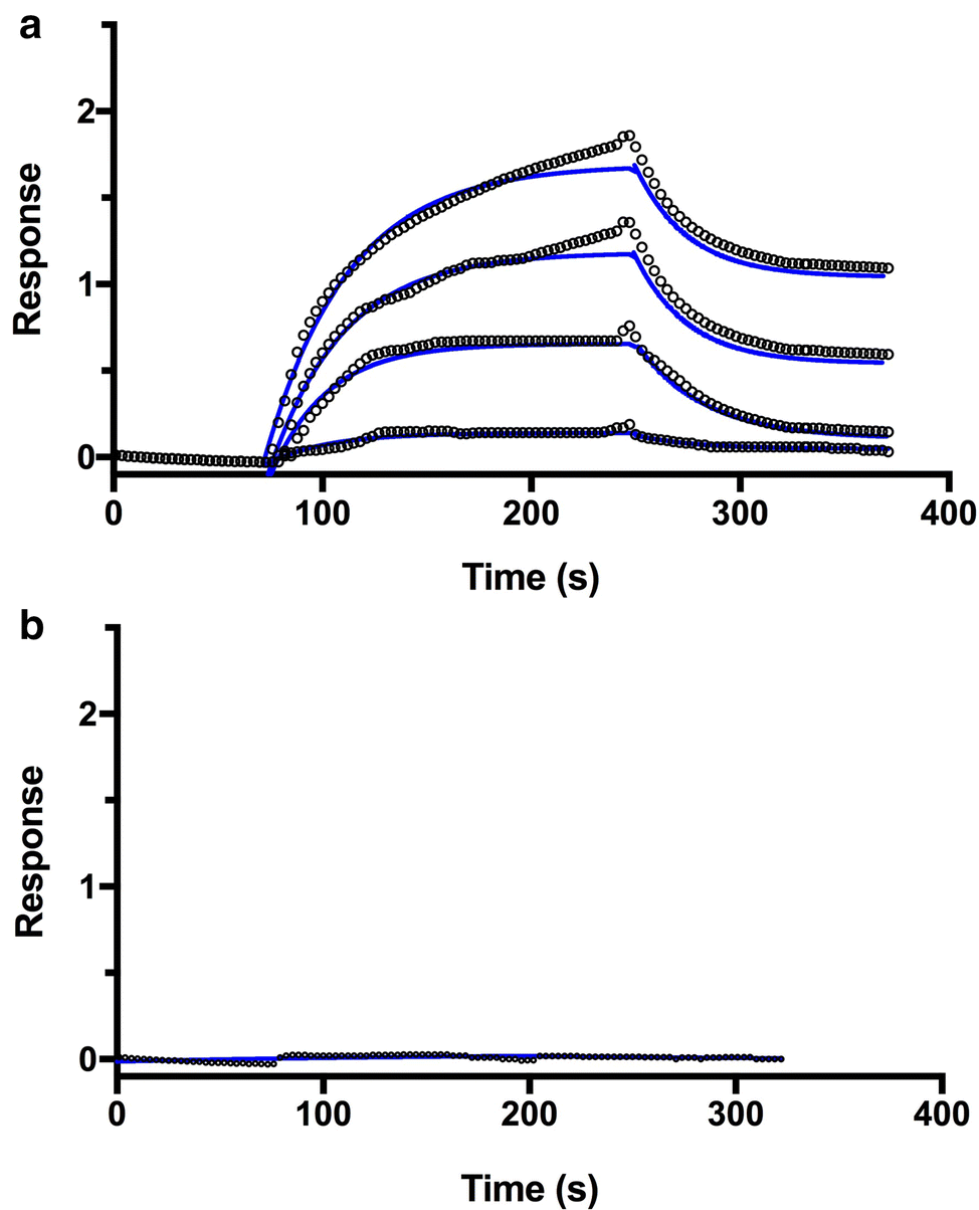
Figure 4.2. Biolayer interferometry sensorgrams of the interaction between immobilized 5G-XoxF and 5G-pMMO.
a, Purified 5G-pMMO samples at concentrations of 5, 10, 15, and 25 µM were tested for binding to immobilized 5G-XoxF. The fitting curves are displayed in *blue*. **b**, A control experiment testing the interaction between immobilized BSA and 25 µM 5G-pMMO was performed. No binding was observed. Each experimental run was repeated a total of three times with new sensors and protein samples.

Structure of XoxF from *Mm. buryatense* 5GB1C

The structure of 5G-XoxF was determined to 1.85 Å resolution (Table 4.2). The asymmetric unit contains one molecule (Fig. 4.3a). The first residue in the structure is Asn 27, due to cleavage of the periplasmic targeting sequence, and the C-terminal residue is Asn 617, with no visible electron density for the residues between Ala 571 and Arg 598 (Fig. 4.3b). Like other MDHs, the monomer consists of eight sets of four-stranded antiparallel beta sheets, forming a beta propeller (Fig. 4.3a), which is surrounded by several short alpha helices. The N- and C-termini are found on the side of the protein opposite to the active site. 5G-XoxF exhibits 51% sequence identity to SolV-XoxF and 52% sequence identity to *Mcc. capsulatus* (Bath) MxaF. Superimposing the main chain of 5G-XoxF with *Mcc. capsulatus* (Bath) MxaF reveals minor differences in secondary structure with an rmsd of 0.69 Å for 574 Cα atoms. Substitutions mainly occur in loop regions on the protein surface, including a prominent loop in 5G-XoxF spanning residues Lys 469 to Gly 478. In addition, residues Lys 238 to Pro 244 form a beta sheet compared to a loop-helix structure in MxaF. Interestingly, these deviations seem to be specific to 5G-XoxF since they are also observed upon comparison to SolV-XoxF, which can be superposed on 5G-XoxF with a rmsd of 0.73 Å for 578 Cα atoms (Fig. 4.4).

Strong electron density observed adjacent to the PQQ cofactor, which is well defined, corresponds to a 35σ peak in the anomalous difference Fourier map generated with data collected at the La(III) absorption edge (6.3 keV). The density was well modeled with a La(III) ion at an occupancy of 0.8 (Fig. 4.3c), consistent with the metal analysis. The PQQ is sandwiched between Trp 267 and a disulfide bond formed between Cys 129 and Cys 130, residues that are conserved in other MDH structures (Fig. 4.3c)[35,79,142]. Hydrogen

Table 4.2. *Mm. buryatense* **5GB1C XoxF data collection and refinement statistics.**
Values in parentheses refer to the highest resolution shell.

	5G-XoxF	5G-XoxF (La anomalous)
Data collection		
Space group	$C\,2\,2\,2_1$	$C\,2\,2\,2_1$
Cell dimensions		
a, b, c	55.31, 92.29,191.71	55.23, 92.20, 191.28
Resolution	30-1.85	30.0-2.9
Wavelength	0.9790	1.968
R_{pim}	0.043 (0.267)	0.076 (0.167)
R_{meas}	0.140 (0.865)	0.150 (0.314)
$CC_{1/2}$	0.99 (0.854)	0.998 (0.941)
$I/\sigma I$	51.0 (9.2)	28.9 (9.9)
Completeness	93.6 (82.0)	99.7 (97.9)
Redundancy	9.7 (8.6)	3.5 (3.0)
Refinement		
No. of reflections	39621 (2620)	
R_{work}/R_{free}	0.15 / 0.18	
Average B-factor (Å^2)	22.15	
Root mean square deviations		
Bond lengths (Å)	0.007	
Bond angles (°)	0.89	
Ramachandran favored	95.17	
Ramachandran allowed	4.29	
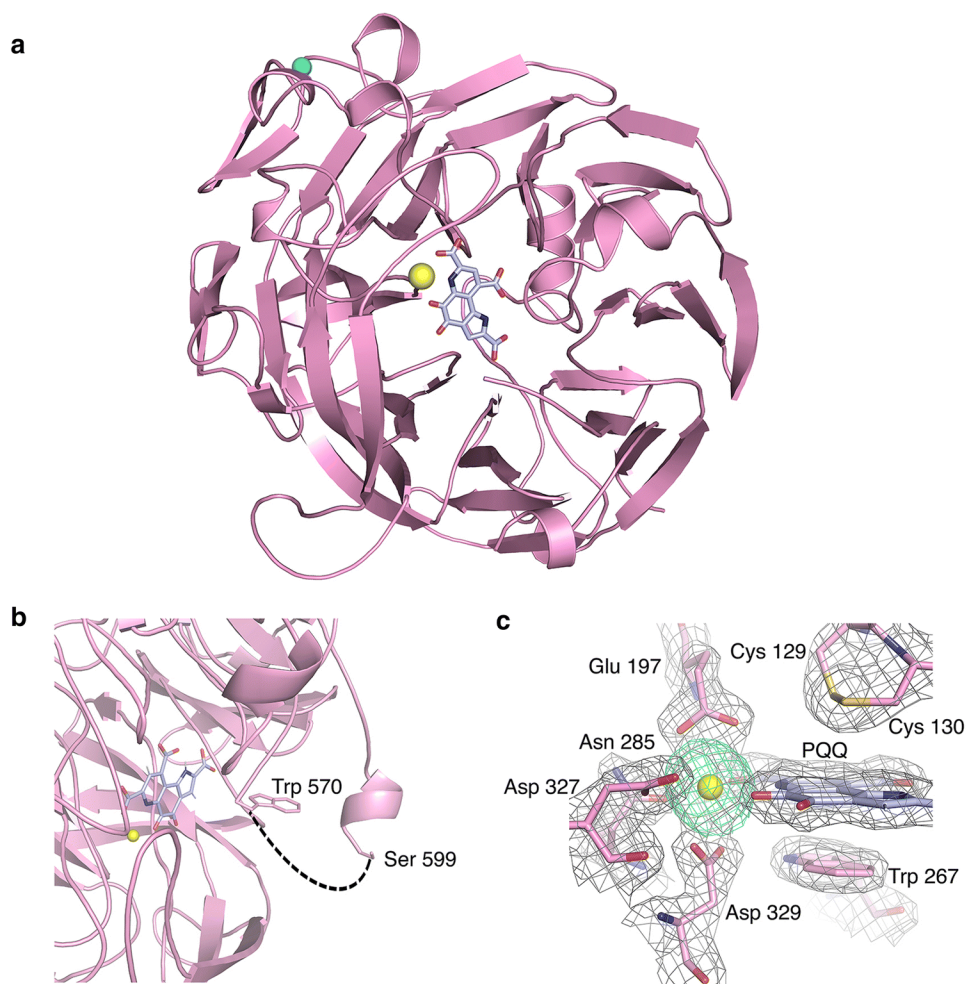
Figure 4.3. Crystal structure of *Mm. buryatense* 5GB1C XoxF.
a, 5G-XoxF monomer. The eight-bladed β-sheet propeller forms a central cavity containing a PQQ ligand (blue) and a La(III) ion (*yellow*). A sodium ion from the solvent is modeled as a cyan sphere. **b**, Disordered C-terminus of 5G-XoxF. Disordered residues 571-598 are represented with a dashed line (*black*). **c,** 5G-XoxF active site. The 2Fo–Fc electron density map contoured at 1σ (*gray*) is shown for the La(III) ion, PQQ cofactor, and coordinating residues (*pink*). The anomalous difference Fourier map calculated using data collected at the La absorption edge (6.3 keV) is shown contoured at 10σ (*green*).
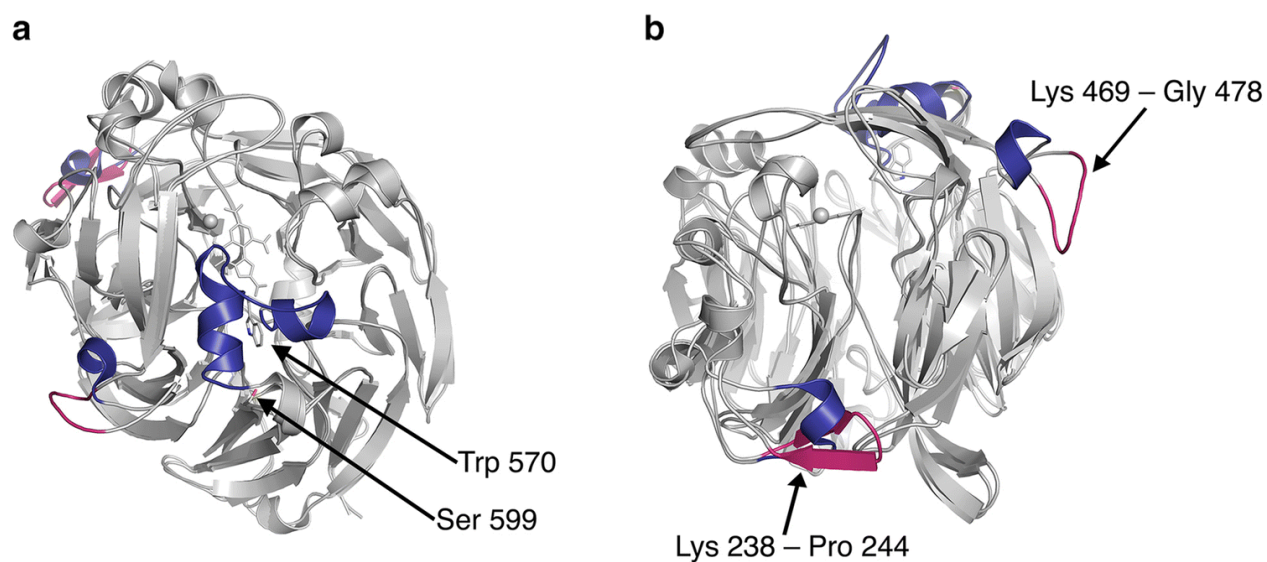
Figure 4.4. XoxF structure comparison.
5G-XoxF with SolV-XoxF (4MAE) (both *gray*), with differing secondary structure elements shown in *magenta* for 5G-XoxF and dark blue for SolV-XoxF. **a**, The disordered residues 571–598 of 5G-XoxF are modeled with α-helices in SolV-XoxF. **b**, Residues Lys 469-Gly 478 form a prominent loop in 5G-XoxF, and residues Lys 238-Pro 244 in 5G-XoxF form a beta hairpin compared to a loop-helix structure in SolV-XoxF.

bonds in the active site stabilize the PQQ cofactor, similar to those in other MDH structures. Residue Asn 420 that interacts with the PQQ in 5G-XoxF is replaced by an aspartic acid in SolV-XoxF, but all other residues interacting with the metal and PQQ in the active site are conserved between the two XoxF structures. Similar to the Ce(III) ion in SolV-XoxF[148], the La(III) ion is 9-coordinate, ligated by the C-7 carboxylate, C-5 carbonyl, and N-6 quinoline nitrogen of the PQQ, as well as residues Glu 197 (bidentate), Asn 285, Asp 327 (monodentate), and Asp 329 (bidentate) (Table 4.3). In MxaF-type MDHs, the residue equivalent to Asp 329 is an alanine, and the Ca(II) ion is 6-coordinate[35]. As in SolV-XoxF, additional residue substitutions help accommodate the La(III) ion. Coordinating residue Asn 285 is positioned further away from the metal center due to the position of Thr 288, which replaces a proline found in MxaF. Similar alterations are observed near Glu 197 with Gly 196 replacing an alanine and Phe 198 replacing a leucine.

The active site appears more exposed than in other MDH structures due to the disordered residues near the C-terminus (Fig. 3b), which are stabilized by crystal contacts in the SolV-XoxF structure[148]. 5G-XoxF residues 575-589 are not conserved in SolV-XoxF and *Mcc. capsulatus* (Bath) MxaF; there is a three amino acid (Asn 597, Ser 598, and Glu 599) insertion, which may contribute to the observed disorder. In addition, there is a negatively charged surface patch encapsulating the active site and neighboring the disordered region (Fig. 5a). These regions may interact with the positively charged surface of cytochrome c_L for electron transfer[163], although cross-linking studies suggest interactions between lysine residues on MDH and carboxylate groups on cytochrome c_L[164,165]. Alternatively, these disordered residues could require other binding partners for stabilization. MxaJ is a periplasmic protein that is believed to serve a chaperone-like

Table 4.3. Distances to metal ion in MDH (Å).

Atom	Distance to La	Distance to Ce in *Ma. fumariolicum* SolV [148]	Distance to Ca in *Mc. capsulatus* (Bath) [35]
Glu 197 OE1	2.6	2.7	2.7
Glu 197 OE2	2.7	2.9	2.8
Asn 285 OD1	2.6	2.7	2.8
Asp 327 OD1	2.8	2.9	2.8
Asp 329 OD1	2.6	2.5	–
Asp 329 OD2	2.7	2.8	–
PQQ O5	2.6	2.6	2.5
PQQ O7	2.5	2.7	2.9
PQQ N6	2.8	2.8	2.8

function in MDH assembly[166]. However, MxaJ has also been proposed to mediate interactions between MDH and its cytochrome c_L electron acceptor[163,167] or even between pMMO and MDH[168]. In the XoxF system, this role could be filled by the MxaJ homolog XoxJ, a protein of unknown function encoded in the *xoxF* operon.

Although 5G-XoxF is a monomer in solution (Fig. 4.1), the dimer observed in other MDH structures is present in the crystal, mediated by crystal lattice contacts with a symmetry-related molecule (Fig. S4.2). This observation suggests that 5G-XoxF may be able to dimerize in solution, but perhaps at much higher concentrations than reported for other MxaFs and XoxFs (2.5–20 mg/mL)[35,148]. Due to difficulty in obtaining high concentrations of purified protein from the native organism, samples at > 10 mg/mL were not analyzed by SEC-MALS. Similar to other MDH dimeric structures, the crystallographic dimer interface of 5G-XoxF forms a saddle shaped structure via β strands from residues 67–73 and 109–115 (Fig. S4.2). There are 14 hydrogen bonds at the interface, in comparison to 18 intermonomer hydrogen bonds in SolV-XoxF, and 30 intermonomer hydrogen bonds in MxaF from *Mcc. capsulatus* (Bath)[35]. Notably, 5G-XoxF lacks two key hydrogen bonding pairs found in SolV-XoxF, Tyr 572 OH-Glu 570 OE2 and Tyr 572 OH-Ser 45 OG, which link β strands comprising residues 4–47 and 570–575 from each monomer. In 5G-XoxF, these three residues are substituted with threonine and positioned too far apart for polar contacts (6–9 Å). Furthermore, SolV-XoxF contains an additional C-terminal glutamic acid residue, Glu 577, which interacts with Arg 41. The lack of these contacts may account for the monomeric behavior of 5G-XoxF in solution. Another difference between 5G-XoxF and SolV-XoxF is the presence of a salt bridge between Glu 114 and Lys 605 in the 5G-XoxF structure; these residues are not conserved in SolV-XoxF.

Surface analysis of 5G-XoxF provides some insight into its interaction with pMMO. The PmoB subunit of *Mm. alcaliphilum* 20Z pMMO (20Z-PmoB) is 95% identical to 5G-pMMO PmoB[7]. MDHs are periplasmic[154-156] and in the case of the *Mcc. capsulatus* (Bath) pMMO, PmoB interacts with pMMO[35]. The surface of 20Z-PmoB exhibits a prominent patch of negatively charged residues conserved in 5G-pMMO (Fig. 4.5b), which are complementary to and could potentially interact with the positively charged residues at the 5G-XoxF dimer interface (Fig. 4.5a). It is possible that these surfaces are involved in the protein–protein interactions observed by biolayer interferometry (Fig. 4.2).

Existence of multiple MDHs in *Mm. buryatense* 5GB1C

The *Mm. buryatense* 5G genome encodes both MxaF- and XoxF-type MDHs, a trend observed in many methylotrophs[144]. XoxF is found in a wider range of bacterial phyla compared to MxaF, and this phylogenetic diversity suggests more environmental importance for REEs than assumed previously[114]. While it has been shown that lanthanides downregulate MxaF expression in *Mm. extorquens* AM1, *Methylosinus trichosporium* OB3b, and *Mm. buryatense* 5G[42,150,169], the significance of having two MDH systems requiring different metals is unknown. The two MDH types may contribute to the modularity of C1 metabolism, which helps the organisms to withstand environmental fluctuations[144]. In addition, an active heterotetrameric complex consisting of XoxF with calcium and MxaI has been described, suggesting a functional relationship between the two systems[158]. The separation of XoxF into several phylogenetic groups (XoxF1–XoxF5) in NC10, *Proteobacteria*, *Verrucomicrobia*, and *Methylophilaceae* suggests that the role of lanthanides in regulation is complex[114,141]. These considerations will be important for future work in studying
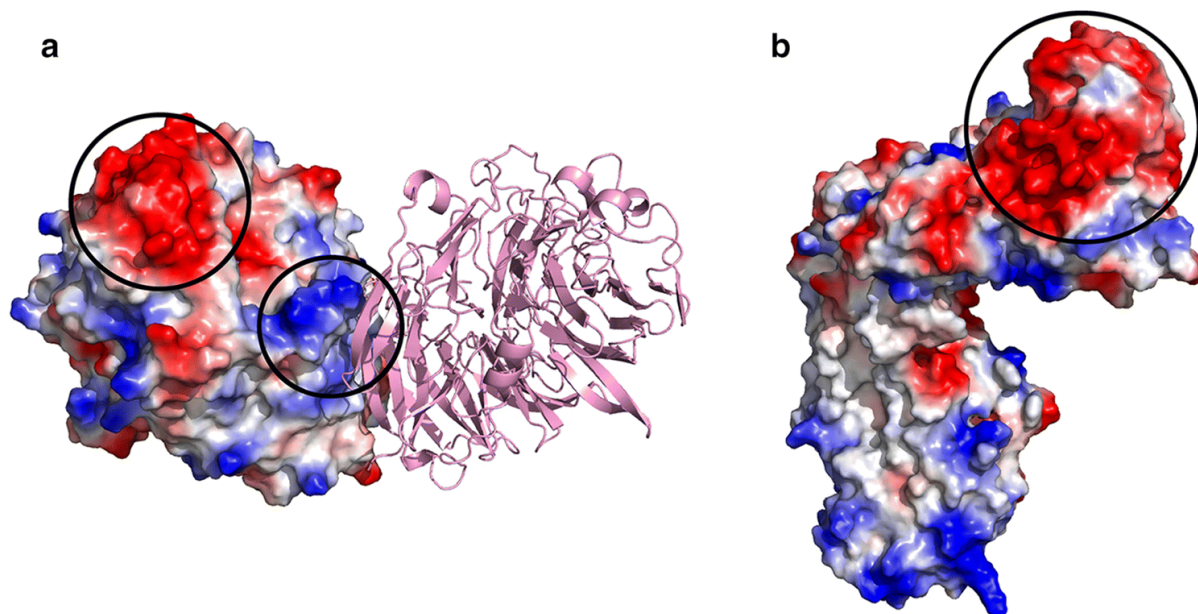
Figure 4.5. Surface electrostatic potentials of 5G-XoxF and pMMO from *Mm. alcaliphilum* 20Z.
Negatively charged surfaces are represented in red and positively charged surfaces in *blue*. **a**, A 5G-XoxF crystallographic dimer, with one monomer represented as a surface. *Black* circles highlight the negative patch surrounding active site and disordered residues 571–598, and the positive patch at the XoxF dimer interface. **b**, The negatively charged surface of the soluble domain of PmoB subunit from *Mm. alcaliphilum* 20Z pMMO (6CXH) is circled in *black*.

lanthanide-dependent MDHs in C1 metabolism and as models for other yet-to-be discovered REE-dependent metalloenzymes.

MATERIALS AND METHODS

Growth of *Mm. buryatense* 5GB1C

Mm. buryatense 5GB1C cells were cultured as described previously[45]. Briefly, *Mm. buryatense* 5GB1C cells were grown in 12-L fermenter growths in 1× modified nitrate mineral salts (NMS2) medium (which contains 95 μM $CaCl_2·2H_2O$), 130 mM NaCl, 2.3 mM phosphate buffer, and 50 mM carbonate buffer, pH 9.5, supplemented with 30 μM $LaCl_3$, 40 μM $CuSO_4$ and 1× trace elements solution (500× is 1.0 g/L $Na_2·EDTA$, 2.0 g/L $FeSO_4·7H_2O$, 0.8 g/L $ZnSO_4·7H_2O$, 0.03 g/L $MnCl_2·4H_2O$, 0.03 g/L H_3BO_3, 0.2 g/L $CoCl_2·6H_2O$, 0.02 g/L $NiCl_2·6H_2O$, 0.05 g/L $Na_2MoO_4·2H_2O$). Cells cultivated for XoxF isolation were supplemented with 0.5% methanol. Approximately 10 g of frozen cell pellet were added to the fermenter to initiate growth at an optical density at 600 nm (OD600) of 0.1–0.2. All cells were cultured under an air-to-methane gas ratio of 3:1 at 30 °C and 300 rpm. Cells were harvested when the OD600 reached 10–11 and centrifuged for 30 min at 8000×g at 4 °C. Pelleted cells were flash frozen in liquid nitrogen and stored at − 80 °C.

Purification of XoxF from *Mm. buryatense* 5GB1C

Mm. buryatense 5GB1C cell pellets (approximately 20 g) were resuspended in 200 mL of lysis buffer (25 mM PIPES, pH 7.3, 250 mM NaCl) and sonicated for 5 min (1 s on–off cycles at 40% amplitude) on ice. The lysed cells were centrifuged at 8000×g, followed by ultracentrifugation of the supernatant at 100,000×g to separate membranes from the soluble

proteins. The supernatant was dialyzed overnight in 20 mM Tris, pH 8.0, 50 mM NaCl using a 10 kDa molecular weight cut off (MWCO) SnakeSkin dialysis tubing (ThermoFisher Scientific), and then loaded onto a Source 15Q anion exchange column (GE Healthcare). 5G-XoxF eluted at approximately 250 mM NaCl using a gradient of 50–400 mM NaCl in 20 mM Tris, pH 8.0. The fractions containing 5G-XoxF were collected and concentrated using an Amicon 30 kDa MWCO device (Millipore). After buffer exchanging into 20 mM Tris, pH 8.0, 250 mM NaCl, 5G-XoxF was loaded onto a Superdex 200 Increase 10/300 size exclusion analytical grade column (GE Healthcare) (Fig. S4.3). Fractions containing 5G-XoxF were concentrated to approximately 20 mg/mL, flash-frozen, and stored at -80 °C. Sample purity was assessed by sodium dodecyl sulfate–polyacrylamide gel electrophoresis (SDS-PAGE) (Fig. S4.4), and protein concentration was measured with the Detergent-Compatible Lowry Assay (Bio-Rad) using bovine serum albumin (BSA) as a standard. The absorption spectrum of the purified enzyme at 40 μM was recorded in a UV-micro cuvette with a 1-cm path length (Chemglass) at room temperature on an Agilent 8453 UV–visible Spectroscopy instrument (Agilent Technologies) (Fig. S4.1). Inductively coupled plasma optical emission spectrometry (ICP-OES) and inductively coupled plasma mass spectrometry (ICP-MS) were performed at Northwestern University's Quantitative Bio-element Imaging Center (QBIC), and lanthanum concentrations were quantified using 0–500 ppb lanthanum standards (Inorganic Ventures).

In-gel protein sequencing of 5G-XoxF

Protein identity was confirmed by in-gel protein sequencing mass spectrometry at Northwestern University's Proteomics Core. Excised gel bands were washed in 100 mM ammonium bicarbonate (AmBic)/acetonitrile (ACN) and reduced with 10 mM dithiothreitol at 50

°C for 30 min. Cysteines were alkylated with 100 mM iodoacetamide in the dark for 30 min at room temperature. Gel bands were washed again in 100 mM AmBic/ACN prior to adding 600 ng trypsin for overnight incubation at 37 °C. The supernatant, which now contained peptides, was saved into a new tube. The remaining gel bands were then washed at room temperature for 10 min with gentle shaking in 50% ACN/5% formic acid (FA), and this solution was combined with the peptide solution. The wash step was repeated using 80% ACN/5% FA followed by 100% ACN. All supernatant was added to the peptide solution, which was then dried using a speed-vac. After lyophilization, peptides were reconstituted with 5% ACN/0.1% FA in water and injected onto a trap column (150 µm ID × 3 cm, in-house packed with ReproSil C18aq 3 µm) coupled with a Nanobore analytical column (75 µm ID × 10.5 cm, PicoChip column packed with ReproSil C18aq, 1.9 µm) (New Objectives, Inc., Woburn, MA). Samples were separated using a linear gradient of solvent A (0.1% formic acid in water) and solvent B (0.1% formic acid in ACN) over 60 min using a Dionex UltiMate 3000 Rapid Separation nanoLC (ThermoFisher Scientific). MS data were obtained on a LTQ Velos Orbitrap (Thermo Fisher, San Jose, CA) mass spectrometer. The peptide sequences were compared to the UniProt *Mm. buryatense* 5G genome using Mascot 2.5.1 (Matrix Science, Boston, MA), and results were reported at 1% false discovery rate (FDR) in Scaffold 4.5 (Proteome Software, Portland, OR).

5G-XoxF methanol oxidation activity assay

Enzyme activity was measured by the 2,6-dichlorophenolindophenol (DCPIP) dye-linked dehydrogenase assay using phenazine methosulfate (PMS) (Sigma-Aldrich) as the mediator and methanol (Sigma-Aldrich) as the substrate as described previously[170]. Reactions were carried out at 30 °C in a 96-well clear, flat bottom, polystyrene Costar assay plate (Corning) containing 1.5

μM 5G-XoxF in a total reaction volume of 100 μL. A Biotek Cytation 5 imaging reader was used to measure the decrease in the absorbance at 600 nm which was monitored for 60 s. For determination of specific activity, change in A_{600} 1 min after methanol addition was used to determine the concentration of reduced DCPIP. For V_{max}, the maximum slope (A_{600}/min) of reaction was used. The molar absorptivity of DCPIP at 600 nm is 1.91×10^4 M^{-1} cm^{-1}.

Size exclusion chromatography with multi-angle light scattering (SEC-MALS)

The molecular mass of purified 5G-XoxF was determined using SEC-MALS. System components consist of an Agilent 1260 series high-performance liquid chromatography system (Agilent Technologies) for size exclusion chromatography equipped with a Wyatt Dawn Heleos II multi-angle static light scattering detector, a Wyatt QELS quasi-elastic (dynamic) light scattering detector, and a Wyatt T-rEx (refractometer with extended range) differential refractive index detector (all from Wyatt Technology, Santa Barbara, CA). 5G-XoxF at a concentration of 1, 5, and 10 mg/mL in 20 mM Tris, pH 8, 50 mM NaCl was injected onto a pre-equilibrated Superdex 200 10/300 GL column (GE Healthcare) with a flow rate of 0.5 mL/min at room temperature. ASTRA software (Wyatt Technology) was used to calculate the molecular mass, and BSA was used as a molar mass reference.

Purification of pMMO from *Mm. buryatense* 5GB1C

Cells grown for pMMO isolation were cultured and lysed as described above, but without 0.5% methanol supplementation. The pelleted membrane was homogenized in 25 mM PIPES, pH 7.3, 250 mM NaCl using a Dounce homogenizer, followed by centrifugation at 100,000×g for 30 min. This step was repeated twice for a total of three washes. The membranes were resuspended

in 25 mM PIPES, 250 NaCl, pH 7.3 buffer to a final concentration of 10–20 mg/mL and flash frozen in liquid nitrogen for storage at $-80°C$. The protein concentration was measured using the Detergent-Compatible Lowry Assay (Bio-Rad) with bovine serum albumin (BSA) as a standard.

Mm. buryatense 5GB1C membranes were solubilized in 1.2 mg n-dodecyl-β-d-maltopyranoside (DDM) (Anatrace) per mg of protein. The sample was centrifuged at 100,000×g for 30 min at 4 °C to pellet the membranes. The solubilized 5G-pMMO protein was then buffer exchanged with 25 mM PIPES, pH 7.3, 50 mM NaCl, 0.02% DDM using a 100,000 MWCO Amicon centrifugal concentrator (Milipore), and loaded onto a Source 15Q anion exchange column (GE Healthcare). 5G-pMMO eluted at approximately 320 mM NaCl using a gradient of 50–800 mM NaCl in 25 mM PIPES, pH 7.3, 0.02% DDM (Fig. S4.5). Fractions containing 5G-pMMO were concentrated in an Amicon 100 kDa MWCO device (Millipore) to 10 mg/mL in 25 mM PIPES, pH 7.3, 250 mM NaCl, 0.02% DDM, and stored at -80 °C. Sample purity was assessed using SDS-PAGE (Fig. S4.6). The 13C methane oxidation activity of the as-isolated membranes was 2.53 ± 0.34 nmol 13C methanol min−1 mg−1 protein (n = 3), performed as described previously[7]. The copper content of purified 5G-pMMO was 2.34 ± 0.18 copper equivalents per pMMO protomer (n = 3) using inductively coupled plasma optical emission spectroscopy (ICP-OES) at the Quantitative Bio-element Imaging Center (QBIC) at Northwestern University and 0–500 ppb copper standards (Inorganic Ventures).

Biolayer interferometry

Interactions between purified 5G-pMMO and purified 5G-XoxF were detected using a ForteBio biolayer interferometer (BLItz) in the Northwestern Keck Biophysics Facility. Amine reactive second-generation (AR2G) biosensors (ForteBio) were hydrated in 15 mM NaOAc, pH 5

for 30 min prior to each experimental run. This pH was chosen because it is slightly below the expected isoelectric point of 5G-XoxF (pI = 5.32), thus allowing electrostatic interactions to facilitate coupling between the sensor and the ligand. Activation of the sensor was carried out in four steps. First, the AR2G sensor was immersed in 15 mM NaOAc, pH 5 for 30 s to establish a baseline. Second, the biosensor was activated for 3 min in a mixture of 40 mg/mL EDC [1-ethyl-3-[3-(dimethylamino)propyl]carbodiimide hydrochloride] and 10 mg/mL NHS [N-hydroxysuccinimide], both dissolved in water. For ligand loading, purified 5G-XoxF diluted to 0.5 mg/mL with 15 mM NaOAc, pH 5 was reacted with the biosensor for 3 min. Finally, any unbound sites were chemically blocked by reacting the sensor with 1 M ethanolamine, pH 8.5 for 3 min. After each step in the procedure, the sensor was immersed in baseline buffer for 1–2 min to wash away excess reagent from the previous step. The final prepared sensor was kept in baseline buffer before use.

Experimental runs were performed using 5G-pMMO diluted to concentrations of 5–25 μM in 15 mM NaOAc, pH 5 and 0.02% DDM. Each experimental run comprised three steps: (1) baseline, in which the 5G-XoxF-loaded sensor was immersed in pMMO buffer to establish a zero baseline for buffer interactions; (2) association, in which the sensor was immersed in purified 5G-pMMO for 2 min; and (3) dissociation, in which the sensor containing 5G-XoxF-pMMO complexes was transferred to baseline buffer for 3 min to dissociate. Each run was repeated with a new biosensor tip, and three total data sets were collected. One data set comprised five runs to test 5G-XoxF interactions with 0, 5, 10, 15, and 25 μM 5G-pMMO. The data were corrected against the 5G-pMMO buffer-only reference obtained at the start of each experimental set and fit

with the global fitting function from ForteBio Data Analysis. A control experiment performed with BSA and 25 μM 5G-pMMO showed no interaction.

5G-XoxF structure determination

5G-XoxF crystals were obtained by the sitting drop vapor diffusion method by mixing 1 μL of 5 mg/mL XoxF with 1 μL of reservoir solution containing 0.2 M magnesium acetate, 0.1 M sodium cacodylate, pH 6.5, and 20% PEG 8000. Rod-shaped crystals formed after 1 week at room temperature. Data collection was performed at the Advanced Photon Source at Argonne National Laboratory. HKL2000[87] was used to process and integrate all data sets. Phaser[89] was used to obtain molecular replacement solutions using the structure of XoxF from *Ma. fumariolicum* SolV (4MAE)[148] as the search model (51% amino acid sequence identity). Starting from the initial model, COOT[90] was used to manually build the structure, followed by refinement using Phenix[89]. The model quality was assessed using MolProbity[91]. The final model for the 5G-XoxF structure includes residues 27–570 and 599–617, 1 La(III) ion, 1 PQQ molecule, 1 sodium ion, and 497 water molecules. The server PDBsum was used to identify hydrogen bonds (3.4 Å cutoff) at the dimer interfaces of 5G-XoxF and SolV-XoxF[171].

CHAPTER 5: RECENT ADVANCES IN THE GENETIC MANIPULATION OF *METHYLOSINUS TRICHOSPORIUM* OB3B

Parts of this chapter has been published as:

S.Y. Ro, A.C. Rosenzweig. *Methods Enzymol*. **2018**, 605:339-345.

L.M. Dassama, et al. *Proc. Natl. Acad. Sci. US.A.* **2016**, 113, 13027-13032.

G.E. Kenney, et al. *Science*, **2018**, 359, 1411-1416.

O.S. Fisher, et al. *Nat. Commun*. **2018**, 9, 4276.

ABSTRACT

Methanotrophic bacteria utilize methane as their sole carbon and energy source. Studies of the model Type II methanotroph *Methylosinus trichosporium* OB3b have provided insight into multiple aspects of methanotrophy, including methane assimilation, copper accumulation, and metal-dependent gene expression. Development of genetic tools for chromosomal editing was crucial for advancing these studies. Recent interest in methanotroph metabolic engineering has led to new protocols for genetic manipulation of methanotrophs that are effective and simple to use. We have incorporated these newer molecular tools into existing protocols for *Ms. trichosporium* OB3b. The modifications include additional shuttle and replicative plasmids as well as improved gene delivery and genotyping. The methods described here render gene editing in *Ms. trichosporium* OB3b efficient and accessible.

INTRODUCTION

Methanotrophic bacteria are unique in their ability to utilize methane, a potent greenhouse gas, as their sole carbon source[1]. In the first step of their metabolic pathway, methane is oxidized to methanol, which can be utilized as a cheap carbon feedstock for industrial chemical processes[60]. For this reason, there have been extensive efforts to understand methanotrophy in multiple species of bacteria. Most aerobic methanotrophs are classified as Type I (γ-proteobacteria) or Type II (α-proteobacteria) based on their use of either the ribulose monophosphate or serine cycles for carbon assimilation, respectively, as well as their phospholipid compositions, cell morphologies, and membrane arrangements[1,2]. Methane is oxidized to methanol by methane monooxygenase enzymes (MMOs), followed by methanol conversion to formaldehyde by methanol dehydrogenases (MDHs). There are two types of MMO, a soluble and cytoplasmic iron-containing enzyme (sMMO) and a "particulate" and inner membrane-bound copper-containing enzyme (pMMO)[3]. With the exception of the genera *Methylocella* and *Methyloferula*, aerobic methanotrophs express pMMO under most conditions[2,4]. Under copper-starved conditions, some Type I and Type II methanotrophs can switch to sMMO expression[2], and some *Methylosinus* and *Methylocystis* species also produce the copper chelator methanobactin[172].

Methylosinus trichosporium OB3b is the best studied Type II methanotroph[173]. This bacterium can express both sMMO and pMMO, produces methanobactin[172], and can express two distinct MDHs, the calcium-binding MxaF and the lanthanide-binding XoxF[174]. Genetic tools developed previously for *Ms. trichosporium* OB3b have been used to mutate or disrupt the genes encoding several important proteins. Recent studies have focused on sMMO[43,175-178], proteins in

the extended *pmo* operon[44], methanobactin transport and biosynthetic proteins[53,172,179], and genes related to MDH[174].

In recent years, new genetic manipulation tools have been developed for two Type I haloalkaliphilic methanotrophs, *Methylomicrobium alcaliphilum* 20Z[39,180] and *Methylomicrobium buryatense* 5G[45,50]. These protocols have been used to engineer methanotrophs for biofuel production[33,47,48] and have also enabled studies of lanthanide-dependent methanol oxidation[42], ectoine biosynthesis[181], and fatty acid biosynthesis[182]. This chapter describes the incorporation of these newer techniques developed for Type I methanotrophs into the traditional mutagenesis protocol for *Ms. trichosporium* OB3b[178,183,184]. By simplifying cloning, gene delivery via conjugation or electroporation, and DNA isolation for genotyping, this hybrid method will facilitate future investigations and engineering of *Ms. trichosporium* OB3b.

MS. TRICHOSPORIUM OB3B GROWTH CONDITIONS

Ms. trichosporium OB3b strains are grown in nitrate minimal salt (NMS) media[185] (Table 5.1). Cultures are grown under either low copper (0.1 μM CuSO4) or high copper (10–25 μM CuSO4) conditions in liquid cultures and agar plates. Many genes of interest in methanotrophs are copper regulated, and it may be necessary to alter the copper concentration to ensure viability and to avoid selection against the genetic modifications. Similar considerations may be appropriate for genes regulated by other environmental factors.

Initially, cells at an OD_{600} of 0.1 are inoculated into 50 mL cultures in 250-mL Erlenmeyer flasks sealed with rubber septa. The flasks are then incubated at 30°C with shaking at 200 rpm, and oxygen and methane levels are maintained via daily sparging with a 1:3 methane-to-air ratio

Table 5.1. *Ms. trichosporium* **OB3b growth conditions**

1X NMS medium (1 L)	Growth	Mating	Selection	Counterselection
$NaNO_3$	0.85 g	0.85 g	0.85 g	0.85 g
K_2SO_4	0.17 g	0.17 g	0.17 g	0.17 g
$MgSO_4 \cdot 7H_2O$	0.037 g	0.037 g	0.037 g	0.037 g
$CaCl_2 \cdot 2H_2O$	0.01 g	0.01 g	0.01 g	0.01 g
40 mM $FeSO_4 \cdot 7H_2O$	1 mL	1 mL	1 mL	1 mL
100 mM $CuSO_4 \cdot 5H_2O$	varies	varies	varies	varies
Agar (plates only)	15 g	15 g	15 g	15 g
LB (Difco)	-	1.2 g	-	-
Phosphate buffer solution	10 mL	10 mL	10 mL	10 mL
Trace elements solution	2 mL	2 mL	2 mL	2 mL
50% sucrose	-	-	-	50 mL

50X Phosphate solution (g/L)	
$Na_2HPO_4 \cdot 7H_2O$	48.06
KH_2PO_4	23.4

500X Trace elements (g/L)

$ZnSO_4 \cdot 7H_2O$, 0.288; $MnCl_2 \cdot 4H_2O$, 0.16; H_3BO_3, 0.06; $Na_2MoO_4 \cdot 2H_2O$, 0.048; $CoCl_2 \cdot 6H_2O$, 0.048; KI, 0.083

at 1 L/min for 5 min. An OD600 of ~ 1.5 is typically reached after 1 week of growth. Agar plates are incubated in GasPak plate incubation chambers (BD) at 30°C, and gas exchange is facilitated by use of a vacuum to create negative pressure inside the chamber followed by gas flow at a 1:1 methane-to-air ratio at 1 L/min for 3 min. Colonies on plates typically appear in 1–2 weeks. Antibiotics such as kanamycin (25 μg/mL) and gentamicin (5 μg/mL) are used to select for mutants, and naladixic acid (10 μg/mL) is used to remove donor *Escherichia coli* strains as described later.

PLASMIDS FOR MUTAGENESIS

For chromosomal site-directed mutagenesis or gene deletion, a broad host range vector pk18mobsacB[41] has been used in several methanotrophs, including *Ms. trichosporium* OB3b[175]. However, it is sometimes difficult to insert methanotroph genes, including those in the *pmo* operon, into this plasmid due to leaky expression at high copy number and subsequent toxicity of the product proteins in *E. coli*[39]. We have employed the following two strategies to circumvent this issue. First, we use the chemically competent *E. coli* strain CopyCutter EPI400 (Lucigen), designed to control plasmid copy number, to increase the success rate for cloning of methanotroph genes. However, the plasmid must then be incorporated into the *E. coli* donor strain S17-1[186] for subsequent conjugation. Transformation into S17-1 can also fail due to leaky expression. As a second, alternative strategy, we have constructed a modified version of pk18mobsacB under p15a copy control[187] to generate the plasmid pk18mobsacB_p15a (Fig. 5.1; Table 5.2). This shuttle vector has improved the efficiency of cloning methanotroph genes, such as those in the *pmo* operon[39].
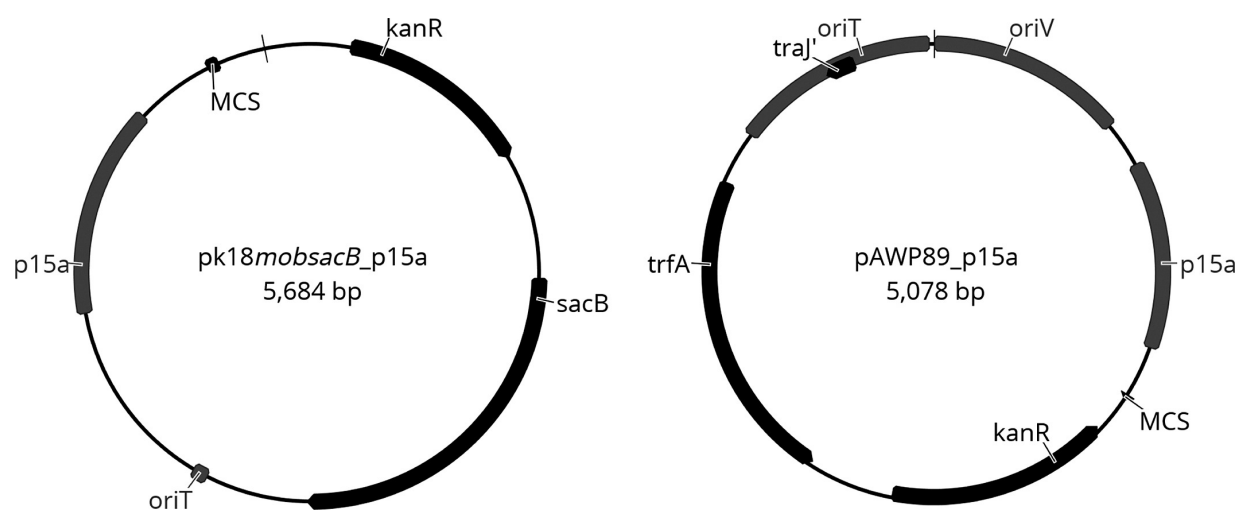
Figure 5.1. Plasmid maps of pk18mobsacB_p15a and pAWP89_p15a.

Table 5.2. Plasmids.

Strain	Source/Reference
pk18*mobsacB*	ATCC (Schafer et al, 1994)
pk18*mobsacB*_p15a	This study
pAWP89	Addgene (Puri et al, 2015)
pAWP89_p15a	This study

Replicative plasmids are useful tools for protein overexpression or probing promoters. We tested a replicative plasmid compatible with Type I methanotrophs for function in *Ms. trichosporium* OB3b. The Lidstrom laboratory has constructed a replicative plasmid pAWP89 that can be maintained in *Mm. buryatense* 5G[45]. We have determined that this plasmid can be maintained in *Ms. trichosporium* OB3b (Fig. 5.2). For the purposes of overexpressing toxic methanotroph genes, we have replaced the origin of replication in pAWP89 with p15a to create pAWP89_p15a (Fig. 5.1; Table 5.2).

GENETIC MANIPULATION VIA CONJUGATION

The most common and efficient method for genetic manipulation in methanotrophs requires conjugation[178,183,188]. Typically after conjugation, the shuttle plasmid is incorporated into the chromosome of the recipient strain, followed by counterselection to ensure double recombination and removal of the vector backbone from the chromosome[189]. In *Ms. trichosporium* OB3b, the established conjugation method involves the addition of liquid cultures of both methanotroph and E. coli cells onto a 0.2-µm sterile filter paper for mating[178]. This protocol requires the use and subsequent dismantling of a plastic filter unit or a Pyrex microfiltration glass assembly, followed by cell recovery from filter paper, which can increase the risk of contamination. A simpler conjugation protocol has been developed for the Type I methanotrophs *Mm. buryatense* 5G and *Mm. alcaliphilum* 20Z[39,45]. We have modified this protocol, which requires only cells grown on agar plates and disposable cell spreaders, for conjugation in *Ms. trichosporium* OB3b (Fig. 5.3):
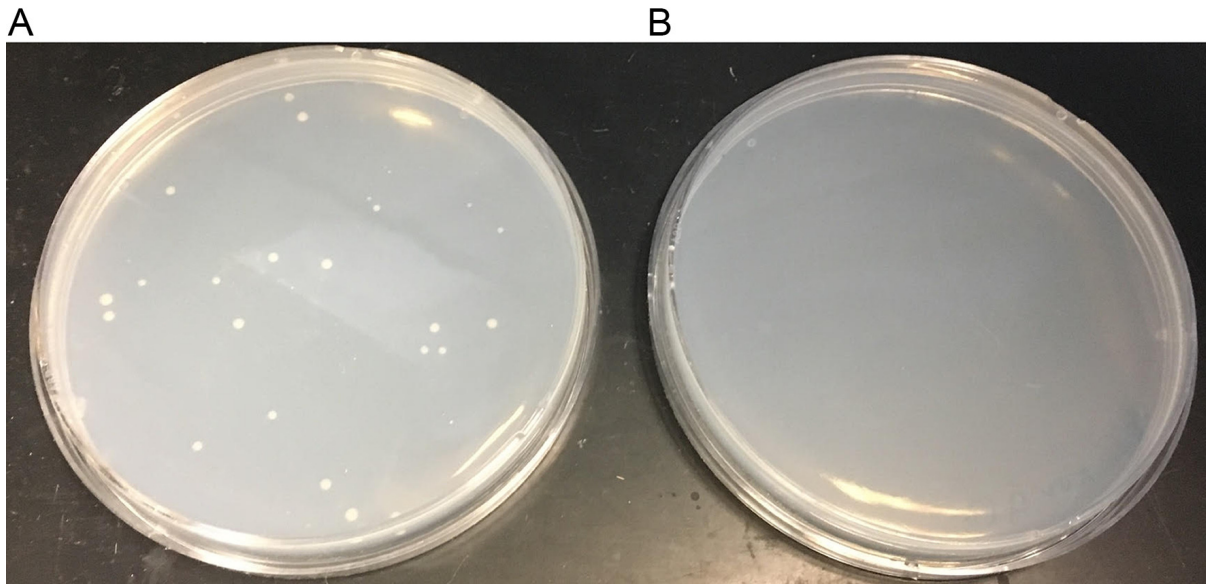
Figure 5.2. Replicative plasmid in *Ms. trichosporium* OB3b.
Ms. trichosporium OB3b transformed with pAWP89_p15a (A) compared to wild-type Ms. trichosporium OB3b (B) on 25 µg/mL kanamycin NMS agar selection plates.
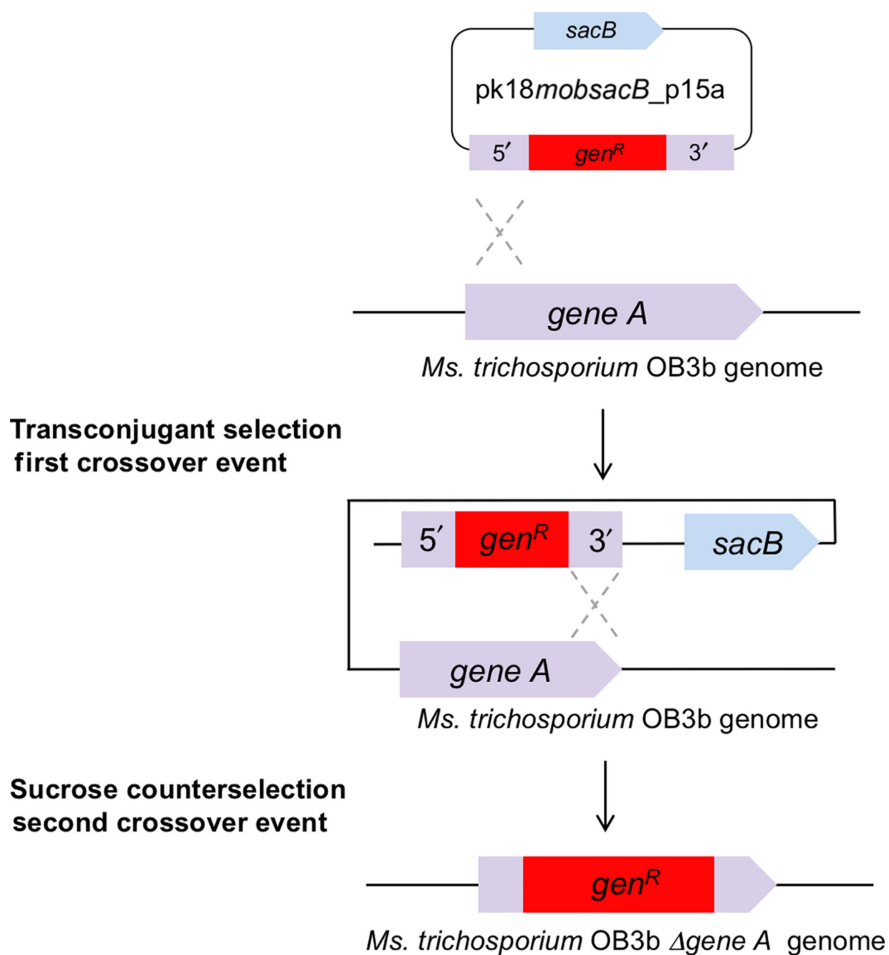
Figure 5.3. Gene deletion via conjugation in *Ms. trichosporium* OB3b.
Following conjugation, the introduced plasmid recombines into the targeted site in the chromosome during the first crossover. Transconjugant selection followed by sucrose counterselection induces a second crossover event to remove the plasmid backbone from the chromosome and produce the mutant with the gentamicin resistance cassette (*genR*) disrupting *gene A*.

1. The vector pk18mobsacB or pk18mobsacB_p15a (carrying an insert consisting of 5′ and 3′ DNA regions flanking the site of gene insertion, deletion, or mutagenesis, as well as any sequence to be inserted or altered) is transformed into the donor strain *E. coli* S17-1 via either heat shock or electroporation[186].

2. One day prior to bacterial mating, the *E. coli* S17-1 cells are streaked onto LB agar plates to obtain a bacterial lawn.

3. The wild-type recipient strain *Ms. trichosporium* OB3b is streaked onto an NMS agar medium plate (Table 5.1) and given 1 week to grow, forming at least a partial bacterial lawn.

4. The donor and recipient strains are harvested from plates and evenly plated and spread onto the same mating agar plate (Table 5.1) with a cell ratio of 2:1 donor-to-recipient strain. Specifically, a sterile cell spreader is dragged once across the plate containing the recipient methanotroph cells, and then is immediately used to inoculate the mating plate (Table 5.1). This is repeated for the donor (*E. coli*) strain, and the donor cells are plated directly on top of the recipient cells in the mating plate.

5. These plates are then incubated at a 1:1 methane-to-air ratio for 48 h at 30°C in a GasPak chamber.

6. A fraction of the mated cells, just enough to be visible on the bottom of the sterile cell spreader, are scraped off the mating plate and directly plated onto a selection agar plate (Table 5.1) containing kanamycin (25 µg/mL). The selection plate is incubated under the same conditions as the mating plate.

7. Single transconjugant colonies that appear are picked with a sterile loop and separately streaked onto selection plates containing kanamycin (25 µg/mL) as well as naladixic acid (10 µg/mL) to eliminate remaining cells from the donor *E. coli* strain.

8. Single transconjugant colonies on selection plates are picked using a sterile loop and streaked onto counterselection agar plates (Table 5.1) containing 2.5% sucrose and appropriate antibiotics. Single colonies from these counterselection plates are then picked and streaked once more to obtain sufficient biomass for genotype screening.

GENE MANIPULATION VIA ELECTROPORATION

In situations where cloning or conjugation fails, electroporation can be employed, as reported for *Methylocella silvestris* BL2, *Methylocystis* sp. strain SC2, and *Mm. buryatense* 5G[28,50,190]. Linear DNA fragments produced via PCR can be also electroporated into *Ms. trichosporium* OB3b and integrated into the chromosome[172]. Thus far, intact plasmids purified from *E. coli* cloning strains have not been successfully incorporated into *Ms. trichosporium* OB3b via this method.

Construction of linear DNA fragment

Homologous recombination of a linear DNA fragment is a technique used for gene disruption, insertion, and modification[191,192]. One common use of this technique is gene disruption via insertion of a linear DNA fragment containing an antibiotic resistance cassette into the middle of the target gene. Construction of the resulting linear DNA fragment can be performed via several methods, including fusion PCR[193]. In that method, ~ 500 bp DNA regions flanking the gene of interest and a gentamicin resistance cassette are amplified by PCR. Primers are designed to add 25

bp regions onto the 5′ and 3′ ends of the gentamicin resistance cassette that overlap with the DNA regions flanking the gene of interest. The three PCR products are then joined together through two rounds of fusion PCR (Fig. 5.4). PCR products for each round of amplification are isolated and purified through gel extraction. In addition, it is necessary to perform a final cleanup of the PCR product using a PCR Purification Kit (Qiagen) or equivalent technique prior to sequencing and electroporation.

Electrocompetent cell preparation

50 mL cultures of *Ms. trichosporium* OB3b cells are grown in NMS medium (0.1 μM CuSO4) as described in Section 2. Cells are harvested at an OD600 of 1.0, centrifuged at 7000 × g at 4°C for 10 min, and washed twice with 20 mL of 10% sterile glycerol at 4°C before a final 1 mL resuspension in 10% glycerol at 4°C. Fresh electrocompetent cells are recommended for every electroporation round.

Electroporation

1. 100–500 ng of the linear DNA fragment is added to 100 μL electrocompetent cells in sterile microcentrifuge tubes kept on ice.
2. The mixture is then transferred into a prechilled sterile electroporation cuvette with a 0.2-cm gap width (Bio-Rad). The cuvette is inserted into an electroporation system (Bio-Rad MicroPulser) and subjected to one pulse at 2.2 kV for 5 ms at 1 Å.
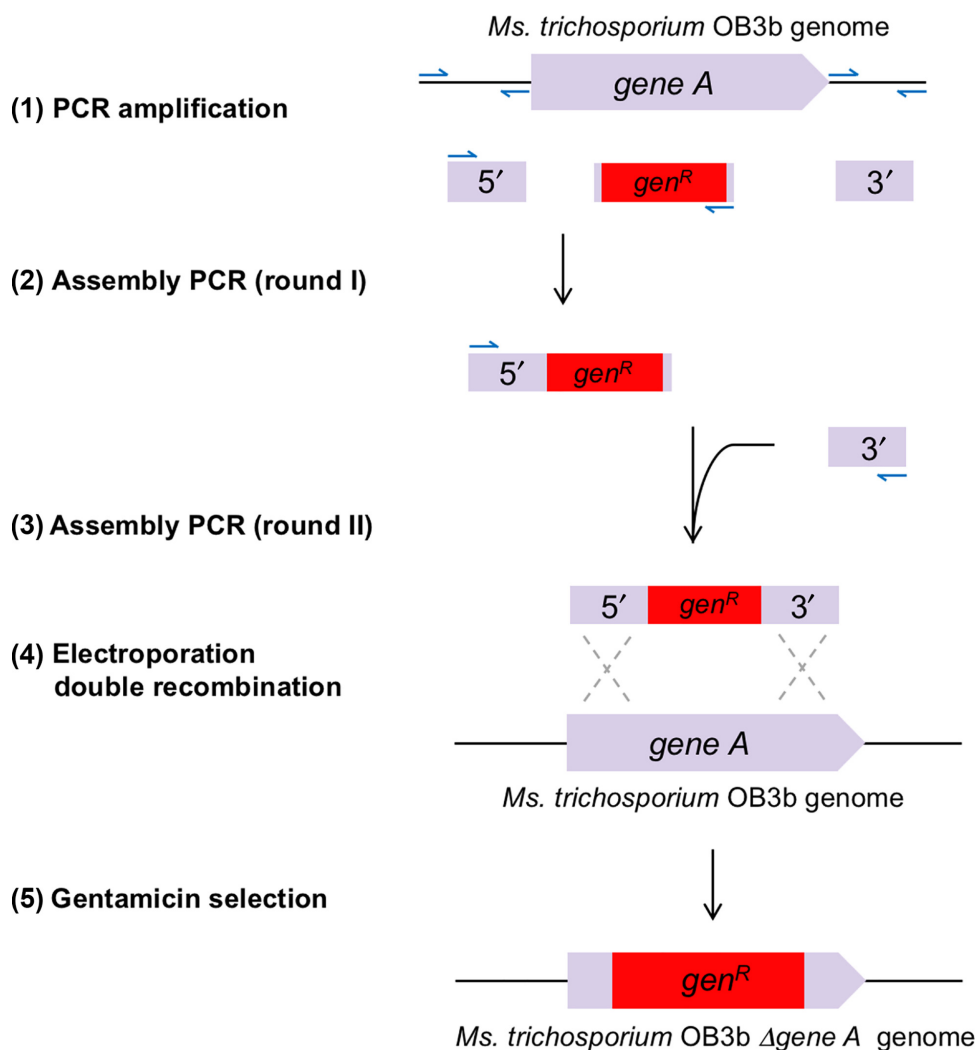
Figure 5.4. Construction of a gene-disrupting linear DNA fragment using fusion PCR. **(1)** PCR amplification of *genR* and the 5′ and 3′ DNA regions flanking gene targeted for disruption. **(2)** The 5′ DNA fragment and *genR* are used as templates for the first round of fusion PCR. **(3)** The resulting PCR product and the 3′ DNA fragment are used as templates for the second round of PCR to produce the final gene-disrupting linear DNA construct. The linear DNA construct is **(4)** electroporated into wild-type *Ms. trichosporium* OB3b followed by **(5)** selection for the *Ms. trichosporium* OB3b Δ*gene A* mutant. Primer binding sites are represented by half arrows.

3. After electroporation, the cell mixture is added to 5 mL of NMS liquid medium (without antibiotics) in borosilicate culture tubes sealed with rubber septa.

4. The cultures are incubated overnight at 30°C and 200 rpm after gas sparging at a 1:3 methane-to-air ratio.

5. After 24 h of growth, the cells (the outgrowth culture) are centrifuged at 7000 × g and 4°C for 10 min, and are then resuspended in 500 μL standard NMS liquid medium.

6. 100–300 μL of the outgrowth culture is then spread onto NMS selection plates containing gentamicin (5 μg/mL).

ANALYSIS OF *MS. TRICHOSPORIUM* OB3B MUTANTS

DNA extraction from *Ms. trichosporium* OB3b cells on agar plates

DNA extraction from *Ms. trichosporium* OB3b is less efficient than DNA extraction from many Type I or Type II methanotrophic bacteria. Existing methods use the neutral lysis/CsCl method or a DNeasy Blood Tissue Kit (Qiagen) for DNA extractions from liquid cultures[178,179]. However, growing liquid cultures to genotype multiple colonies is time-consuming. Instead, an improved method has been developed to extract DNA from cells growing on agar plates using the MasterPure Complete DNA Purification Kit (Epicentre, Cat. No. MC85200). This method allows for higher-throughput of genotype screening and provides increased yields of DNA from smaller amounts of cells. The MasterPure Complete DNA Purification Kit protocol has been modified for *Ms. trichosporium* OB3b:

1. Add 20 μL Proteinase K (NEB, 800 U/mL) into 300 μL 2 × tissue and cell lysis solution for each sample.

2. Drag a sterile inoculating loop across the agar plate culture until the loop is covered with cells.

3. Swirl the inoculating loop in the lysis solution and resuspend fully by pipetting.

4. Incubate the sample at 65°C overnight at 500 rpm.

5. Add 5 μL RNase A (Epicentre, 5 μg/μL). Incubate for 1 h at 37°C without shaking.

6. Place the samples on ice for 5 min.

7. Add 150 μL MPC protein precipitation reagent and vortex.

8. Centrifuge the sample at 10,000 × g at 4°C for 10 min to pellet cell debris.

9. Transfer the supernatant to a new tube and add 500 μL 100% isopropanol on ice. Manually invert the sample 30 times.

10. Centrifuge the sample at 4°C for 30 min at 20,000 × g to pellet DNA.

11. Wash the DNA pellet with 750 μL 70% ethanol on ice. Centrifuge at 20,000 × g at 4°C for 5 min, remove the ethanol, and repeat the wash step once more.

12. Let the pellet dry at 37°C until residual ethanol is gone.

13. Resuspend the pellet with 50 μL TE buffer and incubate overnight at 4°C.

14. DNA yield can vary from 10 to 60 μg. Additional cleanup steps using silica spin columns (Zymo) may be required for uses other than simple Sanger sequencing.

Genotyping mutants

To confirm the genotype of *Ms. trichosporium* OB3b variants, PCR amplification of the altered DNA region is performed. Due to the high genomic GC content of Type II methanotrophs, PCR amplification is more successful under reaction conditions optimized for high-GC samples, such as the 2 × iProof GC Master Mix (Bio-Rad). 100 ng of *Ms. trichosporium* OB3b genomic

DNA is an appropriate starting point for a 50-µL PCR reaction. Gradient or touchdown PCR at annealing temperatures of 55–65°C can be employed to identify conditions for specific amplification. PCR cleanup (QIAquick PCR Purification Kit, Qiagen) will significantly improve sequencing results.

CASE STUDIES

Ms. trichosporium OB3b Δ*mbnN* knockout construction

The *Ms. trichosporium* OB3b Δ*mbnN* mutant was generated by chromosomal gene disruption. The middle of the *mbnN* encoding gene was disrupted by introduction of a gentamicin resistance gene through homologous recombination (Fig. 5.5). DNA regions 550 bps upstream and downstream of the middle of the *mbnN* gene were amplified to flank a gentamicin resistance gene. The PCR products were assembled into the mobilization vector pK18mobsacB using Gibson assembly and transformed into *E. coli* S17-1 ATCC 47055 to produce plasmid pSYR13. This gene disrupting plasmid was introduced into *Ms. trichosporium* OB3b through conjugation. *E. coli* S17-1 and *Ms. trichosporium* OB3b cells were plated together onto NMS mating plates supplemented with LB. After two days, the cells were plated onto NMS selection plates containing kanamycin (25 µg/mL) and nalidixic acid (10 µg/mL). Transconjugants were plated onto NMS plates containing gentamicin (10 µg/mL) and 2.5% sucrose for counter selection to ensure double homologous recombination. Colonies were screened by PCR for the correct mutant genotype and were grown at 30 °C in 50 mL NMS medium with gentamicin (5 µg/mL), no copper, and a gas mix containing a 1:3 methane-to-air ratio.
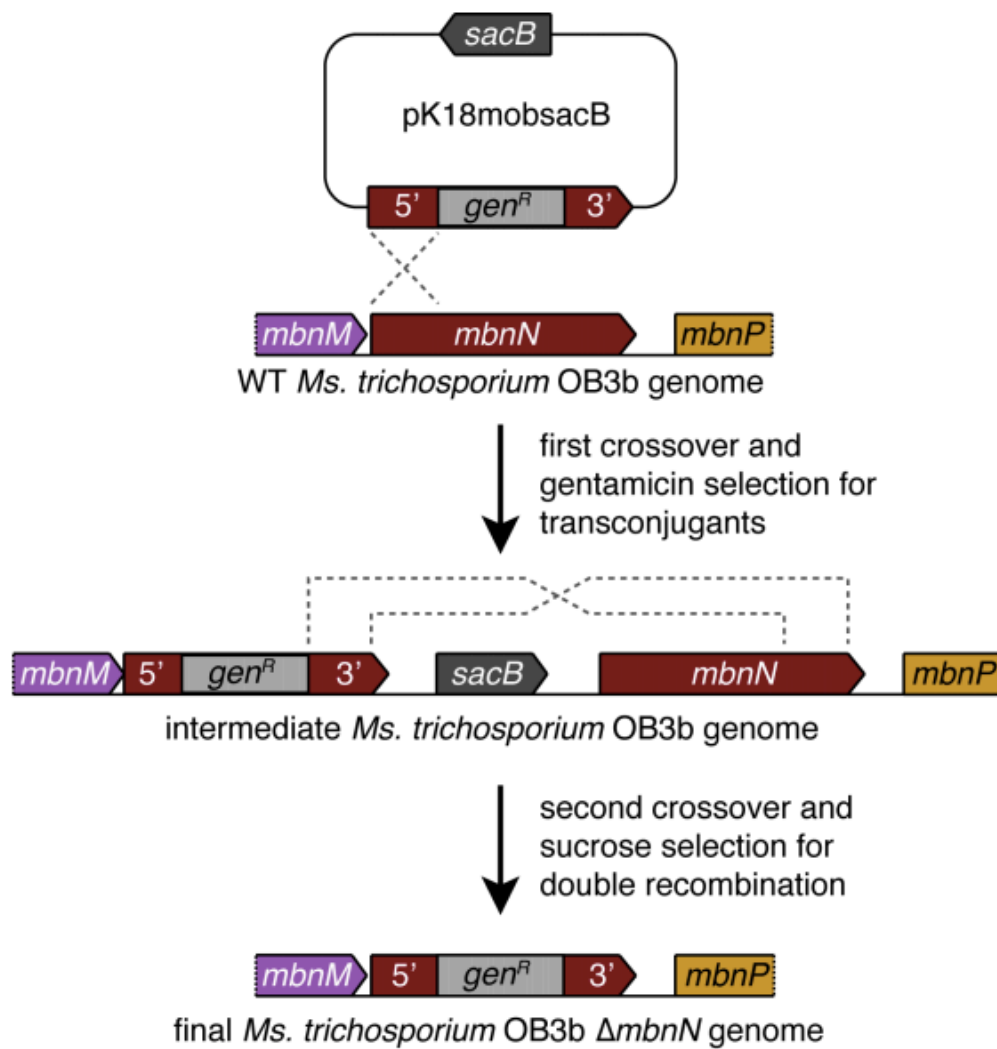
Figure 5.5. Cloning scheme for Δ*mbnN* knockout construction in *Ms. trichosporium* OB3b.

Gene-disruption mutant of *Ms. trichosporium* OB3b Δ*mbnT*

The *Ms. trichosporium* OB3b Δ*mbnT* mutant was generated by removal of the *mbnT* gene through homologous recombination of a gene disrupting linear DNA fragment. The DNA fragment was produced by PCR amplification of the 5' and 3' DNA regions flanking the encoding gene and a gentamicin resistance gene. The PCR products were joined together through assembly PCR. Wild-type *Ms. trichosporium* OB3b cultures were grown in NMS medium with no copper, at 30 °C, and a gas mix containing a 1:3 methane-to-air ratio. 50 mL of cells were harvested at OD of 1.0, centrifuged at $7,000 \times g$, and washed with 10% sterile glycerol several times before a final 1 mL resuspension with 10% glycerol. The linear DNA fragment was introduced into *Ms. trichosporium* OB3b cells through electroporation. 100 µL of electrocompetent transformants were prepared using a Bio-Rad Gene Pulser at 2.2 kV and a 2 mm gap electroporation cuvette (Bio-Rad). The outgrowth cells were plated on NMS plates

containing gentamicin (10 µg/mL). The genotypes of the transformants were confirmed by PCR to detect the loss of 2 kb in the *mbnT* region of the genome.

Construction of a Δ*pmoD* strain of *Ms. trichosporium* OB3b

The *Ms. trichosporium* OB3b Δ*pmoD* mutant was generated by chromosomal gene disruption into wild-type *Ms. trichosporium* OB3b. A gentamicin resistance gene (*gen*[R]) was inserted in the middle of PmoD$_{MettrDRAFT\_0381}$ via homologous recombination. Primers targeting regions 600 bp upstream and 600 bp downstream from the center of the *pmoD* gene were used to amplify the DNA flanking the inserted *gen*[R]. The gentamicin resistance cassette was amplified from vector pFBOH-LIC. The PCR products were assembled into pK18mobsacB_p15a using Gibson assembly and transformed into *E. coli* S17-1 ATCC 47055

to produce plasmid pSYR16. This plasmid was then introduced into *Ms. trichosporium* OB3b via conjugation with *E. coli* S17-1 cells transformed with pSYR16 on NMS mating agar plates (0 µM $CuSO_4$). After 2 days, mated cells were plated on NMS selection agar plates (0 µM $CuSO_4$) containing kanamycin (25 µg/mL) and nalidixic acid (10 µg/mL). Single colonies from selection plates were picked and streaked onto NMS counter selection plates (0 µM $CuSO_4$) containing 2.5% sucrose and gentamicin (10 µg/mL). Single colonies from counter selection plates were then plated and maintained on NMS agar plates (0 µM $CuSO_4$) containing gentamicin (10 µg/mL). Genotyping and sequencing were performed to confirm generation of the mutant. Cells on NMS agar plates were incubated in GasPak plate incubation chambers (BD) at 30 °C and were subjected daily to vacuum and gas-exchange cycles with gas at a 1:1 methane-to-air ratio and 1 L/min for 3 min.

SUMMARY

The modifications in plasmid design, construct delivery, and genotyping described here allow for simpler and more efficient genetic manipulation of *Ms. trichosporium* OB3b, at least until CRISPR or other gene editing methods are developed[194]. These advances will expedite metabolic engineering efforts in this methanotrophic strain and enhance studies of proteins involved in the key processes of methanotrophy.

CHAPTER 6: MUTATION OF A CONSERVED TYROSINE IN THE PMOB SUBUNIT OF PMMO AFFECTS METHANE OXIDATION ACTIVITY

This chapter is in preparation for submission.

INTRODUCTION

In pMMOs from γ-proteobacterial methanotrophs, a highly conserved tyrosine residue resides outside the first coordination sphere of the conserved copper center in PmoB (PmoB Y374) (Fig. 1). Y374 is located 5.2 Å from the copper ion coordinated by His 33 and the N-terminal amino nitrogen in the Cu_B site in pMMO from *Mcc. capsulatus* (Bath) (Bath-pMMO) (Fig. 6.1a) and 6.2 Å from the mononuclear copper ion in pMMO from *Mm. alcaliphilum* 20Z (20Z-pMMO) (Fig. 6.1b). Density functional theory (DFT) calculations[15] of the Cu_B site in Bath-pMMO suggested that Y374 plays an essential role in the formation of a copper active species responsible for the hydroxylation of methane. It should be noted that these calculations were based on the former dicopper active site model, which has recently been reassigned as monocopper[16]. Nevertheless, the study proposes that upon O_2 binding at this site, a $Cu^{II}Cu^{II}$ peroxo species is formed, followed by an H atom transfer from Tyr 374 that leads to O-O bond activation and formation of a reactive (μ-oxo)(μ-hydroxo)$Cu^{II}Cu^{III}$ species that could oxidize methane[15].

Based on this proposal, pMMO function should be affected by the mutation of Y374. However, this residue is not conserved in pMMOs from α-proteobacterial methanotrophs including *Ms. trichosporium* OB3b (OB3b-pMMO) and *Mc.* sp. str. Rockwell (Rockwell-pMMO). However, OB3b- and Rockwell-pMMOs contain a tyrosine residue elsewhere 8.2 Å (Y352) and 5.3 Å (Y341) away from the copper site, respectively, that could function similarly.
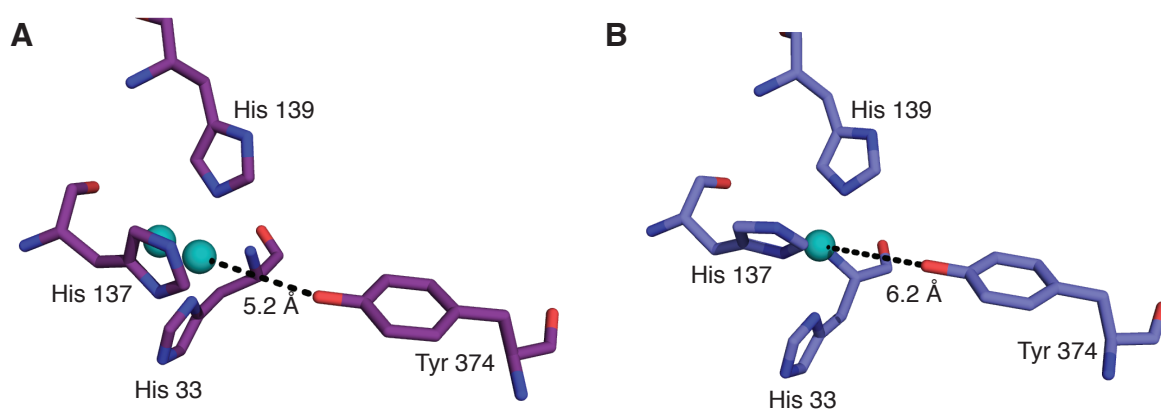
Figure 6.1. The PmoB Y374 residue.
A crystal structure of **A**, Bath-pMMO (3RGB) with ligands His 33, His 137, His 139, and Tyr 374 shown as *purple* sticks and **B**, 20Z-pMMO (6CXH) with ligands shown as blue sticks. Copper ions are shown in *teal*.

of Y374. Inspection of other nearby aromatic residues shows a Trp residue (W156 in Bath-pMMO) ~ 6.5 Å from the active site that is highly conserved in pMMOs from both γ- and α-proteobacterial methanotrophs.

There are several examples of highly conserved tyrosine residues near the active site in copper enzymes. Cytochrome c oxidases (CcOs) reduce oxygen to water as the terminal enzyme in the respiratory chain[195]. In the binuclear heme-Cu_B active site, a tyrosine crosslinked to a coordinating histidine ligand is thought to be involved in O-O cleavage and proton transfer to produce the Cu_B(II)-OH intermediate. Molecular dynamics stimulations suggest this Tyr may also be responsible for channel gating to control proton access to the active site[196].

The role of Tyr is less clear in lytic polysaccharide monooxygenases (LPMOs), responsible for glyosidic bond cleavage at a type 2 copper center resulting in oxidation of either the C1 or C4 carbon of the glycan. A Tyr is located in the axial position of the copper coordination sphere, ~2.8 - 3.0 A away, and is highly conserved in AA9, 11, 13 LPMOs[82]. While it is not essential for activity, mutation to Phe substantially reduces the rate of catalysis. This residue is replaced by Phe in most AA10 LPMOs, and mutation to Tyr abolishes activity whereas mutation to Ala only partially inactivates protein function[197,198]. Furthermore, in strictly C1-oxidizing AA9 LMPOs, the Tyr limits access to the solvent facing axial position of the active site. Interestingly, mixed C1/C4-oxidizers have proline in the same residue position, while C4-oxidizers have an Ala or an Asp, suggesting Tyr may affect regioselectivity by controlling solvent facing axial access[199].

Peptidylglycine α-hydroxylating monooxygenase (PHM) and dopamine β-monooxygenase (DβM) are responsible for the hydroxylation of carboxy-terminal glycine and dopamine, respectively[200]. They contain two noncoupled Cu centers ~11 Å apart. A conserved Tyr

is present at Cu_M, the site of substrate hydroxylation, and was once thought to be involved in generating the reactive copper-oxo species[201]. However, the PHM Y318F variant exhibits only three-fold reduction in activity[202]. In tyramine β-monooxygenase (TβM), a homolog of DβM, mutation of Y216 in the Cu_H site to Trp or Ile did not significantly impact activity. However, Y216A exhibited low activity, which suggests perturbation near the Cu_H site can affect the Cu_M active site via impaired long range electron transfer or changes to substrate access [203].

Copper amine oxidases (CAOs) oxidize primary amines to aldehydes via 1) oxidation of active site Tyr 466 (*E. coli* CAO) for biogenesis of the redox cofactor trihydroxy-phenylalanine quinone (TPQ) followed by 2) oxidative deamination at the mononuclear type 2 copper center[204]. Y369 is H-bonded to TPQ, and mutation to Ala retains deamination activity but slows TPQ formation, while mutation to Phe exhibits lower activity but higher TPQ formation. Studies suggest that this tyrosine is involved in cofactor formation, proper TPQ conformation for catalysis, and possibly prevention of forming oxidative off-path intermediates[204-206].

These examples emphasize the variety of roles of Tyr in copper enzymes. Although DFT calculations suggest PmoB Y374 is essential to the formation of the reactive copper-oxo species, its role is unclear due to lack of experimental studies and low degree of conservation in pMMOs from α-proteobacterial methanotrophs. Instead, Y374 could impact activity via substrate-related roles or have no effect on pMMO function. To investigate the proposed role of PmoB Y374, pMMO from *Mm. buryatense* 5GB1C (5G-pMMO) was subjected to mutagenesis.

RESULTS

Mutagenesis of PmoB Tyr 374 in 5G-pMMO

PmoB Tyr 374 was mutated to an alanine or a phenylalanine residue via markerless integration of SNPs in the genome using a sucrose-based counter selection plasmid platform (Fig. 6.2, Table 6.1). These mutant strains were initially transformed and isolated on copper-depleted media, but exhibited growth under copper-replete conditions (40 μM $CuSO_4 \cdot 5H_2O$). The detailed mutagenesis protocol is described in the methods section.

Activity of pMMO from *Mm. buryatense* 5GB1C

Whole-cell propylene oxidation activity assays were performed on the pMMO variants, in which propylene conversion to propylene oxide (PO) by *Mm. buryatense* 5GB1C cells grown in copper-replete conditions was monitored in 50 mL cultures at stationary phase (OD_{600} 1.0-1.5). On a whole-cell level, propylene oxidation levels were comparable amongst WT, Y374A, and Y374F pMMO variants (362 $\pm$ 75.6, 389.7 $\pm$ 31.1, 395.5 $\pm$ 97.0 nmol PO$\cdot$min$^{-1}\cdot$OD^{-1}, respectively) suggesting that mutation of the tyrosine residue does not affect pMMO activity (Fig. 6.3). However, pMMO concentrations could not be accurately calculated in the cell cultures, hindering the comparison of pMMO activity between cultures. Therefore, membranes from the wild-type and mutant strains were isolated for further characterization.

^{13}C methane oxidation activity assays were performed on as-isolated membranes from WT and PmoB Y374A strains using NADH and duroquinol as reductants at 30 °C (Fig. 6.4). Surprisingly, the NADH-dependent specific activity of as-isolated membranes from the Y347A variant (20.1 $\pm$ 0.41 nmol ^{13}C methanol$\cdot$min$^{-1}\cdot$mg^{-1} protein) was much higher than that of the WT
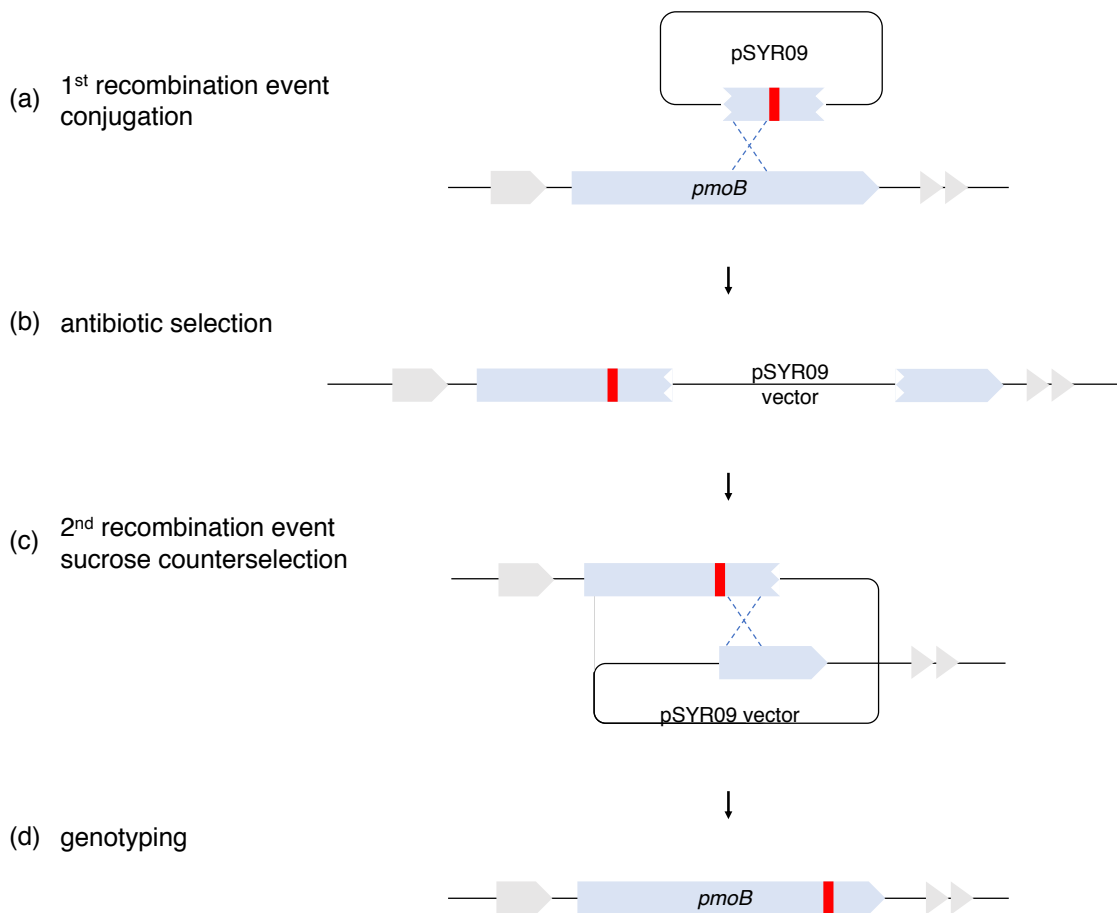
Figure 6.2. Site directed mutagenesis of PmoB Y374 in *Mm. buryatense* 5GB1C.
Following conjugation between the *E. coli* S17 donor strain and *Mm. buryatense* 5GB1C, the plasmid containing the mutation in PmoB Y374 **a**, integrates into the genome of *Mm. buryatense* 5GB1C during the 1st recombination event and successful transconjugants are isolated via **b**, antibiotic selection. Introduction of **c**, a counterselection (3% sucrose) induces the 2nd recombination event, which removes the plasmid backbone but **d**, introduces the SNP into the genome.

Table 6.1. Primers for cloning.

Plasmid	DNA part	Primer sequences	Template
pSYR09	vector	**F:** 5'-ATGTGCAGGTTGTCGGTGTC-3' **R:** 5'-TGGTAACTGTCAGACCAAGTTTACTC-3'	pCM433 kanT
	insert	**F:** 5'-ACTTGGTCTGACAGTTACCAATACTGGTGCCG CAAGCCTGT-3' **R:** 5'-GACACCGACAACCTGCACATTTTGGTGGCTCGA TTGACAGGT-3'	5GB1C gDNA
pSYR09 Y374A		**F:** 5'-TTCTGACGCAGCATGGGAAGTTGCCCGTT TAGCTGACTTG-3' **R:** 5'-CAAGTCAGCTAAACGGGCAACTTCCCATGC TGCGTCAGAA-3'	pSYR09
pSYR09 Y374F		**F:** 5'-TGACGCAGCATGGGAAGTTTTCCGTTTAGCTGAC-3' **R:** 5'-GTCAGCTAAACGGAAAACTTCCCATGCTGCGTCA-3'	pSYR09
sequencing		**F:** 5'-AAGGCGGTGGTCCTATCATTGG-3' **R:** 5'-GCGGTTTTTCAATCAAAAGGGA-3'	colony pcr
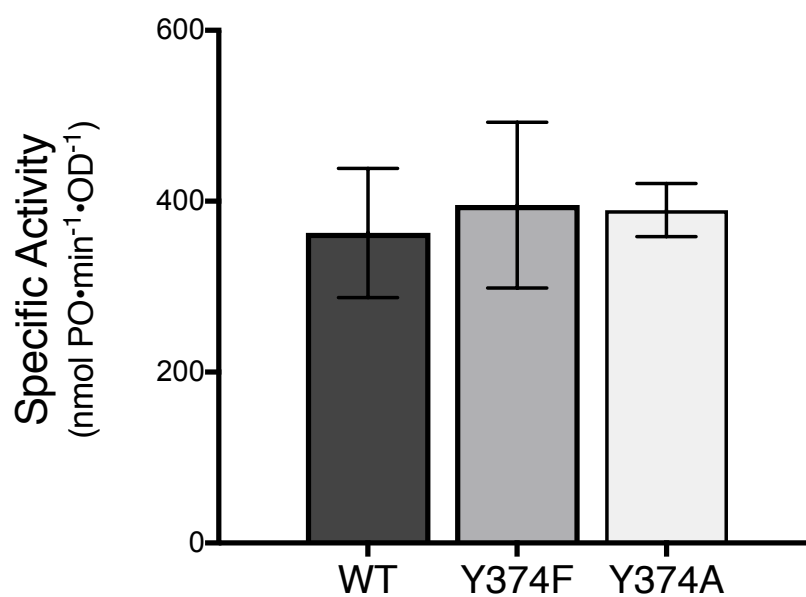
Figure 6.3. Whole-cell propylene oxidation activity assay.
Specific activity of *Mm. buryatense* 5GB1C WT, Y374F, and Y374A variants are shown in nmol propylene oxide·min^{-1}·OD^{-1}. Error bars represent standard deviation of n=3.
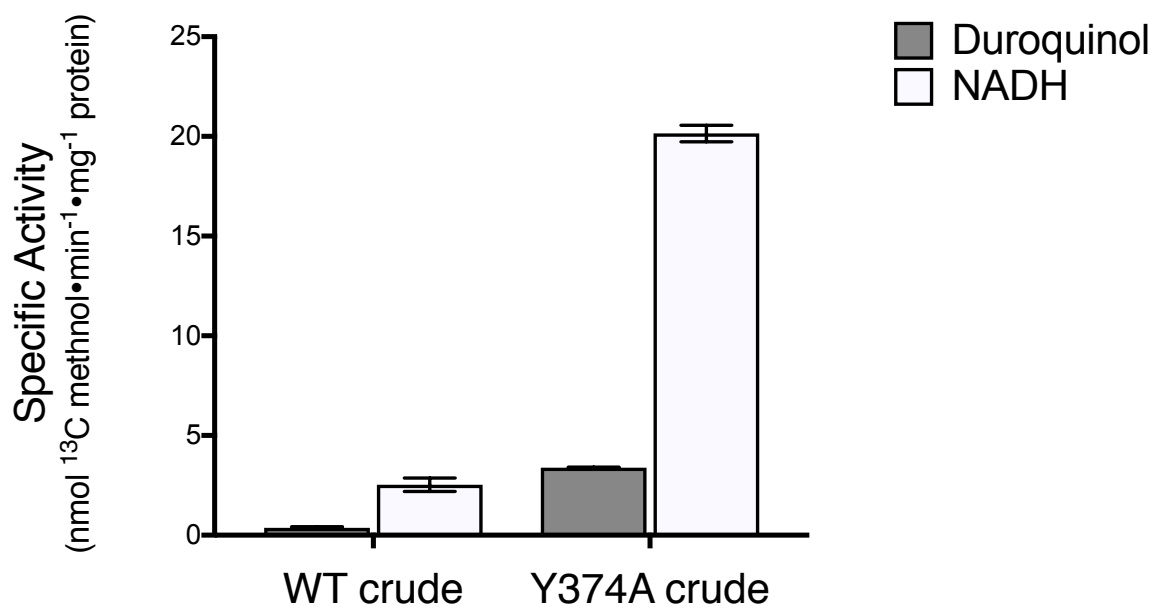
Figure 6.4. ^{13}C methane oxidation activity assay.
Specific activity of *Mm. buryatense* 5GB1C membrane-bound WT and Y374A pMMO are shown in nmol ^{13}C methanol·min^{-1}·mg^{-1} protein for reductants duroquinol (*gray*) and NADH (*white*). Error bars represent standard deviation of individual samples of n=3.

membranes (3.4 nmol ^{13}C methanol·min^{-1}·mg^{-1} protein). Additionally, the enhanced activity of PmoB-Y374A is one of highest values measured at 30°C, on par with Rockwell-pMMO (20 ± 3 nmol of methanol·min^{-1}·mg^{-1} protein using NADH as a reductant)[10]. The highest reported activity is from Bath-pMMO performed at 45°C using NADH (130 nmol ^{13}C methanol·min^{-1}·mg^{-1} protein)[10]. PmoB residue 374 in Rockwell-pMMO is a glutamate, but there is a tyrosine residue at position 341, 5.3 Å from the copper ion in the Cu$_B$ site. Nonetheless, Tyr 374 is nonessential for 5G-pMMO function.

Crystal structures of 5G-pMMO WT and the PmoB Y374A variant

To investigate the enhanced activity exhibited by the PmoB Y374A variant, we determined the crystal structures of both WT and PmoB-Y374A pMMOs to 2.2 Å and 2.8 Å resolutions, respectively (Table 6.1). The 5G-pMMO WT structure represents the highest resolution pMMO structure to date. Both pMMOs were crystallized in conditions containing ammonium sulfate as the precipitant, and exhibit similar overall architecture to other published pMMO structures, with an $\alpha_3\beta_3\gamma_3$ trimeric structure. Similar to the 20Z-pMMO structure[7], there is a single protomer in the asymmetric unit (Fig. 6.5). Eight Cymal 5 molecules are modeled in the protomer, including 3 near the PmoA-PmoB interface, 2 near the PmoA-PmoC interface, and 3 in PmoC.

Comparisons of previous pMMO structures show various conformations of the PmoC subunit. The PmoC metal binding site can be occupied by zinc[6,8-10] or copper or, in the case of 20Z-pMMO, disordered[6-10]. In 5G-pMMO WT, this site does not contain a metal ion. Instead, a 20 Å chain of electron density found in this location was modeled as Cymal 5 (Fig. 6.6a), the detergent used for crystallization. Of the three conserved PmoC metal binding residues, His 132

Table 6.2. Data collection and refinement statistics for 5G-pMMO WT and Y374A variant.
Values in parentheses refer to the highest resolution shell

	5G-pMMO WT	5G-pMMO WT (Cu anomalous)	5G-pMMO Y374A	5G-pMMO Y374A (Cu anomalous)
Data collection				
Space group	$P6_3$	$P6_3$	$P6_3$	$P6_3$
Cell dimensions				
a, b, c	142.98, 142.98, 146.46	142.7, 142.7, 146.34	142.65, 142.65, 146.31	142.89, 142.89, 146.41
α, β, γ	90, 90, 120	90, 90, 120	90, 90, 120	90, 90, 120
Resolution	2.20 (2.28-2.20) Å	3.10 (3.21-3.10) Å	2.80 (2.85-2.80) Å	3.20 (3.31-3.20) Å
Wavelength	0.97872 Å	1.37760 Å	1.078123 Å	1.377602 Å
R_{pim}	0.039 (0.949)	0.033 (0.265)	0.034 (0.278)	0.045 (0.264)
R_{meas}	0.117 (2.48)	0.051 (0.383)	0.112 (0.981)	0.138 (0.787)
$CC_{1/2}$	0.998 (0.660)	0.999(0.904)	0.998 (0.876)	0.998 (0.993)
$I/\sigma I$	274 (10)	13.5 (1.3)	27 (2.0)	17.6 (2.6)
Completeness	99.6% (98%)	99.9% (99.5%)	98.4% (81.4%)	99.1% (92.2 %)
Redundancy	9.1 (6.0)	6.8 (5.7)	11.7 (8.2)	9.3 (6.8)
Anisotropy correction				
Anisotropic truncation limit	2.5, 2.5, 2.2 Å		3.1, 3.1, 2.8 Å	
Completeness	68.5%		79.95%	
Refinement				
No. of reflections	58,619		30,360	
R_{work}/R_{free}	0.230/0.263		0.212/0.258	
Average B-factor ($Å^2$)	30.87		42.39	
Root mean square deviations				
Bond lengths (Å)	0.005 Å		0.010 Å	
Bond angles (°)	0.860°		1.189°	
Ramachandran favored	94.49%		90.81%	
Ramachandran allowed	4.53%		7.72%	
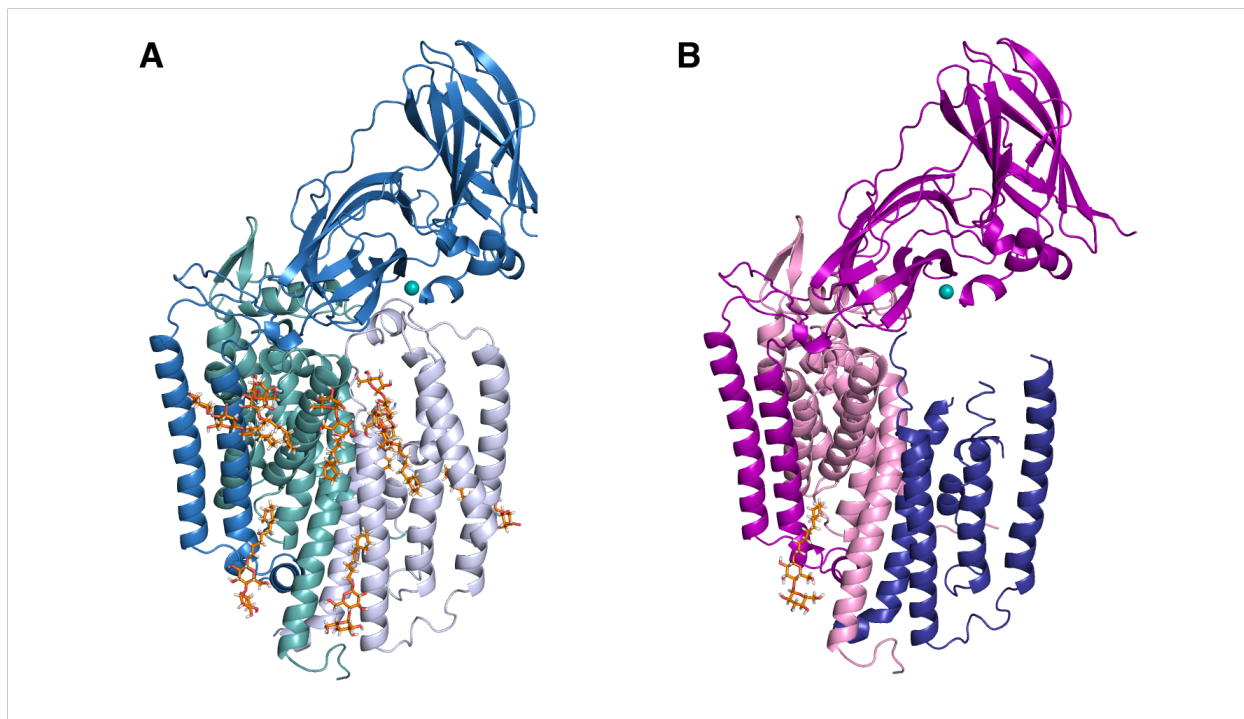
Figure 6.5. Crystal structures of 5G-pMMO WT and Y374A.
A, A protomer of 5G-pMMO WT with PmoB, PmoA, and PmoC shown in *blue*, *green*, and *white*, respectively. ***B,*** A protomer of 5G-pMMO PmoB Y374A variant with PmoB, PmoA, PmoC shown in *purple*, *pink*, and *blue*, respectively. The copper ion and Cymal-5 are shown as a *teal* sphere and *orange* sticks, respectively.
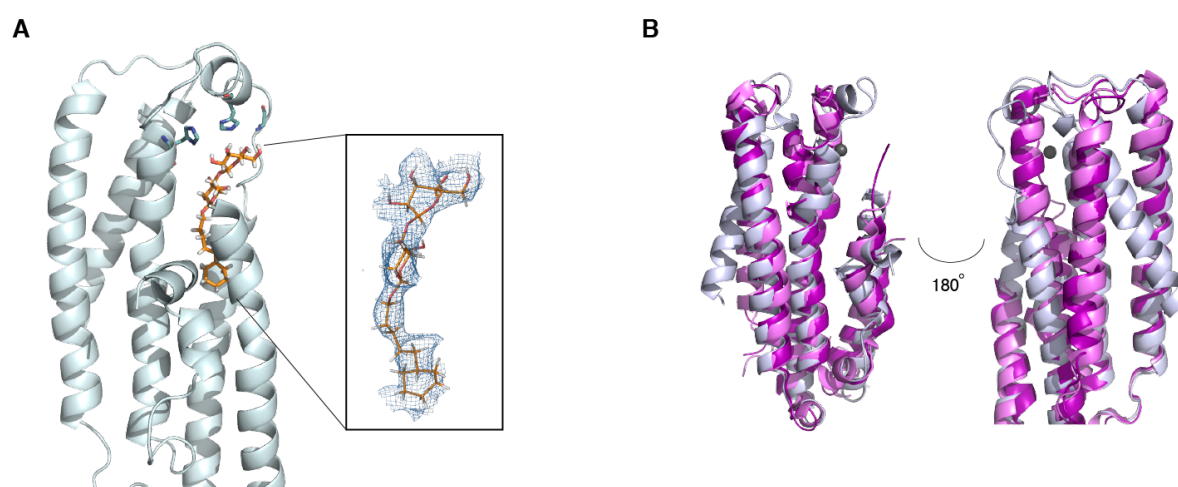
Figure 6.6. The PmoC subunit in 5G-pMMO WT.
A, 5G-PmoC colored *white* with Cymal 5 molecule colored *orange*. Inset depicting $2F_o$ - F_c map (*blue*, 1.0σ) modeled as Cymal 5. **B**, Superposition of PmoC from Bath- (*purple*), Rockwell- (*pink*) and 5G-pMMO (*white*).

interacts with the polar head of Cymal 5. The presence of this detergent molecule causes a tilt of the PmoC transmembrane helices composed of residues 24-44, 56-86, and 144-170 relative to those in Bath-pMMO with a rmsd value of 4.961 Å for 178 C-α atoms (Fig. 6.6b). In comparison, PmoC from Rockwell- and Bath-pMMO superimpose with a rmsd value of 1.770 Å for 191 C-α atoms. The functional relevance of this conformation remains unclear, but indicates that this subunit is flexible under detergent-solubilized conditions. In the Y374A variant, the residues surrounding the PmoC metal center are disordered (Fig. 6.5b), similar to 20Z-pMMO, with assigned residues 58-130, 146-194, and 219-250. 5G-pMMO WT has assigned PmoC residues 23-194 and 219-250. This may be due to the crystal quality since the better diffracting WT crystals (< 2.5 Å) show more electron density in PmoC.

The Cu$_B$ and bis-His sites of 5G-pMMO WT and Y374A are similar to those in 20Z-pMMO (Fig. 6.7). 5G-pMMO lacks electron density attributed to copper in the nonconserved PmoB metal site coordinated by His 48 and His 72 observed only in Bath-pMMO[6]. The conserved PmoB copper site coordinated by residues His 33, His 137, and His 139 can only be modeled with one copper ion for both variants, also similar to 20Z-pMMO. The copper distances to His 33 δN, His 137 δN, His 139 ϵN, and the His 33 N-terminal nitrogen are 2.6, 2.0, 2.0, and 2.3 Å, respectively. EXAFS analysis of 5G-pMMO WT suggests a lack of short range Cu-Cu scattering (Fig. 6.8, Table 6.), consistent with the observed crystal structure.

In the structure of the Y374A variant, PmoB residue 374 is clearly an alanine, in agreement with DNA sequencing (Fig. 6.9a-b). Mutation of Tyr to Ala increases the size of a cavity near the PmoB metal center (Fig. 6.9c-d). The change in cavity size may be responsible for affecting
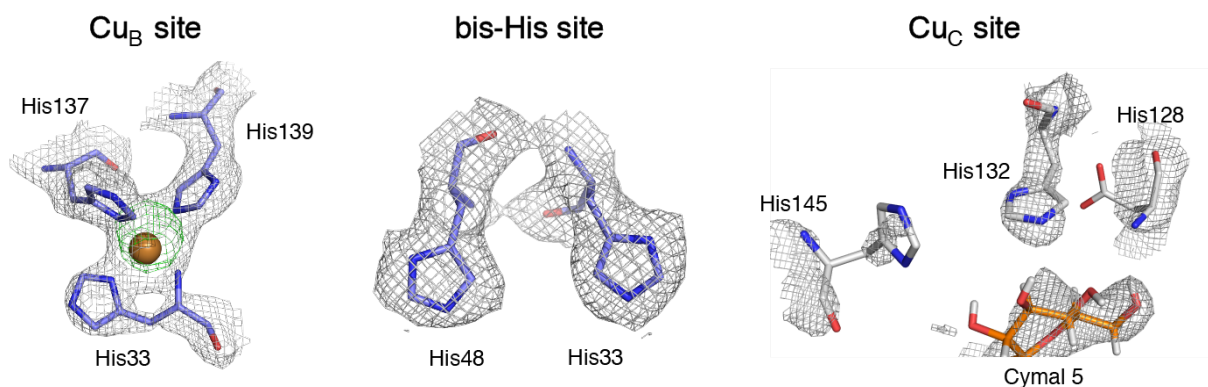
Figure 6.7. The metal centers of 5G-pMMO.
The following metal centers of 5G-pMMO are depicted with ligands: Cu_B site coordinated by His 33, His 137, and His 139 (*blue*); bis-His sites with residues His 48 and His 72 (*blue*); Cu_C site with residues Asp 128, His 132, and His 145 (*gray*). Copper ions, water, and Cymal 5 are shown in *teal*, *red*, and *orange*, respectively. The copper anomalous difference density map (*green*,12σ) is superimposed on the $2F_o$ - F_c map (*gray*, 1.0σ).
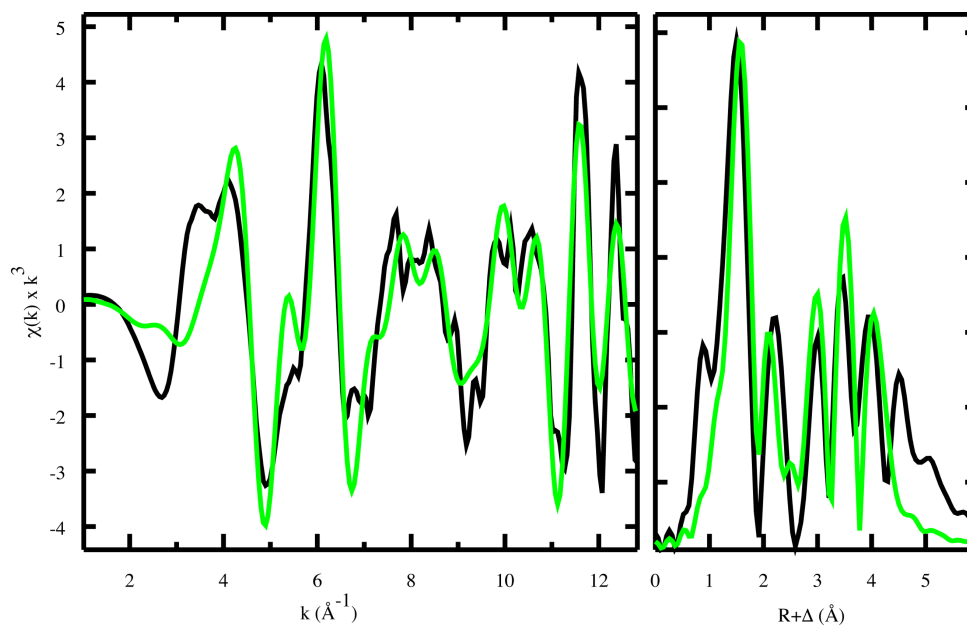
Figure 6.8. EXAFS analysis of 5G-pMMO WT.
The EXAFS spectrum is shown in the left panel, and the Fourier transform of the EXAFS is shown in the right panel. Raw unfiltered data are shown in *black*, and the best fit simulations are shown in *green*.

Table 6.3. Summary of the best fit Cu EXAFS simulations for 5G-pMMO WT sample.
EXAFS were fit over the k range of 1.0 - 12.85 Å^{-1}.

Sample	Atom[b]	R(Å)[c]	C.N.[d]	$\sigma^{2\,e}$	Atom[b]	R(Å)[c]	C.N.[d]	$\sigma^{2\,e}$	F'[f]
	Nearest Neighbor Ligand Environment[a]				**Long Range Ligand Environment[a]**				
5G-pMMO	O/N	1.97	2.0	5.11	C	2.57	2.0	4.57	0.70
					C	3.39	3.0	2.33	
					C	3.94	5.0	1.69	
					C	4.47	5.0	0.79	

[a] Independent metal-ligand scattering environment
[b] Scattering atoms: O (oxygen), N (nitrogen), Cu (copper)
[c] Average metal-ligand bond length from two independent samples
[d] Average metal-ligand coordination number from two independent samples
[e] Average Debye-Waller factor in Å^2 x 10^3 from two independent samples
[f] Number of degrees of freedom weighted mean square deviation between data and fit.
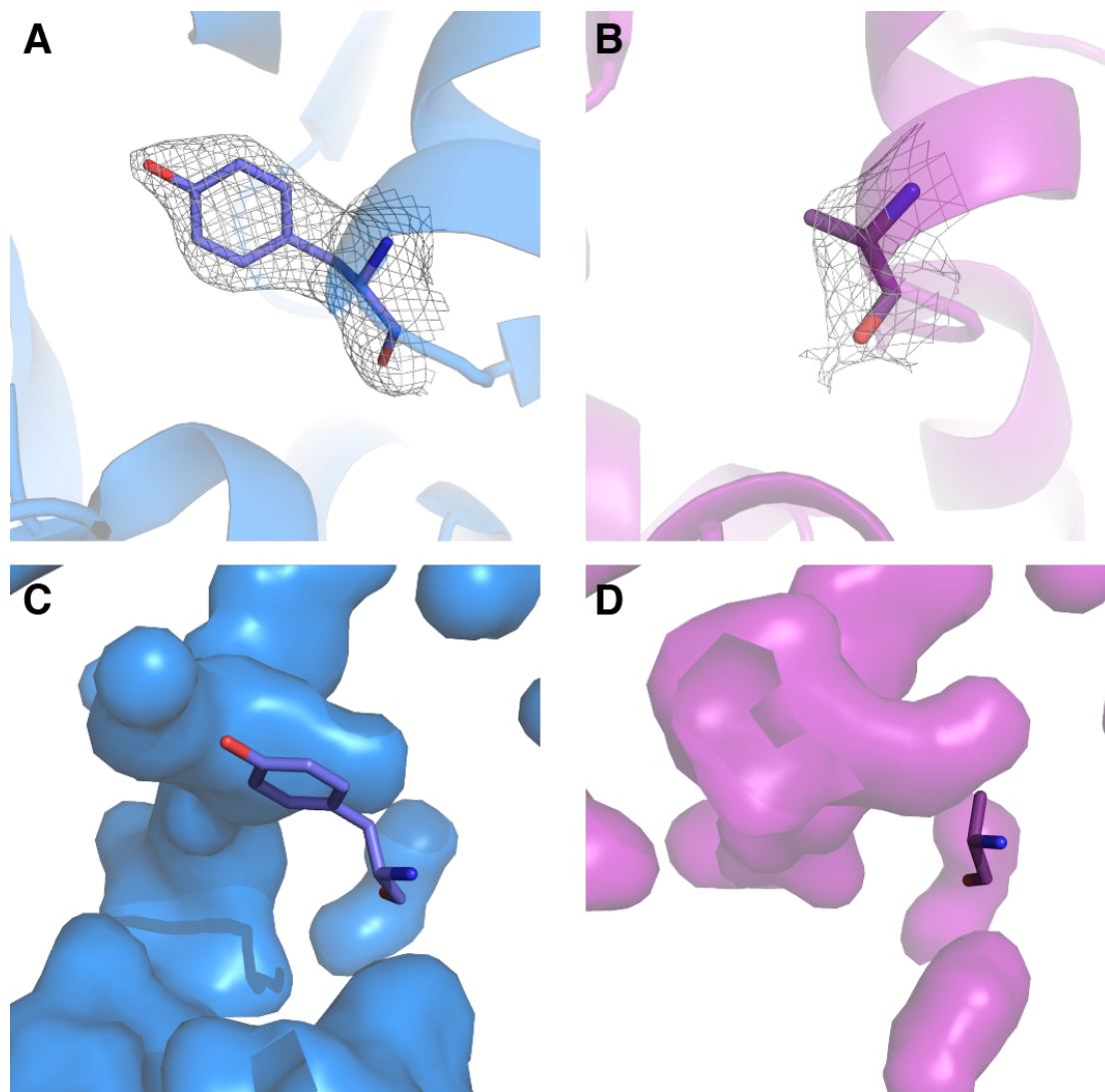
Figure 6.9. Residue 374 of PmoB in 5G-pMMO.
2F$_o$ - F$_c$ map (*gray*, 1.0σ) residue 374 in PmoB for **A**, WT (*blue*) and **B**, the Y374A (*purple*) Pymol was used to depict the cavity near Y374 in the crystal structure for **C**, WT (*blue*) and **D**, the Y374A (*purple*).

activity, which has been reported in flavodiirion oxygen reductase[207]. The Y271S mutant of flavodiirion oxygen reductase from *E. histolytica* (*Eh*Fdp1) exhibits higher O_2 reductase activity than WT but faster inactivation after turnover with O_2. The authors speculate Tyr may stabilize the protein turnover with O_2 by preventing formation of reactive intermediates via controlling substrate access to the active site, and as a result sacrifices catalytic efficiency for preservation of activity. Y271S also exhibits higher NO reductase activity, suggesting Tyr may be involved in substrate specificity. A conserved Tyr has been implicated in substrate specificity in tyrosine hydroxylase (TYH), a non-heme iron enzyme that converts tyrosine to dihydroxyphenylalanine (DOPA)[208]. Mutation of a conserved Tyr 4.5 Å in the iron site to Phe slightly increases V_{max}, eliminating an essential catalytic role. More interestingly, this mutant exhibits higher affinity for phenylalanine than the WT enzyme, suggesting Tyr is involved in substrate specificity by affecting the overall active site structure. In the case of PmoB Y374, the location of the active site has yet to be determined. Hence the possibility of the cavity near the PmoB copper site as the substrate binding site is entirely speculative. In hydrocarbon monooxygenase (HMO), mutagenesis of HmoC residue 139 (Bath-pMMO numbering) to Asp (A139D) shifted the substrate preference of HMO away from longer alkanes[20]. The analogous site in pMMO may be involved in substrate binding.

Alternatively, the hydroxyl group of this tyrosine residue may be linked to electron transfer from or to the active site, like the Tyr in the C_H site in TβM[203]. Additional mutagenesis experiments are required to determine if the enhanced activity is attributed to changes in the cavity or electron transfer. Y374F is a good candidate since phenylalanine closely resembles the structure of tyrosine and maintains the cavity size, but lacks the hydroxyl group involved in electron transfer.

Furthermore, a PmoC D140A variant should be created to determine effects on pMMO substrate specificity. Characterization of these variants will be pursued in future experiments.

METHODS

Mm. buryatense 5GB1C mutagenesis

The *pmoB* gene (METBUDRAFT_3705) (DNA positions 612-1621) was amplified from *Mm. buryatense* 5GB1C gDNA using the primers listed in Table 6.3. The PCR product was inserted into plasmid pCM433kanT (Addgene) via Gibson assembly and transformed into *E. coli* TOP10 cells to produce plasmid pSYR09. Y374 in *pmoB* was mutated to alanine or phenylalanine using the QuikChange Lightening Multi Site-Directed Mutagenesis Kit (Agilent) and the primers listed in Table 6.3 to produce pSYR09_Y374A and pSYR09_Y374F. The two plasmids were transformed into *E. coli* S17-1 cells. Each *E. coli* S17-1 strain was mated with *Mm. buryatense* 5GB1C cells as described previously[45]. Briefly, *Mm. buryatense* 5GB1C cells and *E. coli* S17-1 were plated on top of each other on modified nitrate mineral salts (NMS2) mating agar plates, and placed in plate incubators under a 1:1 methane-to-air gas ratio for 2 days. Mated cells were plated on NMS2 selection agar plates containing 50 µg/mL of kanamycin and 25 µg/mL of rifamycin. These selection plates were also incubated under a 1:1 methane-to-air gas ratio for 1 week until colonies were visible. Colonies were picked and plated onto NMS2 counter selection plates containing 3% sucrose and 25 µg/mL of rifamycin. Colonies from counter selection plates were re-streaked onto NMS2 agar plates (no antibiotic, no sucrose), followed by genotyping via colony PCR using the primers listed in Table 6.3 to confirm successful mutagenesis.

Growth of *Mm. buryatense* 5GB1C

Mm. buryatense 5GB1C cells were cultured as described previously[36]. Briefly, *Mm. buryatense* 5GB1C cells were grown in 12 L fermenter growths in 1X NMS2 media, 130 mM NaCl, 2.3 mM phosphate buffer, and 50 mM carbonate buffer, pH 9.5, supplemented with 40 μM $CuSO_4$ and 1X trace elements solution (500X stock concentration is 1.0 g/L $Na_2 \cdot EDTA$, 2.0 g/L $FeSO_4 \cdot 7H_2O$, 0.8 g/L $ZnSO_4 \cdot 7H_2O$, 0.03 g/L $MnCl_2 \cdot 4H_2O$, 0.03 g/L H_3BO_3, 0.2 g/L $CoCl_2 \cdot 6H_2O$, 0.02 g/L $NiCl_2 \cdot 6H_2O$, 0.05 g/L $Na_2MoO_4 \cdot 2H_2O$). The 12 L cultures were inoculated at an OD_{600} of 0.1–0.2. All cells were cultured at 300 rpm under a methane-to-air gas ratio of 1:3 at 30 °C. Cells were harvested when the OD_{600} reached ~ 10 and centrifuged for 30 min at 8000×g at 4 °C. Pelleted cells were flash frozen in liquid nitrogen and stored at − 80 °C.

Membrane isolation

Cell pellets (15 g) were resuspended in 150 mL of 25 mM PIPES, 250 mM NaCl, pH 7.0, supplemented with EDTA-free protease inhibitor tablets (Roche) and a scoop of DNAse (Sigma). Cells were manually stirred for resuspension on ice. The cell resuspension was sonicated at 4 °C for 2.0 min with an on/off interval of 1 sec/ 3 sec at amplitude of 25% and centrifuged at 12,000 x g for 1 hr to remove cell debris. The supernatant was centrifuged at 100,000 x g for 1 hr to isolate the pelleted membranes containing pMMO. The membrane pellet was washed 2-3 times with a Dounce homogenizer in 25 mM PIPES, 250 mM NaCl, pH 7.0. 1 mL aliquots of pMMO-containing membranes at a total protein concentration of ~10 mg/mL (measured by Bio-Rad DC Assay) were flash frozen in liquid nitrogen and stored at -80°C.

5G-pMMO purification

Membranes were solubilized using 1.2 mg of n-dodecyl-β-D-maltopyranoside (DDM) (Anatrace) per 1 mg of crude protein at 4 °C for 1 hr. The solubilized protein was centrifuged at 100,000 x g for 1 hr, and the supernatant was collected for purification. Solubilized 5G-pMMO was buffer exchanged into 25 mM PIPES, 50 mM NaCl, pH 7.0, 0.02% DDM using a 100 kDa MW cutoff Amicon (Millipore). pMMO was purified using a 15Q anion exchange column (GE Healthcare) and eluted using a 50 mM – 800 mM NaCl gradient. Eluted 5G-pMMO was concentrated using a 100 kDa MW cutoff Amicon to 10 mg/mL in 25 mM PIPES, 250 mM NaCl, pH 7, 0.12% Cymal-5.

Crystallization and structural determination of 5G-pMMO variants

5G-pMMO crystals were obtained from sitting drops containing 1 μL of 10 mg/mL protein in 25 mM PIPES, 250 mM NaCl, pH 7, 0.12% Cymal-5, and 1 μL of 2.2-2.6 M AmSO4, 0.1 M Tris, pH 8. Crystals were transferred into a saturated LiSO4 cryoprotectant solution, harvested, and flash frozen in liquid nitrogen. Crystals were screened for diffraction at the LS-CAT beamlines at the Advanced Photon Source at Argonne National Laboratory. Data sets were processed using HKL2000[87]. Anisotropic processing using the UCLA anisotropy server[88] was found to improve the electron density maps. Phenix[89] was used for molecular replacement with the Bath-pMMO coordinates as a starting model (PDB accession code 3RGB) to solve the structure of 5G-pMMO. 5G-pMMO has 71%:78%:75% identity to the Bath-pMMO PmoB, PmoA, and PmoC subunits, respectively. Structure modeling and refinement were performed using Coot[90] and Phenix[89], and model quality was assessed using MolProbity[91]. The final model for the 5G-pMMO structure includes PmoB residues 33-414, PmoC residues 23-194 and 219-250, PmoA residues 4-245, 1 copper ion, 8 Cymal 5 molecules, 1 sulfate ion, and 56 water molecules. The final model for the

5G-pMMO PmoB-Y374A variant includes PmoB residues 33-414, PmoC residues 23-130 and 137-250, PmoA residues 4-245, 1 copper ion, and 1 sulfate ion.

XAS analysis of 5G-pMMO WT

Purified 5G-pMMO samples were concentrated to 233 μM using a 100 kDa MW cutoff Amicon and diluted in 30 % glycerol. Copper stoichiometric value for 5G-pMMO was 1.75 Cu eq per protomer. Samples were loaded into Lucite cells wrapped with Kapton tape, flash frozen in liquid nitrogen, and stored at – 80 °C. XAS data collection and analysis were conducted as previously described[7].

[13]C methane oxidation activity assay

Methane oxidation activity assays of 5G-pMMO crude membranes were performed as described previously[7]. pMMO membranes (~5 mg/mL) were resuspended in 25 mM PIPES, pH 7.2, 250 mM NaCl in 100 μL reaction volumes containing NADH (4 mg/mL) in 2 mL screw top vials sealed with septa (Agilent). A 1 mL volume of headspace gas was withdrawn from the vial and replaced with 1.5 mL of ^{13}C methane gas (Sigma-Aldrich). All reactions were performed at 30 °C and 200 rpm for 5 min. The reactions were placed on ice for 5 min followed by quenching with 500 μL of chloroform containing 1 mM dichloromethane. The reaction was vortexed at 2,000 rpm for 10 min and centrifuged at 2,000 x g for 30 min. 2.5 μL of the chloroform mixture was injected into a PoraBOND Q column (25 m x 250 μm x 3 μm) on an Agilent 7890B/5977A MSD GC/MS instrument with a split ratio of 10:1. The column was under a constant flow of 1.2 mL/min of helium gas. The GC protocol was as follows: oven temperature was maintained at 80 °C for 3.5

min, ramped 50 °C/min to 150 °C and held for 1.5 min, and then ramped 15 °C/min to 300 °C and held for 1 min. The MS instrument protocol was as follows: 230 °C ion source temperature, 150 °C quad temperature, 70 eV, and a detector voltage of 2,999 V. Ion masses 31, 33, and 49 were monitored for detection of ^{12}C methanol, ^{13}C methanol, and dichloromethane with dwell times of 10 ms, 100 ms, and 10 ms, respectively. ^{13}C methanol concentrations were quantified using a standard calibration curve and the dichloromethane internal standard.

CHAPTER 7: ADDITIONAL WORK AND PROSPECTUS

INTRODUCTION

Particulate methane monooxygenase (pMMO) has been investigated using various biochemical and advanced spectroscopic techniques[3]. However, pMMO characterization has been immensely limited by the lack of pMMO mutagenesis studies, mostly due to difficulties perturbing the *pmo* operon. All previous attempts to knock out the *pmo* operon or the individual subunits have failed to produce viable mutant strains. These studies have been performed by multiple laboratories in many methanotroph species grown under copper-depleted or methanol-supplemented conditions. This difficulty has led to ongoing speculation that the presence of pMMO is required even under copper-depleted conditions in which pMMO is nonfunctional and cell growth is dependent on soluble methane monooxgyenase (sMMO). By contrast, there is a working system for homologous expression of sMMO variants in *Ms. trichosporium* OB3b[178]. This system has been recently utilized to investigate regioselectivity[43,175,176] and transcriptional activation[209,210] of sMMO.

Fortunately, genetic tools for methanotroph mutagenesis have improved in recent years. There are optimized methods for genome editing and replicative plasmids used in *Methylomicrobium*[50,52] species as well as a CRISPR-Cas9 system developed in *Mcc. capsulatus* (Bath)[51]. These advanced genetic tools are especially attractive for pMMO studies; *Methylomicrobium* has only one copy of the *pmo* operon which simplifies the mutagenesis process, and *Mcc. capsulatus* (Bath) expresses the best characterized pMMO with the highest enzymatic activity. Hence this chapter focuses on creating pMMO variants in *Mm. buryatense* 5GB1C and *Mcc. capsulatus* Bath that perturb the residues surrounding the metal centers. These efforts include

introduction of an affinity tag to PmoB, mutagenesis of the metal binding centers in PmoB, and characterization of a pMMO natively lacking the PmoB metal binding residues.

INTRODUCING AN AFFINITY TAG IN PMOB

While pMMO comprises a significant fraction of the total protein present in methanotroph membranes, protein purification from the native organism has limited pMMO biochemical characterization. Bottom-up MS analysis of as-isolated membranes shows the presence of many other membrane proteins[38], including other metalloproteins that interfere with pMMO spectroscopic studies[11,211]. These contaminating proteins are difficult to purify out from pMMO due to the detergent solubilization step required for further purification. All proteins present in the membrane are surrounded by detergent micelles that add approximately 75,000 Da in size, limiting the separation ability of size exclusion chromatography. Introducing isoelectric based chromatography before size exclusion does slightly increase purity, but fails to remove all the contaminating metalloproteins[7]. Additionally, in some cases, it is difficult to separate pMMO embedded nanodiscs from empty nanodiscs, which reduces the quality of pMMO-nanodisc samples and subsequent EM data collection. Hence, introduction of an affinity tag in the *pmo* operon is an attractive strategy to improve protein purity for downstream applications.

pMMO from *Mcc. capsulatus* Bath (Bath-pMMO) exhibits the highest activity and is the most studied pMMO, and was therefore chosen to be tagged via integration of dsDNA containing the affinity tag sequence into the genome. The C-terminus of PmoB was selected as the best candidate to attach the affinity tags, due to exposure of the C-terminus to the outside environment based on the crystal structure (3RGB). 6xHis and Strep were chosen as tag candidates and were preceded by TEV or enterokinase cleavage sites.

To introduce a tag at the C-terminus of PmoB, DNA parts were constructed in the following order: homology arm 1000 bp upstream from *pmoB2*, kanamycin resistance gene (*kanR*), *E. coli* terminator (*rrnB*), affinity tag sequence, cleavage sequence, *pmoB2* (MCA 2853), and homology arm 1000 bp downstream of *pmoB2*. In total, four DNA constructs containing different combinations of affinity tag + cleavage sequence were designed and assembled via yeast assembly[212] to create plasmids p368.17-20 (Fig. 7.1).

All four DNA constructs were transformed into *Mcc. capsulatus* (Bath) cells with 10 μM copper in the growth media. This strategy was used to confirm that the introduction of the affinity tag at the C-terminus of PmoB did not affect pMMO expression and activity. *Mcc. capsulatus* (Bath) transformants were obtained for two of the constructs, both of which contained the Strep-tag. It is unclear if the lack of 6xHis-tag colonies is due to perturbed pMMO function or transformation probability. The Strep-tagged strains were expanded into liquid media supplemented with copper to confirm pMMO function and stored for future cell growth and purification trials.

INTRODUCING SNPS TO THE METAL BINDING RESIDUES IN PMOB

The mutagenesis experiment above showed that introducing SNPs at the end of the *pmoB* gene was feasible. Therefore, the strategy was then used to test if SNPs could be introduced towards the beginning of the *pmoB* gene where the PmoB metal binding residues are located. To introduce SNPs in the metal binding regions of PmoB, DNA parts were constructed in the following order: homology arm 1000 bp upstream from *pmoB*, kanamycin resistance gene (*kanR*), *E. coli* terminator (*rrnB*), *pmoB* gene with SNPs, homology arm 1000 bp downstream of *pmoB*

p368.17: GS linker + Enterokinase cleavage sequence + 6xHis-tag
p368.18: GS linker + Enterokinase cleavage sequence + Strep-tag
p368.19: GS linker + TEV cleavage sequence + 6xHis-tag
p368.20: GS linker + TEV cleavage sequence + Strep-tag
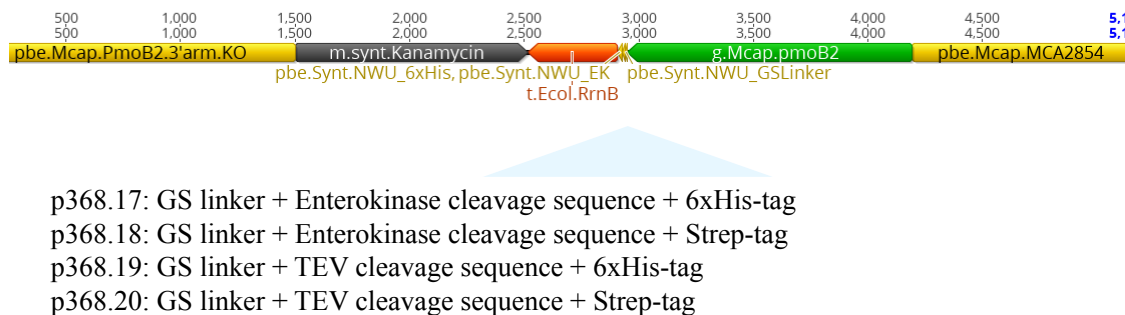
Figure 7.1. DNA construct for the introduction of affinity tags on pMMO.
DNA parts are depicted as arrows facing in the direction of transcription. Four different combinations of cleavage and affinity tag sequences are located between the *rrnB* and *pmoB2* genes. A Gly-Ser (GS) linker was inserted before the cleavage-tag sequence.

(Fig. 7.2). The parts were assembled via yeast assembly to create plasmids p368.13-16. containing the following mutations in PmoB, respectively: H33A, H139A; H33A, H137A; H137A, H139A; H33A, H137A, H139A.

All four constructs were transformed into *Mcc. capsulatus* (Bath) cells in copper-depleted conditions to switch to sMMO-driven cell growth. Transformants were obtained for three DNA constructs and colony PCR sequenced. Interestingly, the transformants integrated the DNA construct in the proper position in the genome but lacked the SNPs. This event is most likely due to the long homology region upstream of the metal binding SNPS in the *pmoB2* gene. Since the SNPs are unfavorable for pMMO function and cell growth, double recombination using the upstream *pmoB* gene is favored (Fig. 7.2). This transformation result suggests that introduction of downstream SNPs via dsDNA integration is not an efficient strategy. Hence, efforts to mutate the metal binding residues are underway using other advanced genome editing methods.
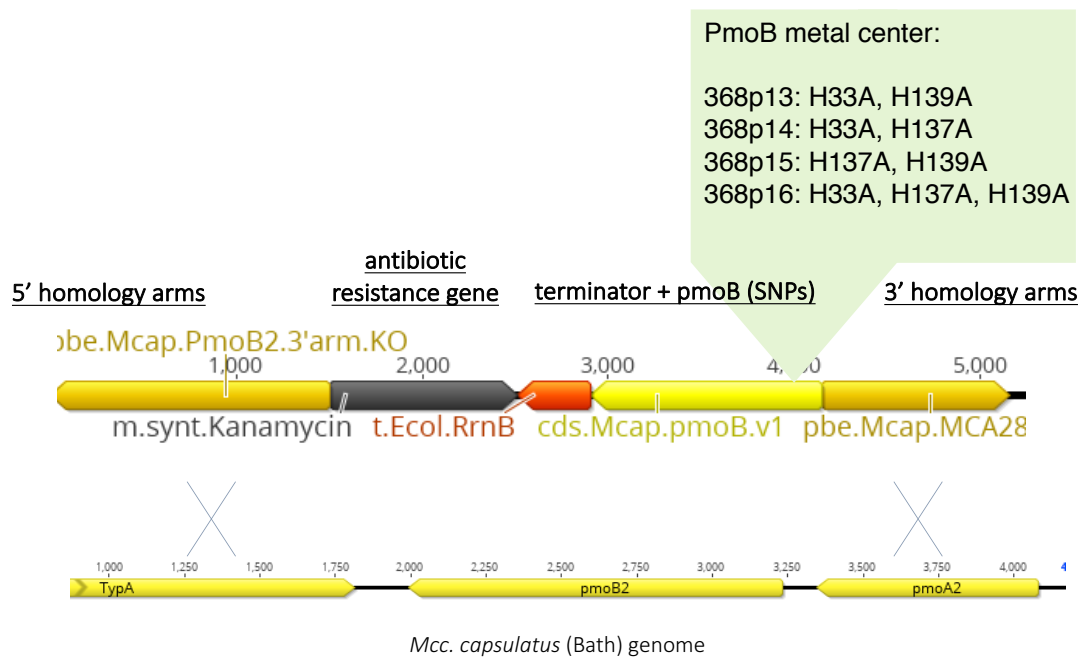
Figure 7.2. DNA construct for mutagenesis of the PmoB metal binding residues.
DNA parts are depicted as arrows facing in the direction of transcription. The *pmoB2* DNA part contains four different combinations of SNPs of the PmoB metal binding residues.

CHARACTERIZATION OF PMMO FROM *MA. KAMCHATKENSE* KAM1, A PMMO LACKING THE CONSERVED PMOB METAL CENTER

Mutagenesis of the metal binding residues in pMMO has been unsuccessful in multiple methanotroph species. While efforts are still underway in *Mcc. capsulatus* (Bath), there is an alternative approach to investigate the metal centers of pMMO individually. *Methylacidiphilum (Ma.) kamchatkense* Kam1 is an extremophile within the *Verruomicrobia* phylum that grows at pH 3.5 and 55°C[213]. Like other methanotrophs, *Ma. kamchatkense* Kam1 has multiple copies of the *pmo* operon in its genome and can use methane as its only carbon source[214]. There are three copies of the full *pmoCAB* operon in its genome, in addition to *pmoCA4* and a lone *pmoC5*; *pmoCAB2* has highest transcription level during growth on methane.

However, *Ma. kamchatkense* Kam1 lacks both the RuMP and serine cycles present in methanotrophic metabolism that allow for carbon assimilation from methane[215]. Instead, studies suggest that in the *Methylacidiphilum* genus, methane is converted to CO_2, which is then assimilated via the Calvin Benson cycle[124]. Furthermore, *Ma. kamchatkense* Kam1 lacks *mxaF* in the genome, which encodes for a Ca^{2+}-dependent methanol dehydrogenase (MxaF), and so requires the expression of XoxF, a lanthanide-dependent methanol dehydrogenase.

Importantly, the His residues coordinating the conserved PmoB metal center are not encoded by the *pmoB* genes of *Ma. kamchatkense* Kam1. H33, H137, and H139 are replaced by a methionine, proline, and glycine residue, respectively[124]. The absence of these residues presents a unique opportunity to investigate a PmoB metal center knockout without the need for mutagenesis. The isolated pMMO from *Ma. kamchatkense* Kam1 could provide an opportunity to study the PmoC metal center individually, to identify the active site, and to obtain insight into the role of the PmoB metal center.

Small scale characterization of *Ma. kamchatkense* Kam1 pMMO

Ma. kamchatkense Kam1 cells were grown in 50 mL cultures in P14 pH 3.5 media (Table 7.1)[216]. 50 mL cultures stalled growth at OD_{600} < 0.5, which is 25% of the biomass from other methanotrophs grown in the lab. These saturated cultures were used to inoculate a 1 L culture to increase biomass. When the 1 L culture saturated at OD_{600} ~ 0.4, cell pellet was harvested and lysed to obtain the protein supernatant. Bottom-up mass spectrometry analysis show the presence of PmoB in the supernatant (Figs. 7.3). Furthermore, these cultures were grown with methane as the sole carbon source, suggesting expression of functional pMMO. Unfortunately, membranes could not be isolated from 1 L cultures due to low biomass yields.

Optimization of large *Ma. kamchatkense* Kam1 cell growths

Supplementing the gas feed with CO_2 has been shown to increase *Ma. kamchatkense* Kam1 cell growth. Saturated 50 mL cultures were used to inoculate a 2.0 L culture in a bioreactor that was fed a continuous 1:3 methane-to-air gas ratio, in which the air tank contained 5% CO_2. The pH of the P14 media was adjusted from 3.5 to 4.5 to decrease risk of vessel corrosion. Additionally, the media was supplemented with 10 μM $CuSO_4 \cdot 5H_2O$ and 2.5 μM $LaCl_3 \cdot 7H_2O$. The final OD_{600} of the 2 L bioreactor growth was ~0.6 (Fig. 7.4a), which was used to inoculate a 12 L fermenter growth using P14 pH 4.5 media supplemented with 10 μM $CuSO_4 \cdot 5H_2O$ and 1.0 μM $LaCl_3 \cdot 7H_2O$. The culture stalled at OD_{600} of 1.0, which was not enough biomass for pMMO characterization (Fig. 7.4b).

Table 7.1. *Ma. kamchatkense* **Kam1 media recipe.**

1X P14 media: (1 L in dH$_2$O)

Component	Amount (grams)	Conc in solution
NaH$_2$PO$_4$ · H$_2$O	0.17799 g	1 mM
MgCl$_2$ · 6H$_2$O	0.04066 g	0.2 mM
Na$_2$SO$_4$	0.14204 g	1 mM
K$_2$SO$_4$	0.348518 g	2 mM
(NH$_4$)$_2$SO$_4$	0.26428 g	2 mM

Adjust to pH 3.5 using H$_2$SO$_4$ and autoclave

1000X Trace elements: (1 L in dH$_2$O)

Component	Amount (grams)	Conc in solution
NiCl$_2$ · 6H$_2$O	0.2377 g	1 mM
CoCl$_2$ · 6H$_2$O	0.23793 g	1 mM
Na$_2$MoO$_4$ · 2H$_2$O	0.24195 g	1 mM
ZnSO$_4$ · 7H$_2$O	0.28756 g	1 mM
FeSO$_4$ · 7H$_2$O	2.7801 g	10 mM
CuSO$_4$ · 5H$_2$O	2.4968 g	10 mM
Nitrilotriacetic acid	8.6013 g	45 mM

Adjust pH to 3.5 using NaOH and sterile filter

0.5 M CaCl$_2$ · 2H$_2$O
50 mM LaCl$_3$ · 7H$_2$O

Final media for 50 mL cultures:

Components	Volume	Final conc
1X P14 pH 3.5	1000 mL	
1000X Trace elements	1 mL	
0.5 M CaCl$_2$ · 2H$_2$O	400 μL	
50 mM LaCl$_3$ · 7H$_2$O	10 μL	0.5 μM

Final media for bioreactor and fermenter growths:

Components	Volume	Final conc
1X P14 pH 3.5	1000 mL	
1000X Trace elements	1 mL	
0.5 M CaCl$_2$ · 2H$_2$O	400 μL	
50 mM LaCl$_3$ · 7H$_2$O	20 μL	1 μM
100 mM CuSO$_4$ · 5H$_2$O	250 μL	25 μM

Ga0070832_101169 (100%), 46,590.9 Da
pmoB particulate methane monooxygenase PmoB subunit apoprotein
22 exclusive unique peptides, 35 exclusive unique spectra, 67 total spectra, 262/420 amino acids (62% coverage)

```
M K K L V R V G G A    I L L S G L M L A P    M S S L F A V Q G M    G A K S Q E A F L R
M R T V T F F D T R    F S F T P S N R V K    V G D E F T C T G K    V M L M P T W P Q E
I P F S G I S F F N    F F V P G P Q V L R    K A I F V N E K Y F    Q F N S V V L E K G
G V Y E Y K M I N Q    A R T P G I W P V G    P M V S M E E A G P    F I G P E E F L T I
E G S G A G F T N P    V K T L L G N T I D    L E N Y G E G R M I    A W T L L T S A I A
V V W L V Y W C S K    P F T R R L G L V A    A G R K E D L F S P    M D R Q V C F L F T
I G T I V L V A A A    A M I T K A Q Y P I    T I P I Q E T K Y Y    I K P L P P E P A L
I Q A E V T D A T Y    D V P G R T L S F H    L Q V K N I G D K P    V V L K E F L T A N
V R F L N P D V P G    N T W N E N Y P E V    N G G P M R V T P S    E P I N P G E T K T
L E V S M Q S A E W    E N Q R L T M Y H E    S T N R F G G L L F    F T D T S G T R Q V
F A I A D Q I V I P    K F G A T M G G G M
```

Figure 7.3. Bottom-up MS peptide coverage of Kam1-PmoB from lysate.
The full PmoB protein sequence is shown, with amino acids in detected peptides highlighted in *yellow*. Green represent oxidation and deamination resulting from the harsh conditions from sample preparation.

a

b
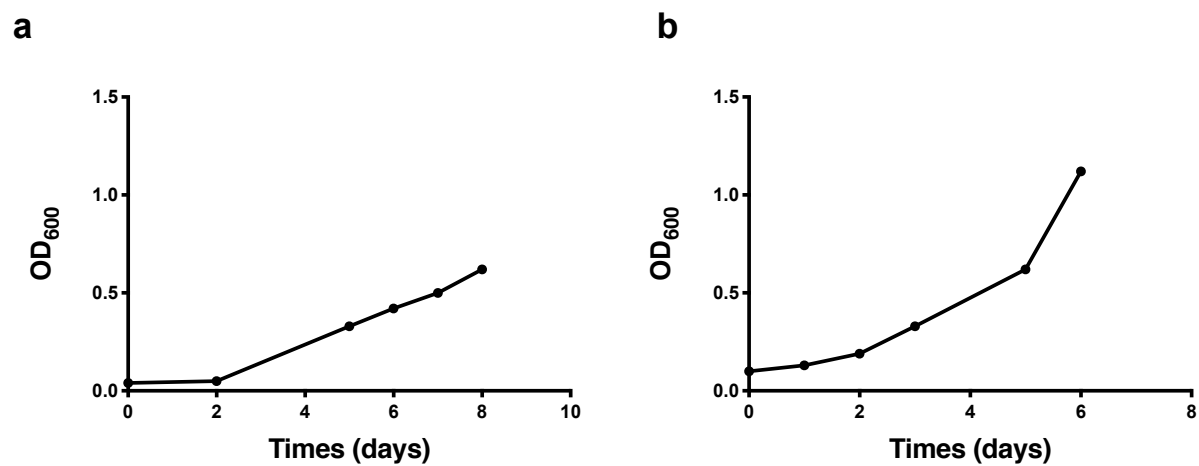
Figure 7.4. *Ma. kamchatkense* Kam1 large scale growths at pH 4.5.
Growth curves for **a**, 2 L bioreactor and **b**, 12 L fermenter growths in pH 4.5 media. The optical density (OD_{600}) at each timepoint (days) is shown as *black* dots.

Hence, a second round of scaling up was performed using P14 media at pH 3.5 supplemented with 10 μM $CuSO_4 \cdot 5H_2O$ and 1.0 μM $LaCl_3 \cdot 7H_2O$. While the cells can grow at pH 4.5, it is not their optimal growth condition. Adjusting the pH back to 3.5 with CO_2 supplementation drastically improved cell growth, in which the 2 L bioreactor reached OD_{600} of ~ 4.8. To further scale up, bioreactor cultures were used to inoculate the 12 L fermenter that was also fed with a gas mixture supplemented with CO_2. The 12 L fermenter growth yielded 30 g of wet cell pellet, which was enough biomass for initial cell lysis and membrane isolation. The final OD_{600} stalled at 3.0 (Fig. 7.5). Future efforts to monitor and maintain the pH at 3.5 during fermenter growths may improve cell yield.

Kam1-pMMO purification and activity

SDS-PAGE analysis of as-isolated membranes from the Kam1 cell pellet shows protein bands corresponding to the three pMMO subunits (Fig. 7.6). Gel bands were submitted for bottom-up mass spectrometry for protein identification (Figs. 7.7-7.8). Solubilization of membranes in DDM and subsequent purification on a Superdex 200 size exclusion column shows that pMMO can be extracted from the membranes and elutes in the same volume range as other pMMOs on the sizing column (Fig. 7.9).

Next, ^{13}C methane oxidation activity assays were performed on as-isolated membranes at pH 7.0 using NADH as reductant. No activity was detected. ICP-OES analysis of the as-isolated membranes showed < 0.5 Cu bound per pMMO protomer, which is significantly lower than other pMMO membranes[7,10] (Table 7.2). A second membrane sample was then prepared with exogenous copper (0.5 mM) added during cell lysis. ICP-OES analysis of the copper-supplemented

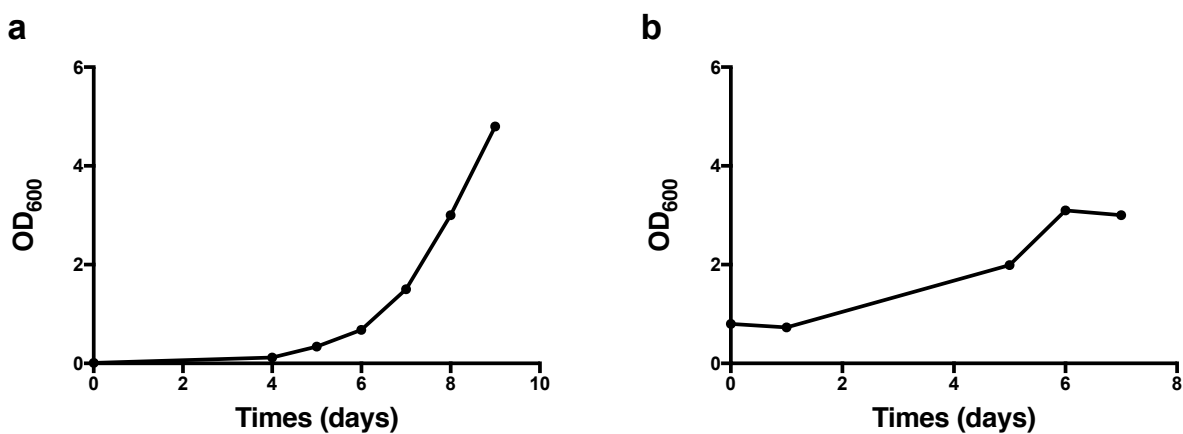**Figure 7.5. *Ma. kamchatkense* Kam1 large scale growths at pH 3.5.**
Growth curves for **(a)** 2 L bioreactor and **(b)** 12 L fermenter growths in pH 3.5 media. The optical density (OD_{600}) at each timepoint (days) is shown as *black* dots.
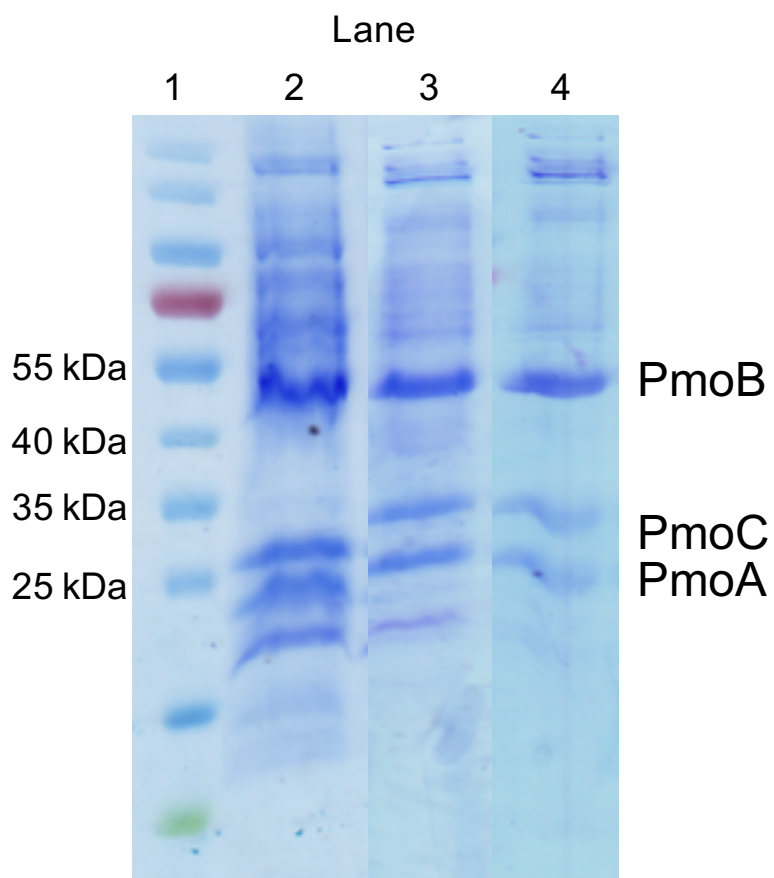
Figure 7.6. SDS-PAGE gel of Kam1-pMMO samples.
Lane 1, MW markers; lane 2, Kam1 crude membranes; lane 3, solubilized Kam1-pMMO in DDM; lane 4, purified Kam1-pMMO in DDM.

	Experiment: 19-1486-S		99% probability, 2 peptide minimum, displaying Total Spectrum Count

Probability Legend:

over 95%	(green)
80% to 94%	(yellow)
50% to 79%	(orange)
20% to 49%	(red)
0% to 19%	(white)

| #	Visible?	Starred?	Bio View: Identified Proteins (318) Including 1 Decoy	Accession Number	Alternate ID	Molecular Weight	Protein Grouping Ambiguity	IGD	IGD
	✓	☆	pmoB particulate methane monooxygenase PmoB subunit apoprotein	Ga0070832_101169		47 kDa		96	
	✓	☆	groL chaperonin GroEL	Ga0070832_10226		59 kDa		14	
	✓	☆	dnaK molecular chaperone DnaK	Ga0070832_10224		70 kDa		12	
	✓	☆	hpr formate dehydrogenase	Ga0070832_101339		44 kDa		3	
	✓	☆	Tubulin like	Ga0070832_101176		115 k...			
	✓	☆	mreB rod shape-determining protein MreB	Ga0070832_102268		41 kDa		17	
	✓	☆	Glycine/serine hydroxymethyltransferase	Ga0070832_10361		80 kDa		2	
	✓	☆	ketol-acid reductoisomerase	Ga0070832_102243		38 kDa		1	
	✓	☆	Nucleoside-diphosphate-sugar epimerase	Ga0070832_103133		37 kDa		9	
	✓	☆	Isoleucyl-tRNA synthetase	Ga0070832_102205		104 k... ★			
	✓	☆	rpoA DNA-directed RNA polymerase subunit alpha	Ga0070832_101220		38 kDa		18	16
	✓	☆	aspartate aminotransferase	Ga0070832_101287		43 kDa		7	29
	✓	☆	groS chaperonin GroES	Ga0070832_10225		11 kDa			34
	✓	☆	degQ serine protease Do	Ga0070832_102274		56 kDa		8	23
	✓	☆	spoVK proteasome-associated ATPase	Ga0070832_101402		63 kDa		3	27
	✓	☆	Methyltransferase domain-containing protein	Ga0070832_103275		47 kDa		13	16
	✓	☆	guaB IMP dehydrogenase	Ga0070832_102109		42 kDa		3	33
	✓	☆	glucose-6-phosphate 1-dehydrogenase	Ga0070832_101172		60 kDa			21
	✓	☆	nuoD NADH-quinone oxidoreductase subunit D	Ga0070832_10278		47 kDa		15	2
	✓	☆	Glyoxylase, beta-lactamase superfamily II	Ga0070832_10334		30 kDa			27
	✓	☆	UDP-N-acetylglucosamine 1-carboxyvinyltransferase	Ga0070832_103177		45 kDa		14	14
	✓	☆	nucleoside diphosphate kinase	Ga0070832_101288		44 kDa		11	13
	✓	☆	aspartate aminotransferase	Ga0070832_10384		41 kDa		1	26
	✓	☆	fbaA2 fructose-bisphosphate aldolase	Ga0070832_102144		36 kDa			24
	✓	☆	clpA ATP-dependent Clp protease ATP-binding subunit ClpC	Ga0070832_102105		94 kDa		1	25
	✓	☆	isoamylase	Ga0070832_101323		81 kDa			25
	✓	☆	rfaG Glycosyltransferase involved in cell wall bisynthesis	Ga0070832_101329		44 kDa		18	2
	✓	☆	cysK cysteine synthase A	Ga0070832_10293		34 kDa		1	28
	✓	☆	aspartate semialdehyde dehydrogenase	Ga0070832_101200		36 kDa		0	21
	✓	☆	malate dehydrogenase (NAD)	Ga0070832_101284		33 kDa			23
	✓	☆	glpX fructose-1,6-bisphosphatase II	Ga0070832_101297		40 kDa		2	24
	✓	☆	Xaa-Pro aminopeptidase	Ga0070832_1029		42 kDa		8	0
	✓	☆	L-2-hydroxyglutarate oxidase	Ga0070832_103130		45 kDa		13	
	✓	☆	recA recombination protein RecA	Ga0070832_10178		37 kDa		6	15
	✓	☆	nusA NusA antitermination factor	Ga0070832_103147		47 kDa		8	2
	✓	☆	alcohol dehydrogenase, propanol-preferring	Ga0070832_103137		36 kDa			19
	✓	☆	phosphoribosylamine--glycine ligase	Ga0070832_102256		48 kDa			21
	✓	☆	N-ethylmaleimide reductase	Ga0070832_103127		42 kDa			18
	✓	☆	mcsB arginine kinase	Ga0070832_102106		41 kDa		6	5
	✓	☆	transcriptional regulator of molybdate metabolism, XRE family	Ga0070832_101256		43 kDa		8	2
	✓	☆	glgC glucose-1-phosphate adenylyltransferase	Ga0070832_10251		49 kDa			16
	✓	☆	phenylacetaldehyde dehydrogenase	Ga0070832_103265		58 kDa			20
	✓	☆	ibpA HSP20 family protein	Ga0070832_103260		19 kDa		1	12
45	✓	☆	hypothetical protein	Ga0070832_10362		18 kDa		9	1
46									

Ga0070832_101169 (100%), 46,590.9 Da
pmoB particulate methane monooxygenase PmoB subunit apoprotein
23 exclusive unique peptides, 40 exclusive unique spectra, 96 total spectra, 282/420 amino acids (67% coverage)

```
M K K L V R V G G A    I L L S G L M L A P    M S S L F A V Q G M    G A K S Q E A F L R
M R T V T F F D T R    F S F T P S N R V K    V G D E F T C T G K    V M L M P T W P Q E
I P F S G I S F F N    F F V P G P Q V L R    K A I F V N E K Y F    Q F N S V V L E K G
G V Y E Y K M I N Q    A R T P G I W P V G    P M V S M E E A G P    F I G P E E F L T I
E G S G A G F T N P    V K T L L G N T I D    L E N Y G E G R M I    A W T L L T S A I A
V V W L V Y W C S K    P F T R R L G L V A    A G R K E D L F S P    M D R Q V C F L F T
I G T I V L V A A A    A M I T K A Q Y P I    T I P I Q E T K Y Y    I K P L P P E P A L
I Q A E V T D A T Y    D V P G R T L S F H    L Q V K N I G D K P    V V L K E F L T A N
V R F L N P D V P G    N T W N E N Y P E V    N G G P M R V T P S    E P I N P G E T K T
L E V S M Q S A E W    E N Q R L T M Y H E    S T N R F G G L L F    F T D T S G T R Q V
F A I A D Q I V I P    K F G A T M G G G M
```

Figure 7.8. Bottom-up MS peptide coverage of Kam1-PmoB from crude membranes.
The full PmoB protein sequence is shown, with amino acids in detected peptides highlighted in
yellow. Green represent oxidation and deamination resulting from the harsh conditions from
sample preparation.
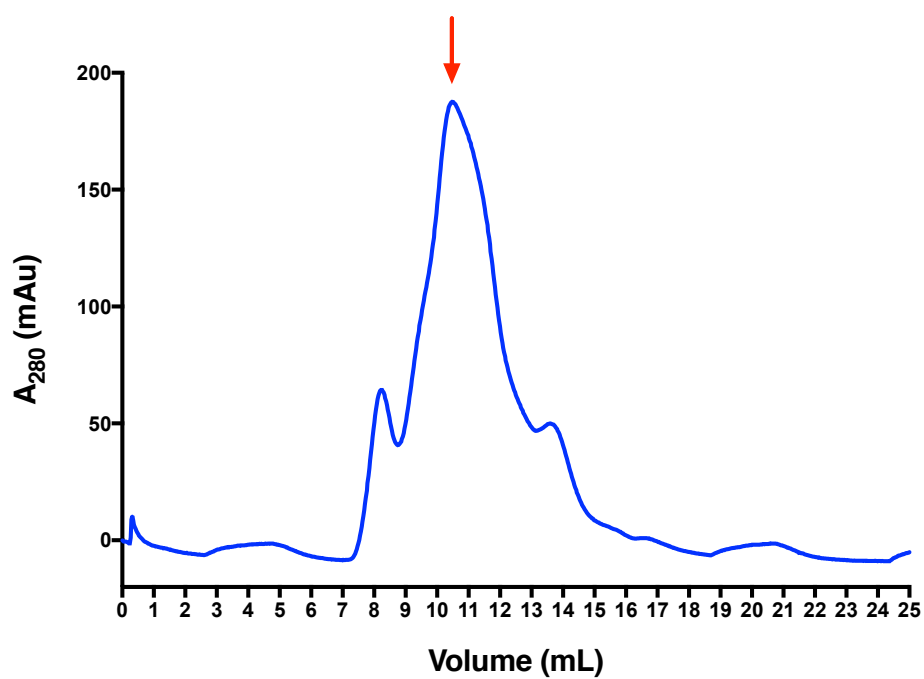
Figure 7.9. Purification of Kam1-pMMO.
The Superdex 200 size exclusion chromatography purification is shown with Kam1-pMMO labeled (red arrow). The absorbance at 280 nm (A_{280}) is shown in blue.

membranes showed ~6.5 copper ions bound per pMMO protomer (Table 7.2), which is significantly higher in copper content than the first isolation. However, methane oxidation activity at pH 7.0 was still not detected. An initial protein purification using PIPES buffer at pH 4.0 yielded membranes with very low pMMO yield. It is possible that the proteins precipitated in this buffer condition. PIPES is not a buffer at pH 4 so a different buffer should be selected for pH-dependent activity assays. Future directions include optimization of buffer conditions and copper reconstitution to produce active pMMO membranes.

METHODS

Ma. kamchatkense **Kam1 cell growth**

50 mL cultures of *Ma. kamchatkense* Kam1 cells (Kam1-cells), generously provided by the Birkeland group, were grown in 250 mL Erlenmeyer flasks and septa. All 50 mL cultures were grown in P14 liquid media (Table 3) at pH 3.5 and fed a 1:3 methane-to-air gas ratio once a week at 55°C and 200 rpm. Excess sparging is not recommended, as accumulation of CO_2 in the headspace is required for cell growth. Each 50 mL culture was maintained for 1 month, followed by passaging 5 mL of culture into new 45 mL of P14 liquid media. Freezing of cells is not recommended, due to poor cell recovery after a freeze-thaw cycle. Hence cells are perpetually passaged in 50 mL cultures on a monthly basis. If cultures become contaminated or fail to grow, it is necessary to use backup 50 mL cultures or contact the Birkeland group at University of Bergen for new cell stocks.

Table 7.2. ICP-OES analysis of Kam1-pMMO.

	Cu eq. per protomer
Kam1 crude	0.50[*]
Kam1 solubilized	0.45[*]
Kam1 purified	0.44[*]
Kam1 crude #2	6.45

*=ICP values were below lowest standard concentration

To scale up, 2.0 L Kam1 cultures were grown in bioreactors. 2x 50 mL saturated cultures were used to inoculate 2.0 L of P14 media (pH 3.5) supplemented with 10 μM CuSO$_4$·5H$_2$O and 1 μM LaCl$_3$. Culture were fed with a continuous 1:3 methane-to-air gas ratio at a flow rate of 1 L/min at 55°C. For bioreactor growths, the air tank is supplemented with 5% CO$_2$ to improve cell yield. The CO$_2$/air gas line can be easily connected to the flow meters that serve the bioreactor or the fermenter, using a wrench to remove the house-air gas line and to replace with the CO$_2$/air gas line. Before each line swap, make sure to close the tanks, house-air valve, and the swagelok valves on the CO$_2$/air and house-air gas lines. The final gas concentrations flowing through the culture are 25% CH$_4$, 3.75% CO$_2$, 15% O$_2$, and the rest N$_2$.

For fermenter growths, the Kam1 cells grown in the bioreactor were used to inoculate 12 L cultures in P14 media (pH 3.5) supplemented with 10 μM CuSO$_4$·5H$_2$O and 1 μM LaCl$_3$ at OD$_{600}$ of 0.2. The cultures were fed a continuous 1:3 methane-to-CO$_2$/air gas ratio at 1.2 L/min at 55°C and 300 rpm. When cells reached stationary phase, cells were harvested via centrifugation at 8,000 xg for 30 min at 4°C. Cell pellets were flash frozen in liquid nitrogen and stored at - 80 °C.

Kam1 crude membrane isolation

Cell pellets (8 g) were resuspended in 60 mL of 25 mM PIPES, 250 mM NaCl, pH 7.0, supplemented with EDTA-free protease inhibitor tablets (Roche) and a scoop of DNAse (Sigma). The cell resuspension was sonicated at 4 °C for 3.5 min with an on/off interval of 1 sec/ 3 sec at amplitude of 25% and centrifuged at 12,000 x g for 1 hr to remove cell debris. The supernatant was centrifuged at 100,000 x g for 1 hr to isolate the pelleted membranes containing pMMO. The membrane pellet was washed 2-3 times with a Dounce homogenizer in 25 mM PIPES, 250 mM

NaCl, pH 7.0. 1 mL aliquots of crude membranes were flash frozen in liquid nitrogen and stored at - 80°C. Copper content was determined by ICP-OES at the Northwestern Quantitative Bio-imaging Center, and copper standards ranging from 0 – 500 ppb (Inorganic Ventures) were used for quantification.

Kam1-pMMO purification

Membranes were solubilized using 1.2 mg of n-dodecyl-β-D-maltopyranoside (DDM) (Anatrace) per 1 mg of crude protein at 4 °C for 1 hr in 25 mM PIPES, 250 mM NaCl, pH 7, 0.02% DDM. The solubilized protein was centrifuged at 100,000 x g for 1 hr, and the supernatant was collected for purification. Solubilized Kam1-pMMO concentrated using a 100 kDa MW cutoff Amicon (Millipore) and loaded onto a Superdex 200 size exclusion chromatography column (GE Healthcare). Eluted Kam1-pMMO was concentrated using a 100 kDa MW cutoff Amicon in 25 mM PIPES, 250 mM NaCl, pH 7.0, 0.02% DDM, flash frozen in liquid nitrogen and stored at - 80°C.

Bottom-up proteomics/ in-gel protein sequencing analysis

Protein identity was confirmed by in-gel protein sequencing mass spectrometry at Northwestern University's Proteomics Core. Excised gel bands were washed in 100 mM ammonium bicarbonate (AmBic)/acetonitrile (ACN) and reduced with 10 mM dithiothreitol at 50 °C for 30 min. Cysteines were alkylated with 100 mM iodoacetamide in the dark for 30 min at room temperature. Gel bands were washed again in 100 mM AmBic/ACN prior to adding 600 ng trypsin for overnight incubation at 37 °C. The supernatant, which now contained peptides, was saved into a new tube. The remaining gel bands were then washed at room temperature for 10 min

with gentle shaking in 50% ACN/5% formic acid (FA), and this solution was combined with the peptide solution. The wash step was repeated using 80% ACN/5% FA followed by 100% ACN. All supernatant was added to the peptide solution, which was then dried using a speed-vac. After lyophilization, peptides were reconstituted with 5% ACN/0.1% FA in water and injected onto a trap column (150 µm ID × 3 cm, in-house packed with ReproSil C18aq 3 µm) coupled with a Nanobore analytical column (75 µm ID × 10.5 cm, PicoChip column packed with ReproSil C18aq, 1.9 µm) (New Objectives, Inc., Woburn, MA). Samples were separated using a linear gradient of solvent A (0.1% formic acid in water) and solvent B (0.1% formic acid in ACN) over 60 min using a Dionex UltiMate 3000 Rapid Separation nanoLC (ThermoFisher Scientific). MS data were obtained on a LTQ Velos Orbitrap (Thermo Fisher, San Jose, CA) mass spectrometer. The peptide sequences were compared to the UniProt *Ma. kamchatkense* Kam1 genome using Mascot 2.5.1 (Matrix Science, Boston, MA), and results were reported at 1% false discovery rate (FDR) in Scaffold 4.5 (Proteome Software, Portland, OR).

^{13}C methane oxidation activity assay

Methane oxidation activity assays of Kam1-pMMO crude membranes were performed as described previously[7]. pMMO membranes (~3 mg/mL) were resuspended in 25 mM PIPES, pH 7.2, 250 mM NaCl in 100 µL reaction volumes containing NADH (4 mg/mL) in 2 mL screw top vials sealed with septa (Agilent). A 1 mL volume of headspace gas was withdrawn from the vial and replaced with 1.5 mL of ^{13}C methane gas (Sigma-Aldrich). All reactions were performed at 30 °C and 200 rpm for 5 min. The reactions were placed on ice for 5 min followed by quenching with 500 µL of chloroform containing 1 mM dichloromethane. The reaction was vortexed at 2,000 rpm for 10 min and centrifuged at 2,000 x g for 30 min. 2.5 µL of the chloroform mixture was

injected into a PoraBOND Q column (25 m x 250 µm x 3 µm) on an Agilent 7890B/5977A MSD

GC/MS instrument with a split ratio of 10:1. The column was under a constant flow of 1.2 mL/min

of helium gas. The GC protocol was as follows: oven temperature was maintained at 80 °C for 3.5

min, ramped 50 °C/min to 150 °C and held for 1.5 min, and then ramped 15 °C/min to 300 °C and

held for 1 min. The MS instrument protocol was as follows: 230 °C ion source temperature, 150 °C

quad temperature, 70 eV, and a detector voltage of 2,999 V. Ion masses 31, 33, and 49 were

monitored for detection of ^{12}C methanol, ^{13}C methanol, and dichloromethane with dwell times of

10 ms, 100 ms, and 10 ms, respectively. ^{13}C methanol concentrations were quantified using a

standard calibration curve and the dichloromethane internal standard.

PROSPECTUS

Impact in bioinorganic chemistry and membrane biology

The copper-dependent mechanism of pMMO is one the biggest mysteries in bioinorganic chemistry. Various computational studies and characterization of synthetic complexes have tried to elucidate a copper active species in pMMO that can activate the strongest C-H bond in nature[15,21,24,217,218]. However, these studies are based on inconclusive models of the pMMO active site and on other copper enzymes that cannot oxidize methane. Hence, mechanistic investigation of pMMO is vital to this field. Additionally, the approaches used for pMMO studies have a broader impact in membrane biology and biochemistry. The successful use of membrane mimetics for pMMO emphasizes the importance of studying membrane proteins in a lipid bilayer context. Although that seems obvious, detergents are preferred due to ease of use and effectiveness in cost and time[64]. By using detergents, these studies forgo the possible contribution of the membrane to protein function and structure, thereby missing the greater picture. Methanotrophs express high amounts of intracytoplasmic membranes that house pMMO and are a good model for advanced whole-cell EM techniques to understand how bacteria can utilize complex membrane systems for growth.

Furthermore, nanodiscs are compatible with recent analytical and biophysical techniques. nTDMS provides the ability to localize metal ions that fills a gap in the traditional bioinorganic toolbox. Moreover, this technique can look for other cofactors, lipid stoichiometry, PTMs, and stable protein interacting partners. pMMO nanodisc complexes can also be subjected to Cryo-EM studies, which can test the resolution limits of this technique with the goal of visualizing the metal ions.

Lanthanides in biology

The discovery of XoxF first suggested that rare earth elements are not biologically inert. Since then, there has been great interest in investigating lanthanide-based biology. Lanthanide-dependent methylotrophy is more widespread among bacteria than previously thought. XoxF is present in *Burkholderiales*, rhizobial symbionts, recently discovered *Rokubacteria*, *Actinobacteria*, and *Firmicutes*[114]. This is actually not surprising as lanthanides are not rare elements and are abundant in the earth's crust. Hence other lanthanide binding proteins with novel biological functions are sure to be discovered in the future. Recently, Cotruvo et al. discovered a lanthanide binding protein LanM that exhibits 100 million-fold selectivity for Ln^{+3} binding[219] over Ca^{+2}. LanM contains a novel architecture of an EF-hand motif that contributes to this high selectivity. Furthermore, research groups are interested in using methylotrophs expressing XoxF to scavenge lanthanides from electronics due to diminishing global supply of rare earth metals and monopolization of this limited supply by one country. Overall, methanotrophs expressing both pMMO and XoxF are examples of bacteria with unique functions that are difficult to mimic, and the discovery of more organisms like them is tantalizing.

Metabolic engineering of methanotrophs

Methanotrophs are also a promising technology for bioremediation. As shale gas fracking becomes the main source for oil extraction, off-gas methane will be more available. Academic research groups and biotechnology companies are interested in using methanotrophs to convert methane to high commodity feedstocks[55]. With recent advances in genome engineering, more products are being developed for commercialization. This field relies heavily on metabolic modeling of methanotrophs. The understanding of pMMO function, its physiological reductant,

and copper acquisition is vital to the accuracy of these models. Additionally, engineering of pMMO and MDH activity is essential to improve product titer. Hence the contents of this dissertation and future pMMO investigation go hand-in-hand with the success of methanotroph metabolic engineering and gas-to-liquid technologies.

REFERENCES

1. Hanson, R. S. & Hanson, T. E. Methanotrophic bacteria. *Microbiol. Rev.* **60,** 439–471 (1996).

2. Semrau, J. D., DiSpirito, A. A. & Yoon, S. Methanotrophs and copper. *FEMS Microbiol. Rev.* **34,** 496–531 (2010).

3. Ross, M. O. & Rosenzweig, A. C. A tale of two methane monooxygenases. *J. Biol. Inorg. Chem.* **22,** 307–319 (2016).

4. Vorobev, A. V. *et al. Methyloferula stellata* gen. nov., sp. nov., an acidophilic, obligately methanotrophic bacterium that possesses only a soluble methane monooxygenase. *Int. J. Syst. Evol. Microbiol.* **61,** 2456–2463 (2011).

5. Kenney, G. E. & Rosenzweig, A. C. Methanobactins: maintaining copper homeostasis in methanotrophs and beyond. *J. Biol. Chem.* **293,** 4606–4615 (2018).

6. Lieberman, R. L. & Rosenzweig, A. C. Crystal structure of a membrane-bound metalloenzyme that catalyses the biological oxidation of methane. *Nature* **434,** 177–182 (2005).

7. Ro, S. Y. *et al.* From micelles to bicelles: effect of the membrane on particulate methane monooxygenase activity. *J. Biol. Chem.* **293,** 10457–10465 (2018).

8. Hakemian, A. S. *et al.* The metal centers of particulate methane monooxygenase from *Methylosinus trichosporium* OB3b. *Biochemistry* **47,** 6793–6801 (2008).

9. Smith, S. M. *et al.* Crystal structure and characterization of particulate methane monooxygenase from *Methylocystis* species strain M. *Biochemistry* **50,** 10231–10240 (2011).

10. Sirajuddin, S. *et al.* Effects of zinc on particulate methane monooxygenase activity and structure. *J. Biol. Chem.* **289,** 21782–21794 (2014).

11. Lieberman, R. L. *et al.* Characterization of the particulate methane monooxygenase metal centers in multiple redox states by X-ray absorption spectroscopy. *Inorg. Chem.* **45,** 8372–8381 (2006).

12. Culpepper, M. A., Cutsail, G. E., Gunderson, W. A., Hoffman, B. M. & Rosenzweig, A. C. Identification of the valence and coordination environment of the particulate methane monooxygenase copper centers by advanced EPR characterization. *J. Am. Chem. Soc.* **136,** 11767–11775 (2014).

13. Lieberman, R. L. *et al.* Purified particulate methane monooxygenase from *Methylococcus capsulatus* (Bath) is a dimer with both mononuclear copper and a copper-containing cluster. *Proc. Natl. Acad. Sci.* **100,** 3820–3825 (2003).

14. Balasubramanian, R. *et al.* Oxidation of methane by a biological dicopper centre. *Nature* **465,** 115–119 (2010).

15. Shiota, Y., Juhász, G. & Yoshizawa, K. Role of tyrosine residue in methane activation at the dicopper site of particulate methane monooxygenase: a density functional theory study. *Inorg. Chem.* **52,** 7907–7917 (2013).

16. Cao, L., Caldararu, O., Rosenzweig, A. C. & Ryde, U. Quantum refinement does not support dinuclear copper sites in crystal structures of particulate methane monooxygenase. *Angew. Chem. Int. Ed. Engl.* **47,** 483 (2017).

17.   Ross, M. O. *et al.* Particulate methane monooxygenase contains only monocopper centers. *Science*

18.   Yuan, H., Collins, M. L. P. & Antholine, W. E. Low-Frequency EPR of the copper in particulate methane monooxygenase from *Methylomicrobium albus* BG8. *J. Am. Chem. Soc.* **119,** 5073–5074 (1997).

19.   Ro, S. Y. *et al.* Native top-down mass spectrometry provides insights into the copper centers of membrane-bound methane monooxygenase. *Nat. Commun.* accepted.

20.   Liew, E. F., Tong, D., Coleman, N. V. & Holmes, A. J. Mutagenesis of the hydrocarbon monooxygenase indicates a metal centre in subunit-C, and not subunit-B, is essential for copper-containing membrane monooxygenase activity. *Microbiology* **160,** 1267–1277 (2014).

21.   Yoshizawa, K. & Shiota, Y. Conversion of methane to methanol at the mononuclear and dinuclear copper sites of particulate methane monooxygenase (pMMO): a DFT and QM/MM study. *J. Am. Chem. Soc.* **128,** 9873–9881 (2006).

22.   Chan, S. I. *et al.* Redox potentiometry studies of particulate methane monooxygenase: support for a trinuclear copper cluster active site. *Angew. Chem. Int. Ed. Engl.* **46,** 1992–1994 (2007).

23.   Chan, S. I. & Yu, S. S. F. Controlled oxidation of hydrocarbons by the membrane-bound methane monooxygenase: the case for a tricopper cluster. *Acc. Chem. Res.* **41,** 969–979 (2008).

24.   Mahyuddin, M. H., Shiota, Y., Staykov, A. & Yoshizawa, K. Theoretical overview of methane hydroxylation by copper-oxygen species in enzymatic and zeolitic catalysts. *Acc. Chem. Res.* **51,** 2382–2390 (2018).

25.   Lu, Y.-J. *et al.* The PmoB subunit of particulate methane monooxygenase (pMMO) in Methylococcus capsulatus (Bath): The CuI sponge and its function. *J. Inorg. Biochem.* (2019).

26.   Miyaji, A., Miyoshi, T., Motokura, K. & Baba, T. The substrate binding cavity of particulate methane monooxygenase from *Methylosinus trichosporium* OB3b expresses high enantioselectivity for n-butane and n-pentane oxidation to 2-alcohol. *Biotechnol. Lett.* **33,** 2241–2246 (2011).

27.   Taylor, A. E. *et al.* Inhibitory effects of C2 to C10 1-alkynes on ammonia oxidation in two *Nitrososphaera* species. *Appl. Environ. Microbiol.* **81,** 1942–1948 (2015).

28.   Baani, M. & Liesack, W. Two isozymes of particulate methane monooxygenase with different methane oxidation kinetics are found in *Methylocystis* sp. strain SC2. *Proc. Natl. Acad. Sci. U.S.A.* **105,** 10203–10208 (2008).

29.   Pham, M. D. *et al.* Inactivation of the particulate methane monooxygenase (pMMO) in *Methylococcus capsulatus* (Bath) by acetylene. *Biochim. Biophys. Acta* **1854,** 1842–1852 (2015).

30.   Gilch, S., Vogel, M., Lorenz, M. W., Meyer, O. & Schmidt, I. Interaction of the mechanism-based inactivator acetylene with ammonia monooxygenase of *Nitrosomonas europaea. Microbiology* **155,** 279–284 (2009).

31.   Choi, D.-W. *et al.* The membrane-associated methane monooxygenase (pMMO) and pMMO-NADH:quinone oxidoreductase complex from *Methylococcus capsulatus* (Bath). *J. Bacteriol.* **185,** 5755–5764 (2003).

32.   Lieven, C. *et al.* A genome-scale metabolic model for *Methylococcus capsulatus*

(Bath) suggests reduced efficiency electron transfer to the particulate methane monooxygenase. *Front. Microbiol.* **9,** 2947 (2018).

33. la Torre, de, A. *et al.* Genome-scale metabolic reconstructions and theoretical investigation of methane conversion in *Methylomicrobium buryatense* strain 5G(B1). *Microb. Cell Fact.* **14,** 188 (2015).

34. Myronova, N., Kitmitto, A., Collins, R. F., Miyaji, A. & Dalton, H. Three-dimensional structure determination of a protein supercomplex that oxidizes methane to formaldehyde in *Methylococcus capsulatus* (Bath). *Biochemistry* **45,** 11905–11914 (2006).

35. Culpepper, M. A. & Rosenzweig, A. C. Structure and protein-protein interactions of methanol dehydrogenase from *Methylococcus capsulatus* (Bath). *Biochemistry* **53,** 6211–6219 (2014).

36. Deng, Y. W., Ro, S. Y. & Rosenzweig, A. C. Structure and function of the lanthanide-dependent methanol dehydrogenase XoxF from the methanotroph *Methylomicrobium buryatense* 5GB1C. *J. Biol. Inorg. Chem.* **23,** 1037–1047 (2018).

37. Zickermann, V., Angerer, H., Ding, M. G., Nübel, E. & Brandt, U. Small single transmembrane domain (STMD) proteins organize the hydrophobic subunits of large membrane protein complexes. *FEBS Letters* **584,** 2516–2525 (2010).

38. Fisher, O. S. *et al.* Characterization of a long overlooked copper protein from methane- and ammonia-oxidizing bacteria. *Nat. Comms.* **9,** 4276 (2018).

39. Beck, D. A. C. & Kalyuzhnaya, M. G. Genetic systems for moderately halo(alkali)philic bacteria of the genus *Methylomicrobium*. *Meth. Enzymol.* **495,** 99–118 (2011).

40. Marx, C. J. & Lidstrom, M. E. Broad-host-range cre-lox system for antibiotic marker recycling in gram-negative bacteria. *BioTechniques* **33,** 1062–1067 (2002).

41. Schäfer, A. *et al.* Small mobilizable multi-purpose cloning vectors derived from the *Escherichia coli* plasmids pK18 and pK19: selection of defined deletions in the chromosome of *Corynebacterium glutamicum*. *Gene* **145,** 69–73 (1994).

42. Chu, F. & Lidstrom, M. E. XoxF acts as the predominant methanol dehydrogenase in the type I methanotroph *Methylomicrobium buryatense*. *J. Bacteriol.* **198,** 1317–1325 (2016).

43. Smith, T. J., Slade, S. E., Burton, N. P., Murrell, J. C. & Dalton, H. Improved system for protein engineering of the hydroxylase component of soluble methane monooxygenase. *Appl. Environ. Microbiol.* **68,** 5265–5273 (2002).

44. Gu, W., Haque, M. F. U. & Semrau, J. D. Characterization of the role of copCD in copper uptake and the 'copper-switch' in *Methylosinus trichosporium* OB3b. *FEMS Microbiol. Lett.* **364,** fnx094 (2017).

45. Puri, A. W. *et al.* Genetic tools for the industrially promising methanotroph *Methylomicrobium buryatense*. *Appl. Environ. Microbiol.* **81,** 1775–1781 (2015).

46. Ro, S. Y. & Rosenzweig, A. C. Recent advances in the genetic manipulation of *Methylosinus trichosporium* OB3b. *Meth. Enzymol.* **605,** 335–349 (2018).

47. Kalyuzhnaya, M. G., Puri, A. W. & Lidstrom, M. E. Metabolic engineering in methanotrophic bacteria. *Metab. Eng.* **29,** 142–152 (2015).

48. Henard, C. A. *et al.* Bioconversion of methane to lactate by an obligate methanotrophic bacterium. *Sci. Rep.* **6,** 21585 (2016).

49. Nguyen, A. D. *et al.* Systematic metabolic engineering of *Methylomicrobium alcaliphilum* 20Z for 2,3-butanediol production from methane. *Metab. Eng.* **47,** 323–333 (2018).

50. Yan, X., Chu, F., Puri, A. W., Fu, Y. & Lidstrom, M. E. Electroporation-based genetic manipulation in type I methanotrophs. *Appl. Environ. Microbiol.* **82,** 2062–2069 (2016).

51. Tapscott, T., Guarnieri, M. T. & Henard, C. A. Development of a CRISPR/Cas9 system for *Methylococcus capsulatus* in vivo gene editing. *Appl. Environ. Microbiol.* AEM.00340–19 (2019).

52. Garg, S., Clomburg, J. M. & Gonzalez, R. A modular approach for high-flux lactic acid production from methane in an industrial medium using engineered *Methylomicrobium buryatense* 5GB1. *J. Ind. Microbiol. Biotechnol.* **98,** 498–13 (2018).

53. Gu, W., Baral, B. S., DiSpirito, A. A. & Semrau, J. D. An aminotransferase Is responsible for the deamination of the N-terminal leucine and required for formation of oxazolone ring A in methanobactin of *Methylosinus trichosporium* OB3b. *Appl. Environ. Microbiol.* **83,** e02619–16 (2017).

54. Fei, Q. *et al.* Bioconversion of natural gas to liquid fuel: opportunities and challenges. *Biotechnol. Adv.* **32,** 596–614 (2014).

55. Cantera, S. *et al.* Bio-conversion of methane into high profit margin compounds: an innovative, environmentally friendly and cost-effective platform for methane abatement. *World J. Microbiol. Biotechnol.* **35,** 16 (2019).

56. Nguyen, D. T. N. *et al.* Metabolic engineering of the type I methanotroph *Methylomonas* sp. DH-1 for production of succinate from methane. *Metab. Eng.* **54,** 170–179 (2019).

57. Garg, S., Wu, H., Clomburg, J. M. & Bennett, G. N. Bioconversion of methane to C-4 carboxylic acids using carbon flux through acetyl-CoA in engineered *Methylomicrobium buryatense* 5GB1C. *Metab. Eng.* **48,** 175–183 (2018).

58. EPA. Overview of greenhouse gases. (2017). Available at: http://epaclimatechange.sfgov.org/ghgemissions/overview-greenhouse-gases#methane. (Accessed: 25 July 2017)

59. Jiang, H. *et al.* Methanotrophs: multifunctional bacteria with promising applications in environmental bioengineering. *Biochem. Eng. J.* **49,** 277–288 (2010).

60. Lawton, T. J. & Rosenzweig, A. C. Methane-oxidizing enzymes: an upstream problem in biological gas-to-liquids conversion. *J. Am. Chem. Soc.* **138,** 9327–9340 (2016).

61. Sirajuddin, S. & Rosenzweig, A. C. Enzymatic oxidation of methane. *Biochemistry* **54,** 2283–2294 (2015).

62. Chen, Y.-S. *et al.* Controlled oxidation of aliphatic CH bonds in metallo-monooxygenases: mechanistic insights derived from studies on deuterated and fluorinated hydrocarbons. *J. Inorg. Biochem.* **134,** 118–133 (2014).

63. Wang, V. C.-C. *et al.* Alkane Oxidation: methane monooxygenases, related enzymes, and their biomimetics. *Chem. Rev.* **117,** 8574–8621 (2017).

64. Garavito, R. M. & Ferguson-Miller, S. Detergents as tools in membrane biochemistry. *J. Biol. Chem.* **276,** 32403–32406 (2001).

65.   Orwick-Rydmark, M., Arnold, T. & Linke, D. *The use of detergents to purify membrane proteins*. **84,** 4.8.1–4.8.35 (Curr. Protoc. Protein Sci., 2001).

66.   Seddon, A. M., Curnow, P. & Booth, P. J. Membrane proteins, lipids and detergents: not just a soap opera. *Biochim. Biophys. Acta* **1666,** 105–117 (2004).

67.   Yang, Z. *et al.* Membrane protein stability can be compromised by detergent interactions with the extramembranous soluble domains. *Protein Sci.* **23,** 769–789 (2014).

68.   Shen, H.-H., Lithgow, T. & Martin, L. Reconstitution of membrane proteins into model membranes: seeking better ways to retain protein activities. *Int. J. Mol. Sci.* **14,** 1589–1607 (2013).

69.   Frey, L., Lakomek, N.-A., Riek, R. & Bibow, S. Micelles, bicelles, and nanodiscs: comparing the impact of membrane mimetics on membrane protein backbone dynamics. *Angew. Chem. Int. Ed. Engl.* **56,** 380–383 (2017).

70.   Bayburt, T. H. & Sligar, S. G. Membrane protein assembly into nanodiscs. *FEBS Letters* **584,** 1721–1727 (2010).

71.   Palsdottir, H. & Hunte, C. Lipids in membrane protein structures. *Biochim. Biophys. Acta Biomembr.* **1666,** 2–18 (2004).

72.   Dürr, U. H. N., Gildenberg, M. & Ramamoorthy, A. The magic of bicelles lights up membrane protein structure. *Chem. Rev.* **112,** 6054–6074 (2012).

73.   Crystallization of membrane proteins in bicelles: methods and protocols. *Methods Mol. Biol.* **914,** 3–16 (2012).

74.   Czerski, L. & Sanders, C. R. Functionality of a membrane protein in bicelles. *Anal. Biochem.* **284,** 327–333 (2000).

75.   Gruss, F., Hiller, S. & Maier, T. Purification and bicelle crystallization for structure determination of the E. coli outer membrane protein TamA. *Methods Mol. Biol.* **1329,** 259–270 (2015).

76.   Khmelenina, V. N. Isolation and characterization of halotolerant alkaliphilic methanotrophic bacteria from Tuva Soda Lakes. *Curr. Microbiol.* **35,** 257–261 (1997).

77.   Kaluzhnaya, M. *et al.* Taxonomic characterization of new alkaliphilic and alkalitolerant methanotrophs from soda lakes of the Southeastern Transbaikal region and description of *Methylomicrobium buryatense* sp.nov. *Syst. Appl. Microbiol.* **24,** 166–176 (2001).

78.   Makula, R. A. Phospholipid composition of methane-utilizing bacteria. *J. Bacteriol.* **134,** 771–777 (1978).

79.   Lee, A. G. How lipids affect the activities of integral membrane proteins. *Biochim. Biophys. Acta* **1666,** 62–87 (2004).

80.   Stemmler, T. L. *et al.* EXAFS comparison of the dimanganese core structures of manganese catalase, arginase, and manganese-substituted ribonucleotide reductase and hemerythrin. *Biochemistry* **36,** 9847–9858 (1997).

81.   Lee, M. H. *et al.* Purification and characterization of *Klebsiella aerogenes* UreE protein: a nickel-binding protein that functions in urease metallocenter assembly. *Protein Sci.* **2,** 1042–1052 (1993).

82.   Frandsen, K. E. H. & Leggio, Lo, L. Lytic polysaccharide monooxygenases: a crystallographer's view on a new class of biomass-degrading enzymes. *IUCrJ* **3,**

448–467 (2016).

83. Simmons, T. J. *et al.* Structural and electronic determinants of lytic polysaccharide monooxygenase reactivity on polysaccharide substrates. *Nat. Comms.* **8,** 1064 (2017).

84. Walton, P. H. & Davies, G. J. On the catalytic mechanisms of lytic polysaccharide monooxygenases. *Curr. Opin. Chem. Biol.* **31,** 195–207 (2016).

85. Blanchette, C. D. *et al.* Printable enzyme-embedded materials for methane to methanol conversion. *Nat. Comms.* **7,** 11900 (2016).

86. Stoll, S. & Schweiger, A. EasySpin, a comprehensive software package for spectral simulation and analysis in EPR. *J. Magn. Reson.* **178,** 42–55 (2006).

87. Otwinowski, Z. & Minor, W. Processing of X-ray diffraction data collected in oscillation mode. *Meth. Enzymol.* **276,** 307–326 (1997).

88. Strong, M. *et al.* Toward the structural genomics of complexes: crystal structure of a PE/PPE protein complex from *Mycobacterium tuberculosis*. *Proc. Natl. Acad. Sci.* **103,** 8060–8065 (2006).

89. Adams, P. D. *et al.* PHENIX: a comprehensive Python-based system for macromolecular structure solution. *Acta Crystallogr. D Biol. Crystallogr.* **66,** 213–221 (2010).

90. Emsley, P., Lohkamp, B., Scott, W. G. & Cowtan, K. Features and development of Coot. *Acta Crystallogr. D Biol. Crystallogr.* **66,** 486–501 (2010).

91. Chen, V. B. *et al.* MolProbity: all-atom structure validation for macromolecular crystallography. *Acta Crystallogr. D Biol. Crystallogr.* **66,** 12–21 (2010).

92. George, G. N., George, S. J. & Pickering, I. J. EXAFSPAK. (2001). Available at: https://www-ssrl.slac.stanford.edu/~george/exafspak/exafs.htm. (Accessed: 4 May 2019)

93. Ankudinov, A. L. & Rehr, J. J. Relativistic calculations of spin-dependent x-ray-absorption spectra. *Phys. Rev. B* **56,** R1712–R1716 (1997).

94. Cotelesage, J. J. H., Pushie, M. J., Grochulski, P., Pickering, I. J. & George, G. N. Metalloprotein active site structure determination: synergy between X-ray absorption spectroscopy and X-ray crystallography. *J. Inorg. Biochem.* **115,** 127–137 (2012).

95. Riggs-Gelasco, P. J., Stemmler, T. L. & Penner-Hahn, J. E. XAFS of dinuclear metal sites in proteins and model compounds. *Coordina. Chem. Rev.* **144,** 245–286 (1995).

96. Leney, A. C. & Heck, A. J. R. Native mass spectrometry: what is in the name? *J. Am. Soc. Mass Spectrom.* **28,** 5–13 (2017).

97. Loo, J. A. Studying noncovalent protein complexes by electrospray ionization mass spectrometry. *Mass Spectrom. Rev.* **16,** 1–23 (1997).

98. Loo, J. A. Electrospray ionization mass spectrometry: a technology for studying noncovalent macromolecular complexes. *Int. J. Mass Spectrom.* **200,** 175–186 (2000).

99. Benesch, J. L. P., Aquilina, J. A., Ruotolo, B. T., Sobott, F. & Robinson, C. V. Tandem mass spectrometry reveals the quaternary organization of macromolecular assemblies. *Chem. Biol.* **13,** 597–605 (2006).

100. Belov, M. E. *et al.* From protein complexes to subunit backbone fragments: a multi-

stage approach to native mass spectrometry. *Anal. Chem.* **85,** 11163–11173 (2013).

101. Skinner, O. S. *et al.* An informatic framework for decoding protein complexes by top-down mass spectrometry. *Nat. Methods* **13,** 237–240 (2016).

102. Smith, L. M., Kelleher, N. L.Consortium for Top Down Proteomics. Proteoform: a single term describing protein complexity. *Nat. Methods* **10,** 186–187 (2013).

103. Haverland, N. A. *et al.* Defining gas-phase fragmentation propensities of intact proteins during native top-down mass spectrometry. *J. Am. Soc. Mass Spectrom.* **28,** 1203–1215 (2017).

104. Skinner, O. S., Schachner, L. F. & Kelleher, N. L. The search engine for multi-proteoform complexes: an online tool for the identification and stoichiometry determination of protein complexes. *Curr. Protoc. Bioinformatics* **56,** 13.30.1–13.30.11 (2016).

105. Li, H., Nguyen, H. H., Ogorzalek Loo, R. R., Campuzano, I. D. G. & Loo, J. A. An integrated native mass spectrometry and top-down proteomics method that connects sequence to structure and function of macromolecular complexes. *Nat. Chem.* **10,** 139–148 (2018).

106. Skinner, O. S. *et al.* Top-down characterization of endogenous protein complexes with native proteomics. *Nat. Chem. Biol.* **14,** 36–41 (2018).

107. Kenney, G. E. *et al.* The biosynthesis of methanobactin. *Science* **359,** 1411–1416 (2018).

108. Wongkongkathep, P. *et al.* Native top-down mass spectrometry and ion mobility ms for characterizing the cobalt and manganese metal binding of α-synuclein protein. *J. Am. Soc. Mass Spectrom.* **29,** 1870–1880 (2018).

109. Gault, J. *et al.* High-resolution mass spectrometry of small molecules bound to membrane proteins. *Nat. Methods* **13,** 333–336 (2016).

110. Hopper, J. T. S. *et al.* Detergent-free mass spectrometry of membrane protein complexes. *Nat. Methods* **10,** 1206–1208 (2013).

111. Laganowsky, A., Reading, E., Hopper, J. T. S. & Robinson, C. V. Mass spectrometry of intact membrane protein complexes. *Nat. Protoc.* **8,** 639–651 (2013).

112. Marty, M. T., Hoi, K. K., Gault, J. & Robinson, C. V. Probing the lipid annular belt by gas-phase dissociation of membrane proteins in nanodiscs. *Angew. Chem. Int. Ed. Engl.* **55,** 550–554 (2016).

113. Grinkova, Y. V., Denisov, I. G. & Sligar, S. G. Engineering extended membrane scaffold proteins for self-assembly of soluble nanoscale lipid bilayers. *Protein Eng. Des. Sel.* **23,** 843–848 (2010).

114. Chistoserdova, L. & Kalyuzhnaya, M. G. Current trends in methylotrophy. *Trends Microbiol.* **26,** 703–714 (2018).

115. Akberdin, I. R. *et al.* Methane utilization in *Methylomicrobium alcaliphilum* 20ZR: a systems approach. *Sci. Rep.* **8,** 2512 (2018).

116. Semrau, J. D. *et al.* Particulate methane monooxygenase genes in methanotrophs. *J. Bacteriol.* **177,** 3071–3079 (1995).

117. Denisov, I. G. & Sligar, S. G. Nanodiscs in membrane biochemistry and biophysics. *Chem. Rev.* **117,** 4669–4713 (2017).

118. Fellers, R. T. *et al.* ProSight Lite: graphical software to analyze top-down mass

spectrometry data. *Proteomics* **15,** 1235–1238 (2015).

119. Yu, S. S. F. *et al.* The C-terminal aqueous-exposed domain of the 45 kDa subunit of the particulate methane monooxygenase in *Methylococcus capsulatus* (Bath) is a Cu(I) sponge. *Biochemistry* **46,** 13762–13774 (2007).

120. Kahnt, J. *et al.* Post-translational modifications in the active site region of methyl-coenzyme M reductase from methanogenic and methanotrophic archaea. *FEBS J.* **274,** 4913–4921 (2007).

121. Petrovic, D. M. *et al.* Methylation of the N-terminal histidine protects a lytic polysaccharide monooxygenase from auto-oxidative inactivation. *Protein Sci.* **27,** 1636–1650 (2018).

122. Nyyssola, A., Kerovuo, J., Kaukinen, P., Weymarn, von, N. & Reinikainen, T. Extreme halophiles synthesize betaine from glycine by methylation. *J. Biol. Chem.* **275,** 22196–22201 (2000).

123. Cowley, R. E., Tian, L. & Solomon, E. I. Mechanism of O2 activation and substrate hydroxylation in noncoupled binuclear copper monooxygenases. *Proc. Natl. Acad. Sci. U.S.A.* **113,** 12035–12040 (2016).

124. Op den Camp, H. J. M. *et al.* Environmental, genomic and taxonomic perspectives on methanotrophic *Verrucomicrobia. Environ. Microbiol. Rep.* **1,** 293–306 (2009).

125. Hakemian, A. S. & Rosenzweig, A. C. The biochemistry of methane oxidation. *Annu. Rev. Biochem.* **76,** 223–241 (2007).

126. Miller, K. W., Hammond, L. & Porter, E. G. The solubility of hydrocarbon gases in lipid bilayers. *Chem. Phys. Lipids* **20,** 229–241 (1977).

127. Chorev, D. S. *et al.* Protein assemblies ejected directly from native membranes yield complexes for mass spectrometry. *Science* **362,** 829–834 (2018).

128. Schneider, C. A., Rasband, W. S. & Eliceiri, K. W. NIH Image to ImageJ: 25 years of image analysis. *Nat. Methods* **9,** 671–675 (2012).

129. Suloway, C. *et al.* Automated molecular microscopy: the new Leginon system. *J. Struct. Biol.* **151,** 41–60 (2005).

130. Zheng, S. Q. *et al.* MotionCor2: anisotropic correction of beam-induced motion for improved cryo-electron microscopy. *Nat. Methods* **14,** 331–332 (2017).

131. Rohou, A. & Grigorieff, N. CTFFIND4: fast and accurate defocus estimation from electron micrographs. *J. Struct. Biol.* **192,** 216–221 (2015).

132. la Rosa-Trevín, de, J. M. *et al.* Scipion: A software framework toward integration, reproducibility and validation in 3D electron microscopy. *J. Struct. Biol.* **195,** 93–99 (2016).

133. Abrishami, V. *et al.* A pattern matching approach to the automatic selection of particles from low-contrast electron micrographs. *Bioinformatics* **29,** 2460–2468 (2013).

134. Sorzano, C. O. S. *et al.* A clustering approach to multireference alignment of single-particle projections in electron microscopy. *J. Struct. Biol.* **171,** 197–206 (2010).

135. Zhang, Z. & Marshall, A. G. A universal algorithm for fast and automated charge state deconvolution of electrospray mass-to-charge ratio spectra. *J. Am. Soc. Mass Spectrom.* **9,** 225–233 (1998).

136. Fornelli, L. *et al.* Accurate sequence analysis of a monoclonal antibody by top-down and middle-down orbitrap mass spectrometry applying multiple ion activation

techniques. *Anal. Chem.* **90,** 8421–8429 (2018).

137.   Stein, L. Y. *et al.* Genome sequence of the methanotrophic alphaproteobacterium *Methylocystis* sp. strain Rockwell (ATCC 49242). *J. Bacteriol.* **193,** 2668–2669 (2011).

138.   L, C. & ME, L. *The prokaryotes.* (Springer Berlin Heidelberg, 2013). doi:10.1007/978-3-642-30141-4

139.   Strong, P. J., Xie, S. & Clarke, W. P. Methane as a resource: can the methanotrophs add value? *Environ. Sci. Technol.* **49,** 4001–4018 (2015).

140.   Pfeifenschneider, J., Brautaset, T. & Wendisch, V. F. Methanol as carbon substrate in the bio-economy: Metabolic engineering of aerobic methylotrophic bacteria for production of value-added chemicals. *Biofuels, Bioprod. Bioref.* **11,** 719–731 (2017).

141.   Keltjens, J. T., Pol, A., Reimann, J. & Op den Camp, H. J. M. PQQ-dependent methanol dehydrogenases: rare-earth elements make a difference. *Appl. Microbiol. Biotechnol.* **98,** 6163–6183 (2014).

142.   Anthony, C. & Williams, P. The structure and mechanism of methanol dehydrogenase. *Biochim. Biophys. Acta* **1647,** 18–23 (2003).

143.   Skovran, E. & Martinez-Gomez, N. C. Just add lanthanides. *Science* **348,** 862–863 (2015).

144.   Chistoserdova, L. Modularity of methylotrophy, revisited. *Environ. Microbiol.* **13,** 2603–2622 (2011).

145.   Hibi, Y. *et al.* Molecular structure of La3+-induced methanol dehydrogenase-like protein in *Methylobacterium radiotolerans*. *J. Biosci. Bioeng.* **111,** 547–549 (2011).

146.   Fitriyanto, N. A. *et al.* Molecular structure and gene analysis of Ce3+-induced methanol dehydrogenase of *Bradyrhizobium* sp. MAFF211645. *J. Biosci. Bioeng.* **111,** 613–617 (2011).

147.   Nakagawa, T. *et al.* A catalytic role of XoxF1 as La3+-dependent methanol dehydrogenase in *Methylobacterium extorquens* strain AM1. *PLoS One* **7,** e50480 (2012).

148.   Pol, A. *et al.* Rare earth metals are essential for methanotrophic life in volcanic mudpots. *Environ. Microbiol.* **16,** 255–264 (2014).

149.   Masuda, S. *et al.* Lanthanide-dependent regulation of methylotrophy in *Methylobacterium aquaticum* strain 22A. *mSphere* **3,** e00462–17 (2018).

150.   Haque, M. F. U. *et al.* Cerium regulates expression of alternative methanol dehydrogenases in *Methylosinus trichosporium* OB3b. *Appl. Environ. Microbiol.* **81,** 7546–7552 (2015).

151.   Vu, H. N. *et al.* Lanthanide-dependent regulation of methanol oxidation systems in *Methylobacterium extorquens* AM1 and their contribution to methanol growth. *J. Bacteriol.* **198,** 1250–1259 (2016).

152.   Bentlin, F. R. S. & Pozebon, D. Direct determination of lanthanides in environmental samples using ultrasonic nebulization and ICP OES. *J. Braz. Chem. Soc.* **21,** 627–634 (2010).

153.   Jahn, B. *et al.* Similar but not the same: first kinetic and structural analyses of a methanol dehydrogenase containing a europium ion in the active site. *ChemBioChem* **19,** 1147–1153 (2018).

154.   Wadzinski, A. M. & Ribbons, D. W. Oxidation of C1 compounds by particulate fractions from *Methylococcus capsulatus*: properties of methanol oxidase and methanol dehydrogenase. *J. Bacteriol.* **122,** 1364–1374 (1975).

155.   Fassel, T. A., Buchholz, L. A., Collins, M. L. & Remsen, C. C. Localization of methanol dehydrogenase in two strains of methylotrophic bacteria detected by immunogold labeling. *Appl. Environ. Microbiol.* **58,** 2302–2307 (1992).

156.   Brantner, C. A., Remsen, C. C., Owen, H. A., Buchholz, L. A. & Perille Collins, M. L. Intracellular localization of the particulate methane monooxygenase and methanol dehydrogenase in *Methylomicrobium album* BG8. *Arch. Microbiol.* **178,** 59–64 (2002).

157.   Kitmitto, A., Myronova, N., Basu, P. & Dalton, H. Characterization and structural analysis of an active particulate methane monooxygenase trimer from *Methylococcus capsulatus* (Bath). *Biochemistry* **44,** 10954–10965 (2005).

158.   Wu, M. L. *et al.* XoxF-type methanol dehydrogenase from the anaerobic methanotroph 'Candidatus Methylomirabilis oxyfera'. *Appl. Environ. Microbiol.* **81,** 1442–1451 (2015).

159.   Schmidt, S., Christen, P., Kiefer, P. & Vorholt, J. A. Functional investigation of methanol dehydrogenase-like protein XoxF in *Methylobacterium extorquens* AM1. *Microbiology* **156,** 2575–2586 (2010).

160.   Page, M. D. & Anthony, C. Regulation of formaldehyde oxidation by the methanol dehydrogenase modifier proteins of *Methylophilus methylotrophus* and *Pseudomonas* AM1. *Microbiology* **132,** 1553–1563 (1986).

161.   Goodwin, M. G. & Anthony, C. Characterization of a novel methanol dehydrogenase containing a Ba2+ ion at the active site. *Biochem. J.* **318 (Pt 2),** 673–679 (1996).

162.   Basu, P., Katterle, B., Andersson, K. K. & Dalton, H. The membrane-associated form of methane mono-oxygenase from *Methylococcus capsulatus* (Bath) is a copper/iron protein. *Biochem. J.* **369,** 417–427 (2003).

163.   Nojiri, M. *et al.* Crystal structures of cytochrome c(L) and methanol dehydrogenase from *Hyphomicrobium denitrificans*: structural and mechanistic insights into interactions between the two proteins. *Biochemistry* **45,** 3481–3492 (2006).

164.   Chan, H. T. & Anthony, C. The interaction of methanol dehydrogenase and cytochrome cL in the acidophilic methylotroph *Acetobacter methanolicus*. *Biochem. J.* **280 (Pt 1),** 139–146 (1991).

165.   Cox, J. M., Day, D. J. & Anthony, C. The interaction of methanol dehydrogenase and its electron acceptor, cytochrome cL in methylotrophic bacteria. *Biochim. Biophys. Acta* **1119,** 97–106 (1992).

166.   Van Spanning, R. J. *et al.* Isolation and characterization of the moxJ, moxG, moxI, and moxR genes of *Paracoccus denitrificans*: inactivation of moxJ, moxG, and moxR and the resultant effect on methylotrophic growth. *J. Bacteriol.* **173,** 6948–6961 (1991).

167.   Anthony, C. The c-type cytochromes of methylotrophic bacteria. *Biochim. Biophys. Acta* **1099,** 1–15 (1992).

168.   Myung Choi, J., Cao, T.-P., Wouk Kim, S., Ho Lee, K. & Haeng Lee, S. MxaJ structure reveals a periplasmic binding protein-like architecture with unique

secondary structural elements. *Proteins* **85,** 1379–1386 (2017).

169.   Skovran, E., Palmer, A. D., Rountree, A. M., Good, N. M. & Lidstrom, M. E. XoxF is required for expression of methanol dehydrogenase in *Methylobacterium extorquens* AM1. *J. Bacteriol.* **193,** 6032–6038 (2011).

170.   Day, D. J. & Anthony, C. in *Methods in methane metabolism, Part B: methanotrophy* **188,** 210–216 (Academic Press, 1990).

171.   Laskowski, R. A. PDBsum: summaries and analyses of PDB structures. *Nucleic Acids Res.* **29,** 221–222 (2001).

172.   Dassama, L. M. K., Kenney, G. E., Ro, S. Y., Zielazinski, E. L. & Rosenzweig, A. C. Methanobactin transport machinery. *Proc. Natl. Acad. Sci. U.S.A.* **113,** 13027–13032 (2016).

173.   Stein, L. Y. *et al.* Genome sequence of the obligate methanotroph *Methylosinus trichosporium* strain OB3b. *J. Bacteriol.* **192,** 6497–6498 (2010).

174.   Haque, M. F. U., Gu, W., DiSpirito, A. A. & Semrau, J. D. Marker exchange mutagenesis of *mxaF*, encoding the large subunit of the Mxa methanol dehydrogenase, in *Methylosinus trichosporium* OB3b. *Appl. Environ. Microbiol.* **82,** 1549–1555 (2015).

175.   Borodina, E., Nichol, T., Dumont, M. G., Smith, T. J. & Murrell, J. C. Mutagenesis of the 'leucine gate' to explore the basis of catalytic versatility in soluble methane monooxygenase. *Appl. Environ. Microbiol.* **73,** 6460–6467 (2007).

176.   Lock, M., Nichol, T., Murrell, J. C. & Smith, T. J. Mutagenesis and expression of methane monooxygenase to alter regioselectivity with aromatic substrates. *FEMS Microbiol. Lett.* **364,** fnx137 (2017).

177.   Semrau, J. D. *et al.* Methanobactin and MmoD work in concert to act as the 'copper-switch' in methanotrophs. *Environ. Microbiol.* **15,** 3077–3086 (2013).

178.   Smith, T. J. & Murrell, J. C. in *Methods in enzymology* (eds. Rosenzweig, A. C. & Ragsdale, S. W.) **495,** 135–147 (Elsevier, 2011).

179.   Gu, W. *et al.* A TonB-dependent transporter is responsible for methanobactin uptake by *Methylosinus trichosporium* OB3b. *Appl. Environ. Microbiol.* **82,** 1917–1923 (2016).

180.   Kalyuzhnaya, M. G. *et al.* Classification of halo(alkali)philic and halo(alkali)tolerant methanotrophs provisionally assigned to the genera *Methylomicrobium* and *Methylobacter* and emended description of the genus *Methylomicrobium*. *Int. J. Syst. Evol. Microbiol.* **58,** 591–596 (2008).

181.   Mustakhimov, I. I. *et al.* Identification and characterization of EctR1, a new transcriptional regulator of the ectoine biosynthesis genes in the halotolerant methanotroph *Methylomicrobium alcaliphilum* 20Z. *J. Bacteriol.* **192,** 410–417 (2009).

182.   Demidenko, A., Akberdin, I. R., Allemann, M., Allen, E. E. & Kalyuzhnaya, M. G. Fatty acid biosynthesis pathways in *Methylomicrobium buryatense* 5G(B1). *Front. Microbiol.* **7,** (2017).

183.   Murrell, J. C. Molecular genetics of methane oxidation. *Biodegradation* **5,** 145–159 (1994).

184.   Lloyd, J. S., Finch, R., Dalton, H. & Murrell, J. C. Homologous expression of soluble methane monooxygenase genes in *Methylosinus trichosporium* OB3b.

Microbiology **145,** 461–470 (1999).

185. Hakemian, A. S. *et al.* The metal centers of particulate methane monooxygenase from *Methylosinus trichosporium* OB3b. *Biochemistry* **47,** 6793–6801 (2008).

186. Simon, R., Priefer, U. & Pühler, A. A broad host range mobilization system for in vivo genetic engineering: transposon mutagenesis in gram negative bacteria. *Nat. Biotech.* **1,** 784–791 (1983).

187. Selzer, G., Som, T., Itoh, T. & Tomizawa, J. The origin of replication of plasmid p15A and comparative studies on the nucleotide sequences around the origin of related plasmids. *Cell* **32,** 119–129 (1983).

188. Lloyd, J. S., De Marco, P., Dalton, H. & Murrell, J. C. Heterologous expression of soluble methane monooxygenase genes in methanotrophs containing only particulate methane monooxygenase. *Arch. Microbiol.* **171,** 364–370 (1999).

189. Lalioti, M. & Heath, J. A new method for generating point mutations in bacterial artificial chromosomes by homologous recombination in *Escherichia coli*. *Nucleic Acids Res.* **29,** e14 (2001).

190. Crombie, A. & Murrell, J. C. Development of a system for genetic manipulation of the facultative methanotroph *Methylocella silvestris* BL2. *Meth. Enzymol.* **495,** 119–133 (2011).

191. Orr-Weaver, T. L., Szostak, J. W. & Rothstein, R. J. Yeast transformation: a model system for the study of recombination. *Proc. Natl. Acad. Sci.* **78,** 6354–6358 (1981).

192. Sharan, S. K., Thomason, L. C., Kuznetsov, S. G. & Court, D. L. Recombineering: a homologous recombination-based method of genetic engineering. *Nat. Protoc.* **4,** 206–223 (2009).

193. Shevchuk, N. A. *et al.* Construction of long DNA molecules using long PCR-based fusion of several fragments simultaneously. *Nucleic Acids Res.* **32,** e19–19 (2004).

194. Tian, P. *et al.* Fundamental CRISPR-Cas9 tools and current applications in microbial systems. *Synth. Syst. Biotechnol.* **2,** 219–225 (2017).

195. Yoshikawa, S. & Shimada, A. Reaction mechanism of cytochrome c oxidase. *Chem. Rev.* **115,** 1936–1989 (2015).

196. Sharma, V. & Wikström, M. The role of the K-channel and the active-site tyrosine in the catalytic mechanism of cytochrome c oxidase. *Biochim. Biophys. Acta* **1857,** 1111–1115 (2016).

197. Forsberg, Z. *et al.* Comparative study of two chitin-active and two cellulose-active AA10-type lytic polysaccharide monooxygenases. *Biochemistry* **53,** 1647–1656 (2014).

198. Harris, P. V. *et al.* Stimulation of lignocellulosic biomass hydrolysis by proteins of glycoside hydrolase family 61: structure and function of a large, enigmatic family. *Biochemistry* **49,** 3305–3316 (2010).

199. Borisova, A. S. *et al.* Structural and functional characterization of a lytic polysaccharide monooxygenase with broad substrate specificity. *J. Biol. Chem.* **290,** 22955–22969 (2015).

200. Klinman, J. P. The copper-enzyme family of dopamine beta-monooxygenase and peptidylglycine alpha-hydroxylating monooxygenase: resolving the chemical pathway for substrate hydroxylation. *J. Biol. Chem.* **281,** 3013–3016 (2006).

201. Tian, G., Berry, J. A. & Klinman, J. P. Oxygen-18 kinetic isotope effects in the

dopamine beta-monooxygenase reaction: evidence for a new chemical mechanism in non-heme metallomonooxygenases. *Biochemistry* **33,** 226–234 (1994).

202.   Francisco, W. A., Blackburn, N. J. & Klinman, J. P. Oxygen and hydrogen isotope effects in an active site tyrosine to phenylalanine mutant of peptidylglycine alpha-hydroxylating monooxygenase: mechanistic implications. *Biochemistry* **42,** 1813–1819 (2003).

203.   Osborne, R. L., Zhu, H., Iavarone, A. T., Blackburn, N. J. & Klinman, J. P. Interdomain long-range electron transfer becomes rate-limiting in the Y216A variant of tyramine β-monooxygenase. *Biochemistry* **52,** 1179–1191 (2013).

204.   Murray, J. M. *et al.* Conserved tyrosine-369 in the active site of *Escherichia coli* copper amine oxidase is not essential. *Biochemistry* **40,** 12808–12818 (2001).

205.   Dubois, J. L. & Klinman, J. P. Role of a strictly conserved active site tyrosine in cofactor genesis in the copper amine oxidase from *Hansenula polymorpha*. *Biochemistry* **45,** 3178–3188 (2006).

206.   Chen, Z.-W., Datta, S., Dubois, J. L., Klinman, J. P. & Mathews, F. S. Mutation at a strictly conserved, active site tyrosine in the copper amine oxidase leads to uncontrolled oxygenase activity. *Biochemistry* **49,** 7393–7402 (2010).

207.   Gonçalves, V. L. *et al.* Flavodiiron oxygen reductase from Entamoeba histolytica: modulation of substrate preference by tyrosine 271 and lysine 53. *J. Biol. Chem.* **289,** 28260–28270 (2014).

208.   Daubner, S. C. & Fitzpatrick, P. F. Mutation to phenylalanine of tyrosine 371 in tyrosine hydroxylase increases the affinity for phenylalanine. *Biochemistry* **37,** 16440–16444 (1998).

209.   Stafford, G. P., Scanlan, J., McDonald, I. R. & Murrell, J. C. rpoN, mmoR and mmoG, genes involved in regulating the expression of soluble methane monooxygenase in *Methylosinus trichosporium* OB3b. *Microbiology* **149,** 1771–1784 (2003).

210.   Scanlan, J., Dumont, M. G. & Murrell, J. C. Involvement of MmoR and MmoG in the transcriptional activation of soluble methane monooxygenase genes in *Methylosinus trichosporium* OB3b. *FEMS Microbiol. Lett.* **301,** 181–187 (2009).

211.   Culpepper, M. A., Cutsail, G. E., Hoffman, B. M. & Rosenzweig, A. C. Evidence for oxygen binding at the active site of particulate methane monooxygenase. *J. Am. Chem. Soc.* **134,** 7640–7643 (2012).

212.   Kuijpers, N. G. A. *et al.* A versatile, efficient strategy for assembly of multi-fragment expression vectors in *Saccharomyces cerevisiae* using 60 bp synthetic recombination sequences. *Microb. Cell Fact.* **12,** 47 (2013).

213.   Islam, T., Jensen, S., Reigstad, L. J., Larsen, O. & Birkeland, N.-K. Methane oxidation at 55 degrees C and pH 2 by a thermoacidophilic bacterium belonging to the *Verrucomicrobia* phylum. *Proc. Natl. Acad. Sci. U.S.A.* **105,** 300–304 (2008).

214.   Erikstad, H.-A., Jensen, S., Keen, T. J. & Birkeland, N.-K. Differential expression of particulate methane monooxygenase genes in the verrucomicrobial methanotroph '*Methylacidiphilum kamchatkense*' Kam1. *Extremophiles* **16,** 405–409 (2012).

215.   Khadem, A. F. *et al.* Autotrophic methanotrophy in verrucomicrobia: *Methylacidiphilum fumariolicum* SolV uses the Calvin-Benson-Bassham cycle for carbon dioxide fixation. *J. Bacteriol.* **193,** 4438–4446 (2011).

216. Mohammadi, S. S., Pol, A., van Alen, T., Jetten, M. S. M. & Op den Camp, H. J. M. Ammonia oxidation and nitrite reduction in the Verrucomicrobial methanotroph *Methylacidiphilum fumariolicum* SolV. *Front. Microbiol.* **8,** 1901 (2017).

217. Woertink, J. S. *et al.* A [Cu2O]2+ core in Cu-ZSM-5, the active site in the oxidation of methane to methanol. *Proc. Natl. Acad. Sci. U.S.A.* **106,** 18908–18913 (2009).

218. Yeh, C.-H., Yu, S. S. F., Chan, S. I. & Jiang, J.-C. Quantum chemical studies of methane oxidation to methanol on a biomimetic tricopper complex: mechanistic insights. *ChemistrySelect* **3,** 5113–5122 (2018).

219. Cook, E. C., Featherston, E. R., Showalter, S. A. & Cotruvo, J. A. Structural basis for rare earth element recognition by *Methylobacterium extorquens* lanmodulin. *Biochemistry* **58,** 120–125 (2019).

APPENDIX 1

SUPPLEMENTARY FIGURES
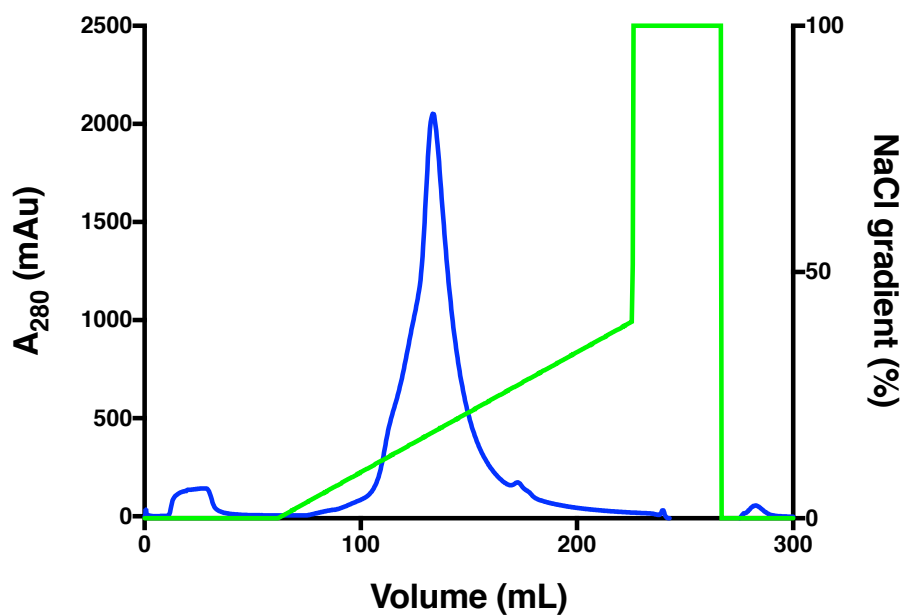
Figure S2.1. Anion exchange chromatography purification of 20Z-pMMO.
The absorbance at 280 nm is shown in blue and the 50-800 mM NaCl (corresponding to 0 - 40 %)
gradient is shown in green. 20Z-pMMO elutes at ~17 % in NaCl gradient.
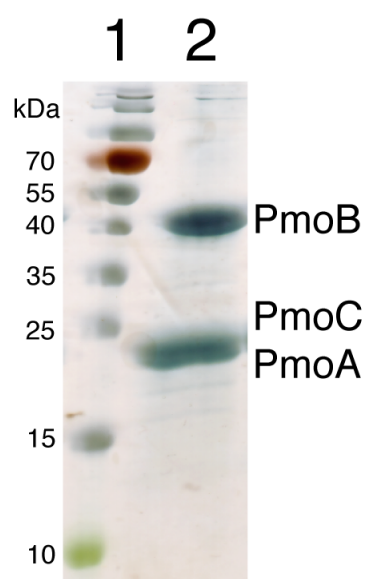
Figure S2.2. SDS-PAGE gel of 20Z-pMMO.
PmoC and PmoA run together on a 15% SDS-PAGE gel due to their similar molecular weights.
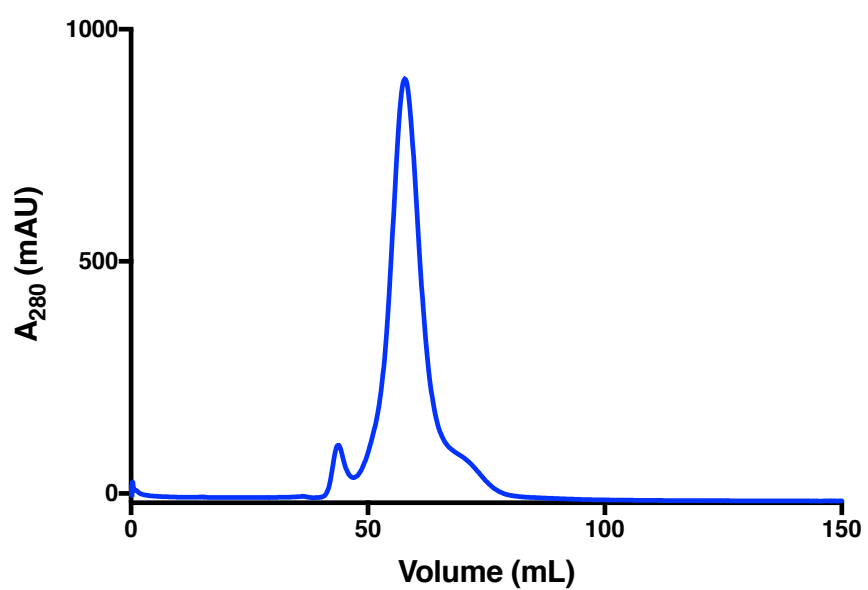
Figure S2.2. Size exclusion chromatography purification of Bath-pMMO.
The absorbance at 280 nm is shown in blue.
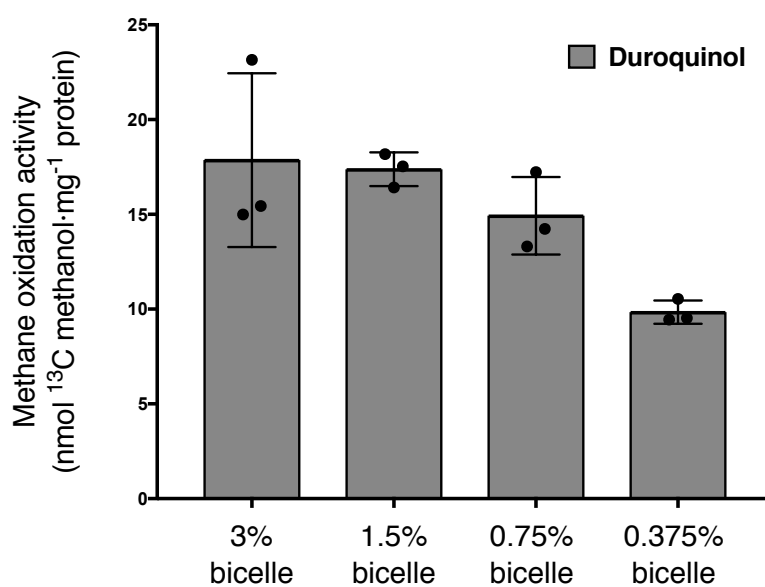
Figure S2.3. Methane oxidation activity as a function of bicelle concentration.
Activity values (nmol ^{13}C methanol·mg^{-1} protein) are shown for Bath-pMMO reconstituted in 0.375% to 3% bicelles using duroquinol as the reductant. Error bars represent standard deviations of three measurements, with each black dot representing individual measurements.

Table S2.1. Methane oxidation activity Bath-pMMO and 20Z-pMMO in native membranes, detergent, and bicelles. (nmol ^{13}C methanol·mg^{-1} protein), n=3

	membrane	solubilized	solubilized + bicelle	purified	purified + bicelle
Bath-pMMO					
Duroquinol	4.0 ± 0.3	5.7 ± 0.2	31.8 ± 3.9	4.5 ± 0.3	17.7 ± 1.1
NADH	41.1 ± 1.7	0	40.1 ± 2.6	0	25.9 ± 2.4
20Z-pMMO					
Duroquinol	0	0	19.4 ± 1.0	0	21.9 ± 3.2
NADH	14.5 ± 1.2	0	0	0	0

Table S2.2. Copper content of Bath-pMMO and 20Z-pMMO. (copper ion per 100 kDa protomer), 3≤n≤6.

	membrane	solubilized	solubilized + bicelle	purified	purified + bicelle
Bath-pMMO Cu^{2+} eq.[*]	3.8 ± 1.5	3.6 ± 1.1	3.7 ± 1.2	3.1 ± 0.6 0.7	3.3 ± 0.8 0.8
20Z-pMMO Cu^{2+} eq.[*]	3.5 ± 1.4	3.1 ± 1.2	3.1 ± 1.1	2.7 ± 0.8 2.3	2.8 ± 0.8 2.9

[*]The equivalents of Cu^{2+} per 100 kDa protomer were determined by EPR quantitation.

Table S23. Methane oxidation activity profiles of as-isolated Bath-pMMO using different detection methods at 45 °C with NADH as reductant. (nmol methanol/min/mg protein)

	membrane	reference
Bath-pMMO		
GC-FID	80 -130	[10]
GC-MS	40 - 70	This study

APPENDIX 2

SUPPLEMENTARY FIGURES

a MS^1: 20Z-pMMO protomer ejected from micelle
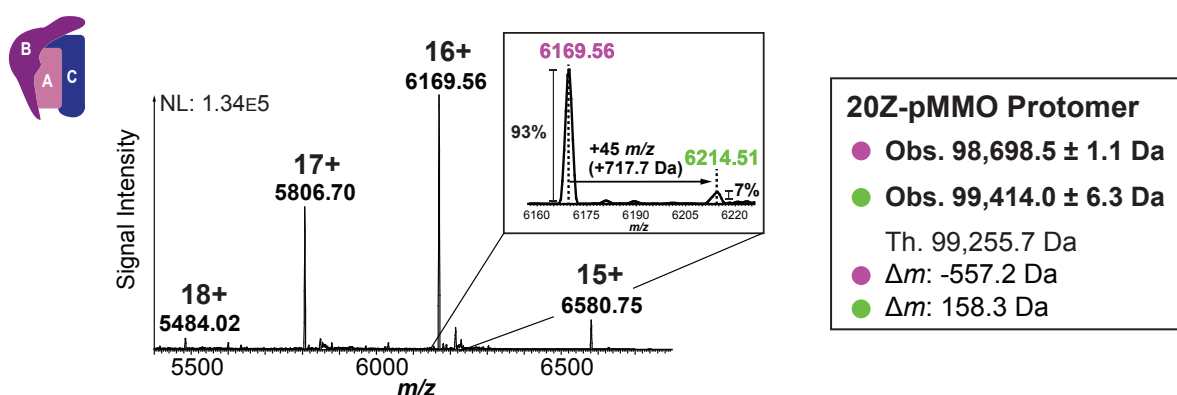
b MS^2: 20Z-pMMO subunits ejected from protomer
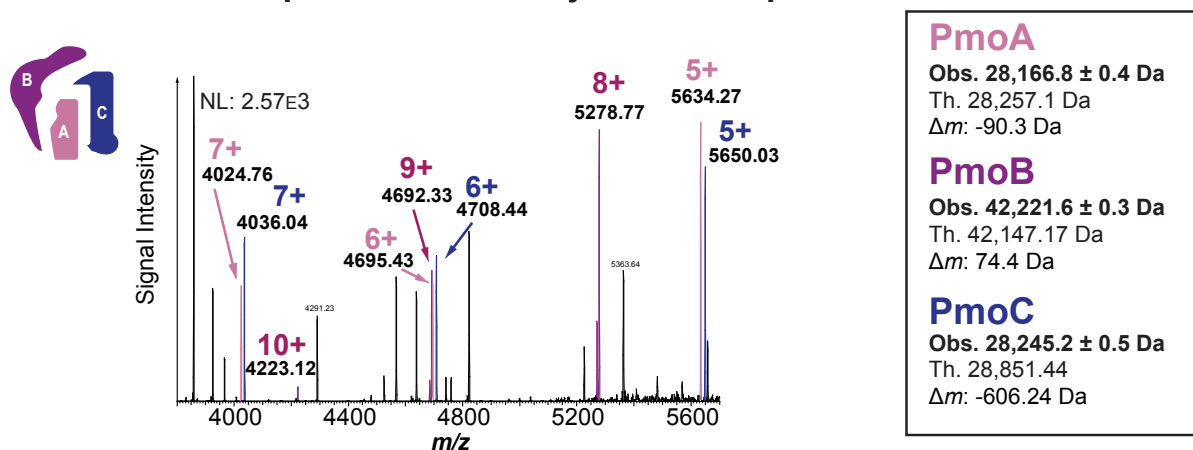
Figure S.3.1. nTDMS analysis of 20Z-pMMO in Triton X-100 micelles.
a, Broadband MS^1 of 20Z-pMMO protomer upon ejection from a Triton X-100 micelle at CID of 195 V. The spectrum shows a charge state distribution of four protonated states of the pMMO protomer generated by native electrospray ionization (nESI). The inset is a zoom-in of the 16+ charge state, showing the presence of two species, one labeled in purple (93% of signal) and one in green (7% of signal). Charge state deconvolution of the two species yields a mass of 98,696 ±

1.1 Da (*purple*) and 99,414.0 ± 6.3 Da (*green*). The theoretical mass (abbreviated "Th." in figure) is derived from the unmodified subunits of pMMO and accounts for the cleavage of a known signal peptide in PmoB. **b**, MS^2 of 20Z-pMMO subunits ejected from the 16+ charge state of the protomer after activation by collisions with neutral gas at HCD of 150 V. The spectrum shows three protonated states for each of the three species detected, labeled *pink*, *purple* and *blue* for PmoA, PmoB, and PmoC, respectively. The addition of the measured masses of the ejected subunits yields 98,633.6 Da, which is 62.4 Da smaller than the major protomer mass measured in the MS^1. Unassigned peaks were attributed to Triton X-100 clusters that did not form discernible charge state distributions. NL values reflect maximum signal intensity in the spectrum.
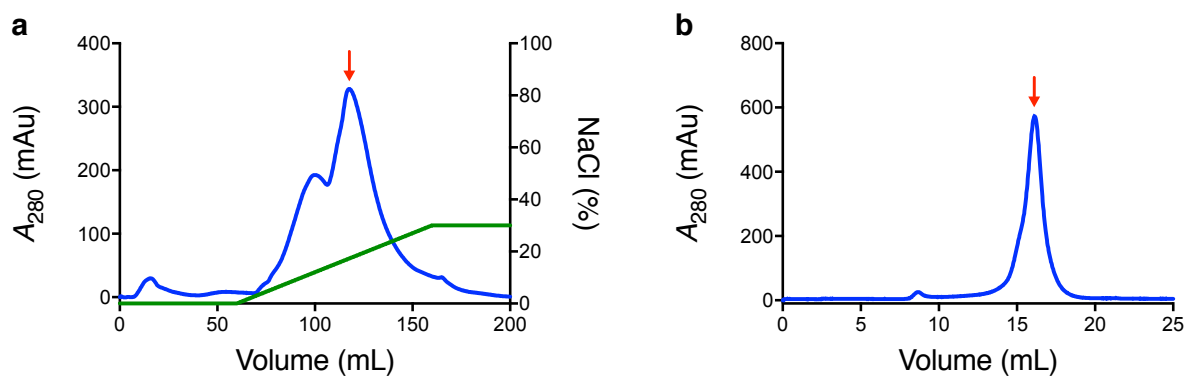
Figure S3.2. Purification of 20Z-pMMO in MSP1E3D1 nanodiscs.
a, HiTrap Q FF anion exchange chromatography purification showing 20Z-pMMO nanodisc complex (*red* arrow) followed by **b**, Superose 6 size exclusion chromatography purification. The absorbance at 280 nm (A_{280}) is shown in blue, and the % of 2 M NaCl in the gradient (v/v) is shown in *green*.
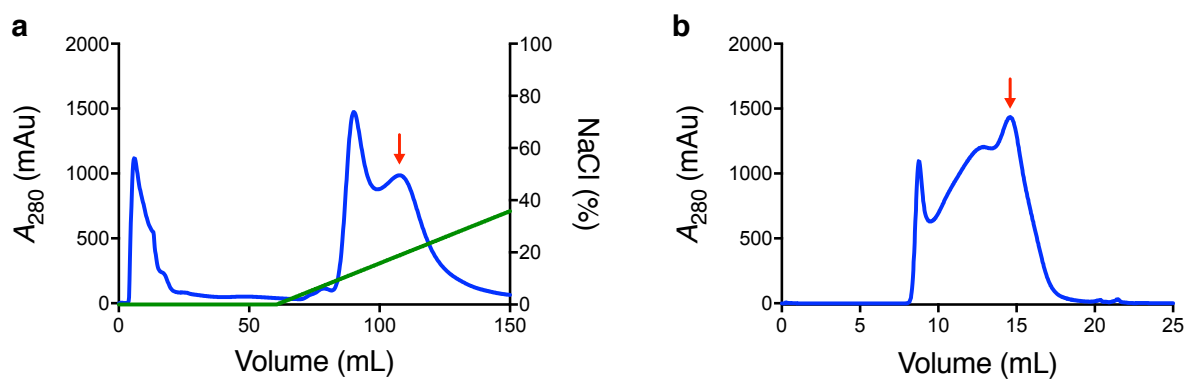
Figure S3.3. Purification of 20Z-pMMO in MSP2N2 nanodiscs. a, HiTrap Q FF anion exchange chromatography purification showing 20Z-pMMO nanodisc complex (*red* arrow) followed by **b**, Superose 6 size exclusion chromatography purification. The absorbance at 280 nm (A_{280}) is shown in *blue* and the % of 2 M NaCl in the gradient (v/v) is shown in *green*.
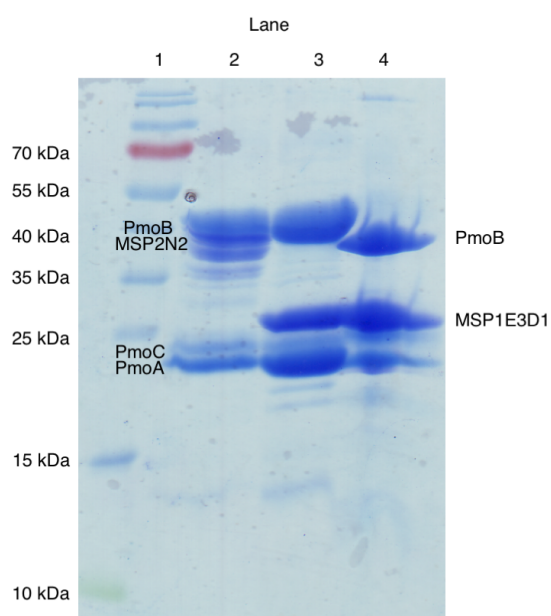
Figure S3.4. SDS-PAGE gel of pMMO samples reconstituted in nanodiscs. Lane 1, MW markers; lane 2, 20Z-pMMO in MSP2N2 nanodiscs; lane 3, 20Z-pMMO in MSP1E3D1 nanodiscs; lane 4, Rockwell-pMMO in MSP1E3D1 nanodiscs.
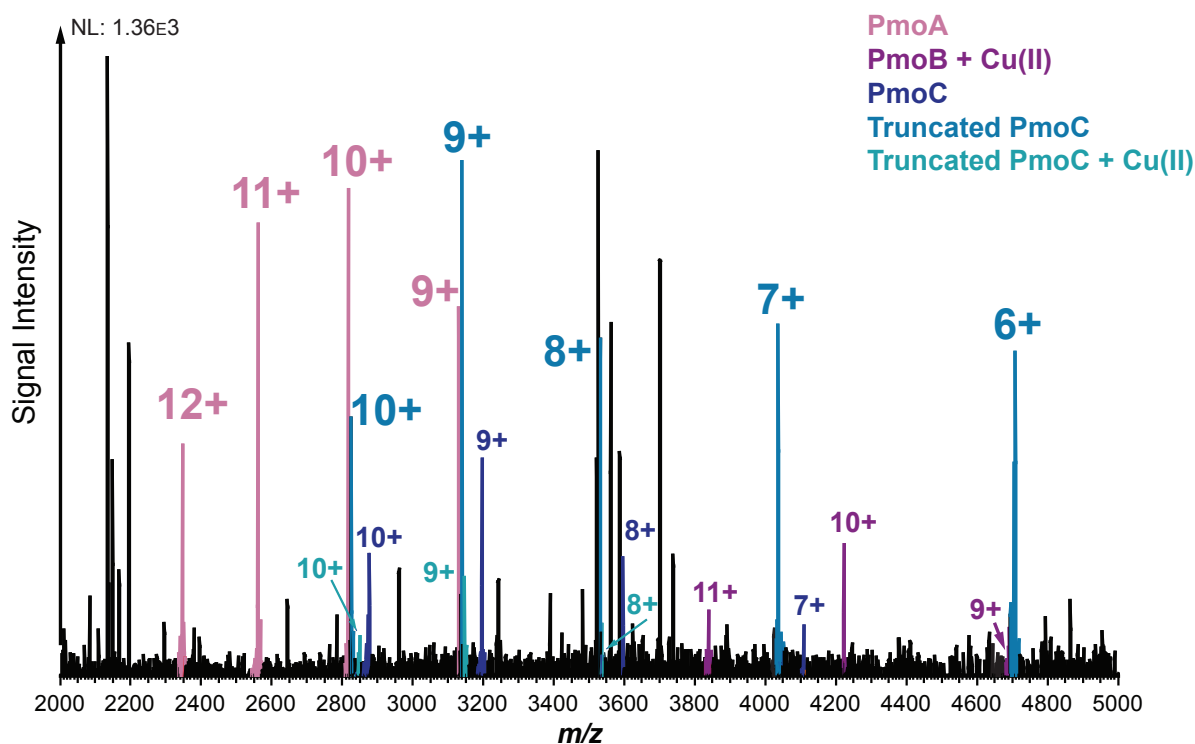
Figure S.3.5. Broadband MS^2 of 20Z-pMMO subunits ejected from MSP2N2 nanodiscs. Comparable results were obtained for 20Z-pMMO ejected from MSP1E3D1 nanodiscs. The spectrum shows charge state distributions for the five species detected, ejected from the nanodisc complex with CID of 195 V. The high intensity unidentified peaks can be attributed to charged lipid clusters of POPC used to assemble the nanodiscs. Notably, as indicated by the graphical fragment maps in Fig. 3.5b, PmoB includes residues His 33-Ile 414, consistent with a leader sequence that is cleaved post-translation. Moreover, PmoB was found to contain a methylation on Lys 36, which was fully localized by the tandem MS analysis of pepsin-digested peptides of 20Z-pMMO (Fig. S3.6a). PmoA was characterized to be Met$_{OFF}$ and NtAc. The MS^2 from the nanodisc reflects two populations of PmoC. One species was characterized to be Met$_{OFF}$ and NtAc. The major PmoC species is a truncated form lacking the first six N-terminal residues (MAATTE).
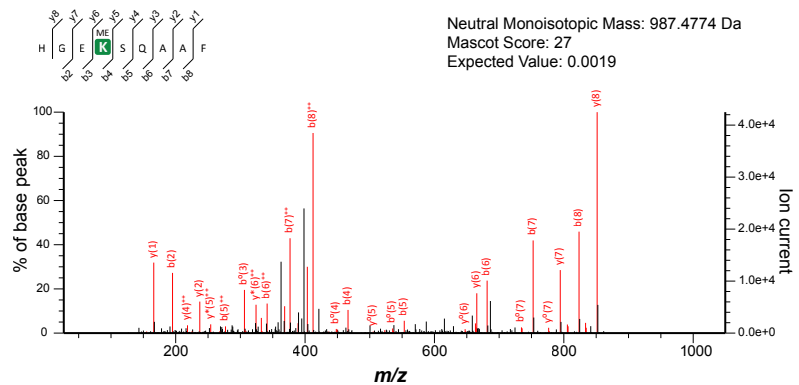
a **MS/MS of pepsin-digested peptide of 20Z-PmoB localizes methylation to Lys 36**

Neutral Monoisotopic Mass: 987.4774 Da
Mascot Score: 32
Expected Value: 0.00057
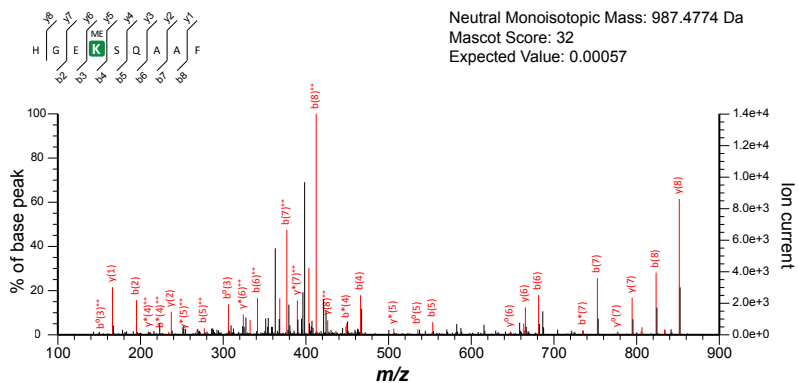
b **MS/MS of pepsin-digested peptides of 20Z-PmoC confirm N-terminal truncation**

Neutral Monoisotopic Mass: 2293.3005 Da
Mascot Score: 58
Expected Value: 1.6E-6
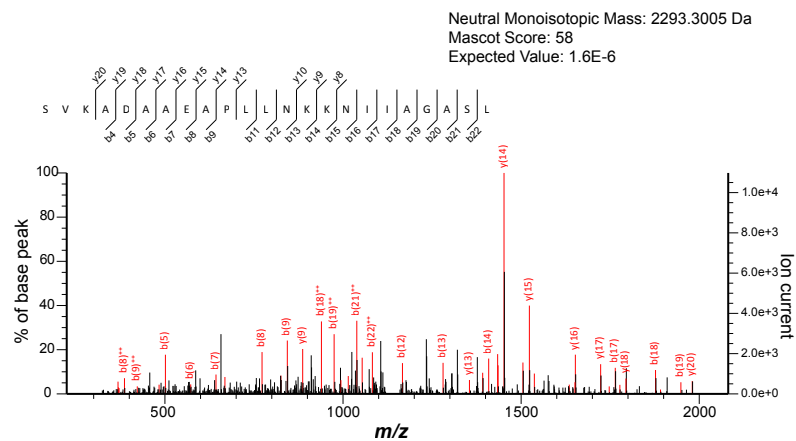
c **MS/MS of pepsin-digested peptides of 5G-PmoB localizes methylation to Lys 36**

Neutral Monoisotopic Mass: 987.4774 Da
Mascot Score: 27
Expected Value: 0.0019

Figure S.3.6. MS/MS fragmentation of pepsin-digested peptides to localize and confirm PTMs.

a, The detected 20Z-PmoB peptide contains a methylation on Lys 36. **b**, The detected 20Z-PmoC peptides indicate there is a population that contains N-terminal truncation of the first six residues MAATTE. **c**, The detected 5G-PmoB peptide contains a methylation on Lys 36. The y-axis on the left indicates the relative signal intensity as a percentage of the tallest peak in the spectrum; the y-axis on the right indicates the signal intensity in terms of ion current.
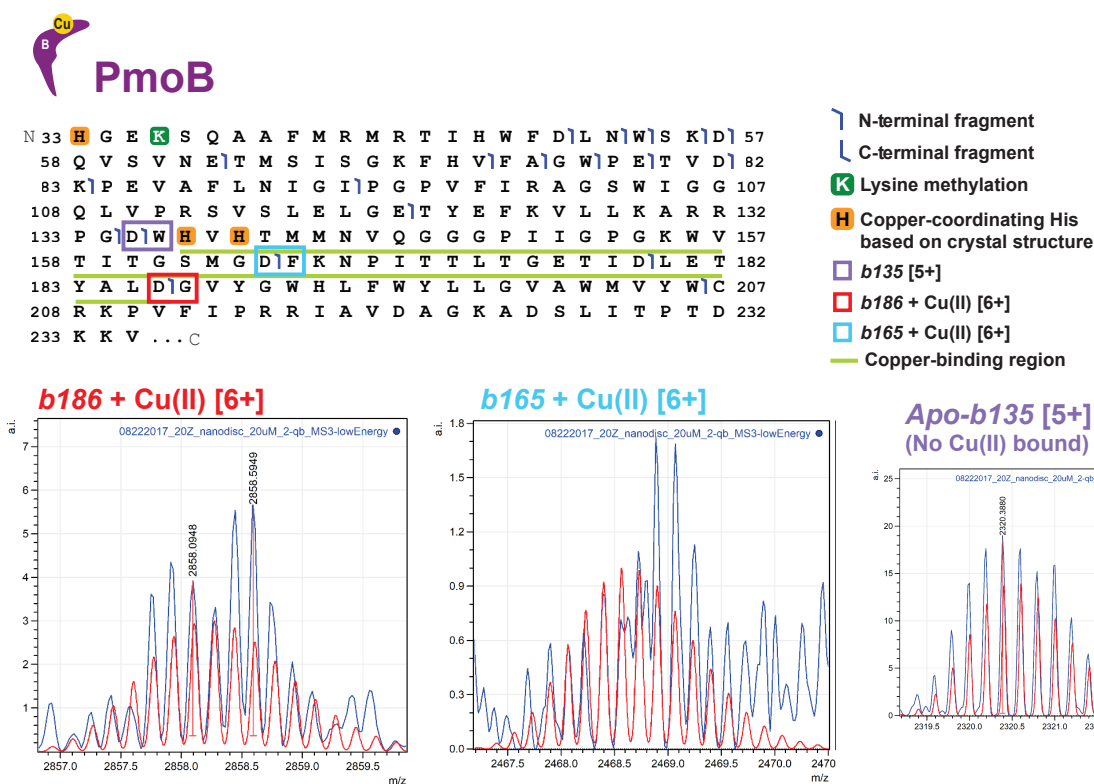
Figure S.3.7. Pseudo-MS³ fragmentation of 20Z-PmoB.
Fragmentation generates Cu(II)-bound *b* fragment ions (b_{186}, b_{165}) and an apo fragment ion (b_{135}) that help to verify the location of the copper center between residues Trp 136 and Asp 186.
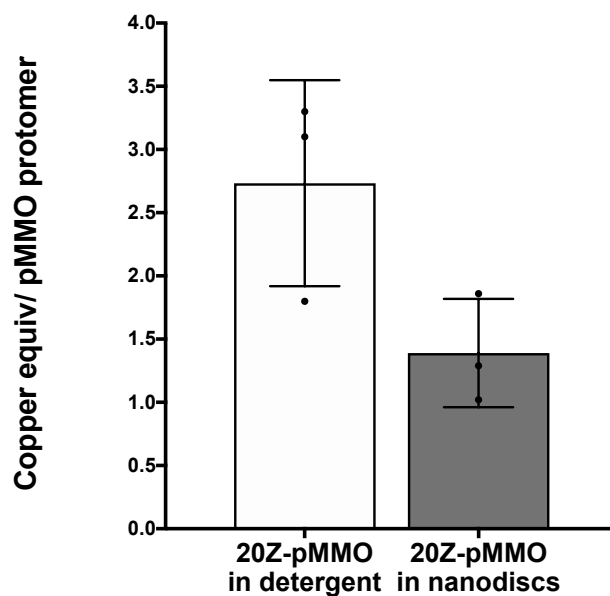
Figure S.3.8. Copper stoichiometry of 20Z-pMMO protomer in DDM and after MSP1E3D1 nanodisc reconstitution; n=3.
The copper content was measured using ICP-OES and pMMO concentration was measured using the DC-Lowry assay. Error bars represent standard deviation, and the *black* dots represent individual measurements.
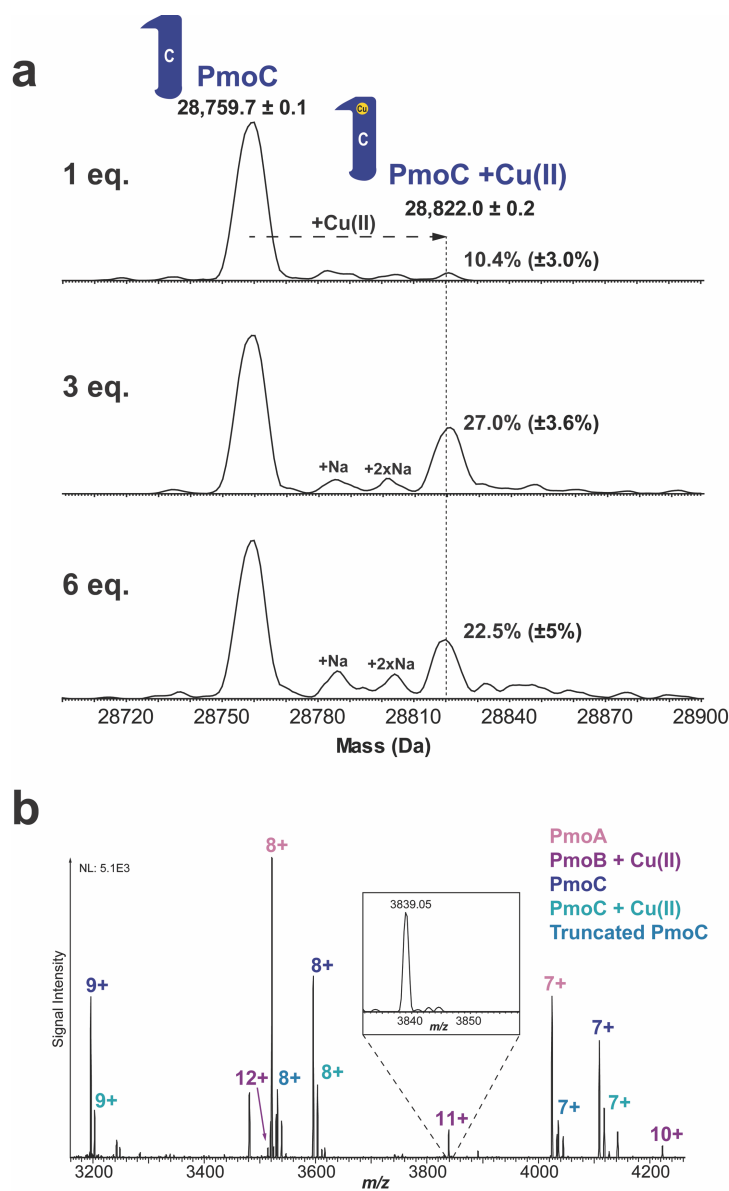
Figure S.3.9. nTDMS analysis of 20Z-pMMO in nanodiscs supplemented with exogenous copper ions post purification.
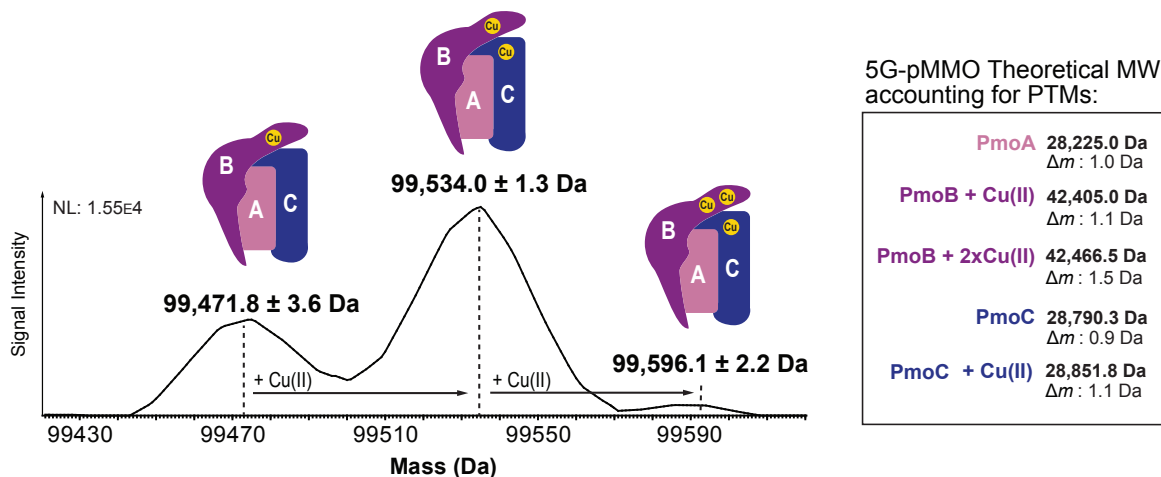**a,** Deconvoluted intact mass spectra reporting average masses and relative abundances of PmoC with and without Cu(II) ejected from 20Z-pMMO in MSP1E3D1 nanodiscs upon addition of 1, 3, and 6 molar equivalents (eq.) of copper per protomer to the electrospray buffer. **b,** Broadband mass spectrum of 20Z-pMMO subunits ejected from MSP1E3D1 nanodiscs incubated with 3 eq. of exogenous Cu(II) at CID energy of 195 V. The inset displays the 11+ charge state of copper-bound PmoB showing no additional copper binding after addition of 3 eq. of Cu(II)

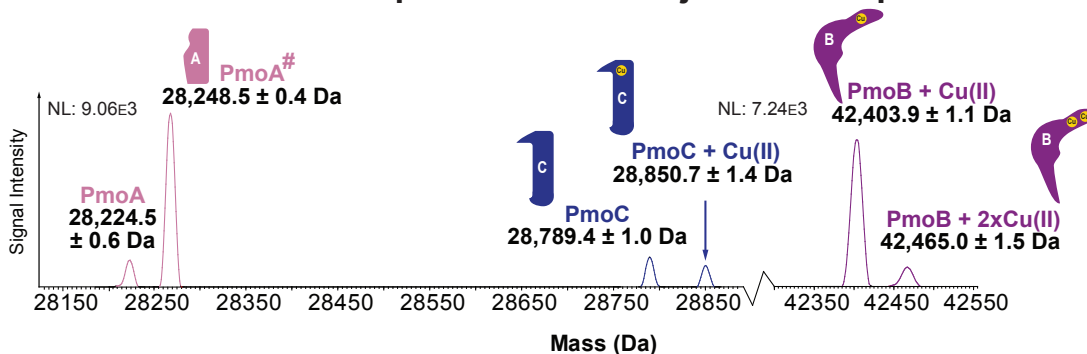**Raw MS¹ of 5G-pMMO protomer ejected from Triton X-100 micelle**
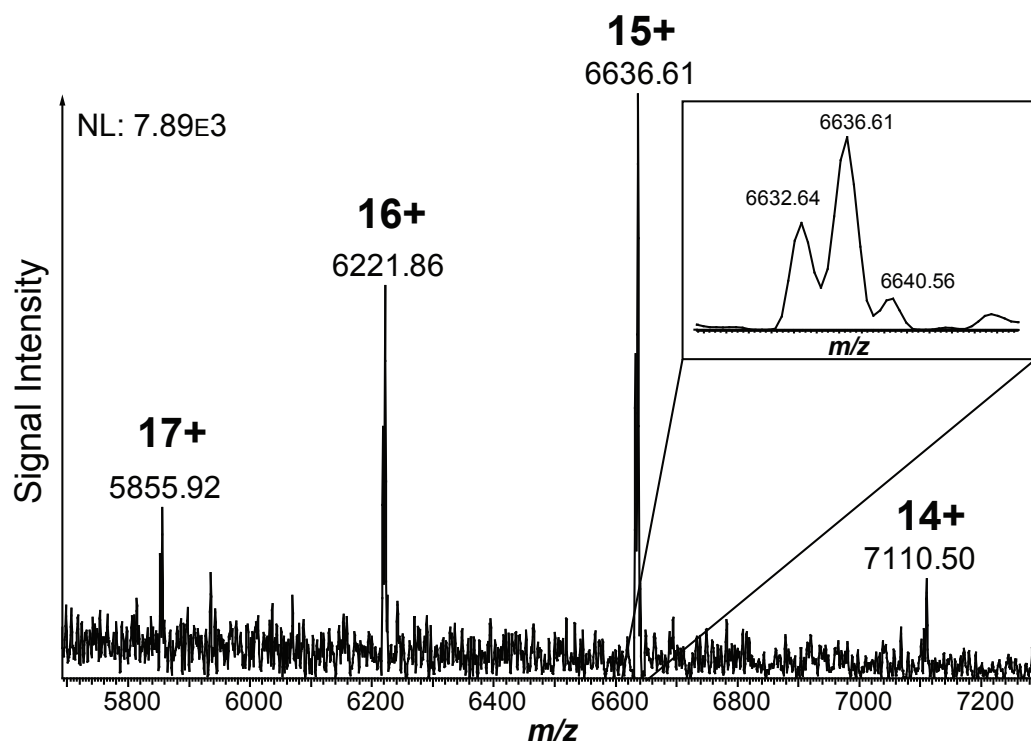
Figure S.3.10. Intact MS¹ spectrum of the 5G-pMMO protomer, showing a charge state distribution spanning the 14-17+ protonated states upon native ESI.
The inset is a zoom-in of the 15+ charge state, showing the presence of three protomer species. See **Figure S.3.10a** for mass deconvolution of this spectrum.

## a Deconvoluted MS[1]: 5G-pMMO protomers ejected from micelle

5G-pMMO Theoretical MW accounting for PTMs:

PmoA	28,225.0 Da Δm: 1.0 Da
PmoB + Cu(II)	42,405.0 Da Δm: 1.1 Da
PmoB + 2xCu(II)	42,466.5 Da Δm: 1.5 Da
PmoC	28,790.3 Da Δm: 0.9 Da
PmoC + Cu(II)	28,851.8 Da Δm: 1.1 Da

NL: 1.55E4

99,534.0 ± 1.3 Da

99,471.8 ± 3.6 Da

99,596.1 ± 2.2 Da

+ Cu(II)   + Cu(II)

b Deconvoluted MS[2]: 5G-pMMO subunits ejected from protomers

NL: 9.06E3

PmoA[#]
28,248.5 ± 0.4 Da

PmoA
28,224.5 ± 0.6 Da

NL: 7.24E3

PmoB + Cu(II)
42,403.9 ± 1.1 Da

PmoC + Cu(II)
28,850.7 ± 1.4 Da

PmoC
28,789.4 ± 1.0 Da

PmoB + 2xCu(II)
42,465.0 ± 1.5 Da

Figure S.3.11. nTDMS analysis of 5G-pMMO in Triton X-100 micelles.
a, Deconvoluted MS[1] of 5G-pMMO protomer upon ejection from a Triton X-100 micelle with CID of 195 V. The deconvoluted spectrum highlights the three protomer species detected, which differ in mass by the mass of Cu(II). The panel on the right contains the theoretical molecular weights of the 5G-pMMO subunits, accounting for Met$_{OFF}$ and NtAc of PmoA and PmoC and the methylation on PmoB Lys 36 characterized by the tandem MS of pepsin-digested peptides (**Figure S.3.6**). **b,** Deconvoluted MS[2] of 5G-pMMO subunits ejected upon protomer activation by collisions with neutral gas at the source. The spectrum shows detection of all subunits and indicates that PmoC and PmoB have mass shifts consistent with the binding of Cu(II). PmoB is found to mostly bind one Cu(II) ion; a small population of PmoB is shifted by a second mass of Cu(II), which could be binding at the bis-His site only observed in Bath-pMMO. PmoA is present as two populations: one with Met$_{OFF}$ and NtAc and another with an additional uncharacterized 24.0 Da modification. The observed masses in the MS[2] were used to infer the identity of the protomers detected by MS[1] in **a**. The masses of the protomers measured in the MS[1] match most closely to PmoA with the 24.0 Da modification. NL values reflect maximum signal intensity in the spectrum.
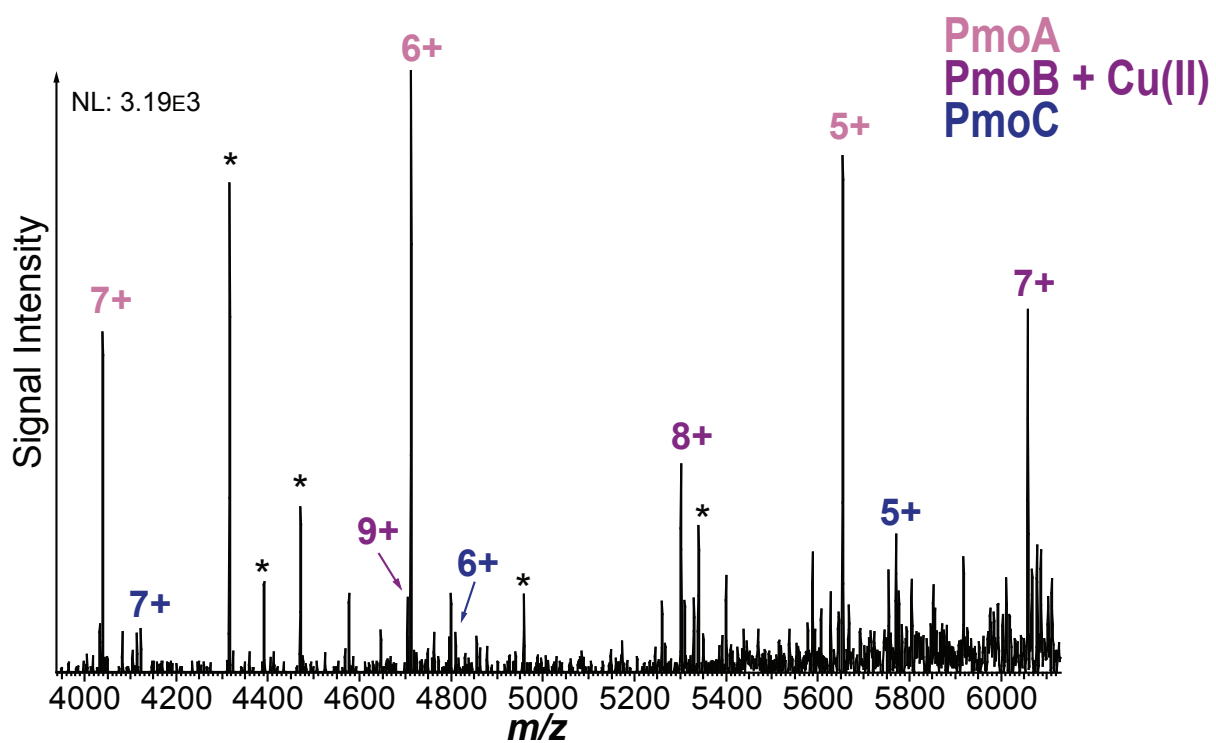
Figure S.3.12. Broadband MS² of 5G-pMMO subunits ejected from a Triton X-100 micelle using both CID and HCD activation (195 V and 150 V, respectively).
The spectrum shows charge state distributions for PmoA, PmoB + Cu(II), and full-length PmoC. The peaks labeled with an asterisk (*)did not form discernible charge state distributions and may originate from Triton X-100 clusters. See **Figure S.3.10b.** for mass deconvolution of this spectrum.
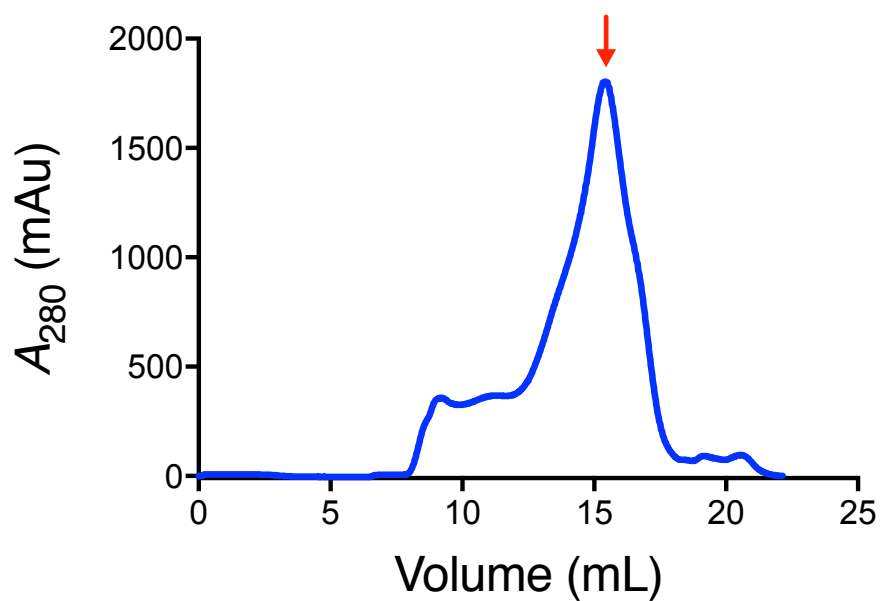
**Figure S.3.13. Purification of Rockwell-pMMO in MSP1E3D1 nanodiscs.**
The Superose 6 size exclusion chromatography purification is shown with the Rockwell-pMMO nanodisc complex labeled (*red* arrow). The absorbance at 280 nm (A_{280}) is shown in *blue*.
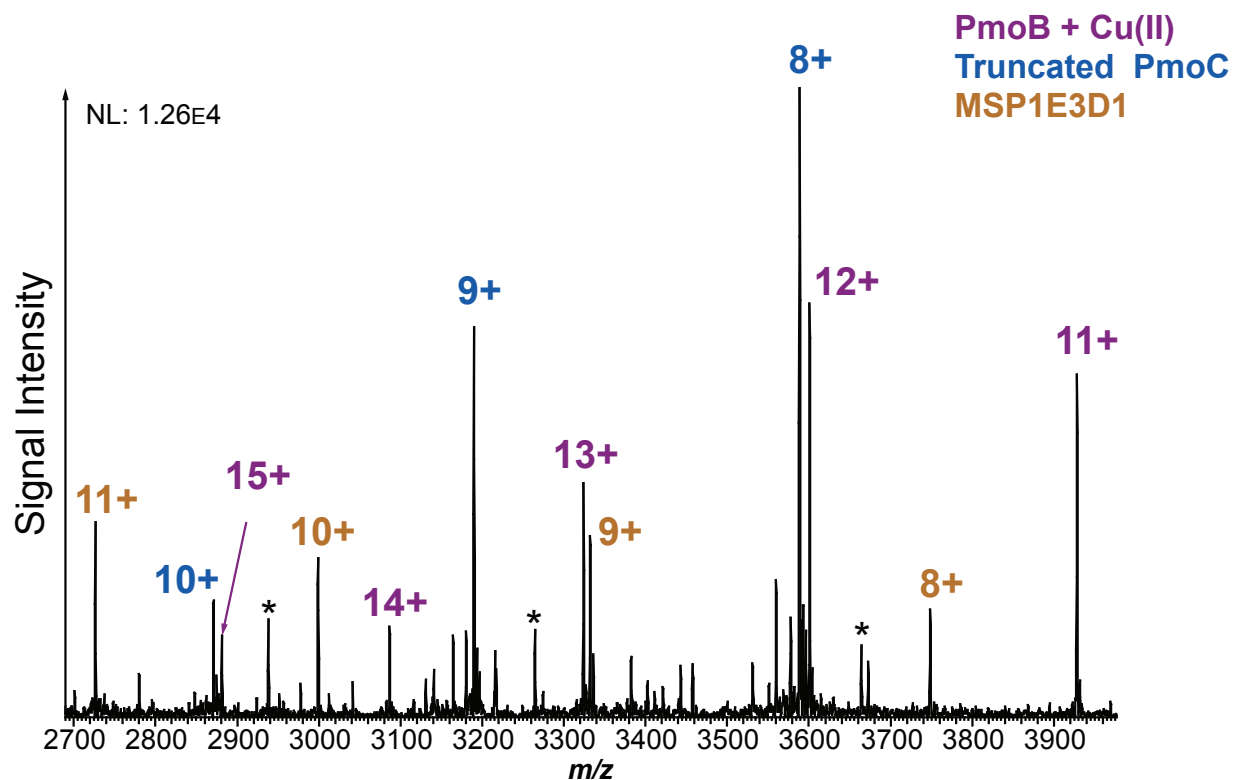
Figure S.3.14. Partial pseudo-MS^2 spectrum of Rockwell-pMMO subunits ejected from MSP1E3D1 nanodiscs.
The spectrum shows charge state distributions for PmoB + Cu(II), truncated PmoC, and MSP1E3D1. The peaks identified with an asterisk (*) correspond to an uncharacterized protein impurity. Other unidentified peaks do not form discernible charge state distributions and likely result from lipid clusters of POPC released upon collisional activation of the nanodisc-pMMO complex.
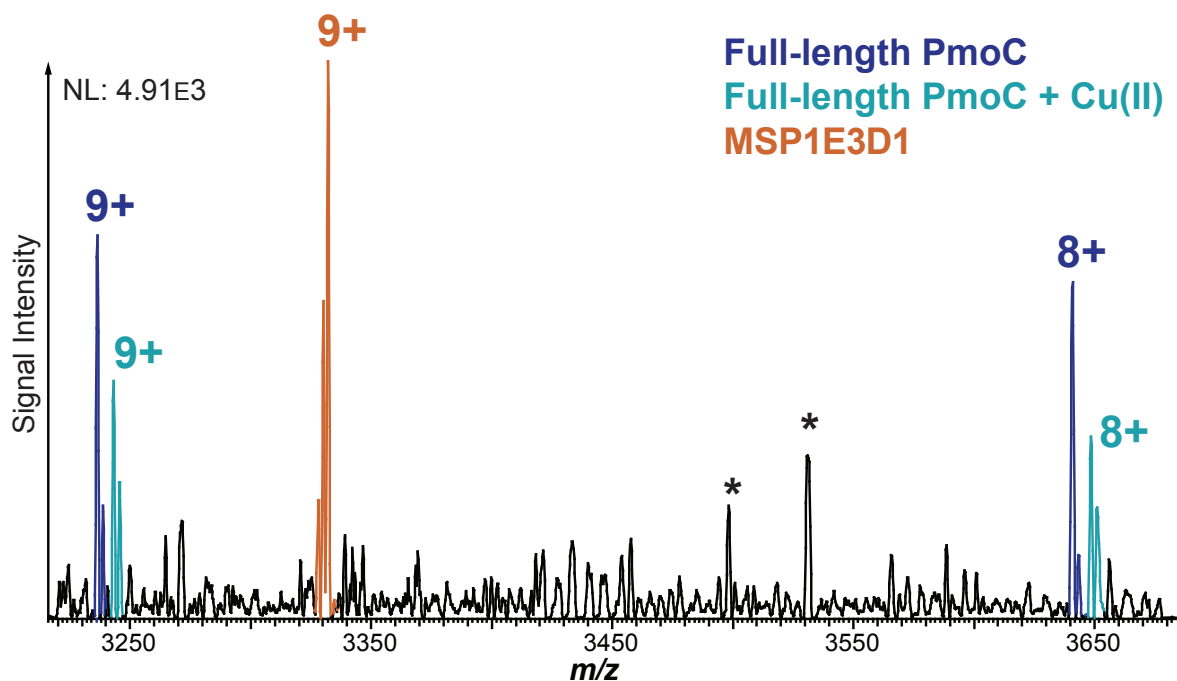
Figure S.3.15. Partial spectrum (~500 *m/z* wide) of the pseudo-MS² spectrum of Rockwell-pMMO subunits ejected from MSP1E3D1 nanodiscs supplemented with additional copper during reconstitution.
The spectrum shows the charge states 8+ and 9+for full-length PmoC and full-length PmoC + Cu(II), and the 9+ charge state for the MSP1E3D1. The peaks identified with an asterisk (*) likely result from lipid clusters released upon collisional activation of the nanodisc-pMMO complex, as they correspond to known cluster masses or do not form discernible charge state distributions.
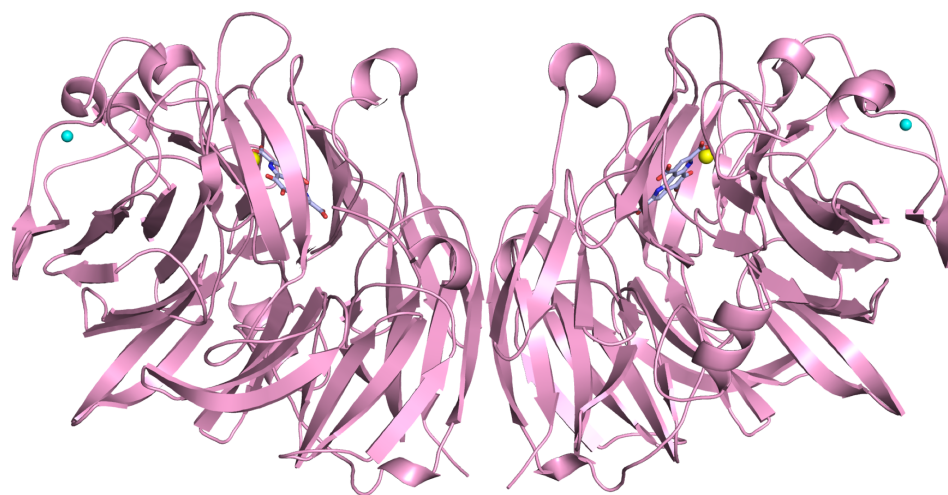
APPENDIX 3

SUPPLEMENTARY FIGURES
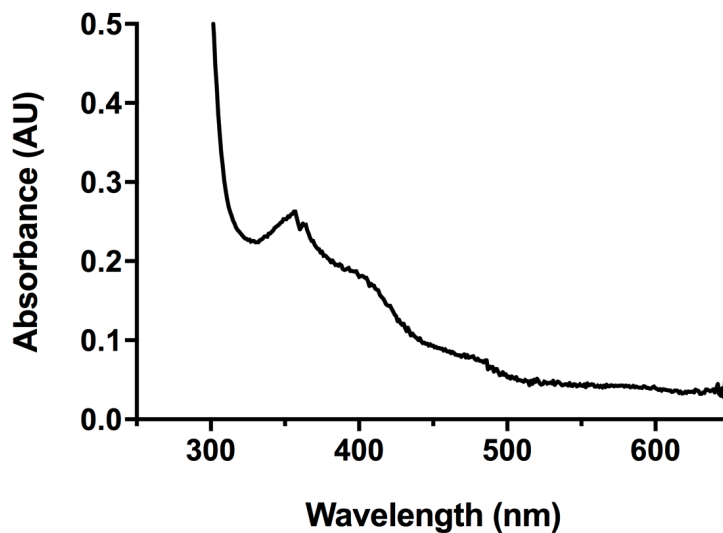
Figure S4.1. 5G-XoxF absorbance spectrum.
Monitoring 5G-XoxF during column chromatography is based on the peak around 345 nm corresponding to the PQQ cofactor. The peak around 415 nm is indicative of cytochrome contamination. A high 345 nm to 415 nm ratio indicates the presence of 5G-XoxF.

Figure S4.2. 5G-XoxF crystal packing.
The 5G-XoxF monomer (*pink*) shown with its symmetry mate forms the standard dimer of other MDHs. The La(III) ion is shown as a *yellow* sphere, the PQQ is shown as sticks, and a modeled sodium ion is shown as a *cyan* sphere.
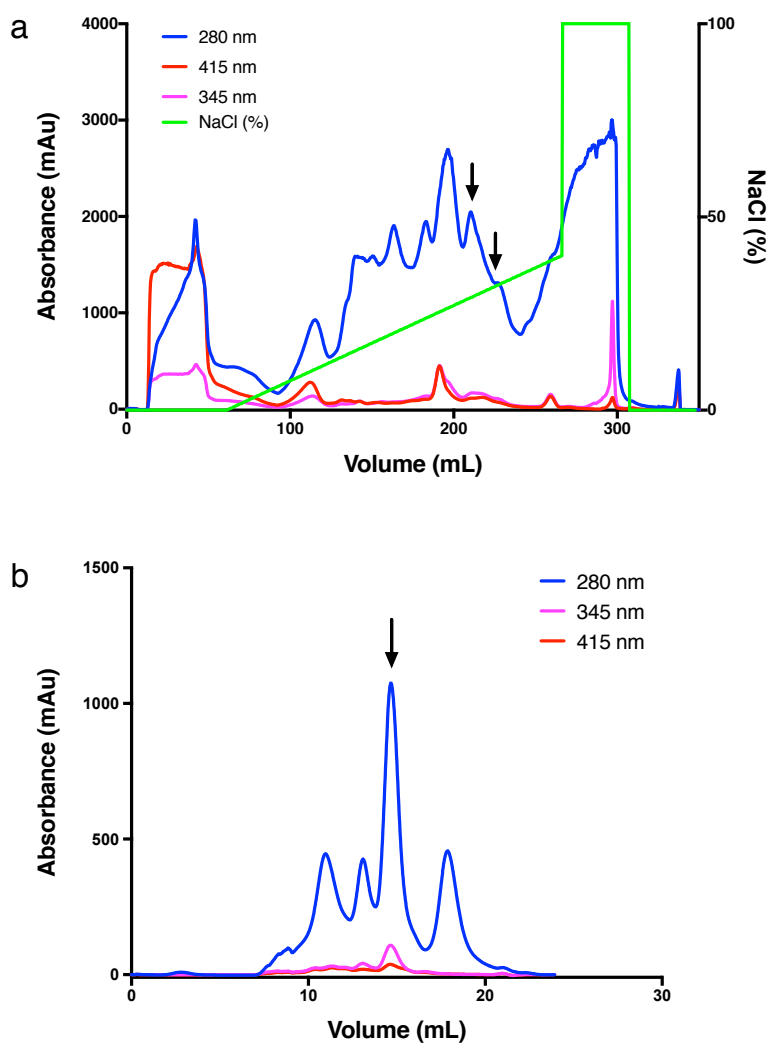
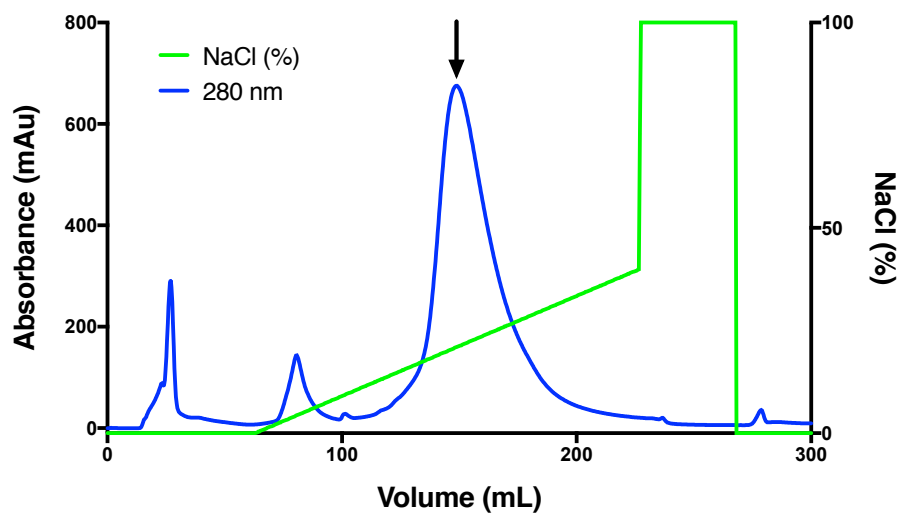**Figure S4.3. Purification of 5G-XoxF.**
a Anion exchange chromatogram of *Mm. buryatense* 5GB1C soluble protein fraction (50 mM-400 mM NaCl gradient shown as a *green* slope) and **b** Superdex 200 size exclusion trace. 5G-XoxF is present in the peaks indicated by black arrows. The absorbance at three wavelengths, 280 nm, 345 nm, and 415 nm, is shown in *blue*, *pink*, and *red*, respectively.
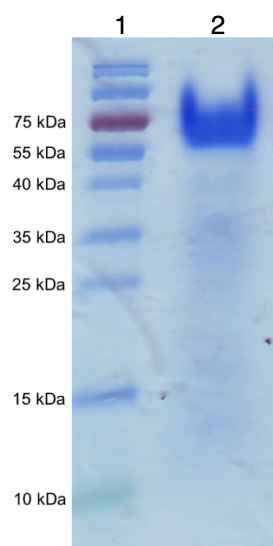
Figure S4.4. SDS-PAGE of 5G-XoxF purified.
Lane 1, molecular weight markers; lane 2, XoxF after the final purification step.

Figure S4.5. Purification of 5G-pMMO.
Anion exchange chromatogram of 5G-pMMO using Source 15Q. The absorbance at 280 nm is shown in *blue*. A 50-800 mM NaCl gradient is shown as a *green* slope (corresponding to 0-40%).
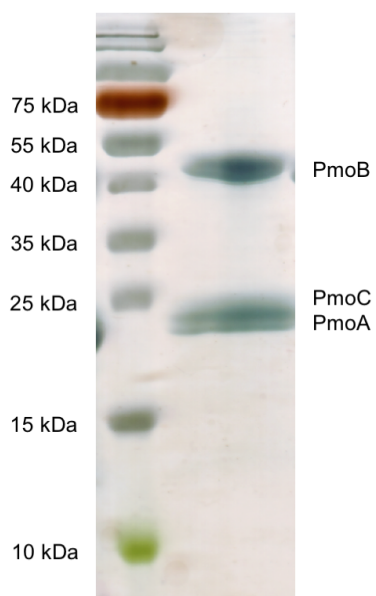
Figure S4.6. SDS-PAGE of pMMO purified from *Mm. buryatense* 5GB1C.
The three subunits of 5G-pMMO are labeled; PmoA and PmoC run closely together on a 15% SDS-PAGE gel.

SOO YEON RO
CURRICULUM VITAE
Email: sooro2017@u.northwestern.edu

Education

Sept 2013 – Present	Ph.D. Degree Northwestern University Interdisciplinary Biological Sciences Program Expected Graduation Date: 06/20/2019
Aug 2007 – Dec 2010	B.A. Degree University of California Berkeley Integrative Biology, *summa cum laude* Classics Civilization minor

Research Experience

Jan 2019 – Mar 2019	Intern Intrexon Corporation Project: Characterization of pMMO from product tolerant *Methyloccocus capsulatus* (Bath) strains
Sept 2013 – Present	Ph.D. Candidate Northwestern University, IBiS Principal Investigator: Amy Rosenzweig Project: A genetic approach to particulate methane monooxygenase
Sept 2012 – Aug 2013	Laboratory Technician University of California Los Angeles, Chemical Engineering Principal Investigator: James Liao Project: Engineering photosynthetic *Cyanobacteria* to produce biofuel
June 2009 – May 2011	Independent Undergraduate Researcher University of California Berkeley, Museum of Vertebrate Zoology Principal Investigator: Elieen Lacey Project: Population and evolutionary genetics of Toll-Like Receptor 4 gene in *Peromyscus*
Sept 2008 - Aug 2009	Volunteer Undergraduate Researcher Children's Hospital Oakland Research Institute Principal Investigator: Janelle A. Noble Project: Genome-wide association studies of Type I Diabetes in the African American population

Leadership/Career development activity

Winter 2016	Member, Northwestern Toastmasters Public Speaking Organization
Fall 2016	NUvention: Entrepreneurship Fellow
Summer 2016	Attendee, ComSciCon-Chicago (Communicating Science Workshop)
Summer 2016	Fellow, Ready Set Go (RSG) Science Communication Program
2015 – Present	Organizer, Northwestern University Biophysics Journal Club
Fall 2014 – Present	Lab Safety Designate
Summer 2012	Administrative Staff, IP Global English Camp

Awards, Fellowships, and Honors

2016   Poster Prize for Gordon Research Conference: Molecular Basis of One-Carbon Metabolism

2016   1st Place Poster Prize for Northwestern University Biophysics Symposium

2015   2nd Place Poster Prize for Northwestern University Biophysics Symposium

2014   NIH Biophysics Training Program Fellowship

2010   Highest Honor in Integrative Biology from UC Berkeley

2008   UC Berkeley International House Scholarship

2007   Korean American Foundation Scholarship

2007   Harvard Prize Book

Publications

Ro, S.Y.[*], Schachner, L.F. [*], Koo, C.W., Purohit, R., Remis, J., Liauw, B., Kelleher, N.L., Rosenzweig, A.C. Native top-down mass spectrometry provides insights into the copper centers of membrane-bound methane monooxygenase. *Nat. Commun*. accepted (2019).

Deng, Y[*], **Ro, S.Y.**[*], Rosenzweig, A.C. Structure and function of the lanthanide-dependent methanol dehydrogenase XoxF from the methanotroph *Methylomicrobium buryatense* 5GB1C. *J. Biol. Inorg. Chem.* **23**, 1037-1047 (2018).

Fisher, O.S., Kenney, G.E., Ross, M.O., **Ro, S.Y.**, Lemma, B.E., Batelu, S., Thomas, P.M., Sosnowski, V.C., Kelleher, N.L., Stemmler, T., Hoffman, B.M., Rosenzweig, A.C. Characterization of a long overlooked copper protein from methane- and ammonia-oxidizing bacteria. *Nat. Commun.* **9**, 4276 (2018).

Ro, S.Y., Ross, M.O., Deng, Y.W., Batelu, S., Lawton, T.J., Hurley, J.D., Stemmler, T.L., Hoffman, B.M., and Rosenzweig, A.C. (2018) From micelles to bicelles: Effect of the membrane on particulate methane monooxygenase activity. *J. Biol. Chem.* **23**, 1037-1047 (2018).

Kenney, G.E.; Dassama, L.M.K.; Pandelia, M.E.; Gizzi, A.S.; Martinie, R.J.; Gao, P.; DeHart, C.J.; Schachner, L.F.; Skinner, O.S.; **Ro, S.Y.**, Zhu, X.; Sadek, M.; Thomas, P.M.; Almo, S.C.; Bollinger, J.M., Jr.; Krebs, C.; Kelleher, N.L.; Rosenzweig, A.C. The biosynthesis of methanobactin. *Science* **359**, 1411-1416 (2018).

Ro, S.Y.; Rosenzweig, A.C. Recent advances in the genetic manipulation of *Methylosinus trichosporium* OB3b. *Methods Enzymol*. **605**, 339-345 (2018).

Dassama, L.M.K.; Kenney; G.E.; **Ro, S.Y.**; Zielazinski, E.L.; Rosenzweig, A.C. Methanobactin transport machinery. *Proc. Natl. Acad. Sci. USA*. **113**, 13027-13032 (2016).

Stine, A., Zhang, M., **Ro, S.Y.**, Clendennen, S., Shelton, M.C., Tyo, K.E., Broadbelt, L.J. Exploring de novo metabolic pathways from pyruvate to propionic acid. *Biotechnology Progress* **32(2)**, 303-11 (2016).

Lan, E., Chen, C., Lee, A., **Ro, S.Y.**, Liao, J. Metabolic engineering of cyanobacteria for photosynthetic 3-hydroxypropionic acid production from CO2 using *Synechococcus elongatus* PCC 7942. *Metabolic Engineering* **31**, 163-170 (2015).

Lan, E., **Ro, S.Y.**, Liao, J. Oxygen-tolerant coenzyme A-acylating aldehyde dehydrogenase facilitates efficient photosynthetic *n*-butanol biosynthesis in cyanobacteria. *Energy Environ. Sci.* **6**, 2672-2681 (2013).

* = authors contributed equally to publication of paper.

Presentations

Ro, S.Y., Rosenzweig, A.C. "Two monocopper centers drive methane oxidation in pMMO". Gordon Research Seminar: Molecular Basis of Microbial One-Carbon Metabolism. Oral Presentation. 2018.

Ro, S.Y., Rosenzweig, A.C. "Two monocopper centers drive methane oxidation in pMMO". Northwestern Biophysics Symposium. Oral Presentation. 2018.

Ro, S.Y., Rosenzweig, A.C. "Understanding particulate methane monooxygenase in a native-like environment". Gordon Research Seminar: Metals in Biology. Oral Presentation. 2017.

Ro, S.Y. "Asking microbes to fix our energy and pollution problems". Ready Set Go (RSG) Seven Minutes of Science Symposium. Oral Presentation. 2016.

Ro, S.Y., Rosenzweig, A.C. "Understanding particulate methane monooxygenase in a native-like environment". Gordon Research Conference: Molecular Basis of One-Carbon Metabolism. Poster Presentation. 2016.

Ro, S.Y., Rosenzweig, A.C. "Understanding particulate methane monooxygenase in a native-like environment". Northwestern Biophysics Symposium. Poster Presentation. 2016.

Ro, S.Y., Rosenzweig, A.C. "Structural characterization of particulate methane monooxygenase from *Methylomicrobium buryatense* 5G". Northwestern Biophysics Symposium. Poster Presentation. 2015.

Ro, S.Y., Macmannes, M., Lacey, E. "Determining the selective force behind TLR-4 in genus *Peromyscus*". UC Berkeley Cal Day. University of California Berkeley Museum of Vertebrate Zoology. Poster Presentation. 2010.

Ro, S.Y., Noble, J. "African American Bloodspots HLA-A". CHORI Summer Research Program.
Children's Hospital Oakland Research Center. Poster Presentation. 2009.

Teaching Experience
2015 – Present	Undergraduate Research Mentor, Northwestern URG
Fall 2016	Teaching Assistant, Protein Structure and Function
Spring 2015	Teaching Assistant, Biochemistry
2011-2013	Math/Science Private Tutor
Summer 2012	English Instructor, IP Global English Camp
Jun 2011 – June 2012	Science/SAT Instructor, Eton Educational Institute
Summer 2009	Math and English Tutor, Lighthouse Education Center
Summer 2007 – 2008	Math Tutor, JEI Learning Center

Community/Volunteer Service
Mar 2016	Judge, IJAS Regional Science Fair
Dec 2016	Judge, Goudy Science Fair
Jan 2015	Judge, Truman Regional Science Fair
Apr 2014	Judge, Chicago Area Undergraduate Research Symposium
Jan 2010 – Dec 2011	Student Mentor, KTMP Tutoring Association UC Berkeley
2009	Member, Habitat for Humanity